LABORATORY AND APPLIED STUDIES USING THERMAL INFRARED SPECTROSCOPY AND OTHER REMOTE SENSING TOOLS FOR THE UNDERSTANDING OF THE GEOLOGIC HISTORY OF MARS

A DISSERTATION SUBMITTED TO THE GRADUATE DIVISION OF THE UNIVERSITY OF HAWAIʻI IN PARTIAL FULFILLMENT OF THE REQUIREMENTS FOR THE DEGREE OF

DOCTOR OF PHILOSOPHY

IN

GEOLOGY & GEOPHYSICS

DECEMBER 2009

By
Meryl L. McDowell

Dissertation Committee:

Victoria E. Hamilton, Chairperson
G. Jeffrey Taylor
Patricia Fryer
F. Scott Anderson
James Bayman

We certify that we have read this dissertation and that, in our opinion, it is satisfactory in scope and quality as a dissertation for the degree of Doctor of Philosophy in Geology & Geophysics.

Dissertation Committee

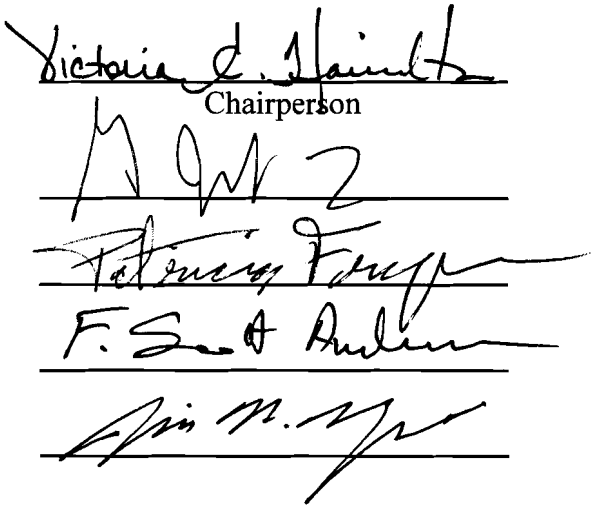

Chairperson

This work is dedicated to my encouraging and supportive family.

ACKNOWLEDGEMENTS

The work in this dissertation was possible only with the help of my advisor Vicky Hamilton and several co-authors- Sherry Cady, Jeff Berger, and Paul Knauth. I am also indebted to Steve Ruff, Josh Bandfield, Jeff Gillis-Davis, Melissa Lane, and Robin Fergason for their discussion, sharing of data, and assistance in sample measurements.

I must also thank Leona Anthony, who has provided such caring guidance to myself and the other students, along with Susan Van Gorder. I am very appreciative of the generosity shown to me by the Southwest Research Institute and its employees in Boulder, Colorado, where I was kindly taken in for a year. The first two years of my PhD was funded by the National Weather Service Research Fellowship awarded to me by the Geology & Geophysics Department at UH. Grants from the NASA programs Mars Data Analysis, Mars Fundamental Research, and 2001 Mars Odyssey Participating Scientist awarded to my advisor provided funding for the rest of my PhD work, for which I am very grateful.

I am so thankful for the people in my life. My family has always supported and encouraged me, and my friends, now and through the years, have given me many much-needed happy times, as well as providing an understanding ear in times of stress. I consider myself fortunate to have had teachers and professors that I respect and admire every step of the way through my years of school. I've always believed that things work out for the best, and I think that is exactly what happened when I came to Hawaii. Not only was I able to do interesting work and learn about things that fascinate me, I entered into one of the most wonderful communities that could possibly exist. My advisor Vicky has been supportive and understanding, and has pushed me to become a much better

scientist than I was when I started. I have to thank each of my committee members as well, Jeff Taylor, Patty Fryer, Scott Anderson, and Jim Bayman, because they have been encouraging and extremely helpful during the past years. My friends and fellow graduate students may be the most special and unique part of my PhD experience. These people share so much of themselves and their lives, it's like a surrogate family. They help anyone and everyone celebrate, commiserate, relax, and work. I wish I could personally thank each of them, but I will have to limit my acknowledgements to those who have had to deal with me on a daily basis. My roommates for several years, Carrie Brugger and Will Koeppen, are at the core of my Hawaiian family. Deon Van Niekirk and Aisha Morris cannot be left out, and neither can Mikki Osterloo, former roommate, officemate, and all-around amazing and inspiring friend. And even beyond all of this that I've found at UH, I come away with the best partner in all aspects of life, Loyc Vanderkluysen. He truly deserves thanks for his support, encouragement, helpful suggestions, and patience throughout this PhD experience.

So many people have helped me on this academic journey; I have certainly failed to mention many of them. Each one shares this achievement with me, and to me they are as integral a part of this dissertation as its numbers, images, and words.

ABSTRACT

Detailed studies reveal the compositional heterogeneity of the Martian surface and give clues to its geologic history. My work analyzes three compositions or phases. The first is the basaltic composition of intracrater deposits in southwestern Margaritifer Terra. These deposits have higher thermal inertia relative to their surroundings and likely are solid, coherent units. The similarity of the deposits' compositions to that of the region suggests that they were formed from lithification of local basaltic sediments, though the emplacement of primary igneous material is also possible.

The second study focuses on detecting and identifying phyllosilicate minerals in thermal infrared (TIR) data. Areas where visible to near-infrared (VNIR) spectra indicate the presence of phyllosilicates show compositional variation in Thermal Emission Imaging System (THEMIS) TIR images consistent with phyllosilicate. Thermal Emission Spectrometer (TES) TIR spectra in our study regions are modeled by phyllosilicate near the 10 – 15% detection limit of the technique. Though TES TIR spectra indicate that the compositions differ from the surrounding regions, the differences are not caused solely by changes in phyllosilicate abundance. We suggest that a phase not included in the spectral library may be used to model phyllosilicates in TES TIR spectra. This could explain the inconsistent trend in phyllosilicate abundance that we observe.

The third part of my work is a fundamental laboratory analysis of chert and amorphous silica. Their spectral character varies in the TIR and VNIR. Chert and amorphous silica spectra differ in the TIR region but may be similar in the VNIR region. Factors such as surface roughness and incidence angle cause variation in the TIR spectra,

but the variation is non-unique. We do not find an obvious way to link spectral character to environment of formation. At TES spectral resolution silica phases may be distinguished from one another but this is more difficult at THEMIS resolution. Spectral indices in the VNIR may not detect all occurrences of chert and amorphous silica, especially if the VNIR spectrum has no features. When applied to three high-silica sites on Mars, this new information confirms that they are dominated by chert or coarsely crystalline quartz.

TABLE OF CONTENTS

Acknowledgements……iv
Abstract……..vi
List of Tables……xi
List of Figures……xii
Preface……xv
Chapter 1……..……1
1. Introduction……1
1.1. Visible to Near-Infrared and Thermal Infrared Spectroscopy……4
1.2. Purpose of the Current Work……..7
Chapter 2: Geologic characteristics of relatively high thermal inertia intracrater deposits in southwestern Margaritifer Terra, Mars……..10
Abstract……10
1. Introduction……..11
2. Approach……..14
2.1. Data Sets and Data Selection……..14
2.2. Thermophysical Properties……16
2.3. Albedo……19
2.4. Dust Cover Index……20
2.5. Composition……20
2.5.1. THEMIS Compositional Variation……20
2.5.2. TES Compositional Analysis……21
2.5.3. THEMIS Compositional Analysis……22
3. Results……..25
3.1. Thermophysical Properties……25
3.2. Albedo……26
3.3. Dust Cover Index……30
3.4. Composition……30
3.4.1. THEMIS Compositional Variation……30
3.4.2. TES Compositional Analysis……32
3.4.3. THEMIS Compositional Analysis……34
3.5. Topography……38
3.6. Geomorphology……..38
4. Discussion……42
5. Summary and Conclusions……..51
Acknowledgements……..53
Chapter 3: Seeking phyllosilicates in thermal infrared data: A laboratory and Martian data case study……..54
Abstract……54
1. Introduction……..56
1.1.The Search for Phyllosilicates……57
1.2. This Study……..61
2. Data Sets and Methods……65
2.1. Thermal Infrared Data……65

2.1.1. TES Data……65
2.1.2. THEMIS Data……71
2.2. Numerical Mixture Analysis……..72
3. Results……74
3.1. TES Regional Phase Abundance Maps……..74
3.1.1. Plagioclase Feldspar……..76
3.1.2. Pyroxene……76
3.1.3. Olivine……78
3.1.4. High Silica Phases……79
3.1.5. Other Phases……..79
3.2. Numerical Mixture Analysis……..80
3.2.1. Behavior at THEMIS Resolution……..80
3.2.2. Effects of Changing Deconvolution Parameters and Other Variables on TES Modeled Abundances……82
3.3. Detailed Examination of Phyllosilicate-bearing Material in TIR Data……..89
3.3.1. THEMIS Data……89
3.3.2. TES Data……92
4. Discussion……100
4.1. Regional Composition……100
4.2. Numerical Mixture Analysis……103
4.3. Phyllosilicate-bearing Material in the Vicinity of the Nili Fossae……..104
4.4. What is the Explanation for Widespread Phyllosilicate Detections by TES? ……105
5. Summary & Conclusions……..110
Acknowledgements……112
Chapter 4: Visible to near-infrared and thermal infrared spectral properties of chert and amorphous silica 1: Laboratory analysis……113
Abstract……113
1. Introduction……114
1.1. Background: Chert and Amorphous Silica and their Spectral Properties….117
2. Samples and Analytical Methods……..122
2.1. Physical Analyses……122
2.2. Thermal Infrared Spectral Measurements……129
2.3. Visible to Near-infrared Spectral Measurements……129
3. Results……130
3.1. Physical Analyses……130
3.2. Thermal Infrared Spectral Measurements……138
3.2.1. Spectral Variation between Samples……..138
3.2.2. Spectral Variation within a Samples……144
3.3. Visible to Near-infrared Spectral Measurements……150
3.3.1. Spectral Variation between Samples……..150
3.3.2. Spectral Variation within a Sample……153
4. Discussion……154
4.1. Comparison with Chert and Amorphous Silica Spectra from Previous Studies……154

4.2. Variations in Silica Spectral Features in Chert and Amorphous Silica……156
4.3. Potential Causes of Thermal Infrared Spectral Variations……..158
4.4. Contribution of Other Phases to Chert and Amorphous Silica Spectra……163
4.5. Interpreting Chert and Amorphous Silica Type or Origin from Spectral Characteristics……..165
5. Summary and Conclusions……167
Acknowledgements……169
Chapter 5: Visible to near-infrared and thermal infrared spectral properties of chert and amorphous silica 2: Application to Mars……170
Abstract……..170
1. Introduction……171
2. Methods……..174
2.1. Effects of Resolution on Thermal Infrared Spectral Features……..174
2.2. Visible to Near-infrared Spectral Indices……175
2.3. Application to Silica-rich Sites on Mars……..182
3. Results……185
3.1. Effect of Resolution on Thermal Infrared Spectral Features……185
3.2. Visible to Near-infrared Spectral Indices……192
3.3. Application to Silica-rich Sites on Mars……..194
4. Discussion……..201
4.1. Detecting Chert and Amorphous Silica in Thermal Infrared Spectra……..201
4.2. Detecting Chert and Amorphous Silica in Visible to Near-infrared Spectra……..203
4.3. Martian Silica-bearing Sites……..205
4.3.1. Gusev Crater……205
4.3.2. Northern Syrtis……206
4.3.3. Western Hellas Basin……..207
4.3.4. Eos Chasma……..210
4.4 Environments of Silica Formation and Associated Phases……211
5. Summary and Conclusions……213
Acknowledgements……216
Works Cited……217

LIST OF TABLES

Table Page

2.1 Spectral Library……..23

2.2 Average Lambert Albedo…….29

2.3 ST1 Modeled Abundances……..35

2.4 Intracrater Deposits Modeled Abundances……..36

2.5 Modeled abundances of Group 3 from *Rogers and Christensen* [2007] Compared to Intracrater Deposits…….47

3.1 Spectral Library for Regional Deconvolution…….67

3.2 Spectral Library for Localized Deconvolutions……..69

3.3 Numerical Mixture Analysis Deconvolution Parameters……75

3.4 TES Modeled Abundances from Local Study Areas……..94

4.1 Chert and Amorphous Silica Samples……..123

4.2 Analyses Performed on Samples……..127

4.3 Petrographic Descriptions of Selected Samples……131

4.4 Range of R_a Values……137

4.5 Positions of Selected Emissivity Minima in Chert and Amorphous Silica...141

5.1 VNIR Spectral Indices Used in This Study……..179

5.2 Range of Index Values for Common Igneous Minerals……181

5.3 Parameters Combined for Each Summary Parameter Composite Image…..184

LIST OF FIGURES

Figure Page

2.1 Southwestern Margaritifer Terra Study Area……..12

2.2 Nighttime Thermal Infrared Image of an Intracrater Deposit……..17

2.3 Thermal Inertia of an Intracrater Deposit……27

2.4 Maximum Thermal Inertia vs. Mean Albedo of Intracrater Deposits…….28

2.5 DCS Images Indicating Spectral Variation……..31

2.6 TES Emissivity Spectra of Intracrater Deposits……..33

2.7 THEMIS Emissivity Spectra of Intracrater Deposits……..37

2.8 Spatial Distribuation, Size, and Elevation of Intracrater Deposits……..39

2.9 Selected MOC Images of Intracrater Deposits……40

2.10 THEMIS Visible Image of Intracrater Deposit……..43

3.1 VNIR Identification of Phyllosilicates in the Vicinity of the Nili Fossae…..60

3.2 Map of the Nili Fossae and Surrounding Region……63

3.3 TES Regional Abundance Maps for Selected Phases……..77

3.4 Numerical Mixtures of Nontronite and ST1 Spectra at THEMIS Resolution.81

3.5 Effects of Noise and Wavelength Range on Modeled Phyllosilicate Abundances……83

3.6 Phyllosilicate Spectra Used in Numerical Mixture Analysis Deconvolutions……..85

3.7 Effect of Wavelength Range and Spectral Library on Modeled Phyllosilicate Abundances……86

3.8 Modeled Abundances of Phyllosilicate Compared to Known Abundances When Phyllosilicates are Reported as a Group……..88

3.9 THEMIS DCS Images and Spectra of Local Study Areas……..90

3.10 TES Spectra of Local Study Areas……93

4.1 Spectra of Coarsely Crystalline Quartz, Chert, and Amorphous Silica in the TIR and VNIR……..120

4.2 Photos of Chert and Amorphous Silica Samples……...124

4.3 SEM Secondary Electron Images of Cut and Rough Surfaces……..133

4.4 SEM Secondary Electron Images of 9X Cut and Rough Surfaces……134

4.5 Surface Profile Adjustment for Largest-scale Variation……135

4.6 Adjusted Profiles of the Cut and Rough Surfaces of Chert and Amorphous Silica……136

4.7 Thermal Infrared Emissivity Spectra of Chert and Amorphous Silica……..139

4.8 Variation of Thermal Infrared Emissivity Spectra with Sample Orientation……...146

4.9 Variation of Thermal Infrared Emissivity Spectra with Incidence Angle….147

4.10 Variation of Thermal Infrared Emissivity Spectra with Surface Roughness……148

4.11 Visible to Near-infrared Reflectivity Spectra of Chert and Amorphous Silica……151

4.12 Phyllosilicate Features in Thermal Infrared and Visible to Near-infrared Spectra of Chert and Amorphous Silica……..155

4.13 Comparison of R_a Values with the Relative Depths of the Quartz Doublet Minima……161

4.14 Carbonate Features in Thermal Infrared and Visible to Near-infrared Spectra of Chert and Amorphous Silica……164

5.1 Visible to Near-infrared Spectra of Chert and Amorphous Silica at CRISM Resolution……176

5.2 Illustration of Spectral Indices Positions……...180

5.3 Thermal Infrared Spectra of Chert and Amorphous Silica at 20 cm^{-1} (TES) Resolution……186

5.4 Thermal Infrared Spectra of Chert and Amorphous Silica at THEMIS Resolution……188

5.5 Thermal Infrared Spectra of Other High Silica and Amorphous Phases…...191

5.6 Index Values Calculated for Chert and Amorphous Silica Spectra……..193

5.7 THEMIS DCS Images and Spectra of our Martian Study Sites……195

5.8 High-silica Material at Home Plate in Gusev Crater……196

5.9 Martian High-silica Material Spectra and similarly shaped Chert and Amorphous Silica Spectra……198

5.10 CRISM Summary Parameter Composite Images for our Martian Study Sites……..199

5.11 CRISM Ratio Spectra from our Martian Study Sites……..200

PREFACE

This dissertation is a collection of four manuscripts, two of which have been published in a peer-reviewed scientific journal. Chapter Two, "Geologic characteristics of relatively high thermal inertia intracrater deposits in southwestern Margaritifer Terra, Mars" was published in volume 112 of the Journal of Geophysical Research- Planets and is doi:10.1029/2007JE002925. Chapter Three, "Seeking phyllosilicates in thermal infrared data: A laboratory and Martian data case study", was also published in the Journal of Geophysical Research- Planets, volume 114, and is doi:10.1029/2008JE003317. The third and fourth manuscripts (Chapters Four and Five) will undergo minor additions and be submitted as companion papers to a peer-reviewed scientific journal as well.

Though there are multiple authors for these papers, I am the lead author on each. In Chapter Two I performed all the analyses and writing, whereas the co-author Victoria Hamilton acted as a teacher and advisor. All tasks for Chapter Three were conducted by myself; Victoria Hamilton provided direction, mentoring, and helpful discussion. I collected and analyzed the thermal infrared and visible to near-infrared spectra used in Chapters Four and Five. The physical and chemical analyses of the samples were done by co-authors Sherry Cady and Jeff Berger. Sherry Cady also supplied some of the samples along with Paul Knauth. I did the integration of the spectral, physical, and chemical analyses, as well as the applications to Martian data in Chapter Five and preparation of the manuscripts. Co-author Victoria Hamilton provided advice and direction. In every case the co-authors contributed by suggesting revisions for the manuscript.

CHAPTER 1

1. Introduction

The work I present here concerning Martian surface mineralogy is one piece in the large and complex puzzle that planetary scientists have been striving to assemble. Though each of the following chapters focuses on a small question, they are important stepping stones to the larger picture. Information on composition and its variation across the surface of Mars helps us to understand the processes that have acted in the past and allows us to extrapolate from the characteristics of the surface to the composition, structure, and history of the planet's interior. Until we are able to delve beneath the surface, our knowledge of the inner workings of Mars must come from these types of clues and the few Martian meteorites in our possession. From the elemental abundances of the interior of the planet we can infer something about its formation and the happenings in the inner solar system at that time. Ultimately, any information about the solar system has potential to be related back to our own world and our seemingly unique place within it.

To gather this integral compositional information of the Martian surface we must rely on remote observations from orbit or from landers and rovers on the ground. Some amount of compositional information can be interpreted from visible images showing the morphology of the surface. Mineralogy and elemental abundance can be more directly measured using instruments that detect energy in the thermal infrared (TIR), visible to near-infrared (VNIR), and gamma ray regions. Landers and rovers can use additional instruments such as a Mossbauer spectrometer and alpha particle X-ray spectrometer to determine the chemistry.

Of these methods, thermal infrared and visible to near-infrared spectroscopy are particularly helpful in providing information on the general composition of the Martian surface and spotting local variations in mineralogy. Both approaches can be used remotely from orbit, allowing for the examination of expansive areas and distant locations across the globe. These two techniques are well-suited to compositional investigation because silicates, the primary minerals of rocky planets such as Mars, have fundamental features in the thermal infrared region that enable their identification, and the non-silicate phases generally have components that produce characteristic features in the VNIR region. They are complimentary to one another and their usefulness is maximized when used in conjunction.

Our current understanding of Mars geology has been shaped predominantly by information gathered by TIR and VNIR spectroscopic instruments. Thermal infrared spectra from the Thermal Emission Spectrometer (TES) [*Christensen et al*., 1992] showed that the composition of the planet is dominantly basaltic and can be divided into two general categories, the surface type 1 (ST1) basalt and the surface type 2 (ST2) basaltic andesite [*Bandfield et al*., 2000b]. ST2 has also been suggested to be weathered basalt [*Wyatt and McSween*, 2002]. More recently *Rogers et al*. [2007] have looked at detailed regional compositions and found that they can be better represented by 11 spectral shapes.

More local studies using TES and the TIR multispectral Thermal Emission Imaging System (THEMIS) [*Christensen et al*., 2004] have shown the small scale heterogeneities of the Martian surface. Areas of olivine enrichment have been identified by *Hoefen et al*. [2003], *Hamilton et al*. [2003], and *Koeppen and Hamilton* [2008].

Crystalline hematite is present in some regions such as Meridiani Planum [*Christensen et al*., 2000a; *Christensen et al*., 2001b]. *Bandfield et al*. [2004b] and *Bandfield* [2006; 2008] have located spectrally unique spots suggested to be silica-rich phases. Chlorides have also been proposed by *Osterloo et al*. [2008].

The two most recent spectrometers, the Observatoire pour la Mineralogie, l'Eau, les Glaces et l'Activité (OMEGA) [*Bibring et al*., 2005] and the Compact Reconnaissance Imaging Spectrometer for Mars (CRISM) [*Murchie et al*., 2007], both operate in the visible to near-infrared range and provide new details to the Martian story. Higher spatial resolution refines the distribution and identification of phases such as the olivine-rich materials in some areas [*Mustard et al*., 2007b]. These visible to near-infrared spectrometers also made an important discovery, which is the positive identification of clay minerals on Mars [*Bibring et al*., 2005; *Bishop et al*., 2008; *Mustard et al*., 2008; *Poulet et al*., 2005]. Researchers had been looking for concrete evidence of weathering that they expected based on the planet's basaltic composition and the presence of water-carved features. Visible to near infrared observations also suggest the presence of other minerals such as sulfate, carbonate, and hydrated silica [*Bibring et al*., 2005; *Ehlmann et al*., 2008b; *Gendrin et al*., 2005; *Milliken et al*., 2008].

Many questions surrounding the history of Mars still remain, however. My work addresses several poorly understood aspects of Martian geology by investigating surface composition and its derivation from TIR and VNIR spectroscopy. One such question is about the other kinds of processes that are or have been active on Mars beyond the obvious large-scale basaltic volcanism. We can learn more about this by studying compositional heterogeneity. Each of the following chapters in this dissertation is based

on identifying unique areas on Mars or better constraining the methods used for their identification. Another area of interest is water; what was the extent and timing of water on the Martian surface? Researchers have been looking to secondary phases such as phyllosilicates (specifically, clay minerals) and easily weathered primary phases such as olivine to provide constraints for this issue. Because the identification and distribution of phyllosilicates are important in answering this question, we consider the differences that may be encountered between TIR and VNIR detection methods in Chapter Three. Many scientists are interested in questions surrounding Martian silica, such as chert or opal, for its ability to indicate habitable environments and preserve signs of life. Others are concerned with the sedimentary processes or environments it may indicate. Knowledge of the fundamentals of TIR and VNIR spectra of these silica phases is lacking but essential to their accurate detection, identification, and interpretation. Gathering this information and applying it are the goals of Chapters Four and Five. The purpose of each of these chapters and their applicability to the bigger picture is discussed further below.

1.1. Visible to Near-infrared and Thermal Infrared Spectroscopy

A more detailed discussion of the methods we use in our studies, namely TIR and VNIR spectroscopy, may help in understanding how we can confidently transition from measuring energy's interaction with matter to compositional information that contributes to answering the questions posed above. At VNIR and TIR wavelengths we see variations in emitted or reflected energy due to the interaction of light with electronic and vibrational transitions occurring in a material. The optical properties of the material dictate the presence and shape of a feature at each particular wavelength, as well.

Features from electronic transitions occur mainly in the VNIR, whereas features originating from vibrational transitions are produced predominantly in the TIR and, to a lesser extent, the VNIR. The information discussed in the following two paragraphs can be found in *Burns* [1993] and *Gaffey et al*. [1993], among others.

Many types of electronic transitions are possible. Transitions occur when electrons move between the orbitals formed in a covalent bond. Electrons may be transferred between oxygen and metal or between two metals when the cations have different valence states (i.e., intervalence charge transfer). Crystal field absorptions occur when incompletely filled d- or f-orbitals in the transition elements are split into different energy levels depending on the surrounding structural environment. The presence, position, and combination of features in VNIR tell us what element or cation is present and, in some cases, what kind of structure it is in, indicating the phase. However, not all phases produce features in the VNIR. Energy in the VNIR wavelength range is commonly referred to in terms of reflectivity, which is the amount of energy reflected by a material at each wavelength compared to that reflected by a perfectly diffuse reflector at each wavelength.

Molecular bonds vibrate at specific frequencies determined by the characteristics of that bond (e.g., bond length, bond strength, mass of the atoms). In solids these vibrations may alter the bond by causing a stretch or bend, each of which could be symmetric or asymmetric. These movements result in the displacement of electrons, inducing a dipole moment in certain cases. When a dipole is created, any photon encountered that has the same frequency as that vibration will be absorbed. These are IR-active modes, meaning they cause features in the emittance or reflectance of energy in the

IR region. If no dipole is induced by the vibration, it is an IR-inactive mode and causes no features in the IR. Fundamental features are the initial, strongest features, but, like a harmonic oscillator, features may also form at multiples or combinations of the fundamental frequencies. These combination and overtone bands are commonly found in the VNIR, whereas the fundamental bands are in the IR. Because the frequency of bond vibrations is due to the structure and chemistry unique to every mineral, the resulting features are also unique to that mineral. In remote sensing energy in the TIR is most commonly discussed in emissivity, which is the amount of energy emitted at each wavelength divided by the amount of energy emitted at each wavelength for a blackbody (i.e., a perfect emitter) at that same temperature. The emissivity spectrum is determined by the chemistry and structure of the material, along with its optical properties.

Because VNIR and TIR spectra reflect different types of information on the composition of a material, they can be used together to great advantage. The VNIR range is particularly helpful in indicating the presence of water and hydrated minerals. The presence of transition metals is also easy to spot in VNIR spectra because they undergo many of the electronic transitions mentioned above. The TIR range hosts the fundamental features of the silicate minerals and is useful for identifying the common minerals on rocky planets. In the TIR the spectra of components add linearly unless at very small particle sizes, and therefore quantitative abundance can be determined. Mixing in the VNIR is generally non-linear and abundance determination is difficult, especially because some minerals such as plagioclase have no features in the VNIR. Using data from both techniques takes advantage of the most helpful aspects of each and helps to constrain questions that might arise from a single type of observation.

1.2. Purpose of the Current Work

In the next chapter (Chapter Two), I use TIR spectroscopy along with data on the visible, thermophysical, and morphologic properties to characterize high thermal inertia intracrater deposits in southwestern Margaritifer Terra, Mars. The high thermal inertia indicates that the interior surfaces of these craters have an effective grain size larger than the surrounding terrain; in this case we believe the deposits are indurated and relatively free of fine particulates. THEMIS TIR images indicate spectral variation over these deposits, although TES spectra do not show compositional differences beyond the technique's uncertainty. I believe that the deposits are most likely created by the infill and induration of basaltic sediments with a cementing agent such as sulfate. This is an example of a sedimentary process that initially appears to be igneous because it is dominated by a basaltic composition. Although Mars is thought to be primarily an igneous planet, sedimentary processes are likely ubiquitous.

In Chapter Three I contribute to the search for phyllosilicates on Mars. Previous studies using TIR spectroscopy have found widespread but uncertain evidence of phyllosilicates. More recent observations with VNIR spectroscopy have detected phyllosilicates in fewer, more discrete areas. I investigate the characteristics of the TIR spectra from the areas where phyllosilicates are identified in VNIR data to determine how they may be distinguished in the TIR range and consider why phyllosilicates are suggested in TIR spectra but not in VNIR spectra in some places. The areas I analyzed are distinct in THEMIS TIR images but do not have compositional differences with the surrounding non-phyllosilicate-bearing plains, as determined by TES TIR spectra, that

are uniquely attributable to phyllosilicates. I suggest that phyllosilicates are used in models of TIR spectra over much of Mars because they are substituting for a poorly crystalline phase such as allophane that is on the Martian surface but not represented in our spectral libraries. Correctly detecting, identifying, and interpreting phyllosilicates on the surface of Mars is important because they have implications for past Martian environment and climate.

Chapters Four and Five are companion papers; in Chapter Four I conduct a laboratory study of chert and amorphous silica and then apply that new knowledge to silica-rich materials on Mars in Chapter Five. Chert and amorphous silica commonly form in aqueous environments and have an excellent ability to preserve biological signatures. These associations with water and life have interesting potential implications to any detection of these forms of silica on the Martian surface. Silica-rich material has been detected in several locations on Mars but there has not yet been enough information for a positive identification of chert and amorphous silica in most cases. Using TIR and VNIR spectrometers in the laboratory I measure the spectra of a variety of chert and amorphous silica samples and analyze their spectral variation. I observe how their TIR spectra differ under varying conditions such as surface roughness, orientation, and incidence angle. By comparing the TIR and/or VNIR spectra of samples from similar environments, I show that they do not necessarily have the same spectral characteristics. Spectra from samples originating in different environments may have very similar spectra, however. This indicates that we cannot use spectral character to determine physical information such as environment of origin for chert and amorphous silica.

Constraints such as this are important to be aware of to prevent over-interpretation of spectra.

CHAPTER 2

Geologic characteristics of relatively high thermal inertia intracrater deposits in southwestern Margaritifer Terra, Mars

ABSTRACT

Twenty-one craters in southwestern Margaritifer Terra exhibit unusually warm interior deposits in nighttime Thermal Emission Imaging System (THEMIS) infrared images. These deposits exhibit nighttime temperatures as high as 223 K and are 5 to 18 degrees warmer than the surrounding plain. Thermal inertia values, derived from Thermal Emission Spectrometer (TES) data, are greater for the deposits than the plains, with maximum values between ~455 and 675 J m^{-2} K^{-1} $s^{-1/2}$. Analysis of THEMIS thermal inertia data having nearly an order of magnitude better spatial resolution shows that the deposits can have a thermal inertia as high as ~1060 J m^{-2} K^{-1} $s^{-1/2}$. Albedo and dust cover index values suggest that both the deposits and the surrounding region are generally dust-free. Compositional analysis with TES and THEMIS data show that, though a small number of the deposits may have isolated compositional differences, the majority of the deposits have a composition similar to that of the surrounding plains. The geomorphology of the craters as viewed from Mars Orbiter Camera (MOC) images shows that the deposits are coherent units rather than sand deposits, an observation that is consistent with the relatively high thermal inertia values. If these deposits are coherent rock units as the results of our study suggests, possible methods of formation include emplacement of primary igneous material or lithification of sediments from surrounding terrain.

1. Introduction

Our investigation of nighttime thermal infrared images recorded by the Thermal Emission Imaging System (THEMIS) onboard the 2001 Mars Odyssey spacecraft reveals ~20 craters in the region of southwestern Margaritifer Terra with unusually warm floor deposits relative to the surrounding materials. The appearance of these craters varies from the more typical nighttime appearance of craters in which the rims and possibly the ejecta exhibit warm nighttime temperatures while the crater interior is cooler, more similar to the surrounding terrain. Here we define an intracrater 'deposit' as a mass of material emplaced by any process subsequent to crater formation. The deposits evaluated in this study differ from classic intracrater deposits, e.g. *Christensen* [1983], in that they do not appear to be eolian deposits of loose sand. To understand their composition and origin, we have analyzed the albedo, spectral, thermophysical, topographic, and geomorphic characteristics of these anomalous deposits using remote sensing data from the Mars Odyssey THEMIS, Mars Global Surveyor Thermal Emission Spectrometer (TES), Mars Orbiter Laser Altimeter (MOLA), and Mars Orbiter Camera (MOC).

Margaritifer Terra is centered at 4.9° S, 335° E; our study area is in the southwestern quadrant, between 11° and 22° S, and 320° and 335° E (Figure 1) and is part of the heavily cratered Noachian plateau sequence [*Scott and Tanaka*, 1986]. Regional elevation decreases to the northeast, and the Ladon Basin, an ancient multi-ringed impact basin, is located in the eastern half of the study area. The most recent study of this region was conducted by *Grant and Parker* [2002]; the remainder of this description of the region is drawn from that work. The topography and geologic evolution of the area is largely dictated by Ladon Basin and other components of the

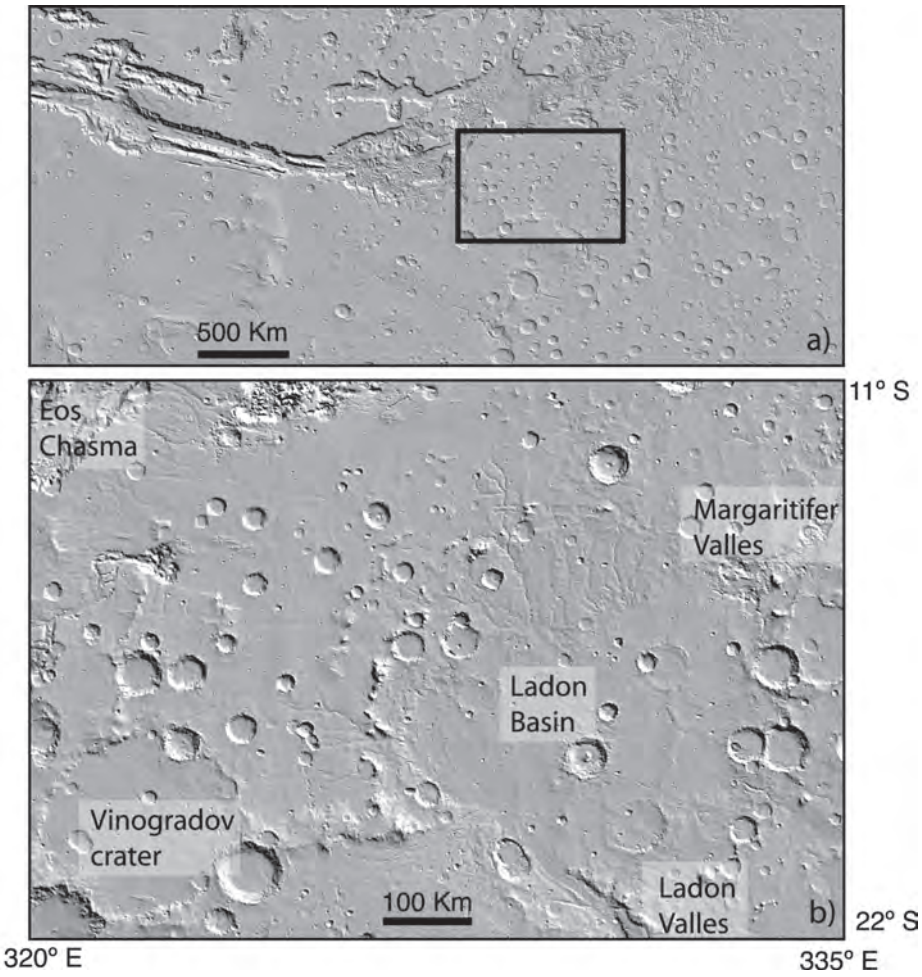

Figure 2.1: The black box in a) illustrates the location of the study area in southwestern Margaritifer Terra. b) shows the the study area in more detail. The shaded relief map was created from 128 ppd MOLA topographic data [Smith et al., 2001a].

Uzboi-Ladon-Margaritifer mesoscale outflow system (ULM). The ULM is a system of channels and basins that stretch from the Argyre impact basin to the northeast through Uzboi Vallis, Holden Basin, Ladon Valles, Ladon Basin, and Margaritifer Valles, ending in Margaritifer Basin. This large system and its tributaries are estimated to have provided drainage for ~9% of the Martian surface. Multiple resurfacing events concluding in the Late Noachian overprint the older Holden and Ladon basins. Resurfacing from an additional, more localized event may have continued into the middle Hesperian. Channel and valley formation began in the Late Noachian and extended into the Middle Hesperian, likely occurring in several stages as evidenced by terrace deposits in the channels. The water thought to have pooled in Margaritifer Basin (also an outlet for the Samara and Parana-Loire Valles systems to the east) is suggested to have infiltrated the heavily fractured surface and been released later, beginning in the Middle Hesperian, through the formation of Margaritifer and Iani Chaos, creating the Ares Vallis outflow channel.

In a study of intracrater thermal anomalies using Viking IRTM data, *Edgett and Christensen* [1994] found that deposits in Margaritifer Terra differ from those in the other regions they studied. According to their model, which is based on an inverse relationship between dune cover and thermal inertia, the Margaritifer Terra deposits have a much higher thermal inertia (440 ± 60 J m^{-2} K^{-1} $s^{-1/2}$) and an inferred lack of significant dune cover relative to the other areas studied (where average thermal inertia values range from ~120 to 300 J m^{-2} K^{-1} $s^{-1/2}$). Limited image resolution available at the time of that study prohibited further investigation as to the cause of these differences from intracrater deposits in other regions.

In this study we investigate the geologic characteristics of these thermally anomalous deposits to determine how their properties differ from those of their surroundings and likely explanations for their occurrence. We analyze and compare temperature, thermal inertia, dust coverage, and morphology to better understand these physical properties. In addition, we examine the spectral properties of these deposits using multispectral and hyperspectral thermal infrared data. Below, we explain the data sets and approach in detail, followed by the results of these analyses and a discussion of their implications to the geologic characteristics of the deposits. We also consider the potential origins of the thermally anomalous deposits suggested by our results.

2. Approach

2.1. Data Sets and Data Selection

The THEMIS instrument on Mars Odyssey consists of two subsystems, the first of which is a thermal infrared imager with 10 bands centered at nine wavelengths in the range of 6.78 to 14.88 μm to produce nighttime and daytime thermal infrared images, each at a resolution of ~100 m/pixel. THEMIS also carries a visible imaging subsystem that produces images of the surface with five bands centered at wavelengths between 0.425 and 0.860 μm and a resolution of ~18 m/pixel [*Christensen et al.*, 2004]. The high spatial resolution of THEMIS provides an excellent complement to the high spectral resolution of TES, described below.

The TES instrument onboard Mars Global Surveyor mapped Mars from 1999 to 2006, providing information on the composition and thermophysical properties of the surface. As described in *Christensen et al.* [2001a], TES consists of a Michelson

interferometer that measures emitted thermal infrared energy from 5.8-50 μm in 143 or 286 channels (10 and 5 cm^{-1} sampling, respectively), along with thermal (5.1-150 μm) and visible/near-infrared (0.3-2.9 μm) bolometers. Energy is collected by a 3 × 2 array of detectors, with each detector having a spatial resolution of ~ 3 × 3 km, though down-track smear increases that to ~3 × 6 km in the along-track direction [*Christensen et al.*, 2001a].

We selected TES emissivity spectra for each crater based on surface temperature (>260 K), total atmospheric dust (<0.22), and ice (<0.07) nadir opacity values. Spectra were also restricted to those between OCK (orbit counter keeper) 1683 and 7000 to avoid the additional noise from the spacecraft introduced in the data after this time in the mission [*Bandfield*, 2002; *Hamilton et al.*, 2003]. Other constraints, such as HGA motion and solar panel motion, were not used because the number of spectra obtained was small enough to be visibly inspected for quality. To further reduce noise, spectra from individual detectors covering the same region were averaged before being analyzed to produce the results presented here.

We also utilize data from the MOLA and MOC instruments on the Mars Global Surveyor spacecraft. MOLA uses laser altimetry to determine the topography of the Martian surface [*Smith et al.*, 2001a]. The 128 pixel/degree gridded MOLA topography, resampled to THEMIS IR spatial resolution, is used to extract the elevation data for the present work. The topography data is oversampled to allow for direct comparison to the high inertia deposits in the nighttime THEMIS IR images. MOC consists of three visible imaging systems; two cameras provide low resolution (up to 230 m/pixel), wide angle context images of the surface and a telescope on the third system creates high resolution

(up to 1.5 m/pixel), narrow angle images [*Malin et al.*, 1992; *Malin and Edgett*, 2001]. The narrow angle images used in this study have a resolution of ~3 m/pixel.

In our study area, 21 of the 53 craters we examined exhibited high brightness temperatures relative to the surrounding terrain in THEMIS nighttime thermal infrared images, an example of which is shown in Figure 2. These deposits are observed in craters of various diameters (15 to 66 km). For the purpose of this study we label the craters by their south latitude and east longitude (e.g., 14335 indicates the crater at 14°S and 335°E).

2.2. Thermophysical Properties

Thermophysical properties are material properties that relate to heat transfer and storage, such as thermal conductivity, heat capacity, and thermal inertia. Nighttime temperatures primarily represent the thermophysical properties of the top 10s of cm of the surface [e.g., *Kieffer et al.*, 1977; *Mellon et al.*, 2000]. A higher nighttime temperature typically indicates a material that has a higher thermal inertia, absorbing and emitting heat more slowly, than neighboring lower temperature materials. However, because temperature can be affected by variables such as latitude and season, thermal inertia is used to compare between different areas or separate observations rather than temperature. Thermal inertia variations on Mars commonly can be linked to differences in effective particle size, with larger particles having greater thermal inertia [e.g., *Christensen*, 1982; *Kieffer et al.*, 1977; *Mellon et al.*, 2000; *Presley and Christensen*, 1997].

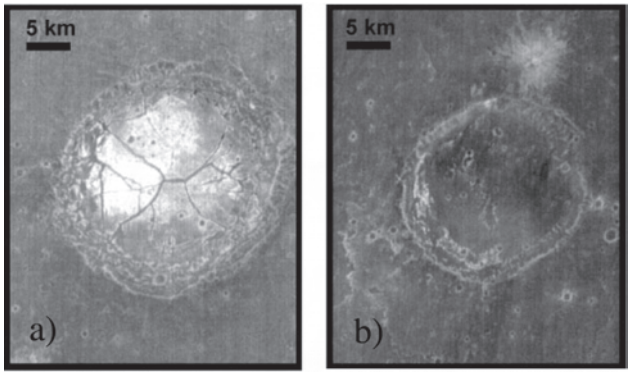

Figure 2.2: THEMIS nighttime thermal infrared images of two craters in southwestern Margaritifer Terra. a) a crater with a thermally anomalous intracrater deposit. b) a crater with no anomaly.

TES bolometric thermal inertia is determined using a look-up table that matches a measured nighttime temperature value with the appropriate season, time of day, latitude, albedo, surface pressure, dust opacity, and thermal inertia [*Mellon et al.,* 2000; *Putzig et al.,* 2005]. An uncertainty of up to 6% is associated with TES bolometric thermal inertia values [*Mellon et al.*, 2000]. The global thermal inertia values determined by *Mellon et al.* [2000] from TES data fall into three modes centered at 70-80, 180-250, and 240-260 J m^{-2} K^{-1} $s^{-1/2}$ and indicate that the bulk of the planet's surface materials correspond to clay to coarse sand sized particles [*Fenton and Bandfield*, 2003; *Presley and Christensen*, 1997]. Particularly high values of thermal inertia (>~1500 J m^{-2} K^{-1} $s^{-1/2}$) could indicate outcrops of bedrock [*Fergason et al.*, 2006; *Mellon et al.*, 2000; *Presley and Christensen*, 1997], but sub-pixel mixing would cause the observed values to be lower in remotely-sensed measurements of the Martian surface. Additionally, the maximum TES thermal inertia calculated for the look-up table is 800 J m^{-2} K^{-1} $s^{-1/2}$, though some surfaces on Mars may have values far above this.

THEMIS thermal inertia values are determined using a look-up table similar to that for TES data but created from a different thermal model [*Fergason et al.*, 2006]. The high spatial resolution of the THEMIS instrument results in the ability to see smaller-scale anomalies due to less sub-pixel mixing than with TES. Additionally, the thermal inertia from THEMIS data has been calculated for a possible range from 24 to 3000 J m^{-2} K^{-1} $s^{-1/2}$, higher than that for TES. THEMIS thermal inertia values are calculated directly from the band 9 (12.57 μm) brightness temperatures of a THEMIS nighttime thermal infrared image for each of the craters and have an accuracy of ~20% [*Fergason et al.*, 2006]. Uncertainty of THEMIS nighttime temperature data is ~2.8 K (at ~180 K)

[*Fergason et al.*, 2006]. An alternative method of determining thermal inertia from THEMIS data has been developed by Putzig and colleagues [*Putzig et al.*, 2004], but was not used in this study.

In our analysis we found TES thermal inertia values from the solar longitude (L_s) period of ~150-270º to be abnormally high and variable relative to the values from the rest of the Mars year. Included in this L_s range is the southern hemisphere summer season, a time of year when high dust opacity is common [*Smith et al.*, 2001b]. Such variations in dust opacity are not taken into account in the TES thermal inertia derivation and can cause artificially high thermal inertia values to be derived [*Mellon et al.*, 2000]. Therefore, we exclude values from L_s=150-270º in the TES thermal inertia values reported in the Results section below.

2.3. Albedo

Albedo is the ratio of the amount of light reflected by a surface to that of the light incident upon the surface; visible reflectance at Mars, measured by the TES visible/near infrared bolometer, is converted to and presented as Lambert albedo [*Christensen et al.*, 2001a]. Albedo can vary due to the effects of particle size on the scattering of light. Typically, for regions away from the poles, higher albedo (brighter) areas are due to dust. We are interested in the distribution of fine particles because their presence can cause scattering of infrared energy and could potentially affect our analysis. Our study has observed that albedo, like TES thermal inertia, can also vary with L_s. The range in average albedo values for the craters from L_s=150-270º is higher than the range of values during the rest of the year. These elevated values are likely from the inclusion of data

that are affected by variations in dust opacity and possible surface dust removal and deposition during the southern summer season [*Smith et al.*, 2001b]. Because these values are not representative of the albedo during the majority of the Martian year, they are not included.

2.4. Dust Cover Index

Ruff and Christensen [2002] developed a dust cover index (DCI) to complement albedo as a means of evaluating the distribution of fine particulates. Based on known spectral trends as a function of particle size, these investigators developed a spectral parameter (the average TES emissivity from 1350 to 1400 cm^{-1}) that can be used as a proxy for dust cover. Values of less than 0.940 indicate a dust-covered area, whereas values greater than 0.962 indicate a dust-free area, and values falling between these numbers suggest partial dust cover.

2.5. Composition

2.5.1. THEMIS Compositional Variation

THEMIS daytime thermal infrared calibrated radiance images were used to produce decorrelation stretched (DCS) images of each intracrater deposit identified in the study area. Two deposits have no available daytime IR image coverage, however, and so are not included in the compositional study, though they are part of the thermophysical study. The DCS enhances three user-selected bands by redefining the coordinate system in a way that amplifies variations by removing highly correlated information, and then combines these band images to make a false color image [*Gillespie et al.*, 1986; *Kahle et*

al., 1993]. Multiple DCS images were created for each crater using the 6/4/2 (10.21, 8.56, and 6.78 μm), 8/6/4 (11.79, 10.21, and 8.56 μm), and 9/7/5 (12.57, 11.04, and 9.35 μm) THEMIS spectral band combinations for the red, green, and blue colors in each image. Using multiple band combinations helps to ensure that a spectral difference in any band will be detected. We visually inspected the decorrelation stretched images to determine which crater deposits exhibit spectral variation from their immediate surroundings. For those deposits showing possible spectral variation, we performed further spectral analyses as described below.

2.5.2. TES Compositional Analysis

Each thermal infrared emissivity spectrum is assumed to be a linear mixture of the emissivities of all of the minerals located within that pixel in proportions relative to their abundance [e.g., *Ramsey and Christensen*, 1998]. At Mars this includes not only the surface, but contributions from the Martian atmosphere as well [*Smith et al.*, 2000]. By using this linear mixing property, an unknown spectrum can be deconvolved with an iterative least squares method that calculates the best fit of a combination of components and abundances taken from a predetermined spectral library [*Smith et al.*, 2000]. The user provides the deconvolution algorithm with the measured spectrum, a spectral library of known spectra from which to model the measured spectrum, and constraints on the wavelength range over which to do the deconvolution. The algorithm returns the best-fit model spectrum to the measured spectrum and a list of the library spectra used and their proportions. A blackbody component, used to equalize the differences in spectral

contrast, and atmospheric components are subtracted, and the remaining concentrations are then normalized to produce the modeled surface abundances.

The spectral library for our study underwent multiple revisions, with phases not used in the deconvolution removed (e.g., albite, anorthite) and the process repeated until we were confident that the library spectra could model the unknown spectra well. The final set of phases is listed in Table 1 and consists of many typical igneous phases, along with their alteration products. Our spectral library was tailored to the specific area we analyzed and is likely not applicable to other regions or global studies. Individual TES spectra over the specified area were averaged (number of spectra averaged range from 4 – 25), and the average spectrum was deconvolved from 1300 cm^{-1} to 235 cm^{-1} (~8 to 43 μm) with the exclusion of the region of high atmospheric CO_2 opacity, ~ 800-500 cm^{-1} (~12.5-20 μm).

2.5.3. THEMIS Compositional Analysis

We cannot use the linear deconvolution method of atmospheric correction with THEMIS because of its lower spectral resolution. Instead, to derive surface emissivity from THEMIS daytime calibrated radiance images, we removed the effects of atmospheric emission and attenuation through a process outlined by *Bandfield et al.* [2004a]. First, we corrected differences in atmospheric emission due to temperature variation on the surface (i.e. shaded or sunlit slopes) through a constant radiance offset removal. We did this by selecting an area of the THEMIS image that is likely to have no variation in composition but contains slopes exhibiting temperature differences (e.g., a small crater, < ~3 km) as a training region and using an algorithm that isolates the

Table 2.1: Phases and atmospheric components used in the spectral library for this study.

Phase	Sample #	Source*
Dust Low CO2		a,b
Dust High CO2		a,b
Water Ice Cloud (High Latitude)		a,b
Water Ice Cloud (Low Latitude)		a,b
CO2 Gas		c
H20 Gas		c
Oligoclase	WAR-0234	d,e
Oligoclase (Peristerite)	BUR-060	d,e
Oligoclase (Peristerite)	BUR-060D	d,e
Labradorite	WAR-4524	d,e
Labradorite	BUR-3080A	d,e
Labradorite	WAR-RGAND01	e
Andesine	BUR-240	d,e
Andesine	WAR-0024	d,e
Bytownite	WAR-1384	d,e
Enstatite	HS-9.4B	d,f
Bronzite	NMNH-93527	d,f
Hypersthene	ALH84001	g
Pigeonite**		f
Diopside	BUR-1820	d,f
Diopside	NMNH-R15161	d,f
Diopside	WAR-6474	d,f
Augite	DSM-AUG01	d,f
Augite	NMNH-9780	f
Olivine Fo68 KI	3115	h
Olivine Fo60 KI	3362	h
Olivine Fo35 KI	3373	h
Olivine Fo10 KI	3008	h
Forsterite	BUR-3720A	d
Forsterite	AZ-01	d

(Continued Next Page)

Table 2.1: (Continued) Phases and atmospheric components used in the spectral library for this study.

Phase	Sample #	Source*
Kaolinite (granular)	Kga-1	d,i
Nontronite (granular)	WAR-5108	d,i
Fe-Smectite (granular)	SWa-1	d,i
Illite (granular)	Imt-2	d,i
Halloysite (granular)	WAR-5102	d,i
Na-Montmorillonite (granular)	SWy-2	d,i
K-rich Glass		j
Silica Glass		j
Hematite	BUR-2600	d
Gypsum	S5	d,k
Gypsum (Selenite)	S8	d,k
Anhydrite	S9	d,k

* Further details about these spectra and how they were collected can be found in the following: a) *Smith et al*. [2000b]; b) *Bandfield et al*. *[2000a]*; c) *Bandfield* [2002]; d) *Christensen et al*. *[2000a]*; e) *Ruff* [1998]; f) *Hamilton* [2000]; g) *Hamilton et al*. [2003]; h) *Hamilton et al*., in prep; i) *Piatek* [1997]; j) *Wyatt et al*. [2001]; k) *Lane* [2007]

** minor transparency features removed

contribution of atmospheric emission, subtracting it from each pixel of the image [*Bandfield et al.*, 2004a]. The next step consisted of selecting a training region having uniform emissivity in the THEMIS image, and identifying co-located TES pixels (meeting the quality criteria defined above). We took the average of the TES spectra and linearly deconvolved it to obtain the surface emissivity for the training region. We then convolved the TES-derived surface emissivity spectrum to THEMIS spectral resolution. Assuming that this is the surface emissivity for the training region, we calculated and removed the shape of the atmospheric component in the THEMIS data from each pixel in the image. This process requires the absence of clouds and makes the assumption that the atmosphere is not variable over the image, which is likely valid in regions without significant elevation change (< ~1000 m) [*Bandfield et al.*, 2004a]. The topographic deviations of the craters we studied by this method do not appear to affect the analysis.

3. Results

3.1. Thermophysical Properties

The thermally anomalous deposits show average nighttime temperatures in the range of 182 to 213 K (with standard deviations of 2.2 to 5.6), with maximum temperatures as great as 223 K. In contrast, the average and maximum temperatures for the areas outside of the craters are between 171 and 204 K (with standard deviations of 0.9 to 3.0) and 184 and 213 K, respectively. This results in average nighttime temperatures 5 to 18 K greater for the thermally anomalous deposits than the surrounding areas, which is greater than the ~2.8 K uncertainty for nighttime temperature data [*Fergason et al.*, 2006]. Both the deposits and the adjacent areas exhibit the highest

nighttime temperatures during southern summer, when they receive greater insolation during the day.

Figure 3 provides an example of two craters in our study area that have greater values of TES thermal inertia than the surrounding plains. The values here are rounded to the nearest 5 J m^{-2} K^{-1} $s^{-1/2}$. Maximum values for all craters are between 455 and 675 J m^{-2} K^{-1} $s^{-1/2}$ and are plotted with the mean albedo values (described below) in Figure 4. For two craters we are unable to determine their thermal inertia values due to lack of coverage. The average THEMIS-derived thermal inertia also increases for the warm deposits. The maximum values of the deposits measured range between 450 and 1060 J m^{-2} K^{-1} $s^{-1/2}$, with averages from 287 to 616 J m^{-2} K^{-1} $s^{-1/2}$ (standard deviations of 45 to 116).

3.2. Albedo

The average Lambert albedo values for the craters are shown in Table 2. The values are averages of an area in a box around the crater, which includes the anomalous deposit, the crater interior, and a small amount of the surrounding plains. Individual inspection of the values in each area shows that the albedo does not significantly vary between the intracrater deposit and the surroundings, and therefore the average value reported is a reasonable representation of the albedo over both the deposit and the surrounding area. The average values range between ~0.120 and 0.142 (standard deviations between 0.011 and 0.025).

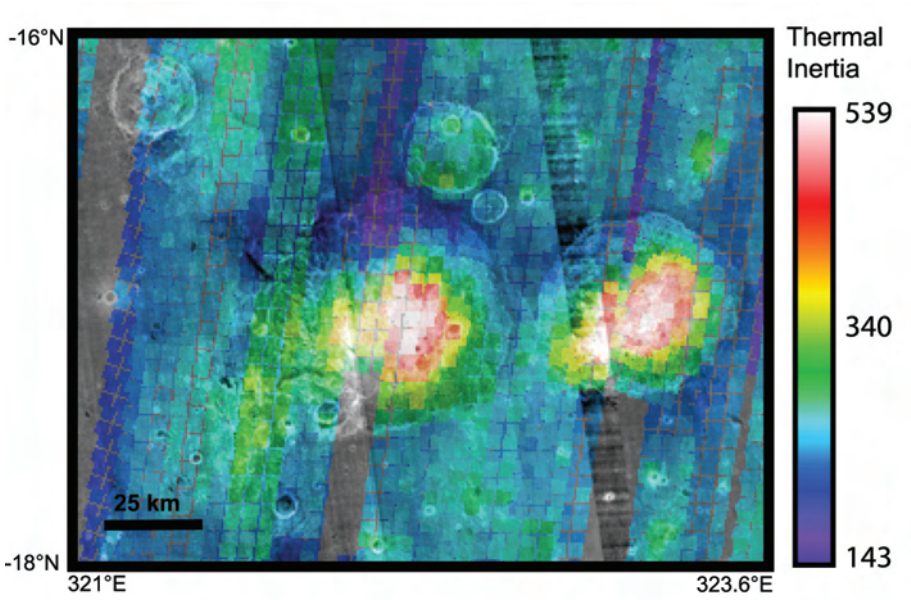

Figure 2.3: TES nighttime bolometric thermal inertia overlaid on a nighttime thermal IR THEMIS mosaic. This figure shows an example of the increase in thermal inertia over the anomalous intracrater deposits. In this image are craters 16322 (left) and 16323 (right).

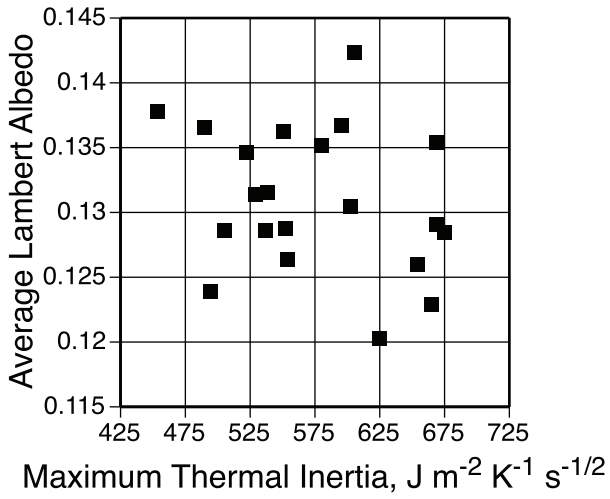

Figure 2.4: Maximum bolometric thermal inertia values plotted with mean Lambert albedo.

Table 2.2: Average Lambert albedo

Crater	Average	Standard Deviation
12331	0.123	0.013
13324	0.136	0.013
13326	0.138	0.013
14325	0.142	0.021
15324	0.131	0.015
16323	0.129	0.011
16327	0.136	0.0127
16331	0.126	0.014
16334	0.135	0.012
17324	0.120	0.011
17331	0.126	0.011
18323	0.124	0.012
18330	0.128	0.016
18333	0.129	0.018
18334	0.135	0.014
20324	0.130	0.016
11335	0.129	0.013
14332	0.134	0.25
16322	0.131	0.014
16330	0.129	0.012
19931	0.137	0.024
Range	**0.120 - 0.142**	**0.011 - 0.025**

3.3. Dust Cover Index

The DCI values are also presented as average values from a small box surrounding the crater and deposit, as with albedo. There is no discernable difference between the deposits and the plains, so an average of values taken from the crater and a small area around it appear to provide a good representation of dust cover. The average DCI values for the craters are between 0.967 and 0.974 (standard deviations of 0.007 to 0.040).

3.4. Composition

3.4.1. THEMIS Compositional Variation

Of the nineteen intracrater thermal anomalies analyzed, five show color variations in at least one of the decorrelation stretched images, indicating possible differences in composition between the deposits and their surroundings. The variations are not observed in the same set of bands for every crater; for example, crater 11335 exhibits its most notable variations in the 8/6/4 DCS, whereas crater 16322 has more obvious variation in the 9/7/5 DCS. This suggests that there may be compositional variations among the deposits. Figure 5 gives an example DCS image for each of these five craters. Two of the craters contain DCS color variations within the intracrater deposit and are designated by letter as described in Figure 5. The results of the quantitative compositional analysis of these five craters are presented below.

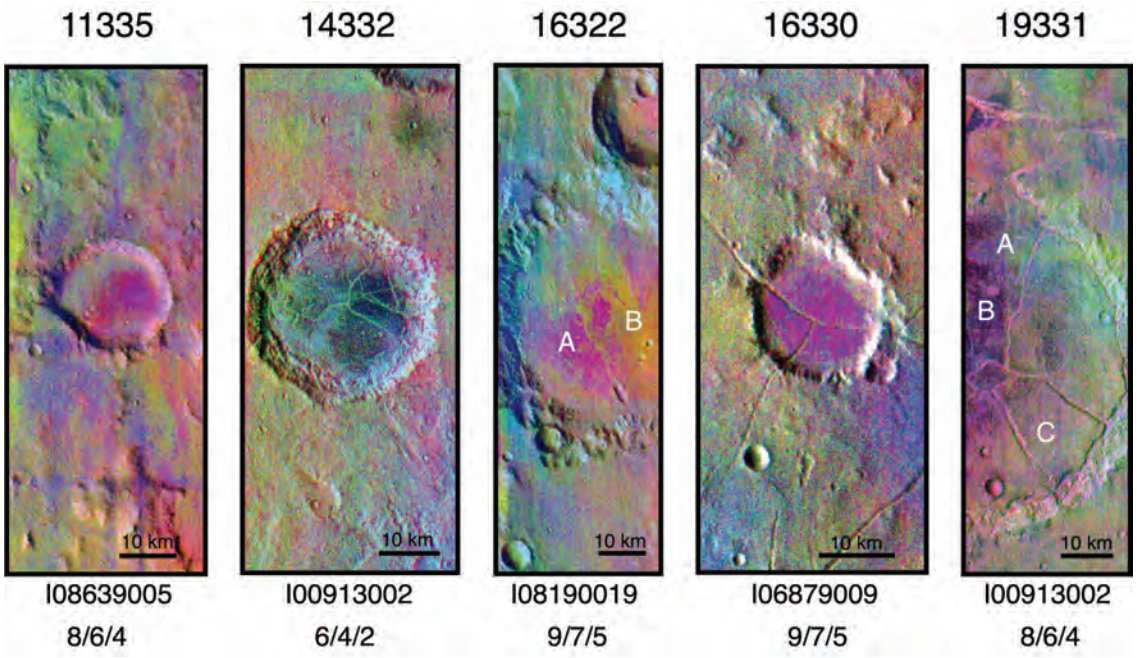

Figure 2.5: DCS images of the five craters showing possible compositional variation. The crater's designation for this study is shown above the image. The number of the THEMIS radiance image used in the DCS is given just below each image. The bands used for the red, green, and blue components of the color image are also shown below the image. Crater 16322 exhibits two deposits, one pink and one orange in this band combination, designated by the letters A and B, respectively. Crater 19331 also has multiple deposits, shown as blue, purple, and orange in this DCS image, designated by A, B, and C, respectively.

3.4.2. TES Compositional Analysis

Figure 6 shows our average surface spectra for each thermally anomalous intracrater deposit and the surrounding plain, along with the Mars surface type 1 and 2 (ST1, ST2) spectra from *Bandfield et al.* [2000b] for reference. *Bandfield et al.* [2000b] describe ST1 as a basalt and ST2 as a basaltic andesite or andesite. *Wyatt and McSween* [2002] demonstrated that ST2 can be modeled as a weathered basalt as well. The Margaritifer spectra resemble the ST1 spectrum more closely than the ST2 spectrum, though none of them appear to be identical to the ST1 shape. In many cases the deepest band minimum (~1100 cm^{-1}) is shifted to shorter wavelengths than in ST1, and the spectral shape varies at long wavelengths (e.g. lack of a minimum at ~470 cm^{-1}, location and depth of the emissivity minimum in the 300-400 cm^{-1} range).

The majority of the deposit spectra resemble the spectrum of the plains region surrounding them, though a few are not consistent in shape and spectral contrast, such as the 16330 deposit (e.g. long wavelength variation), the A and B deposits of crater 16322 (e.g. shape in 8-12 μm region), and possibly the A deposit of crater 19331 (e.g. shape in 8-12 μm region). A comparison of the plains spectra adjacent to each crater reveals that all are very similar in shape. Given the general agreement among all of the plains spectra, the deposits deviating from this shape (i.e. 16330, 16322 A and B, 19331 A) are most likely to have a composition differing from that of the plains. The 16330 deposit spectrum contains more noise due to fewer detectors available for averaging, though our confidence in its difference from the plains' spectra and composition is bolstered by the THEMIS data described in the next section.

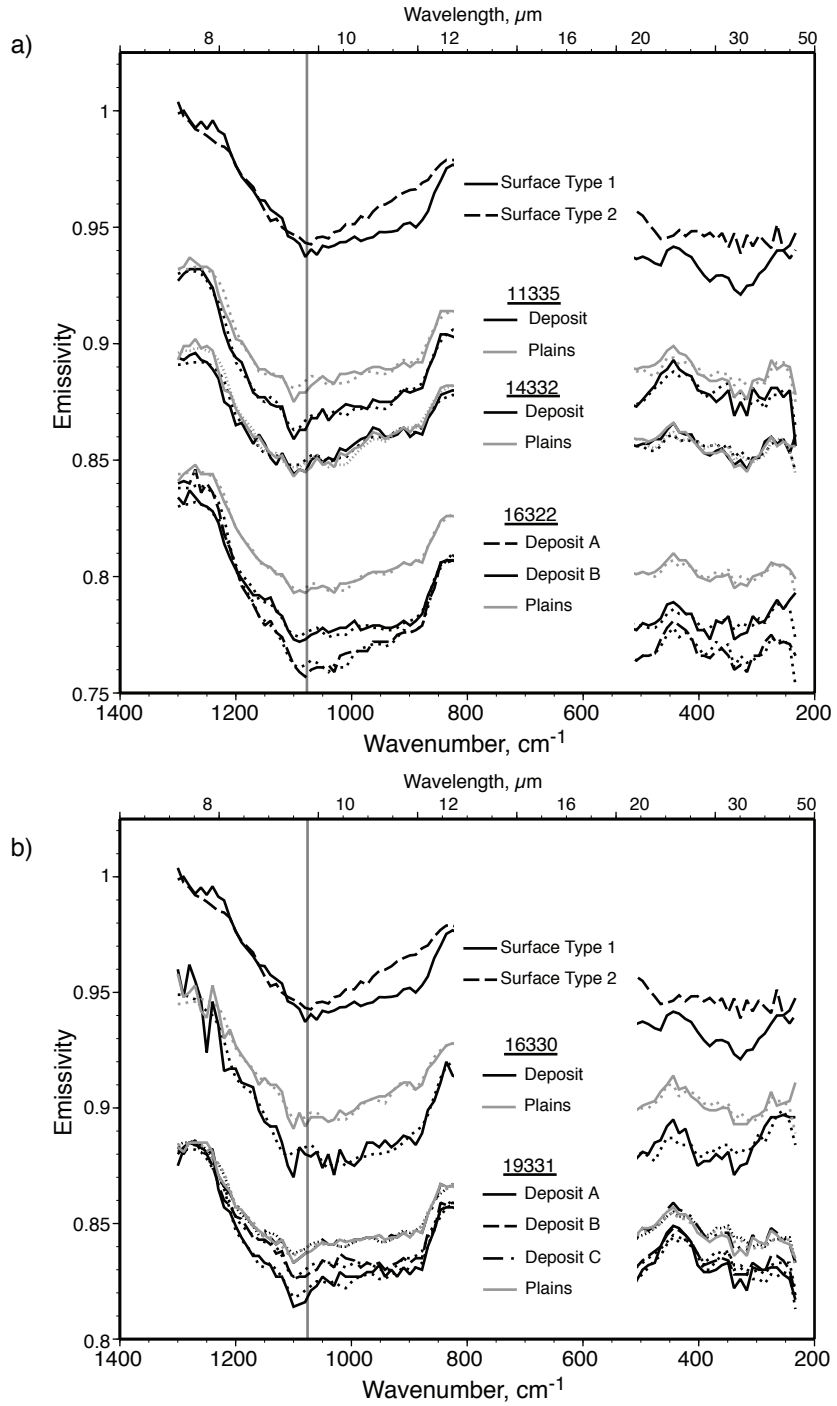

Figure 2.6: The average emissivity spectra of each of the units for the five craters. Measured spectra are shown in continuous or dashed lines, while all modeled spectra are shown by dotted lines. The group of spectra for each crater is offset by 0.05 from the previous group. The surface type 1 and type 2 spectra from Bandfield et al. [2000b] are included for reference. The vertical grey line is present to help in comparison of the spectra. 6a) shows craters 11335, 14332, 16322 while 6b) shows craters 16330 and 19331.

Deconvolution of the ST1 shape with our library spectra results in slightly different modeled abundances than those of *Bandfield et al.* [2000b], as shown in Table 3. This is due to small variations in our spectral library, such as the inclusion of more olivine spectra of different compositions and the use of an alternate hematite spectrum. Our modeled phase abundances for each intracrater deposit and surrounding plains material are presented in Table 4, rounded to the nearest 5%. The detection limits and uncertainty of each value is 10-15% [*Christensen et al.*, 2000c]. The values for each mineral group vary slightly between the deposit and surrounding plains and from crater to crater. However, in most cases the variation in abundance between the deposit and surrounding plains and between each of the deposits or each of the plains units is still well within the uncertainty. The deposit and plains associated with crater 16330 provide the only exception, with a difference in abundance between the deposit and plains of 15% for plagioclase feldspar and 25% for pyroxene. The deposit in crater 16330 also varies from the other deposits in plagioclase and pyroxene abundance by up to 20%. Variations of plagioclase and pyroxene between the other four deposits are 5% and 10%, respectively. With the exception of the crater 16330 deposit, the modeled abundances for the thermally anomalous intracrater deposits cannot be said to differ beyond the uncertainty from that of the surrounding plains.

3.4.3. THEMIS Compositional Analysis

Our atmospherically corrected surface spectra from THEMIS data are shown in Figure 7. Each spectrum shown is the average of ~600 or more spectra (~6 km^2). The majority of the deposit and plains spectra are similar in shape, but differences can be seen

Table 2.3: Modeled abundances of the type 1 surface spectrum*.

	Feldspar	Pyroxene	Olivine	Clay/ Sheet Silicates	Hematite	Other**
This study	30	25	5	20	10	10
Bandfield et al. [2000b]	50	30	0	15	0	5

*Values are reported to the nearest 5%.

**This includes phases modeled well below the detection limit, such as evaporite minerals and glasses.

Table 2.4: Modeled abundances for five intracrater deposits and the surrounding terrains*

	11335 Deposit	11335 Plains	14332 Deposit	14332 Plains	16322 Deposit A	16322 Deposit B	16322 Plains	16330 Deposit	16330 Plains	19331 Deposit A	19331 Deposit B	19331 Deposit C	19331 Plains
Plagioclase Feldspar	25	30	25	25	20	25	25	40	25	20	25	25	25
Pyroxene	45	40	40	35	40	35	35	25	50	40	40	40	35
Olivine	10	10	10	5	10	15	10	15	5	10	10	10	10
Sheet Silicates	0	0	5	5	10	0	5	10	5	10	5	5	10
K-rich Glass	5	5	5	5	5	10	5	5	0	5	5	5	5
Silica Glass	0	0	0	0	0	0	0	0	0	0	0	0	0
Hematite	0	5	10	10	5	0	5	5	10	0	0	5	5
Evaporites	10	10	10	10	10	10	10	0	5	10	10	10	10

*Modeled abundances are derived from the deconvolution of an average spectrum of the area and have been rounded to the nearest 5%. The values have an uncertainty of 10-15 %.

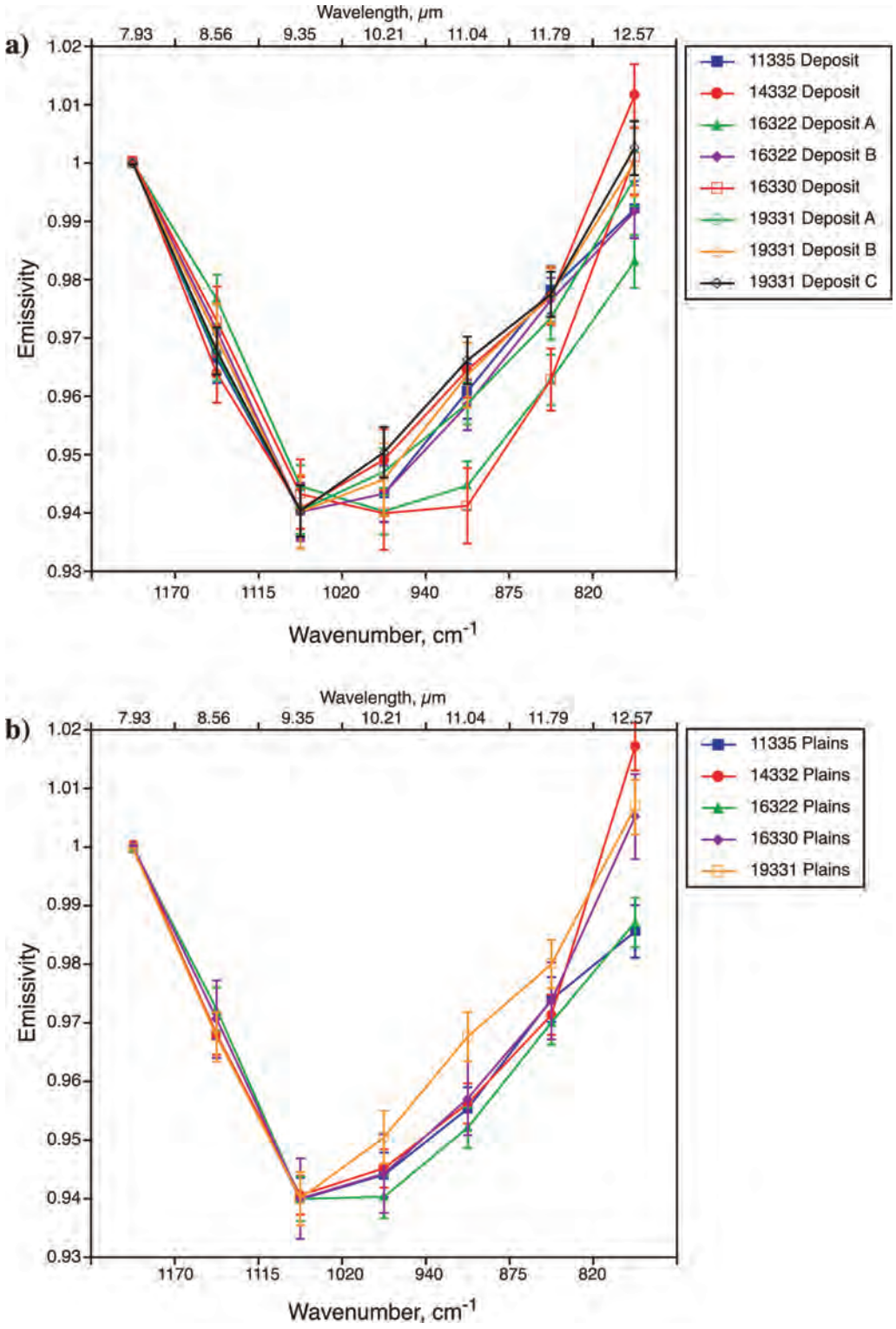

Figure 2.7: Atmospherically corrected THEMIS spectra (bands 3-9) for the a) deposits and b) surrounding plains of each crater. Each spectrum is an average and the error bars represent one standard deviation. Spectra are normalized to the same contrast to better evaluate differences in shape.

in the spectra for the 16330 and 16322 A deposits (lower emissivity in THEMIS bands 7 and 8 relative to the other spectra) and the 19331 plains (higher emissivity in band 7 than the other spectra). In the case of the 16330 and 16322 A deposits, this supports the slight differences that we observed in their TES spectra. For the 19331 plains deposit that has no noticeable variation in its TES spectra, the THEMIS spectra may be identifying differences that cannot be resolved at the lower spatial resolution of TES. Any other differences observed between TES spectra may not be significant enough to be apparent in the lower spectral resolution of the THEMIS spectra.

3.5. Topography

The elevation of the thermally anomalous materials is always lower than the surface adjacent to the crater, as expected for typical Martian craters [*Strom et al.*, 1992]. Mean elevation values for the deposits vary from –491 m to –3103 m and mean values for the surrounding plains vary from ~1000 m to –2000 m. Figure 8 illustrates this topographic information. Slightly lower deposit elevation in the eastern part of the study region may reflect the overall eastward decrease in elevation of the region. We do not observe any relationship between the deposits and crater diameter, elevation, or location.

3.6. Geomorphology

Crater 11335 is covered by the MOC narrow angle image S06-01399 (Figure 9a). A dark-toned spot at the eastern edge of the crater interior can be seen in the context image (#S06-01400, not shown) and the narrow angle image captures a small part of that area. At ~3 m/pixel resolution, the dark-toned feature appears to be caused by the filling

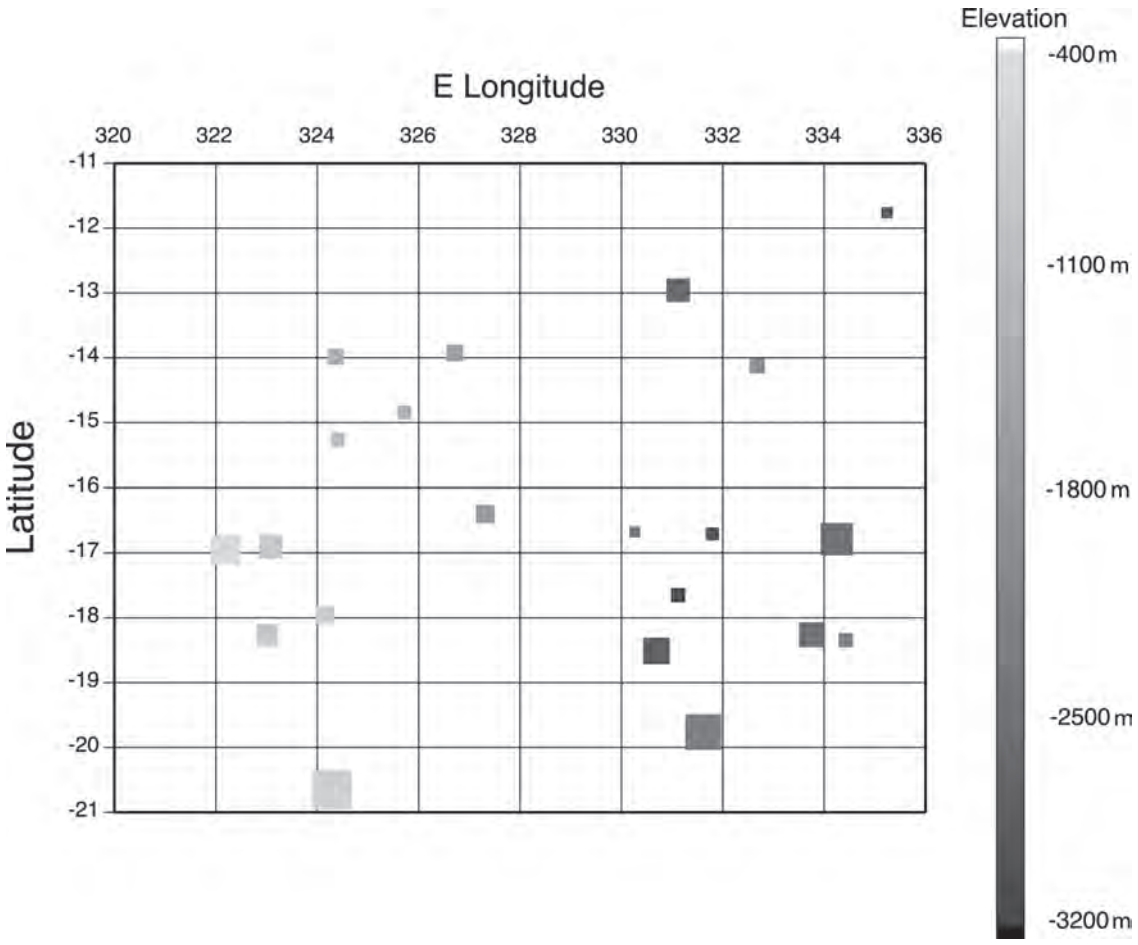

Figure 2.8: This plot illustrates the spatial distribution of anomalous intracrater deposits, along with their average elevation and crater diameter (ranging from 15 to 66 km, indicated by relative size of symbol). No relationship with crater diameter or elevation is observed.

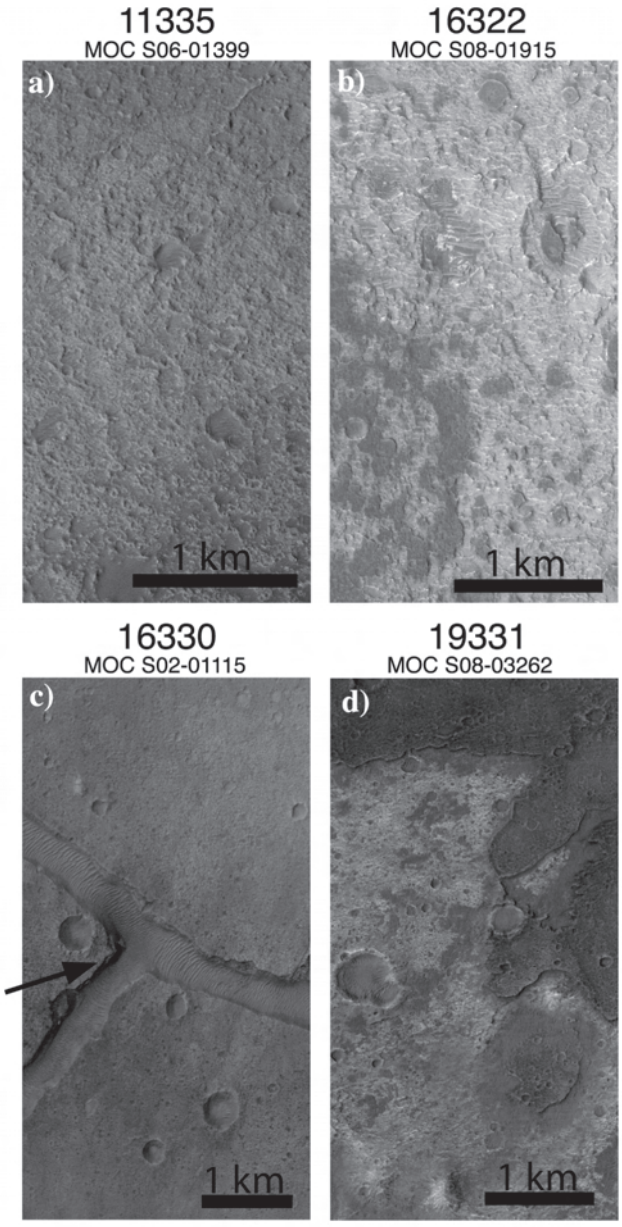

Figure 2.9: a) A portion of the MOC image S06-01399 showing part of the high thermal inertia intracrater deposit. b) A section of the MOC image S08-01915 showing the light- and dark-toned high thermal inertia material. c) A portion of the MOC image S02-01115 covering the junction of fractures within the thermally anomalous deposit. The arrow indicates an example of possible layering. d) A portion of the MOC image S08-03262 illustrating two of the high thermal inertia deposits in this crater.

of small depressions within the lighter-toned, coherent floor with a darker, dune-forming material. The concentration of this darker-toned material is only in this area of the crater, however, and the coherent floor material, which is a characteristic of a large portion of the crater floor, must be the source of the high nighttime temperatures and thermal inertia.

MOC narrow angle image S08-01915 (Figure 9b) reveals the detail of an area of the crater 16322 deposits. This narrow angle image shows a high-standing, dark-toned material, which appears to have been eroded in places, exposing a lower-lying light-toned rough terrain. To the best of our ability to determine by comparison with the DCS image, the dark-toned material corresponds to Unit A, whereas the light-toned material corresponds to Unit B. Isolated mesas of the dark material within the light-toned material are also observed. Although there is some infilling material in topographic lows forming dunes, both the light- and dark-toned materials are likely coherent units because of their ability to form steep-sided topography.

Figure 9c, a portion of the MOC narrow angle image S02-01115, shows the intersection of troughs in the middle of crater 16330. From the steep trough walls it is apparent that the crater floor is composed of a coherent unit, homogeneous in tone. The image also shows what might be layering within the deposit, exposed on the sides of the troughs. The 16330 deposit does not appear as rough as some of the other deposits (e.g. the 16322 B deposit) at the ~3 m/pixel scale, and the only visible dune forms are in the material infilling the troughs and larger craters.

The MOC narrow angle image S08-03262 provides information about the A and B deposits from crater 19331 (the area of the crater containing the C deposit was not

imaged). As can be seen in Figure 9d, the A deposit appears to be a high-standing dark-toned material, in places seeming to be stratigraphically above the light-toned B unit. A darker loose material, possibly eroded from the A unit, forms dunes in the pits of the B deposit. Though there is some dune material, the actual unit that makes up the high temperature B deposit appears to be solid.

From THEMIS VIS image V17875002 (Figure 10), the intracrater deposit in crater 14332 is relatively homogeneous in tone. Higher resolution imaging of this crater is not available, but the high thermal inertia area seems to be correlated with a coherent unit with fractures creating troughs through it.

4. Discussion

Low albedo and high DCI values suggest that dust cover is not significant over the intracrater deposits and their surroundings. The maximum TES thermal inertia values of 455 to 675 J m^{-2} K^{-1} $s^{-1/2}$ for the anomalous deposits correspond to effective particle sizes as large or larger than granules and pebbles [*Fenton and Bandfield*, 2003; *Presley and Christensen*, 1997]. The higher spatial resolution of the THEMIS thermal inertia calculated for the anomalous deposits returns greater maximum values, as high as 1060 J m^{-2} K^{-1} $s^{-1/2}$.

A plot of the thermal inertia and albedo values of the intracrater deposits (e.g. Figure 4) overlaps the high thermal inertia/low albedo mode B of *Mellon et al.* [2000], though much of the data extends outside of this mode to higher thermal inertia values. *Putzig et al.* [2005] divide the albedo/thermal inertia plot further, creating a unit F for thermal inertia values greater than 386 J m^{-2} K^{-1} $s^{-1/2}$, an appropriate category for the

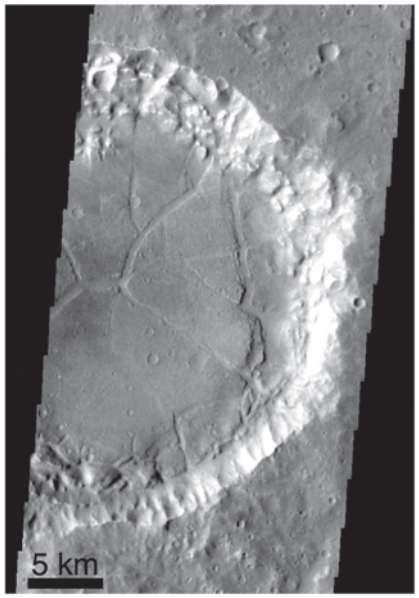

Figure 2.10: A portion of THEMIS visible image V17875002, showing part of the crater 14332 anomalous deposit.

deposits of this study. They indicate that unit F is characteristic of rocks, bedrock, duricrust, or polar ice. Thermal inertia unit B (thermal inertia of 160-355 J m^{-2} K^{-1} $s^{-1/2}$) is described by *Putzig et al.* [2005] as sand, rocks, bedrock, and possibly duricrust. These descriptions suggest that a likely interpretation of the intracrater deposits in the present study, based on their range of thermal inertia and latitude, is that they are composed of rocks, bedrock, or duricrust with the areas of slightly lower thermal inertia containing a higher abundance of smaller, sand sized particles.

An integration of the information gained from thermal inertia values and the deposits' geomorphology helps to determine the most accurate description of the deposits' physical character. The MOC images of the thermally anomalous intracrater deposits show that the high thermal inertia surfaces are predominantly composed of a coherent material with little dune cover, though a more dispersed population of small particles below the image resolution is possible and could explain the spread in thermal inertia values within the deposit, as could isolated accumulations of particles within small depressions, which we have observed.

Intersecting fractures cut half of the craters analyzed in this study, including craters 14332, 16330, and 19331. Floor-fractured craters such as these have been identified on Mars predominantly along the border between the southern highlands and the northern lowlands, and areas surrounding parts of the Valles Marineris and the outflow channels [e.g., *Schultz*, 1978; *Schultz and Glicken*, 1979]. The fractures are believed to result from modification of the crater floor due to intrusion of magma through fragmented rock beneath the crater. The extent of this modification may range from concentric grabens and/or polygonal fractures to extrusion of igneous material, as seen in

many of the lunar floor-fractured craters [e.g., *Schultz*, 1976]. In contrast to the Moon, there is also the potential on Mars for the presence of subsurface ice to affect the formation of floor-fractured craters [*Schultz*, 1978; *Schultz and Glicken*, 1979]. *Schultz* [1978] suggests that the release of volatiles from the heat of intrusion could aid in disruption of the crater floor. Differences in regional properties may lead to varying styles of modification in separate areas [*Schultz and Glicken*, 1979]. The style of floor-fractures observed in our study area consists mainly of a polygonal network of shallow fractures across a flat crater floor and/or concentric fractures at the intersection of the crater floor and wall. Though the fractures of most floor-fractured craters on Mars (including our study area) are limited to the crater interior, there is one example within the craters we investigated where the fractures extend beyond the crater rim (crater 16330). We cannot be sure of the process that created this difference in fracture occurrence, but it may be explained by the crater's location within the larger Ladon basin and could be due to an instance of floor fracturing at a more massive scale.

Our compositional analysis of the thermally anomalous intracrater deposits suggests that there is little difference between the deposits and the surrounding region. Our quantitative studies of TES modeled abundances show no distinguishable difference in composition above the uncertainty, even though a few of the spectra vary slightly in shape. Although some degree of compositional deviation exists for deposit of crater 16330, this specific deposit is an exception and not representative of the other 19 deposits in the compositional study.

The region as a whole appears to be broadly similar in composition. The ST1 spectrum was identified by *Bandfield et al.* [2000b] as one of two spectra that

characterize the general composition of the low-albedo Martian surface. The global maps of surface types 1 and 2 concentration given in *Bandfield et al.* [2000b] indicate that ST1 models the composition in Margaritifer Terra more adequately than ST2. Our results confirm this, but the TES spectral shape and modeled abundances also show that the composition of the region differs noticeably even from that of ST1. For the surface type 1 spectrum, the modeled abundance of plagioclase feldspar is greater than that of pyroxene (Table 3), whereas the modeled abundances from the deposit and plains TES spectra of this study have the opposite trend.

Recent results from *Rogers et al.* [2007] indicate that the Martian low albedo regions can be described in further detail by eleven spectral shapes derived from representative regions. The modeled compositions of these representative spectra were used to define four compositional groups [*Rogers and Christensen*, 2007]. The resulting global maps, Figure 7 of *Rogers and Christensen* [2007], suggest that Margaritifer Terra is most adequately described by the spectrum and modeled composition of Group 3, consisting of the representative spectra of Tyrrhena Terra, Hesperia Planum, Cimmeria-Iapygia, and Meridiani. The average modeled abundances of phases for Group 3 is fairly consistent with the values we report here for the deposits and plains in southwestern Margaritifer Terra (see Table 5).

With little variation in composition between the deposits and their surroundings, there does not appear to be a correlation between thermal and mineralogical characteristics. Variation in effective particle size is the dominant difference between the anomalous deposits and the plains. If the deposits are solid, coherent units as they appear in visible images and their thermal inertia values suggest, it is likely that they represent

Table 2.5: Comparison of the range of modeled abundances (%) from this study with the abundances of Group 3 from *Rogers and Christensen* [2007].

	Plagioclase Feldspar	Pyroxene	Olivine	High-Si Phases	Other
This study*	20 - 40	25 - 50	5 -15	5 -15	5 - 20
Group 3, *Rogers and Christensen* [2007]	25	30	11	18	16

*Values from this study are reported to the nearest 5%.

outcrops of bedrock. The emplacement of bedrock could have occurred after crater formation by a primary volcanic process (e.g., a lava flow or an upwelling from below the crater) or by lithification of sediments (epiclastic and/or pyroclastic) transported into the crater by eolian or fluvial activity, or mass movements of the crater walls and rim. Such sediments could then be cemented by a material that is present in low abundances not detectable by TES or that lacks significant spectral features in the thermal infrared (e.g., halides).

Impact melts are expected to be produced during impacts on Mars [e.g., *Osinski*, 2006; *Schultz and Mustard*, 2004] and may be present within the craters analyzed in our study. However, little to no relief of crater rims and central peaks, along with shallow interior depths, indicate that erosion and infill have caused the degradation of most of these craters. We believe it likely that any impact-generated melts and/or breccias are buried by this later infill. The anomalous deposits are not seen in all the impact craters in this area of Mars, suggesting that they are not linked directly to the impact process (assuming the impact and target conditions are similar throughout this region). Additionally, we do not observe a variation in glass abundance between these deposits and the surrounding plains, and the glass abundances are all below detection limits.

The compositions determined in this study are dominantly basaltic, which might be consistent with either a primary igneous process or lithification of basaltic sediments that have undergone little chemical weathering. However, no lava flow features are observed on the deposits or leading into these craters, and there are no obvious vents nearby to deliver the material. Though floor-fractured craters, like the ones observed in the study area, are thought to be associated with localized magmatic intrusions [*Schultz*,

1978; *Schultz and Glicken*, 1979], evidence for surficial igneous activity is lacking (e.g., volcanic dark-halo craters such as seen along floor fractures of some craters on the Moon [*Head and Wilson*, 1979; *Schultz*, 1976]). Additionally, any relation between the process forming the floor-fractured craters and the high thermal inertia deposits studied here is tenuous because fractures are not observed in all of the craters exhibiting anomalous intracrater deposits, although this logic is complicated by the slight possibility that continued infill of the craters could have obscured fractures or volcanic constructs.

Lithification of basaltic sediments seems to fit more closely with the observations, including possible layering within the 16330 deposit (though layering is not unique to this method of formation). In this hypothesis, water would have interacted with the sediments in the past and resulted in the formation of a coherent unit that retained its bulk composition, adjusted slightly for the small percentage of a cementing phase. The quantity of water likely involved in this type of scenario is unknown and could range from small transitory amounts, including groundwater, to standing bodies of water. The outcome of a similar process has been observed at Meridiani Planum, where sediments are believed to be cemented by sulfates and possibly other evaporites resulting from groundwater fluctuations [e.g., *McLennan et al.*, 2005; *Squyres et al.*, 2004; *Squyres and Knoll*, 2005].

In light of the identification of sulfates by the MER Opportunity rover in Meridiani Planum, and also by the Observatoire pour la Mineralogie, l'Eau, les Glaces et l'Activité (OMEGA) instrument on the Mars Express spacecraft [e.g., *Gendrin et al,* 2005], we added the spectra of additional Fe-, Mg-, and Ca-sulfate minerals to our original spectral library. We then repeated the deconvolutions to perform an initial test of

the idea of lithification by evaporite cements. With the modified spectral library, the abundance of evaporite minerals was modeled at a consistently higher percentage (up to 35%), though the observed fit of the modeled spectrum was not significantly improved and the RMS error did not show significant improvement above the noise; it therefore cannot be said with certainty which combination of modeled abundances is more accurate. Because deconvolutions using the original spectral library did not result in any obvious misfits in modeled spectra, this observation is not surprising. The information gained from the additional deconvolution does illustrate the possibility that evaporite minerals may be present in significant (>15%) proportions, though there is no clear trend of increased modeled sulfate abundance for intracrater deposits above that of the plains, as would be expected in order to strongly support the idea of sulfate as a cementing agent for the intracrater deposits. It is possible that the differences in sulfate abundance between deposits and plains may be so small that the uncertainty of the data may obscure any potential trend. Analysis of these anomalous deposits by the two visible to near-infrared instruments currently at Mars, OMEGA and the Compact Reconnaissance Imaging Spectrometer for Mars (CRISM) on the Mars Reconnaissance Orbiter spacecraft, may be helpful in detecting any cementing material.

Lithification of sediments may be the most straightforward way to explain the presence of these anomalous deposits in low-lying areas, where sediments may become trapped. The region also hosts remnants of the Uzboi-Ladon-Margaritifer mesoscale outflow system [*Grant and Parker*, 2002], evidence that water has been available there in the past. Even if the deposits formed during a time of no surficial water flow, melting of

subsurface ice could be another potential source of fluid, an idea supported by the proximity of chaos regions and outflow channels.

We are unsure as to why these deposits are present in some craters but not in others of similar size in the same region. There does not appear to be a connection with elevation or location. These observations suggest that the occurrence of these high thermal inertia deposits may be the result of a highly localized process. We cannot be certain that a single process or event produced the deposits in this area. The high density of these deposits in southwestern Margaritifer Terra does suggest that the process(es) forming high thermal inertia deposits preferentially occurred, or was preferentially preserved, in this region.

5. Summary and Conclusions

The results and interpretations determined by this work are outlined below:

- The thermally anomalous intracrater deposits studied in Margaritifer Terra have higher thermal inertia values than their surroundings. These values can be as large as 1060 J m^{-2} K^{-1} $s^{-1/2}$ and suggest a rocky or bedrock surface.
- This proposed rocky to bedrock character is supported by MOC images exhibiting a coherent surface. Smaller, unconsolidated particles likely exist on the surface of these units but are not concentrated in association with the thermal anomalies.
- Our compositional analysis of these deposits with TES and THEMIS data show little difference in the composition between the thermally anomalous deposits and that of the surrounding region.

- Hypotheses for the origin of these intracrater thermal anomalies include the emplacement of primary igneous material, but lithification of basaltic sediments may be the more likely process.
- The process that formed the intracrater deposits seems to have occurred on a local scale.

Thermally anomalous deposits are not restricted to this study area. It is possible that the interpretations derived from this study may be extrapolated to other deposits, implying that they also formed by processes similar to those proposed for the origin of the intracrater thermal anomalies in this area of Margaritifer Terra. Evaluation and comparison to similar deposits in adjacent areas may augment the results of the present study.

Acknowledgements

The authors would like to thank R. Fergason for the use of the program to derive the THEMIS thermal inertia measurements and M. Lane for additional sulfate spectra. We are also grateful to Malin Space Science Systems for the use of the Mars Orbiter Camera images, available at http://www.msss.com/moc_gallery/, specifically images S02-01115, S06-01399, S08-01915, S08-03262, and their context images obtained through the Public Target Request Site. THEMIS images are provided courtesy of THEMIS Public Data Releases and are available at http://themis-data.asu.edu. The helpful discussions and guidance provided by F. S. Anderson and W. Koeppen are greatly appreciated. We are thankful for the thorough reviews by D. Rogers and S. Ruff, which helped to clarify and improve the manuscript. This work was supported by grants from the Mars Data Analysis (NAG5-13421) and Mars Fundamental Research (NAG5-12685) programs. This is HIGP publication 1489 and SOEST publication 7152.

CHAPTER 3

Seeking phyllosilicates in thermal infrared data:

A laboratory and Martian data case study

ABSTRACT

Previous analyses of Thermal Emission Spectrometer (TES) data produce results that could suggest a widespread distribution of phyllosilicate minerals over the surface of Mars, whereas studies of visible to near-infrared (VNIR) data indicate a more limited distribution. We use VNIR detections of phyllosilicates in the vicinity of the Nili Fossae to determine the spectral characteristics of phyllosilicate-bearing material in the thermal infrared (TIR). By investigating areas of VNIR phyllosilicate detection in more detail, we find that the phyllosilicate-bearing material corresponds to spectral variation in Thermal Emission Imaging System (THEMIS) decorrelation-stretched TIR images and differences in infrared spectral shape that are consistent with, but not uniquely attributable to, mixtures of phyllosilicates and basalt. Phyllosilicate phases are modeled from TES data at abundances that average 5% over the region and at abundances near the 10 – 15% detection limit in our specific regions of interest. Deconvolution of numerical mixtures of phyllosilicate and basalt spectra indicate that these low abundances of phyllosilicates likely are not influenced by uncertainties greater than the 10 – 15% uncertainty of the method. TES spectra and modeled abundances vary between the phyllosilicate-bearing material and the surrounding region, but this difference in composition cannot be attributed solely to the presence of phyllosilicates. We believe the inconsistencies in phyllosilicate occurrence between TES and VNIR analyses may be explained by the

inclusion of phyllosilicates in the models of TES data as substitutes for poorly crystalline phases (e.g., allophane) not currently available in public infrared spectral libraries.

1. Introduction

For many years researchers have debated several questions concerning liquid water on the surface of Mars. Landforms such as valley networks and outflow channels suggest the flow of water, but current pressure and temperature conditions do not allow liquid water to exist at the surface and past conditions are not completely known. It appears that liquid water was present on the surface at some time in the past, but how long was it there and in what amount? Was it widespread or limited in spatial extent? One approach to answering these questions is to determine the minerals present on the surface and consider the conditions required for their formation. Minerals identified on Mars inform our understanding of the past environment and climate. Some researchers have used the presence of olivine on the Martian surface to suggest that the planet has always been cold and dry [e.g., *Hoefen et al*., 2003; *Stopar et al*., 2006], a conclusion drawn from the susceptibility of olivine to alteration in aqueous conditions. The more recent identification of phyllosilicates and other hydrated minerals indicates that water must have been available for their formation [e.g., *Poulet et al*., 2005]. The views of either a cold and dry or warm and wet past Martian climate do not appear to account for the complexity of the actual history. The identification of phyllosilicate minerals on the Martian surface may help to answer some questions about water on Mars. If clay minerals are ubiquitous, that would suggest that water was likely widespread and present for an extended time. If there are few or no occurrences of clay minerals then the events of liquid water on the surface were likely transitory. The potential implications make the identification of phyllosilicate minerals on the Martian surface an important issue. In remote investigations researchers use spectroscopy (i.e., the interaction of

electromagnetic energy with particles) to determine the mineralogy of a surface. Below we describe the spectroscopic studies focused on locating and identifying phyllosilicates on Mars.

1.1. The Search for Phyllosilicates

Since the beginning of telescopic and orbital observations of Mars, researchers have been searching for evidence of phyllosilicates, specifically the clay minerals they expect to be produced by the weathering of basaltic rocks. The spectral features of phyllosilicates allow for their identification in both the visible to near-infrared (VNIR) and thermal infrared (TIR) wavelength ranges. Because the TIR and VNIR wavelength ranges are sensitive to different properties of minerals and other geologic phases, the data collected from these two ranges are complementary. For example, phyllosilicates are identified in VNIR data by reflectance minima at ~1.4, 1.9, 2.2 – 2.4, and 3 μm from O-H, H-O-H, and metal-OH bonds in the minerals. In TIR data (Si, Al)-O bonds result in the most prominent features in phyllosilicates in the ~1200 – 900 cm^{-1} and ~600 – 400 cm^{-1} regions. As researchers accumulated spectral observations of Mars from the Earth and eventually from spacecraft, they discovered many lines of evidence that were consistent with the presence of phyllosilicates. These include absorptions at ~3 μm (consistent with molecular H_2O) [e.g., *Beer et al.*, 1971; *Houck et al.*, 1973; *Murchie et al.*, 1993; *Pimentel et al.*, 1974; *Singer et al.*, 1986; *Sinton*, 1967], ~9 μm (proposed to be consistent with a phyllosilicate phase like montmorillonite [e.g., *Aronson and Emslie*, 1975; *Hanel et al.*, 1972; *Hunt et al.*, 1973; *Toon et al.*, 1977] or palagonite [e.g., *Clancy et al.*, 1995; *Roush et al.*, 1993]), and others at ~1.9 μm and ~2.3 μm (consistent with

hydrated phases) [e.g., *McCord et al*., 1982; *Singer et al*., 1985]. However, due to resolution and atmospheric constraints, this evidence was not definitive.

With the Thermal Emission Spectrometer (TES) on the Mars Global Surveyor spacecraft scientists were able to acquire thermal infrared data at a spectral and spatial resolution high enough to make advances in the continuing search for definitive evidence of phyllosilicates on the Martian surface. Modeled phyllosilicate abundances of ~15% have been reported from TES over much of the Martian surface [e.g., *Bandfield et al*., 2000b; *Wyatt and McSween*, 2002]. The reliability of these derived abundances has been debated because of the possibility that they may not be distinguished from silica or poorly crystalline phases [*Michalski et al*., 2006b; *Wyatt and McSween*, 2002]. *Martinez-Alonzo et al*. [2006] devised a spectral variance index for TES data that identified the region around the Nili Fossae as being one of the most compositionally diverse areas on Mars and in a few small locations in the area they detected spectral signatures consistent with high-Si glass and/or phyllosilicates.

The newest generation of VNIR instruments are also allowing for higher spatial and spectral resolution measurements. The Observatoire pour la Mineralogie, l'Eau, les Glaces, et l'Activité (OMEGA) instrument on the Mars Express orbiting spacecraft detected the presence of phyllosilicates, specifically clay minerals, in a few locations on the Martian surface, particularly in Mawrth Valles and the region surrounding the Nili Fossae [*Bibring et al*., 2005; *Poulet et al*., 2005]. The OMEGA signatures in Mawrth Vallis are consistent with Al-smectites (e.g., montmorillonite) and Fe-Mg smectites (e.g., nontronite, chamosite) [*Loizeau et al*., 2007; *Poulet et al*., 2005]. Recently, VNIR data collected by the Compact Reconnaissance Imaging Spectrometer for Mars (CRISM)

[*Murchie et al*., 2007] instrument have mapped phyllosilicates in Mawrth Vallis at an even higher spatial resolution and have detected kaolinite, hectorite, and hydrated silica in addition to montmorillonite and Fe-Mg smectite [*Bishop et al*., 2008]. *Poulet et al*. [2005] describe the phyllosilicate minerals in the vicinity of the Nili Fossae as Fe-Mg rich based on OMEGA data. *Mangold et al*. [2007] conducted a more detailed investigation of the hydrous phases detected by OMEGA in the region around the Nili Fossae. They determined that the signatures of hydrous phases correspond to Fe-rich smectites and other phyllosilicates whose specific type is currently undetermined due to a broad or absent metal-OH feature. Recent CRISM observations have identified a greater diversity of phyllosilicate types in the region surrounding the Nili Fossae, including chlorite, kaolinite, and illite or muscovite, along with hydrated silica and a carbonate phase [e.g., *Ehlmann et al*., 2008a; *Ehlmann et al*., 2007; *Ehlmann et al*., 2008b; *Mustard et al*., 2008]. Some of the phyllosilicate detections from OMEGA and CRISM in this area are shown in Figure 1. A study by *Poulet et al*. [2008] suggests that phyllosilicate abundances are 20 – 65% in Mawrth Vallis and 20 – 35% in the region surrounding the Nili Fossae.

Following the recent VNIR observations, *Michalski and Fergason* [2008] have investigated the area around Mawrth Vallis with TES data and find that phyllosilicate minerals are a component of the modeled spectra for all units, not just the light-toned unit associated with the detection of phyllosilicates in the VNIR data. Additionally, these authors apply spectral indices to the TES spectra in the region that are designed to identify features consistent with nontronite and silica phases. The silica index results in a weak correlation with OMEGA and CRISM detections of phyllosilicates, whereas the

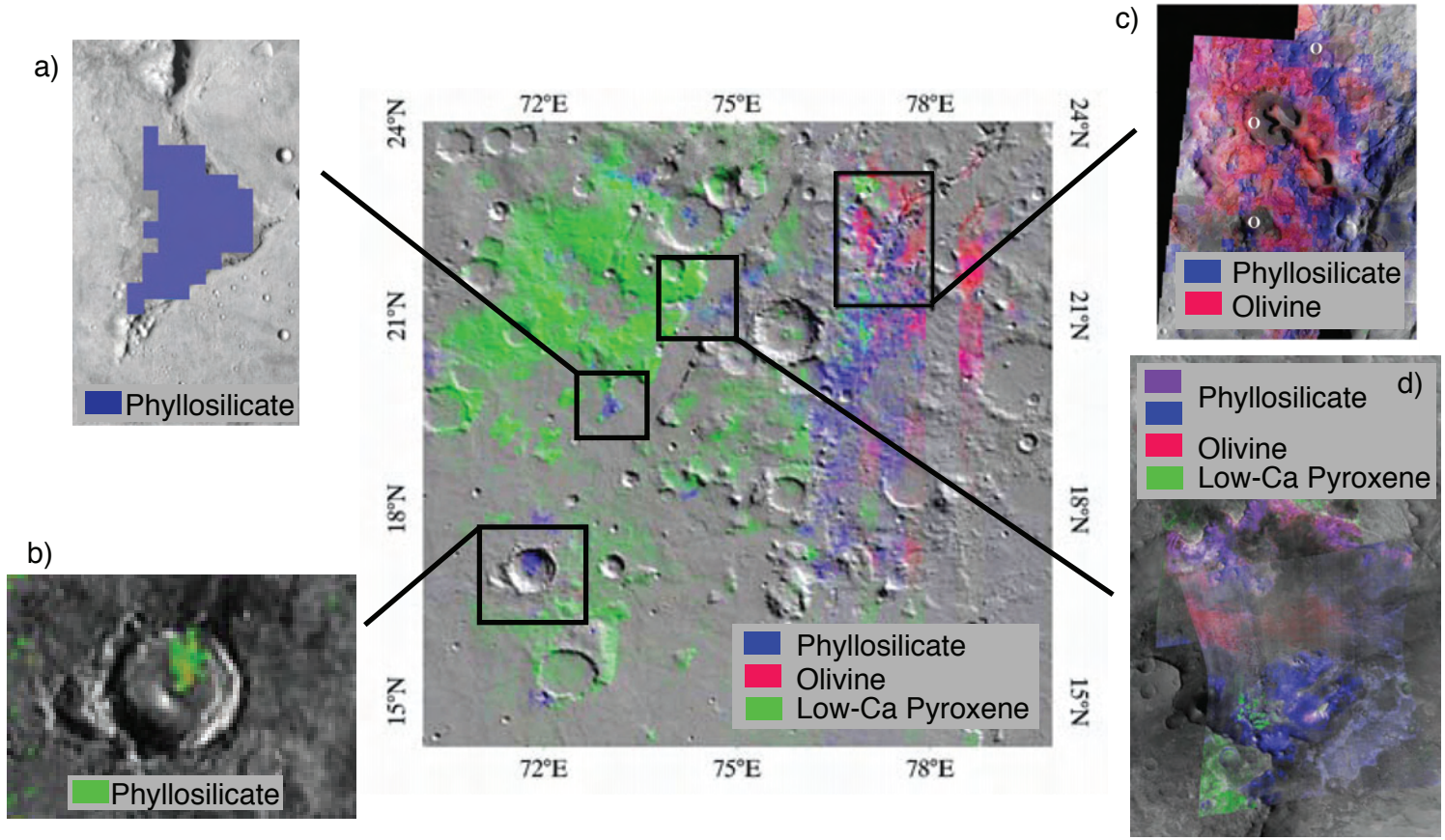

Figure 3.1: Identification of minerals in the vicinity of the Nili Fossae from visible to near-infrared data. The basemap is modified from Mustard et al. [2006]. The black boxes on the basemap show the locations of our local study areas, which are shown in more detail in a-d. a) 19N73E, modified from Poulet et al. [2005], showing phyllosilicate detections from OMEGA, b) 17N71E, modified from Mustard et al. [2008], showing phyllosilicate detections from CRISM, c) 22N77E, modified from Mustard et al. [2006], showing phyllosilicate detections from OMEGA, d) 21N74E, modified from Mustard et al. [2008], showing phyllosilicate detections from CRISM. Figures a, b, and d have been adapted with permission from Macmillan Publishers Ltd.

nontronite index shows no correlation. *Michalski and Fergason* [2008] propose multiple hypotheses, which we discuss in section 4.4 below, to explain this disconnect between the TIR and VNIR datasets. Their study does not find a single, obvious cause explaining all observations. Our study will build on the work of *Michalski and Fergason* [2008] by examining the TIR data in another region of Mars and investigating possible origins of this disconnect.

1.2. This Study

After many years of searching, scientists finally have strong evidence of phyllosilicate minerals on the Martian surface. However, VNIR detections of phyllosilicate-bearing material appear to be more limited on the Martian surface than TES TIR data would suggest if modeled phyllosilicate abundances are accurate. This inconsistency must be addressed and understood before the occurrence and type of phyllosilicate phases can be used to infer current or past environment and weathering activity.

We use the recent detections of phyllosilicate phases from VNIR instruments as a calibration point to test the characteristics and detectability of these materials in the TIR. With information from both the VNIR and TIR wavelength ranges we have the opportunity to determine if the compositions (derived from TIR data) of the known phyllosilicate-bearing areas (i.e., places where phyllosilicates are identified by VNIR data) differ from adjacent non-phyllosilicate-bearing areas at both THEMIS and TES resolution. If THEMIS data show spectral variation between the two areas we may be able to connect the spectral differences to the presence (or absence) of phyllosilicate

phases. From linear deconvolution of TES spectra we can determine if the modeled phyllosilicate abundances derived from the known phyllosilicate-bearing areas are greater than the modeled abundances of the non-phyllosilicate-bearing areas. If they are not, we may be able to discover possible reasons for the discrepancy between the VNIR and TIR detections.

We investigate the possibility of systematic over- or underestimation of modeled phyllosilicate abundance from linear deconvolution of spectra using numerical mixture spectra containing known amounts of phyllosilicate phases. In addition, we determine if modeled phyllosilicate abundance are affected by noise, wavelength range, and available library spectra. If we find any systematic over- or underestimation or influence of these variables that is greater than the 10 – 15% uncertainty generally cited for the method [*Christensen et al*., 2000c], these factors must be considered when analyzing modeled phyllosilicate abundances in TES data. Each of these tests contributes to the "big-picture" question of our confidence in the widespread detection of phyllosilicate minerals on the Martian surface by TES.

We focus our study in the vicinity of the Nili Fossae, a region notable for VNIR phyllosilicate detections [e.g., *Ehlmann et al*., 2007; *Mangold et al*., 2007; *Poulet et al*., 2005]. The Nili Fossae are located at the northern edge of the southern highlands near the dichotomy boundary, just west of the Isidis impact basin and north of the Syrtis Major volcanic complex. The fossae (centered at 22.6° N, 76.8° E), shown in Figure 2, are ring fractures and graben arranged in concentric arcs around the northwest edge of the Isidis impact basin and likely formed in association with that event [*Greeley and Guest*, 1987; *Tanaka et al*., 1992]. The fractures cut through the Noachian cratered unit (Npl_1),

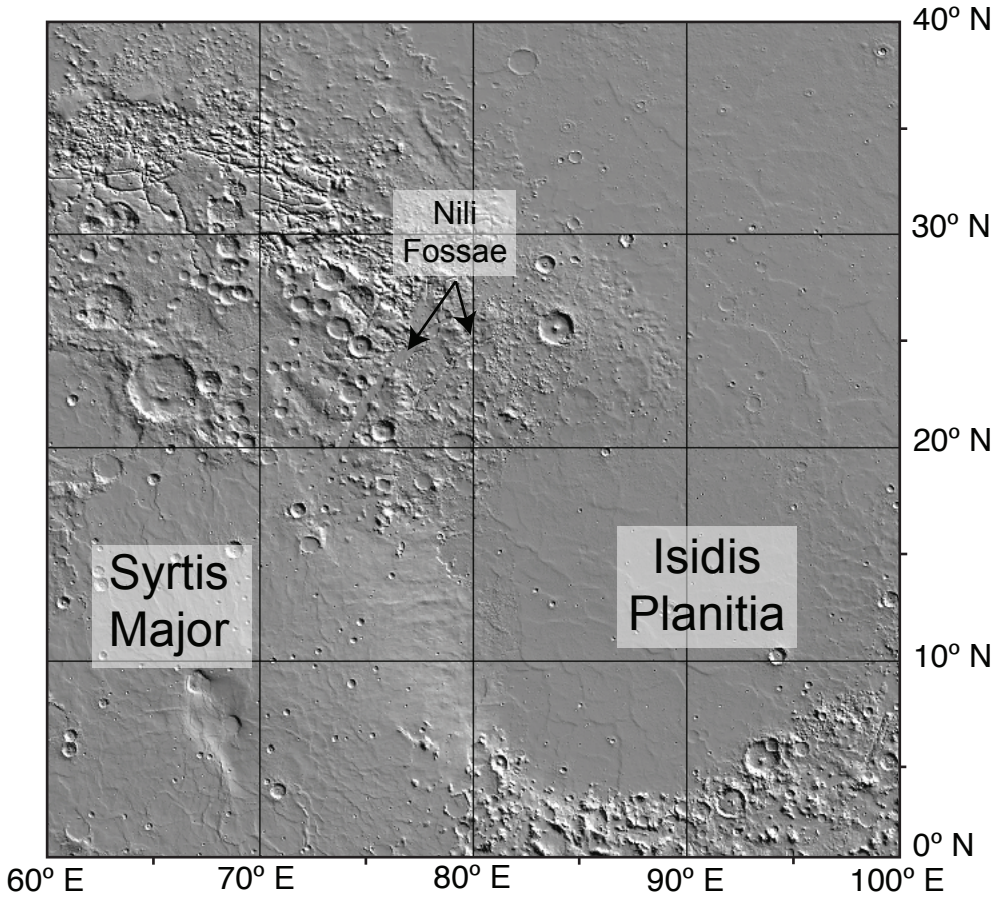

Figure 3.2: Shaded relief map showing the Nili Fossae and surrounding region.

subdued crater unit (Npl_2), and etched unit (Nple), whereas the more recent (Amazonian) smooth plains material (Aps), likely of eolian origin, covers the floor of the large graben [*Greeley and Guest*, 1987]. *Hiesinger and Head* [2004] suggest that lava flows of the Syrtis Major formation to the south (unit Hs in *Greeley and Guest* [1987]) previously covered the graben floor and are now overlain by the Aps unit. The subdued crater and etched units are thought to be cratered plains modified by partial burial by thin igneous or sedimentary deposits and dissection by eolian erosion along with deposition of probable eolian material, respectively [*Greeley and Guest*, 1987].

The presence of the largest exposure of olivine-rich basaltic material [e.g., *Hamilton and Christensen*, 2005] makes the region around the Nili Fossae unique from most other areas of the Martian surface, which are, to first order, consistent with two general compositional groupings as determined by TES thermal infrared spectral data. Surface type 1 (ST1) is interpreted as a basalt and is largely located in the southern highlands, and surface type 2 (ST2) is thought to be either a basaltic andesite or a weathered basalt and is found mainly in the northern lowlands [e.g., *Bandfield et al*., 2000b; *Wyatt and McSween*, 2002]. The olivine enrichment around the Nili Fossae was initially identified in TES spectra by *Hoefen et al*. [2003] and also by *Hamilton et al*. [2003] as a candidate site for olivine-rich Martian meteorites. The olivine-rich material and its possible geologic origins is further described in *Hamilton and Christensen* [2005], *Mustard et al*., [2007b], and *Tornabene et al*. [2008].

Our analyses of data in the region around the Nili Fossae are conducted at two scales. The large scale is regional, with a study area encompassing the region 71 – 82° E and 16 – 27° N. The other is a smaller, local scale in which we have multiple study

areas. We chose these areas because VNIR data have identified phyllosilicate-bearing material in these locations [e.g., *Mustard et al*., 2007a; *Mustard et al*., 2006; *Poulet et al*., 2005]; they are shown in Figure 1 and are designated by their approximate latitude and longitude. They include 19N73E, the peninsula-shaped outcrop at ~19° N, 73° E; 17N71E, the northern interior of the crater at ~17° N, 71° E; 22N77E, the low-lying phyllosilicate deposits containing dikes and in close proximity to olivine-rich materials at ~22° N, 77° E; and 21N74E, the phyllosilicate exposures along the western wall of the largest Nili Fossae trough at ~21° N, 74° E.

We analyze the regional and local study areas using the data sets and methods described below. In subsequent sections we present the results of the analyses and then discuss their significance. To conclude we summarize our findings and consider their impact on our current understanding of the detection of phyllosilicate phases by thermal infrared data.

2. Data Sets and Methods

2.1. Thermal Infrared Data

2.1.1. TES Data

We use hyperspectral thermal infrared (TIR) data collected by TES; this instrument was carried onboard the Mars Global Surveyor spacecraft, which mapped the surface of Mars from 1999 to 2006. TES was a Michelson interferometer that measured the emitted energy in 143 or 286 channels ranging from ~1724 to 200 cm^{-1} (resulting in 10 or 5 cm^{-1} sampling) [*Christensen et al*., 1992; *Christensen et al*., 2001a]. The 3 × 2 array of detectors had an effective spatial resolution of ~3 × 6 km. The TES instrument

also contained thermal (~1960 – 67 cm^{-1}) and visible/near-infrared (0.3 – 2.9μm, ~33,333 – 3448 cm^{-1}) bolometers for mapping thermophysical properties and albedo, respectively [*Christensen et al*., 2001a].

Because mineral spectra in a mixture are assumed to combine linearly in the thermal infrared in proportion to their abundance [*Lyon*, 1963], the spectrum of a mixture can be linearly deconvolved using an iterative least squares method that determines the best fit combination of components and abundances based on a library of likely phases [*Ramsey and Christensen*, 1998]. A TES spectrum of Mars includes both surface and atmospheric components; the atmospheric components have been shown to combine linearly with the surface components [*Smith et al*., 2000], allowing them to be accounted for in the model and subtracted from the best-fit spectrum. The remaining components are then normalized to 100% to obtain the abundance values for the surface phases. *Christensen et al*. [2000c] estimate a general uncertainty and detection limit of 10 – 15% for the modeled abundances from this technique for TES data, though the detection limit of some phases may be higher or lower depending on the strength of their spectral features [*Hamilton et al*., 2003].

Koeppen and Hamilton [2008] used this deconvolution method on the global TES data set to produce modeled abundances of many phases, which can also be displayed as mineral abundance maps, though they were specifically interested in the occurrence of olivine. Their spectral library is listed in Table 1. We map the modeled abundances of *Koeppen and Hamilton* [2008] in the vicinity of the Nili Fossae to analyze the presence and distribution of the phases in regional detail. Modeled abundance values are binned at

Table 3.1: Spectral library used in the regional deconvolution of TES data, from *Koeppen and Hamilton*, [2008]

Phases	Class	Sample #	Reference
CO_2	Atmosphere		c
Dust, Low CO_2	Atmosphere		a,b
Dust, High CO_2	Atmosphere		a,b
Water Vapor	Atmosphere		c
Water Ice Cloud (High Latitude)	Atmosphere		a,b
Water Ice Cloud (Low Latitude)	Atmosphere		a,b
Olivine, Fo_{91}	Olivine	BUR-3720A	d
Olivine, Fo_{68}	Olivine	KI-3115	h
Olivine, Fo_{53}	Olivine	KI-3372	h
Olivine, Fo_{39}	Olivine	KI-4143	h
Olivine, Fo_{18}	Olivine	KI-3354	h
Olivine, Fo_{1}	Olivine	WAR-RGFAY01	d
Albite	Feldspar	WAR-0244	d,e
Oligoclase	Feldspar	WAR-0234	d,e
Andesine	Feldspar	BUR-240	d,e
Labradorite	Feldspar	WAR-4524	d,e
Bytownite	Feldspar	WAR-1384	d,e
Anorthite	Feldspar	BUR-340	d,e
Diopside	Clinopyroxene	WAR-6474	d,f
Augite	Clinopyroxene	NMNH-9780	d,f
Augite	Clinopyroxene	NMNH-122302	d,f,g
Hedenbergite, manganoan	Clinopyroxene	DSM-HED01	d,f
Pigeonite ($Wo_{10}En_{36}Fs_{54}$ 33,34)	Clinopyroxene		f
Enstatite	Orthopyroxene	HS-9.4B	d,f
Bronzite	Orthopyroxene	BUR-1920	f
ALH84001 (orthopyroxene)	Orthopyroxene		g
Gypsum	Sulfate	ML-S6	d,k
Kieserite	Sulfate	C5492-1	k
Anhydrite	Sulfate	ML-S9	d,k
Quartz	Silica/Phyllo	BUR-4120	d
K-rich Glass	Silica/Phyllo		j
SiO_2 Glass	Silica/Phyllo		j
Serpentine	Silica/Phyllo	HS-8.4B	d
Illite	Silica/Phyllo	IMt-2 (granular)*	d,i
Ca-Montmorillonite	Silica/Phyllo	STx-1 (solid)	d,i
Saponite	Silica/Phyllo	<0.2 μm**	l
Crystalline Heulandite	Silica/Phyllo		m
Crystalline Stilbite	Silica/Phyllo		m
Calcite	Carbonate	C40	d
Dolomite	Carbonate	C20	d
Hematite	Hematite		n

Further details about these spectra and how they were collected can be found in the following: a) *Smith et al*. [2000]; b) *Bandfield et al*. [2000a]; c) *Bandfield* [2002]; d) *Christensen et al*. *[2000a]*; e) *Ruff* [1998]; f) *Hamilton* [2000]; g) *Hamilton et al*. [2003]; h) *Hamilton et al*., in prep; i) *Piatek* [1997]; j) *Wyatt et al*. [2001]; k) *Lane* [2007]; l) *Michalski et al*. [*Michalski et al*., 2005b]; m) *Ruff* [2004]; n) *Bandfield et al*. [2000b]

*Minus 60% blackbody.
**Plus 60% blackbody.

a spatial resolution of 16 pixels per degree. We report the median abundance values for each phase (or combination of phases) in each bin.

Along with examining abundances from binned data, we perform additional deconvolution analysis on four local study areas (shown in Figure 1) using hand-selected TES daytime TIR data collected over the region of interest. The number of spectra averaged for the phyllosilicate-bearing and non-phyllosilicate-bearing spots in each area range from two to twenty-four. In some cases, especially the 22N77E study area, the phyllosilicate-bearing area is small and therefore the TES pixels are not solely on the region of interest but also include a small part of the immediately adjacent terrain. Unless otherwise noted, the TES data used in our study are limited to those with a temperature greater than 270 K, low atmospheric dust (best fit opacity value = 0.15 or less), and low water ice (best fit opacity value = less than 0.04). Deconvolution is performed with 10 cm^{-1} resolution spectra over the range of 1302 – 305 cm^{-1} (excluding the area of high CO_2 absorption, 825 – 508 cm^{-1}). Because the spectral library from *Koeppen and Hamilton* [2008] was designed for deconvolution of data globally, it may not be the best collection of phases for our local study areas. We have created another spectral library tailored through multiple preliminary trials to be suitable for this region (Table 2), providing all the phases necessary for a good fit to the spectra and allowing for more accurate results. This library includes a larger number of phyllosilicate mineral spectra and a greater variety of primary mineral spectra that represent a mineral's range in composition and, thus, spectral shape (e.g., two spectra of the mineral oligoclase with slight differences). It also contains phyllosilicate spectra from the smectite, kaolinite and illite groups; these groups correspond to many types of phyllosilicates detected around

Table 3.2: Spectral library used in the deconvolution of TES data from local study areas.

Phase	Class	Sample #	Reference
Dust Low CO_2	Atmosphere		a,b
Dust High CO_2	Atmosphere		a,b
Water Ice Cloud (High Latitude)	Atmosphere		a,b
Water Ice Cloud (Low Latitude)	Atmosphere		a,b
CO_2 Gas	Atmosphere		c
H_2O Gas	Atmosphere		c
Microcline	Alkali Feldspar	BUR-3460	d,e
Oligoclase	Plagioclase Feldspar	WAR-0234	d,e
Oligoclase (Peristerite)	Plagioclase Feldspar	BUR-060	d,e
Labradorite	Plagioclase Feldspar	BUR-3080A	d,e
Labradorite	Plagioclase Feldspar	WAR-RGAND01	e
Andesine	Plagioclase Feldspar	BUR-240	d,e
Bytownite	Plagioclase Feldspar	WAR-1384	d,e
Enstatite	Orthopyroxene	HS-9.4B	d,f
Bronzite	Orthopyroxene	NMNH-93527	d,f
ALH 84001	Orthopyroxene		g
Pigeonite*	Clinopyroxene		f
Diopside	Clinopyroxene	NMNH-R15161	d,f
Diopside	Clinopyroxene	WAR-6474	d,f
Augite	Clinopyroxene	DSM-AUG01	d,f
Augite	Clinopyroxene	NMNH-122302	f
Augite	Clinopyroxene	NMNH-9780	f
Forsterite	Olivine	BUR-3720A	d
Olivine Fo_{68}	Olivine	KI-3115	h
Olivine Fo_{53}	Olivine	KI-3372	h
Olivine Fo_{39}	Olivine	KI-4143	h
Olivine Fo_{18}	Olivine	KI-3354	h
Fayalite	Olivine	WAR-RGFAY01	d
Kaolinite	Phyllosilicate	KGa-1b (solid)	d,i
Nontronite	Phyllosilicate	WAR-5108 (solid)	d,i
Fe-smectite	Phyllosilicate	SWa-1 (solid)	d,i
Ca-montmorillonite	Phyllosilicate	STx-1 (solid)	d,i
Illite**	Phyllosilicate	IMt-2 (granular)	d,i

(Continued Next Page)

Table 3.2: (Continued) Spectral library used in the deconvolution of TES data from local study areas.

Phase	Class	Sample #	Reference
K-rich Glass	High-Silica		j
Avg. Martian Hematite	Hematite		l
Gypsum	Evaporite	ML-S5	d,k
Gypsum (Selenite)	Evaporite	ML-S8	d,k
Anhydrite	Evaporite	ML-S9	d,k
Calcite	Carbonate	C40	d
Dolomite	Carbonate	C20	d
Montmorillonite***	Phyllosilicate	SWy-1	m
Nontronite***	Phyllosilicate	Nau-2	m
Illite***	Phyllosilicate	IMt-1	m
Kaolinite***	Phyllosilicate	KGa-1	m

Further details about these spectra and how they were collected can be found in the following: a) *Smith et al*. [2000]; b) *Bandfield et al*. [2000a]; c) *Bandfield* [2002]; d) *Christensen et al*. *[2000a]*; e) *Ruff* [1998]; f) *Hamilton* [2000]; g) *Hamilton et al*. [2003]; h) *Hamilton et al*., in prep; i) *Piatek* [1997]; j) *Wyatt et al*., [2001]; k) *Lane* [2007]; l) *Glotch et al*., [2004]; m) *Michalski et al*., [2006b]

* Minor transparency features removed
**Minus 60% blackbody
***Spectrum used to replace the mixture phyllosilicate spectrum in the spectral library for deconvolution of the numerical mixture spectra (see Section 3.2.2. and Figure 6). These spectra were measured by *Michalski et al*., [2006b] in pellet form.

the Nilli Fossae [e.g., *Ehlmann et al*., 2008a; *Ehlmann et al*., 2007; *Mangold et al*., 2007]. This set of phases is designed for our study and may not be the most appropriate spectral library to use in the deconvolution of other areas of Mars. Another location may have different phases that must be included in the spectral library. Because the number of spectra in the library is necessarily limited by the number of TES spectral bands, we cannot use every reference spectrum available and must chose the group of spectra that is geologically reasonable and provides the best fit to the data.

2.1.2. THEMIS Data

We also use multispectral data from the Thermal Emission Imaging System (THEMIS) on the Mars Odyssey spacecraft. The THEMIS instrument has two subsystems, one of which is a thermal infrared imager with ten spectral bands centered at nine wavelengths between 1474 and 672 cm^{-1} (one spectral band is redundant) [*Christensen et al*., 2004]. It takes both nighttime and daytime thermal infrared images with a spatial resolution of ~100 m/pixel. In addition, THEMIS has a visible imaging subsystem that produces higher spatial resolution (up to ~18 m/pixel) images with five bands centered in the range of 0.425 to 0.860 μm (~23,530 to 11,628 cm^{-1}) [*Christensen et al*., 2004].

Multispectral TIR data from THEMIS allow us to analyze the spectral character of our local study areas. Spectral variation in THEMIS images is enhanced by applying a decorrelation stretch (DCS) [*Gillespie et al*., 1986]. This stretch applies a principle components (PC) transformation to three user-specified bands, redefining the axes in the way that maximizes variation and removes correlated information between the bands

(like that due to surface temperature), and then inverses this transformation to display the three user-defined bands as red, green, and blue in a false-color image. In this study we use the Bands 8, 7, and 5 as red, green and blue, a combination that enhances differences in low silica and high silica materials. Within a scene the most mafic compositions will be a magenta or purple color, whereas the most felsic compositions will be a yellowish color.

We remove the atmospheric contribution from THEMIS spectra using the method described in *Bandfield et al*. [2004a]. Atmospheric emission is removed using a constant radiance offset removal over an area with constant emissivity but affected by shaded and sunlit slopes (e.g., a crater) that result in varying proportions of atmospheric and surface emission between measurements. Attenuation of surface emissivity by the atmosphere is determined from comparison of an average THEMIS spectrum with a TES surface spectrum from the same area convolved to THEMIS resolution; the difference is attributed to atmospheric effects and is subtracted from each pixel in the image. This method assumes that there are no large changes in elevation (e.g., <~1000 m) or atmospheric opacity (e.g., clouds, dust) in the image. Also, it assumes that the surface composition of the test area is homogeneous at both THEMIS and TES spatial scales and has not changed in the time between observations. We believe these assumptions are reasonable for the analysis of our data.

2.2. Numerical Mixture Analysis

To determine if a detection limit and uncertainty of 10 – 15% is appropriate for modeled abundances of phyllosilicate phases under a variety of common linear

deconvolution conditions, we perform a controlled test on the uncertainty of modeled phyllosilicate abundances by creating numerical mixture spectra from combinations of basalt and phyllosilicate spectra in proportions of 0:100 to 100:0, increasing in 5% increments. We use two different basaltic components, an artificially constructed basalt spectrum (composed of 40% plagioclase feldspar, 30% clinopyroxene, 20% orthopyroxene, and 10% olivine) and the surface type 1 spectrum, to represent a best case scenario where all the basaltic mixture components are known and available in the spectral library (artificial spectrum) and a more realistic scenario where the basaltic mixture components are not as well known (surface type 1). We combine the spectrum of each basaltic component with each of four phyllosilicate spectra (illite, nontronite, montmorillonite, and kaolinite), resulting in eight sets of mixture spectra (yielding a total of 168 individual spectra). We linearly deconvolve the mixture spectra and compare the modeled phyllosilicate abundance with the known abundance in the mixture. We run the deconvolution over three commonly used wavelength ranges, 1302 – 400 cm^{-1}, 1302 – 350 cm^{-1}, and 1302 – 305 cm^{-1}, to analyze the effect of including or omitting spectral features at these low wavenumbers. We conduct this test using three spectral libraries, one containing the exact phyllosilicate spectrum used in the mixture spectrum, another in which the exact phyllosilicate spectrum has been replaced by a similar one from the same phyllosilicate group, and one in which no phyllosilicate spectrum from that group is present.

We also investigate the effect of noise on the deconvolution. Because the noise contribution from some sources can be difficult to quantify (e.g., systematic error from the instrument response function), we use twice the random noise of a TES observation to

produce an estimate of the total noise. We calculate the average radiance of a series of 257 continuous TES observations (ICKs) of space yielding 1548 individual spectra (*J. Bandfield*, personal communication, 2005). The radiance of space is theoretically zero and therefore radiance values that deviate from zero are assumed to be due to noise. The radiance values from the observations are averaged and the standard deviation of that average is calculated. To add this standard deviation, which represents the noise of a typical TES spectrum, we convert a mixture emissivity spectrum to radiance using a blackbody curve of a certain temperature. The two radiance spectra are added together and then converted to emissivity using a blackbody curve at the same temperature used previously. This process results in realistically noisy spectra for the purposes of our analysis. Table 3 illustrates the way in which we combine each of these parameters and the conditions for each deconvolution (3024 deconvolutions in total).

3. Results

3.1. TES Regional Phase Abundance Maps

Below we present the maps of modeled abundance values for each common primary mineral and groups of secondary minerals in the vicinity of the Nili Fossae, using results from *Koeppen and Hamilton* [2008]. We report the spectra used most commonly or in the greatest abundance, along with any spatial trends observed in the values that may indicate variations in composition. Because we are looking at these phases in a regional context, we do not focus on isolated pixels of high abundance that are not spatially contiguous.

Table 3.3: Combination of parameters used for each deconvolution in our numerical mixture analysis.

		No Added Noise			Added Noise		
		Mixture Spectrum in Library	Spectrum of Similar Phase in Library	No Spectrum of Similar Phase in Library	Mixture Spectrum in Library	Spectrum of Similar Phase in Library	No Spectrum of Similar Phase in Library
Numerical Basalt Mixtures							
Kaolinite Mixture Spectra	1301 – 400 cm^{-1}	✓	✓	✓	✓	✓	✓
	1301 – 350 cm^{-1}	✓	✓	✓	✓	✓	✓
	1301 – 305 cm^{-1}	✓	✓	✓	✓	✓	✓
Illite Mixture Spectra	1301 – 400 cm^{-1}	✓	✓	✓	✓	✓	✓
	1301 – 350 cm^{-1}	✓	✓	✓	✓	✓	✓
	1301 – 305 cm^{-1}	✓	✓	✓	✓	✓	✓
Nontronite Mixture Spectra	1301 – 400 cm^{-1}	✓	✓	✓	✓	✓	✓
	1301 – 350 cm^{-1}	✓	✓	✓	✓	✓	✓
	1301 – 305 cm^{-1}	✓	✓	✓	✓	✓	✓
Ca-Montmorillonite Mixture Spectra	1301 – 400 cm^{-1}	✓	✓	✓	✓	✓	✓
	1301 – 350 cm^{-1}	✓	✓	✓	✓	✓	✓
	1301 – 305 cm^{-1}	✓	✓	✓	✓	✓	✓
ST1 Mixtures							
Kaolinte Mixture Spectra	1301 – 400 cm^{-1}	✓	✓	✓	✓	✓	✓
	1301 – 350 cm^{-1}	✓	✓	✓	✓	✓	✓
	1301 – 305 cm^{-1}	✓	✓	✓	✓	✓	✓
Illite Mixture Spectra	1301 – 400 cm^{-1}	✓	✓	✓	✓	✓	✓
	1301 – 350 cm^{-1}	✓	✓	✓	✓	✓	✓
	1301 – 305 cm^{-1}	✓	✓	✓	✓	✓	✓
Nontronite Mixture Spectra	1301 – 400 cm^{-1}	✓	✓	✓	✓	✓	✓
	1301 – 350 cm^{-1}	✓	✓	✓	✓	✓	✓
	1301 – 305 cm^{-1}	✓	✓	✓	✓	✓	✓
Ca-Montmorillonite Mixture Spectra	1301 – 400 cm^{-1}	✓	✓	✓	✓	✓	✓
	1301 – 350 cm^{-1}	✓	✓	✓	✓	✓	✓
	1301 – 305 cm^{-1}	✓	✓	✓	✓	✓	✓

3.1.1. Plagioclase Feldspar

Figure 3a shows that plagioclase feldspar is identified throughout the region in abundances averaging ~30% (ranging up to 50 – 60%). We observe a small area of lower abundances between ~21 – 23° N and 77 – 80° E (black box in Figure 3a), which corresponds to an area of increased olivine abundance, described below.

Compositions ranging from albite to anorthite are included in the spectral library, and the most commonly identified phases are intermediate in composition (oligoclase, andesine, labradorite, and bytownite). For every bin, there is typically a combination of two or more of these plagioclase compositions (a behavior observed in other studies [e.g., *Milam et al*., 2004; *Ruff*, 1998; *Wyatt et al*., 2001]), though oligoclase and bytownite most commonly make up the largest percentage of the plagioclase abundance. We have calculated the average anorthite (An) composition for each bin; values of An 40 – 70 are the most common.

3.1.2. Pyroxene

Pyroxene is ubiquitous in the region around the Nili Fossae (Figure 3 b & c). The TES phase abundance maps show that clinopyroxene generally is more abundant than orthopyroxene. Additionally, whereas the abundance of clinopyroxene is relatively constant over the entire region, the abundance of orthopyroxene is lower in the southwest corner of the region, corresponding to the younger lava flows from the Syrtis volcanic complex. We do not observe a change in pyroxene abundance in the area of decreased plagioclase feldspar abundance mentioned above (21 – 23° N, 77 – 80° E).

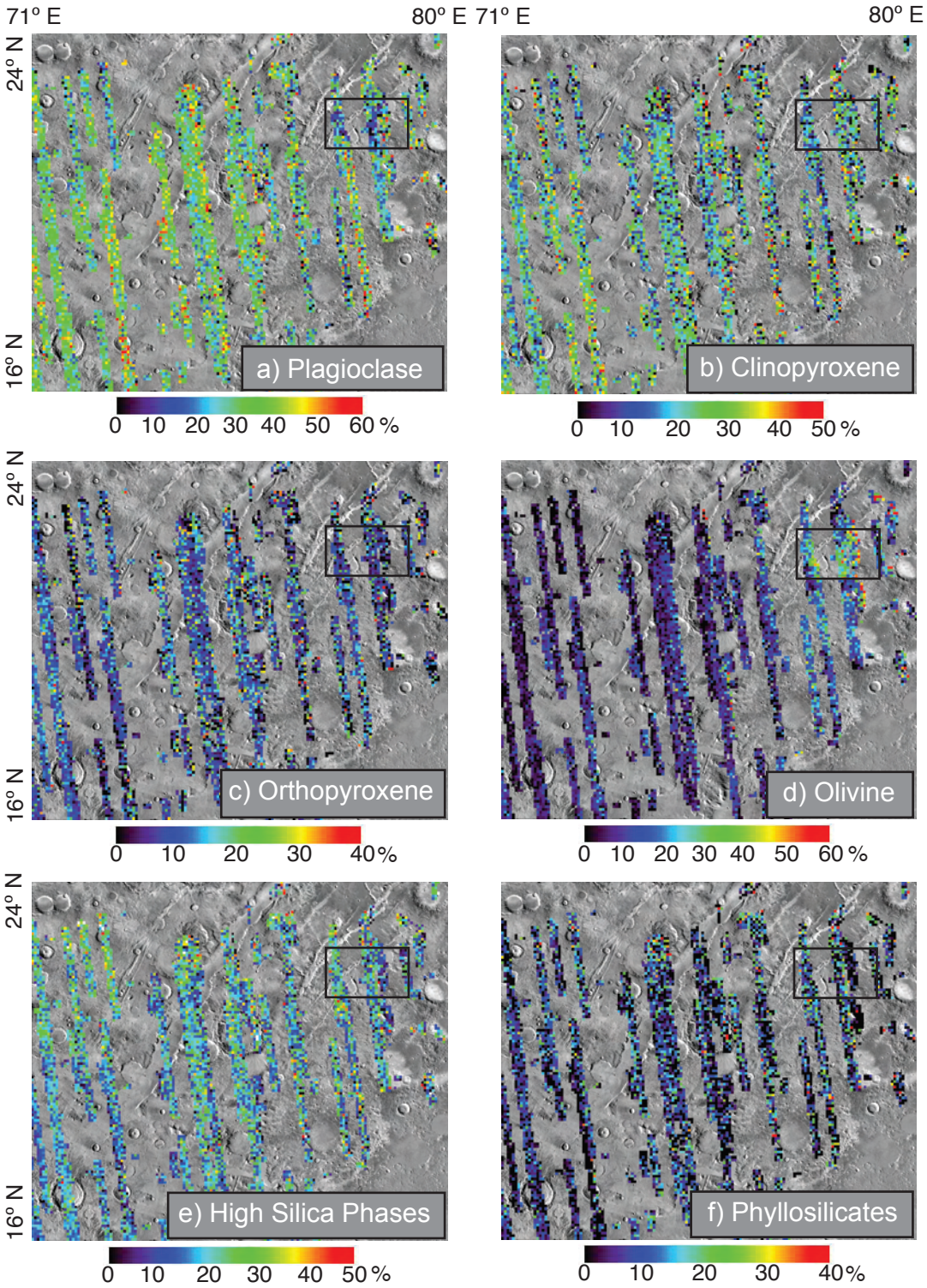

Figure 3.3: TES regional abundance maps for the a) plagioclase, b) clinopyroxene, c) orthopyroxene, and d) olivine groups overlayed on a THEMIS daytime infrared mosaic. See Table 1 for the individual phases combined to produce these group maps. Black boxes, centered at ~22.2° N, 78.7° E, indicate areas of low and high abundance for plagioclase and olivine, respectively. The pixels are not continuous because data is restricted for quality.

Abundance values have an average of ~20% for clinopyroxene and ~10% for orthopyroxene in the study area; maximum values are as high as ~50% and ~40%, respectively. Five clinopyroxene spectra are included in the spectral library. The spectrum used most commonly is an augite with moderately high titanium (NMNH 122302) [*Hamilton*, 2003]. The most common orthopyroxene phase has a composition of $Wo_{3.3}En_{69.4}Fs_{27.3}$ (ALH84001) [*Mittlefehldt*, 1994].

In our study we analyze clinopyroxene and orthopyroxene separately, with pigeonite included with the clinopyroxenes. It is important to note that VNIR data may be displayed differently, grouped into high-calcium and low-calcium pyroxene; the spectral features of pigeonite may be intermediate between the two [*Adams*, 1974]. The assignment of pigeonite in this system generally is unspecified.

3.1.3. Olivine

The average of olivine abundance values in this region is ~10%, and olivine is modeled at abundances of up to ~60% (Figure 3d). The highest abundances are concentrated in an area in the eastern part of the region (roughly 21 – 23° N, 77 – 80° E, corresponding to the black box in Figure 3d and the region of low plagioclase abundance mentioned above). These are the olivine-rich materials identified by *Hoefen et al*. [2003], *Hamilton et al*. [2003] , *Hamilton and Christensen* [2005], and *Mustard et al*. [2007b].

The modeled abundances for each phase in the solid solution series included in our spectral library (Fo_{91}, Fo_{68}, Fo_{53}, Fo_{39}, Fo_{18}, Fo_{1}) indicates that each phase is scattered throughout the area in abundances consistent with typical Martian basalt (less than 15 – 20%) [e.g., *Christensen et al*., 2000c; *Rogers and Christensen*, 2007]. The olivine-rich

location mentioned above is dominated by Fo_{68} and Fo_{53} compositions at up to 25-30 % each.

3.1.4. High Silica Phases

The combined modeled abundance of the high silica phases (quartz, K-rich glass, silica glass, phyllosilicates, and zeolites) is mapped in Figure 3e; these phases are generally present at abundances of ~20%. If we examine only phyllosilicate phases (Figure 3f), abundance values are, on average, ~5%. Three types of phyllosilicate minerals are represented in the spectral library (illite, montmorillonite, and saponite); the best fit models do not use any one of these spectra more commonly than the others. The high silica phases do not show a change in abundance over the area of 21 – 23° N, 77 – 80° E.

3.1.5. Other Phases

The combined modeled abundances of the minerals serpentine, gypsum, anhydrite, calcite, dolomite, and hematite have an average of ~20% in this area. Separately, the average modeled abundances are each less than ~15% throughout the region. Abundances such as these that are near or below the 10 – 15% detection limit may be unreliable; some may also be modeling noise or misfits in the data rather than actual phases present. Because the abundances of these phases are low, exhibit no trends, and are not directly of interest to our study, we do not show maps of these phases.

3.2. Numerical Mixture Analysis

In this section we describe the results of our numerical mixture tests. We begin by presenting our observations of the behavior of mixtures of phyllosilicate mineral spectra (nontronite, illite, montmorillonite, and kaolinite) and basalt spectra at THEMIS resolution. We then report the effects of each parameter in our TES numerical mixture deconvolution tests on the modeled phyllosilicate abundance values.

3.2.1. Behavior at THEMIS Resolution

In an effort to understand the qualitative spectral behavior that might be expected when phyllosilicates are mixed with basaltic material within the same THEMIS pixel, we produce numerical mixtures of ST1 and phyllosilicate at THEMIS resolution in proportions of 0:100%, 10:90%, 20:80%, 30:70%, 40:60%, 50:50%, 60:40%, 70:30%, 80:20%, 90:10%, and 100:0% (Figure 4). As the proportion of phyllosilicate in the mixture increases, THEMIS bands 5 and 6 decrease in emissivity (or increase minimally in some cases) whereas bands 4 and 7 increase substantially in emissivity. The large emissivity increase in band 7 relative to band 6 results in an increase in slope between these two bands. Mixtures using nontronite are shown in this example, but the other phyllosilicates in this study (illite, kaolinite, Ca-montmorillonite, and Fe-smectite) exhibit the same behavior.

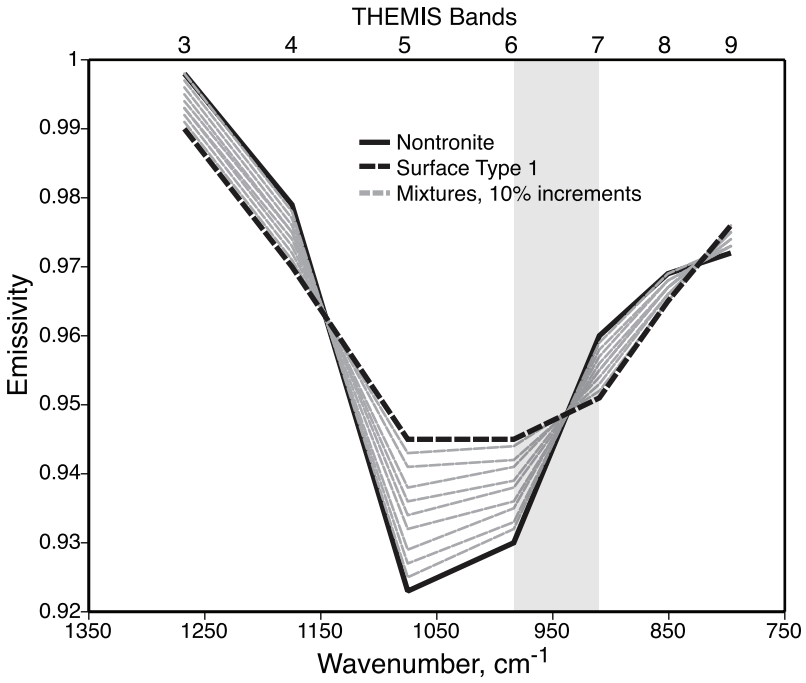

Figure 3.4: Nontronite and surface type 1 spectra at THEMIS resolution and numerical mixtures of the two. The vertical gray bar highlights the increase in slope between bands 6 and 7 as the proportion of nontronite in the mixture increases.

3.2.2. Effects of Changing Deconvolution Parameters and Other Variables on TES Modeled Abundances

To help interpret the modeled phyllosilicate abundances from Martian data (Section 3.3.2.), we first present the results of our numerical mixtures analysis, which investigates the effects of noise, wavelength range, and available phases on modeled abundances from deconvolution. Though in some instances we use graphs showing results for only the nontronite mixtures to illustrate our results, our statements encompass all of the phyllosilicate mixtures. The modeled abundances for the mixtures using ST1 are more variable than for the numerical basalt mixtures because we do not know the exact composition of ST1, whereas we do have the correct spectra in the library to model the numerical basalt spectrum.

To begin, we consider how results vary with noise and wavelength range when the spectral library includes the specific phyllosilicate spectrum used in the mixture; this is the best-case scenario. We observe that modeled abundances from deconvolution of the numerical mixtures of basalt and phyllosilicate spectra with added noise are virtually indistinguishable (i.e., differences less than 5% in most cases) from those of the spectra without added noise (compare gray and black curves, Figures 5a & b). In the cases where the addition of noise causes a larger than 5% difference (e.g., ~10% for the 1302 – 400 cm^{-1} deconvolutions of nontronite), this difference is still less than the 10 – 15% uncertainty of the method. Because it appears to have a minor effect, the remainder of this discussion refers only to data without added noise. In addition to showing the effect of noise, Figure 5 also shows the effect on the modeled abundances of the wavelength range over which the deconvolution is run. For each range, 1302 – 305 cm^{-1}, 1302 – 350

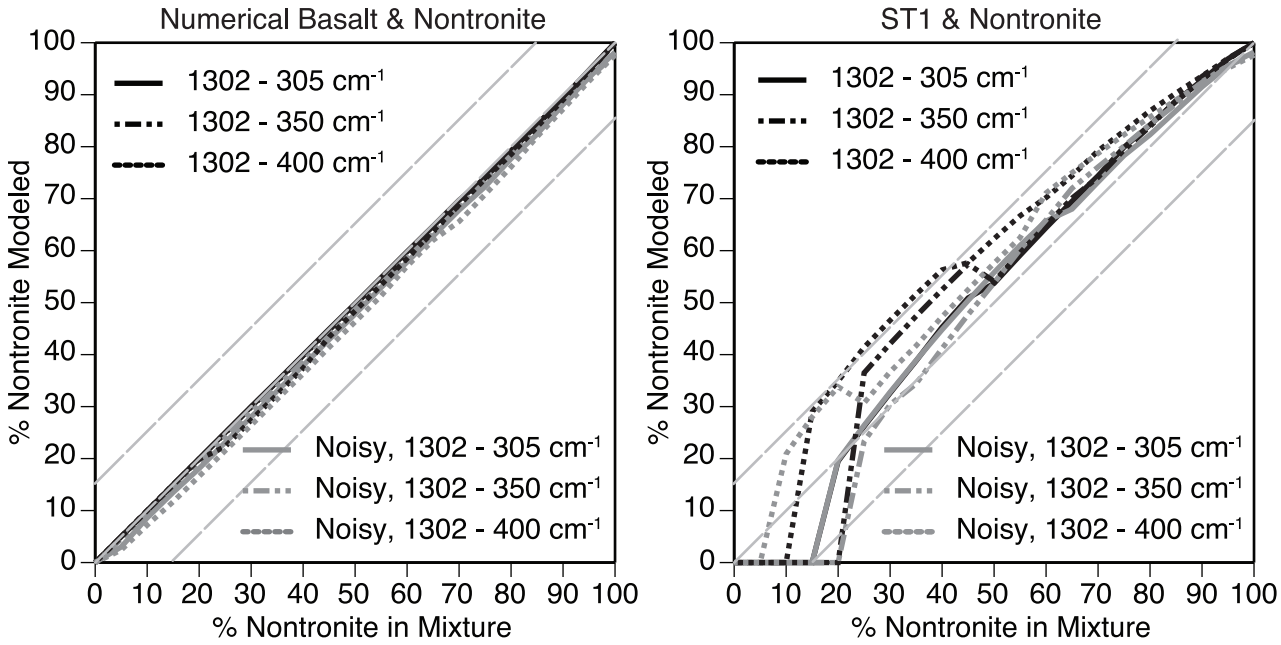

Figure 3.5: Plots of known vs. modeled abundance from deconvolutions of mixture spectra to illustrate the effect of added noise over three wavelength ranges. The spectral library used in the deconvolution includes the specific phyllosilicate spectrum used in the mixture. The gray dashed lines indicate a 0 to ±15% deviation.

cm^{-1}, and 1302 – 400 cm^{-1}, the modeled values are within 15% of the known abundance. The only exception is for the ST1/nontronite mixture deconvolved over the 1302 – 350 cm^{-1} range (Figure 5b); with 20% nontronite in the mixture, no nontronite is modeled. At abundances of 20% or less it appears that other phyllosilicate spectra are used in the model instead of nontronite.

To increase the complexity of these tests we next provide the deconvolution algorithm with a spectral library that does not include the specific phyllosilicate spectrum that was used to create the mixture spectra. Instead, we include a spectrum similar in shape and representing a similar composition. These replacement spectra are shown with the original phyllosilicate spectra in Figure 6. All other phases in the library are kept the same and include the spectra of the other phyllosilicate types. This is a more realistic test because Martian phyllosilicate mineral spectra may not exactly match our library spectra. From Figure 7 we see that the modeled and known phyllosilicate abundances may vary by more than 15%, and the wavelength range used for the deconvolution may affect the extent of the variation. The effect of the wavelength range is not consistent; it varies between the different phyllosilicate phases. For the nontronite mixtures in Figure 7, the wavelength range 1302 – 305 cm^{-1} results in more accurately modeled abundances more consistently than the other two ranges. However, the modeled abundances from the montmorillonite mixtures (not shown) are more accurate in the majority of cases when the 1302 – 350 cm^{-1} wavelength range is used. Unfortunately, one range is not clearly better than another in all cases, so the wavelength range over which deconvolutions are done must be determined by other criteria. To encompass as many of the spectral features at long wavelengths as possible to help with phase identification, we chose the

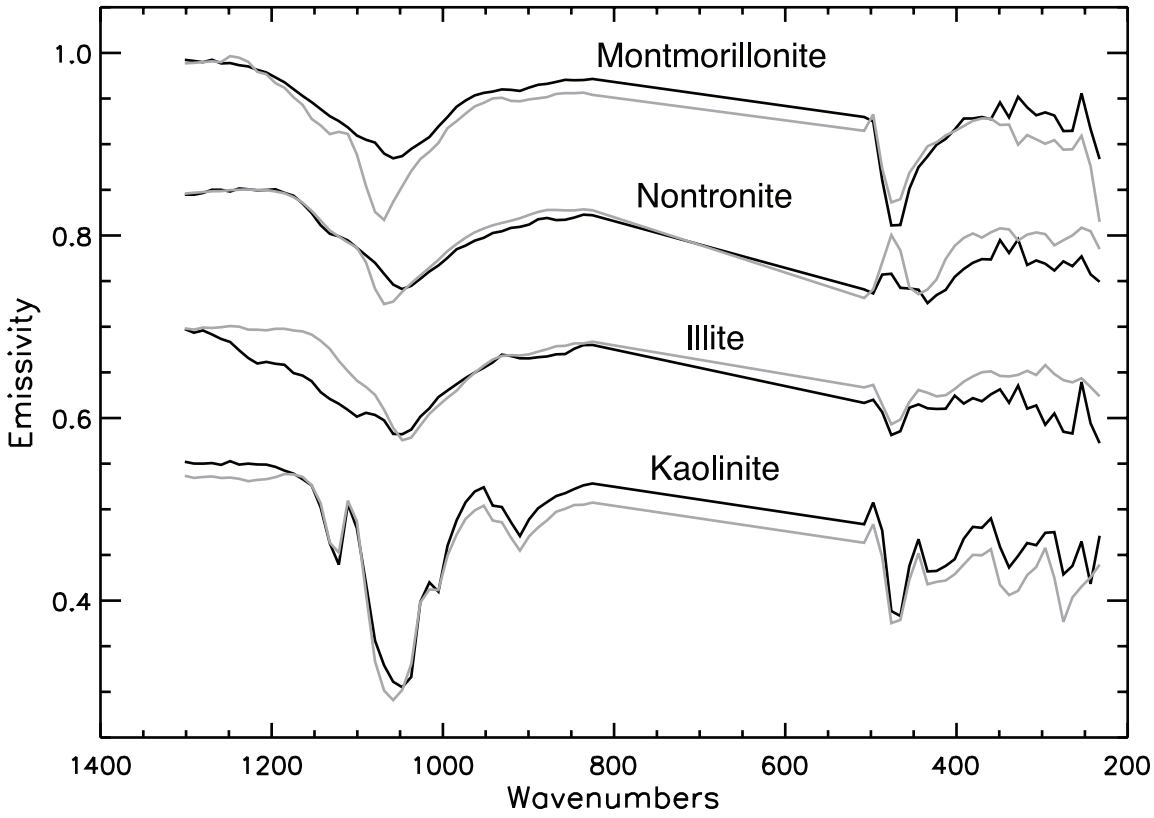

Figure 3.6: Plot of phyllosilicate spectra used in linear least squares models of numerical mixtures. Black spectra represent spectra used in numerical mixtures and initial models. Grey spectra represent different samples of the same phase and are used in a modified spectral library described in the text. Each set of spectra is offset for clarity.

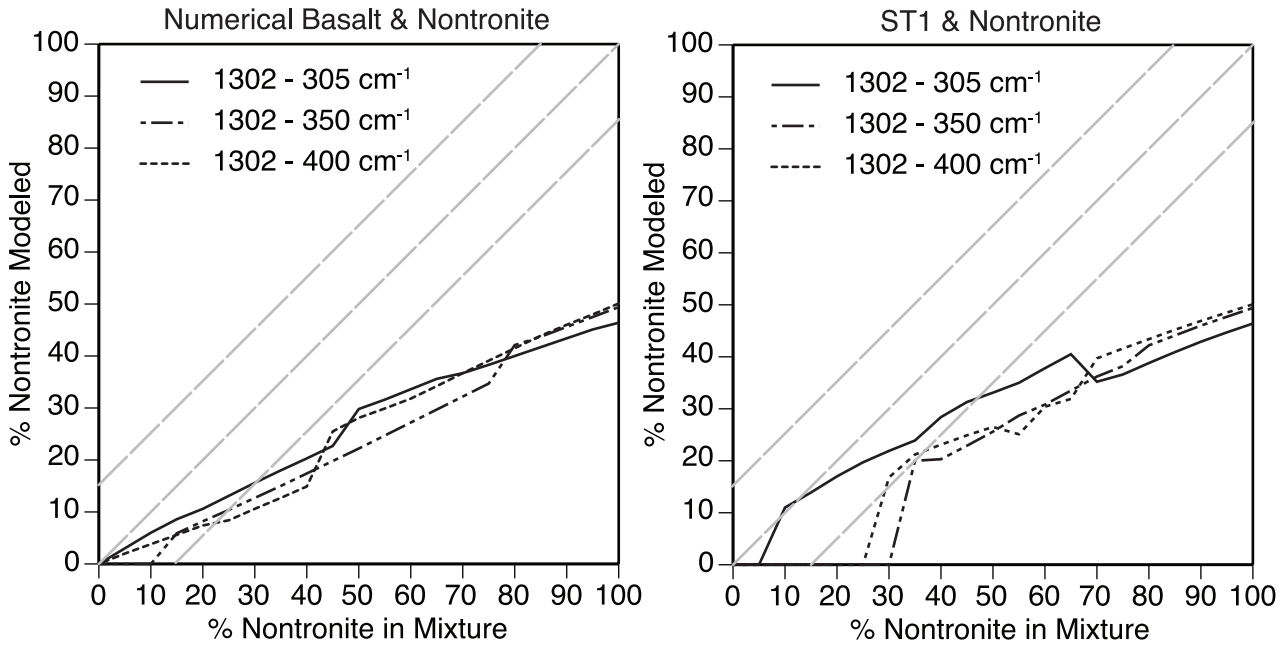

Figure 3.7: Plots of known vs. modeled phyllosilicate abundance illustrating the effect of a modified library on phyllosilicate abundance at different wavelength ranges. The specific phyllosilicate spectrum in the mixture is replaced by a similar spectrum in the spectral library. The gray dashed lines indicate a 0 to ±15% deviation.

widest range and in our further analysis use the range 1302 – 305 cm^{-1}. Because we focus the rest of our discussion on the 1302 – 305 cm^{-1} range, we do not take into further account the results of the other wavelength ranges (e.g., the significant underestimation for the other two ranges in the ST1 & nontronite example in Figure 7).

When deconvolving the mixture spectra from 1302 – 305 cm^{-1} (black lines in Figure 7), modeled abundances of a single phyllosilicate phase are not significantly (i.e., >10 – 15%) under- or overestimated unless its abundance is greater than 25-30%. Specifically, for mixtures containing >25-35% montmorillonite or >30-45% illite or nontronite, underestimations of >10-15% occur (up to 50% or more). Kaolinite is most commonly slightly overestimated but does not exhibit significant additional uncertainties in any case.

In remote sensing data (e.g., TES data), phyllosilicate abundances commonly are examined as a group; in this case, when the specific phyllosilicate spectrum in the mixture is replaced in the spectral library by the spectrum of a similar phase (i.e., the same spectral library as in the previous test), phyllosilicate abundances are underestimated by more than 10-15% only when at least 65-70% montmorillonite, 100% nontronite, or 95% illite is present (upper plots in Figure 8). These results show that the modeled and known phyllosilicate abundances are more consistent when all phyllosilicate phases are considered together as a whole rather than individually.

Finally, we determine the effect on modeled phyllosilicate abundances when the spectral library includes neither the specific phyllosilicate spectrum from the mixture nor the similar spectrum used in the previous tests. In this scenario the deconvolution algorithm must create the best fit to the mixture spectra from the remaining phyllosilicate

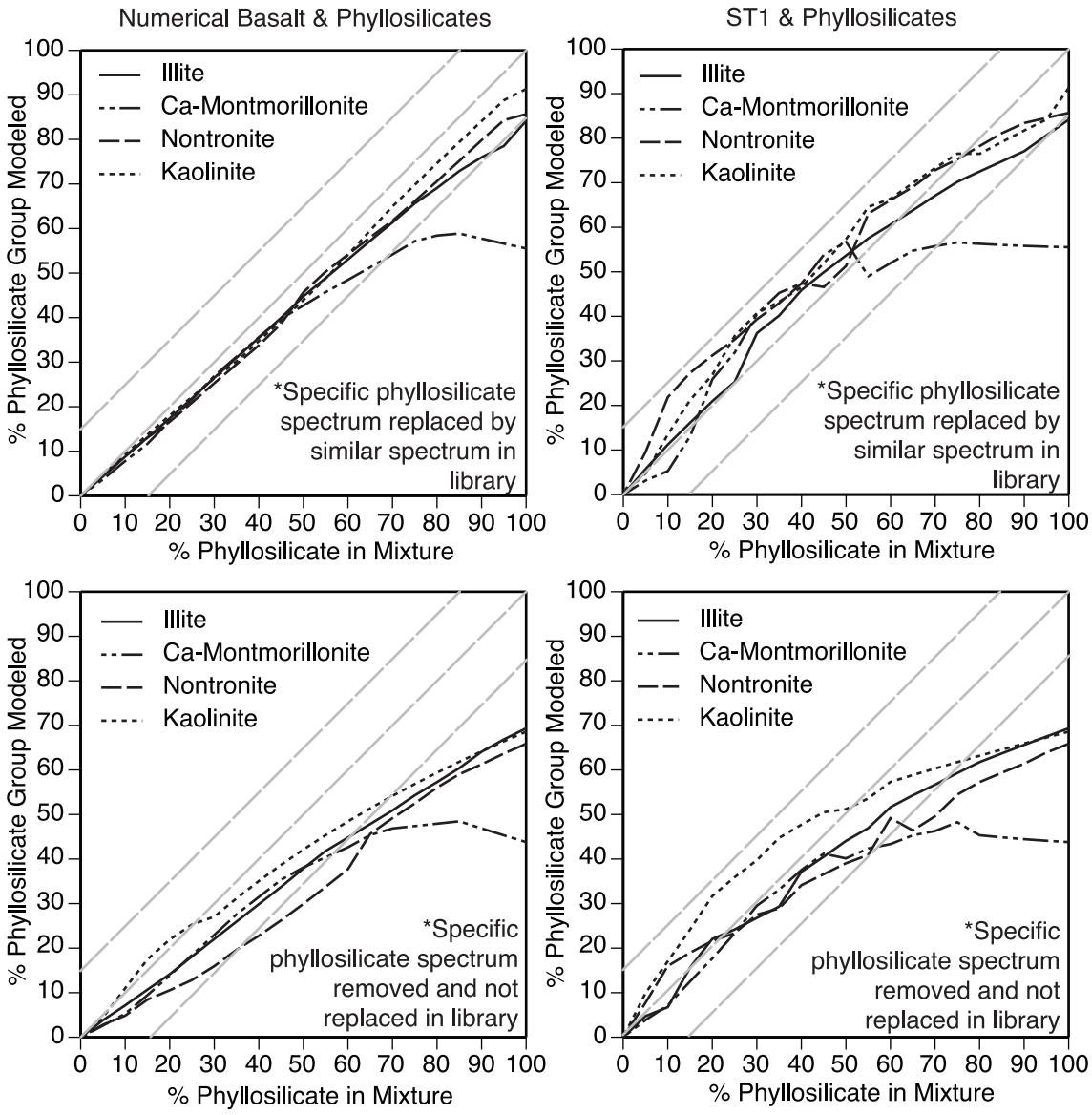

Figure 3.8: Plots of known vs. modeled phyllosilicate abundance where modeled abundances are reported for phyllosilicates as a group. Results from the numerical basalt and phyllosilicate mixtures are in the left column and results from the ST1 and phyllosilicate mixtures are in the right column. The upper plots show the modeled abundances when the specific phyllosilicate spectrum is replaced in the spectral library by a similar spectrum. The lower plots show the modeled abundances when the phyllosilicate in the mixture is removed from the spectral library, requiring the remaining phyllosilicate (and other) spectra to be used in the model instead. The gray dashed lines indicate a 0 to ±15% deviation.

spectra, which may be of a slightly different composition or another phyllosilicate class than the actual phyllosilicate phase in the mixture. This test is applicable to a situation that may be encountered in remote sensing of the Martian surface if a phyllosilicate mineral is present that is of a composition or structure not represented in the spectral library. We find that phyllosilicates as a group are underestimated in abundance by more than 10 – 15% when at least 60% montmorillonite, 35 – 65% nontronite, 60 – 75% illite, or 70 – 80% kaolinite is present (lower plots in Figure 8).

3.3. Detailed Examination of Phyllosilicate-bearing Material in TIR Data

Here we present measurements collected from the Martian surface. We look at spectral variation and spectral shape in THEMIS data associated with known phyllosilicate bearing areas identified by the OMEGA and CRISM instruments [e.g., *Ehlmann et al*., 2007; *Mangold et al*., 2007; *Mustard et al*., 2007b; *Poulet et al*., 2005]. We also investigate the TES spectra and resulting modeled abundances for these areas.

3.3.1. THEMIS Data

Spectral variation is expressed as differences in color in the DCS images. In Figure 9a we present DCS images for four areas in the region surrounding the Nili Fossae that are identified as containing phyllosilicates in OMEGA data [*Mustard et al*., 2006; *Poulet et al*., 2005]. These DCS images clearly show that there are spectral differences between the phyllosilicate-bearing areas and the surrounding plains. In this 8/7/5 band combination, the phyllosilicate-bearing areas appear yellow compared to the adjacent areas, which are more green, blue, or pink in color. The distinct magenta spots in the

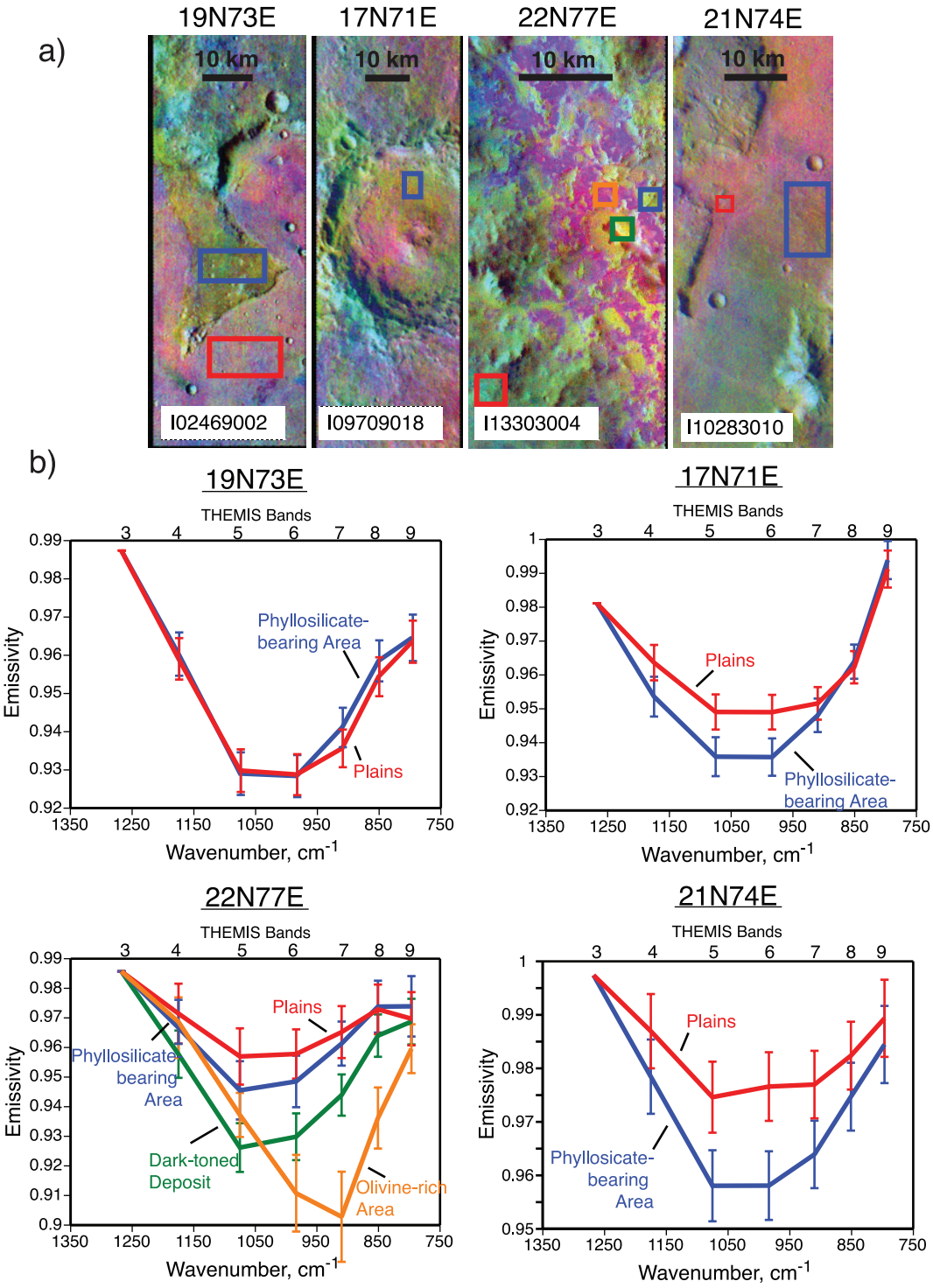

Figure 3.9: a) Decorrelation stretched THEMIS images (bands 8/7/5 in R/G//B) of four phyllosilicate-bearing study areas. The boxes in the images show the area where spectra were averaged to get atmospherically corrected spectra. b) THEMIS atmospherically corrected spectra of a phyllosilicate-bearing area and the surrounding plain. Error bars represent one standard deviation. For '22N77E' we have also included the interesting dark-toned deposit and olivine-rich area spectra.

22N77E image are olivine-rich materials. Also present in the 22N77E study location is a high-standing, rough, dark-toned deposit that is yellowish-orange in this 8/7/5 DCS image. We mention these other compositions because they may be of interest for future studies of the area.

The colored boxes on the DCS images indicate the areas over which THEMIS spectra were averaged to produce the atmospherically corrected spectra shown in Figure 9b. The shape of the THEMIS spectra from the phyllosilicate-bearing materials differs from that of the non-phyllosilicate-bearing materials for each the study areas except the 19N73E, where both units have spectra with similar shape and contrast. The spectrum of the phyllosilicate-bearing area in the 17N71E study location has a lower emissivity in bands 4, 5, and 6 than the nearby plains, but has similar emissivity values in bands 7, 8, and 9. In the 21N74E study area the emissivity for all bands is lower for the phyllosilicate-bearing area compared to the nearby plains, especially for bands 5, 6, and, to some degree, 7. The spectrum of the phyllosilicate-bearing material in 22N77E has lower emissivity in bands 5, 6, and 7, though the difference is not above the standard deviation of the values averaged. The dark-toned deposit in this area has a much lower emissivity in bands 5, 6, and 7, whereas the lowest emissivity for the olivine-rich material is in bands 6, 7, and 8. By their spectral shape we can determine that the amount of silica polymerization of the dark-toned deposit is more similar to that of the phyllosilicate-bearing material than to the olivine-rich material, which is more mafic (i.e., less silica polymerization). A larger particle size may cause the dark-toned deposit spectrum to have a larger spectral contrast than the plains spectrum.

3.3.2. TES Data

Taking a ratio of spectra from a region of interest and an adjacent area is one way to determine the spectral differences between two surfaces. The ratio may result in a single mineral spectrum, but also can represent a combination of phases that differ in abundance between the two surfaces. Ratios of TES spectra (not shown) between the phyllosilicate-bearing materials in the four regions of interest and their surrounding plains do show small differences. However, these ratio spectra do not appear to be strongly similar to the spectra of phyllosilicates from the kaolinite, illite, and smectite classes. Therefore we cannot use this approach to say if phyllosilicate abundance differs between the surfaces.

Atmosphere-removed TES surface spectra from the study areas, shown in Figure 10, differ in shape between the phyllosilicate-bearing areas and the adjacent units. The modeled abundances of these surface spectra are shown in Table 4. Rounding errors may result in values that do not add to exactly 100%. Also listed in Table 4 are the RMS errors for the modeled spectra. The RMS error is helpful in comparing the goodness of fit between multiple deconvolutions of the same spectrum. However, one RMS value cannot be directly compared to the RMS value of another modeled spectrum because it is influenced by factors that may differ between the spectra, such as spectral contrast and wavelength range, in addition to goodness of fit [e.g., *Hamilton et al*., 2008]. Below we discuss in detail the more applicable products of the deconvolution, the atmosphere-removed surface spectra and their modeled abundances, for each study area.

For the 19N73E study area, the spectra of the phyllosilicate-bearing material and the adjacent plains have an emissivity minimum at ~1100 cm^{-1} and a low slope between

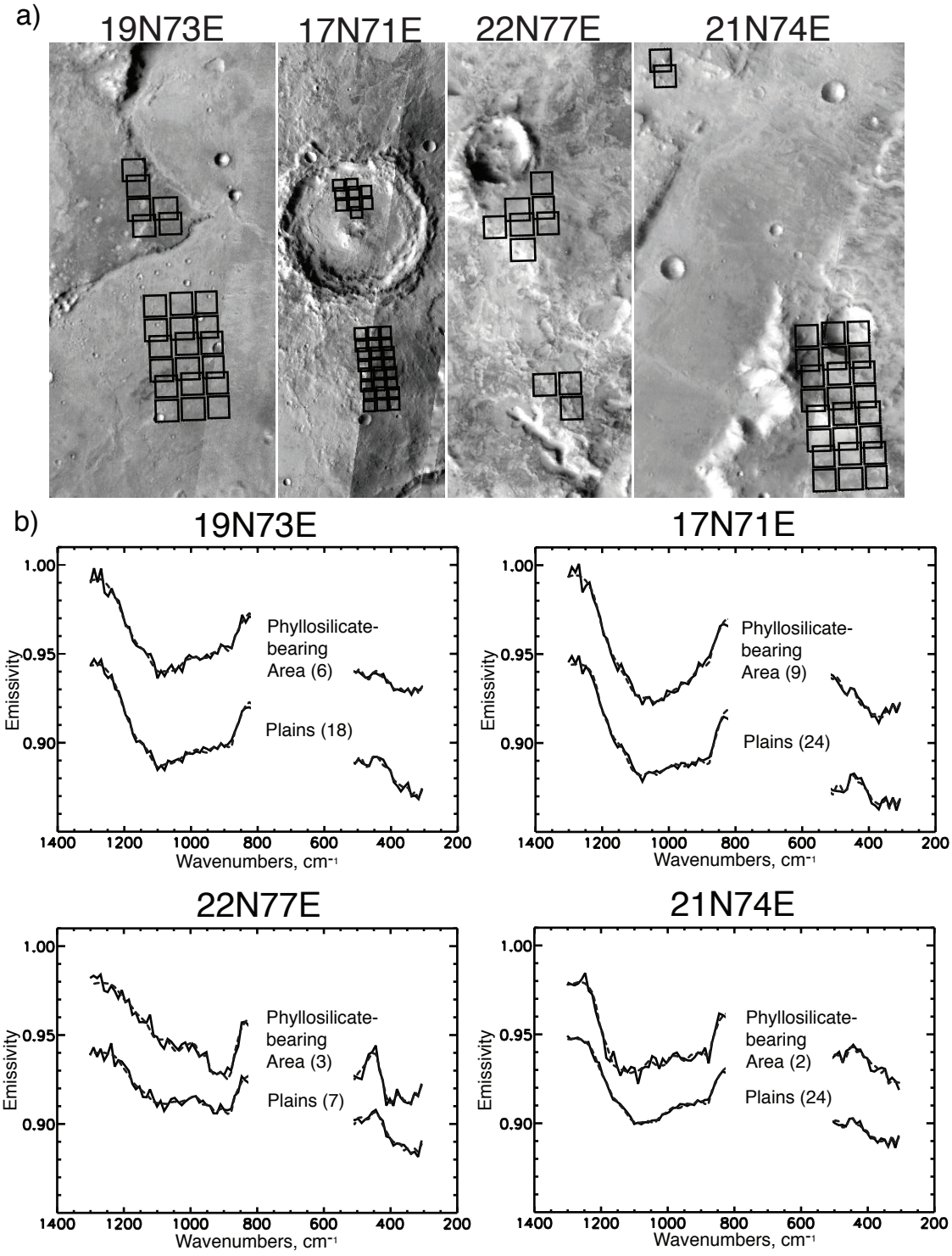

Figure 3.10: a) Outlines of TES pixels averaged to produce spectra of the phyllosilicate-bearing and non-phyllosilicate-bearing surfaces used in deconvolution for each study area. b) TES atmosphere-removed spectra from phyllosilicate-bearing areas and nearby plains (offset by -0.05 from each other). Solid lines are the measured spectra and dashed lines are the modeled spectra. The number of individual spectra averaged to produce these spectra is included in parentheses after the labels on each graph.

Table 3.4: Modeled abundances from TES atmosphere-removed spectra from phyllosilicate-bearing areas and nearby plains (see Figure 10) and RMS error. Uncertainty on modeled abundances is estimated at 10 – 15%.

	19N73E		17N71E		22N77E		21N74E	
Phase	Phyllo silicate-bearing Area	Plains	Phyllo silicate-bearing Area	Plains	Phyllo silicate-bearing Area	Plains	Phyllo silicate-bearing Area	Plains
Alkali Feldspar	0	2	0	0	0	0	0	0
Plagioclase Feldspar	21	22	37	28	10	19	27	21
Pyroxene	31	30	20	33	36	32	33	26
Olivine	3	5	6	8	29	12	11	6
Phyllo-silicates	23	19	15	13	9	19	0	21
K-rich Glass	8	8	14	6	2	0	8	11
Other*	14	14	9	12	12	18	18	16
RMS error	0.0023	0.0018	0.0024	0.0021	0.0029	0.0022	0.0028	0.0012

*The 'Other' category includes phases modeled well below detection limits, such as hematite, calcite, and dolomite.

~1100 and ~885 cm^{-1}. At lower wavenumbers both spectra have a local minimum at ~470 cm^{-1} and a local maximum at ~445 cm^{-1}. Beyond this point the spectra differ; the plains spectrum has a greater negative slope from 445 cm^{-1} to 305 cm^{-1} than the phyllosilicate-bearing area spectrum. The overall shape of both spectra is generally basaltic.

The modeled abundances for the phyllosilicate-bearing area and the adjacent plains in the 19N73E location are the same or very similar for each mineral group. The phyllosilicates have the largest difference in abundance; the phyllosilicate-bearing area is modeled with 23% phyllosilicate minerals and the plains area is modeled with 19% phyllosilicate minerals. The phyllosilicate phase identified from VNIR data in this area is Fe-rich smectite (e.g., nontronite) [*Poulet et al.*, 2005]. Linear deconvolution of TES data models Fe-smectites and montmorillonite.

The spectrum of the phyllosilicate-bearing area in the 17N71E study location has a more narrow and round shape, indicating a more felsic or polymerized composition, than the broad and square basaltic shape of the adjacent plains spectrum. The emissivity minimum of the phyllosilicate-bearing area spectrum is at ~1050 cm^{-1} whereas the minimum of the plains spectrum is at ~1090 cm^{-1}. The slope of the spectrum between ~1050 cm^{-1} and 885 cm^{-1} is much lower for the plains than the phyllosilicate-bearing location. At lower wavenumbers the phyllosilicate-bearing area spectrum has a more narrow and shallow local emissivity minimum at ~470 cm^{-1} and local emissivity maximum at ~450 cm^{-1} than the plains spectrum.

In the 17N71E study area the modeled abundances are more varied. The larger abundances of plagioclase (37% compared to 28%) and K-rich glass (14% compared to

6%) and smaller abundances of pyroxene (20% compared to 33%) and olivine (6% compared to 8%) in the phyllosilicate-bearing material are consistent with its more felsic spectral shape relative to the plains material. The values for the 'Other" group are 9% and 12% for the phyllosilicate-bearing material and plains, respectively. *Ehlmann et al.* [2008a] identify Fe/Mg smectite, hydrated silica, and chlorite from CRISM data in this area. The modeled phases we derive from TES spectra are consistent with the presence of Fe-smectite.

The spectrum from the 22N77E phyllosilicate-bearing material exhibits features attributable to olivine, which likely is a result of sub-pixel mixing between the small regions of interest and adjacent olivine-rich material. We believe this is sub-pixel mixing because THEMIS DCS images (e.g., Figure 9a) indicate the extent of the phyllosilicate-bearing materials in this area are smaller than a TES pixel, and also, the VNIR data suggest that the phyllosilicate-bearing material is in a separate stratigraphic layer than the olivine-rich material in this area [*Mustard et al.*, 2007b]. The contribution of the olivine results in an emissivity minimum at ~890 cm^{-1} for both spectra. We do observe a difference in the slope of the spectra between ~1250 cm^{-1} and the minimum at ~900 cm^{-1}; the spectrum of the phyllosilicate-bearing area is steeper in this region than the spectrum of the plains, apparently due to a difference in olivine abundance (an increase producing a steeper slope), and felsic phases (an increase producing a more shallow slope), accordingly. At lower wavenumbers the spectra also differ in shape. The local emissivity maximum at ~450 cm^{-1} is much greater for the phyllosilicate-bearing area spectrum, likely due to a larger abundance of olivine. A local minimum is positioned at

~400 cm^{-1} for the phyllosilicate-bearing material spectrum, whereas the minimum is at ~370 cm^{-1} for the plains spectrum.

The modeled abundances of olivine for the phyllosilicate-bearing material (29% ol) and the plains (12% ol) of the 22N77E location reflect the differences in spectral shape due to olivine mentioned above. The phyllosilicate-bearing material is modeled with less plagioclase feldspar (10% compared to 19%), more pyroxene (36% compared to 32%), less phyllosilicate (9% compared to 19%), more K-rich glass (2% compared to 0%), and less phases in the 'Other' grouping (12% compared to 18%) than the plains. Though VNIR data indicate the presence of Fe/Mg smectite in this area [*Mustard et al*., 2006], illite is the phyllosilicate phase used in our best fit model to the TES spectrum.

The difference in number of spectra available to create an average spectrum of the region of interest is apparent between the phyllosilicate-bearing material and plains spectra for the 21N74E study area. The phyllosilicate-bearing material spectrum is noisy because it is the average of two spectra, whereas the plains spectrum is the average of 24 spectra. We should also note that the 21N74E region of interest spectrum was measured during a time of lower temperature (~260 K) and higher dust opacity (best fit opacity ~0.3) than is ideal, but no other data are available. The two spectra have roughly similar shapes, which are that of a generally basaltic material, but differ in some important details. The emissivity minimum is at ~1125 cm^{-1} in the spectrum of the phyllosilicate-bearing area but is at ~1100 cm^{-1} in the spectrum of the nearby plains, indicating that the plains composition is slightly more mafic. Both spectra are relatively flat between their emissivity minimums and ~885 cm^{-1}. In the low wavenumber region the spectrum of the phyllosilicate-bearing area has a sharp local emissivity minimum at ~475 $cm^{-1}$and a broad

emissivity maximum at ~ 450 cm^{-1}, whereas the local emissivity minimum and maximum in the plains spectrum are much shallower and are at ~460 cm^{-1} and ~450 cm^{-1}, respectively.

Modeled abundances for the 21N74E study area indicate that the phyllosilicate-bearing material has a higher proportion of primary igneous minerals (i.e., plagioclase, 27% compared to 21%; pyroxene, 33% compared to 26%; and olivine, 11% compared to 6%) than the surrounding plains. The plains have a greater modeled abundance of secondary and more polymerized phases such as phyllosilicates (21% compared to 0%) and K-rich glass (11% compared to 85), and similar abundances of calcite, hematite, etc. (16% compared to 18%).

Comparisons of the modeled abundances confirm that the phyllosilicate-bearing materials generally differ in composition relative to adjacent materials, as suggested by the THEMIS DCS images. However, the modeled phyllosilicate abundances show either little variation between the region of interest and the plains (e.g., a 4% difference in modeled abundance for the 19N73E study area and a 2% difference in modeled abundance for the 17N71E study area), or have the opposite trend than would be expected (i.e., have a higher phyllosilicate abundance for the plains than the region of interest). This opposite trend is shown by the lower modeled phyllosilicate abundance of 9% for the 22N77E study area and 0% for the 21N74E study area, in comparison to the 19% and 21% modeled phyllosilicate abundances for the surrounding plains from the two study areas, respectively. Also, many of these modeled abundances are near or below the general detection limit of 10-15%. We will discuss the implications of these results on TES modeled phyllosilicate abundances in general in Section 4.4.

We have performed an additional analysis on these TES spectra. *Ruff and Christensen* [2007] and *Michalski and Fergason* [2008] both applied spectral indices to TES data (globally and in the region of Mawrth Vallis, respectively) that were designed to identify features of phyllosilicate phases. The 465 index indicates an emissivity minimum at ~465 cm^{-1}, a feature present in some high silica materials and smectites [*Ruff and Christensen*, 2007]. The 530 index detects an emissivity minimum at ~530 cm^{-1} that is present in smectites, though it is also consistent with olivine [*Ruff and Christensen*, 2007]. A spectrum of smectite would have high values in both of these indices. *Michalski and Fergason* [2008] use the 530 index from *Ruff and Christensen* [2007] along with an index suited to detecting the 510-520 cm^{-1} emissivity minimum of the Fe-bearing smectite nontronite. We have calculated these indices for the TES spectra from the phyllosilicate-bearing materials and plains in our local study areas. *Ruff and Christensen* [2007] determined threshold values for the 465 and 530 indices by calculating the index values for very dusty regions, which are spectrally neutral in this range; values above the threshold indicate the presence of that feature. The majority of spectra from the study areas have values of the 465 and 530 indices above the thresholds of 1.006 and 1.005, respectively, including the spectra from the phyllosilicate-bearing areas and the adjacent plains. In some cases the majority of spectra from the phyllosilicate-bearing material have higher index values than the majority of spectra from the plains, but in other cases it is the opposite. The values for the 510-520 cm^{-1} spectral index designed for nontronite are similarly inconsistent. We cannot be certain that the presence of both 465 and 530 indices indicates the presence of smectite in this case because the features are identified in both the phyllosilicate-bearing materials and non-

phyllosilicate-bearing materials. The contribution of olivine throughout much of the these areas, reflected in the THEMIS DCS images in Figure 9 and the modeled abundances in Table 4, likely affects the 530 index [*Ruff and Christensen*, 2007]. If the high 530 index values are not due to smectite, the high values of the 465 index would suggest the presence of an amorphous high silica material (or perhaps a zeolite phase) [*Ruff and Christensen*, 2007].

4. Discussion

4.1. Regional Composition

From the minerals most widespread and present in the largest abundances, (orthopyroxene, clinopyroxene, plagioclase feldspar, and olivine), we confirm that the general lithology of the region surrounding the Nili Fossae is basaltic. We see variation in composition between the older Noachian terrain and the younger Hesperian lavas to the southwest; the Syrtis lavas have a lower abundance of orthopyroxene than the older units, though clinopyroxene is dominant in both units, consistent with the results of *Mangold et al*. [2007]. The clinopyroxene (augite, NMNH-122302) modeled in the highest abundance throughout the region has a TiO_2 of 1.03 wt% [*Hamilton*, 2003], higher than the typical upper limit of 0.8 wt% for calcic pyroxenes [*Deer et al*., 1992]. A study by *Hamilton* [2003] demonstrates that an increased amount of titanium in augite causes discernable differences in the thermal infrared spectrum and therefore the spectrum of a higher titanium augite can be distinguished from that of a lower titanium augite. *Hamilton and Koeppen* [2007] found that this relatively high titanium augite was the clinopyroxene modeled at the highest abundances globally. The TiO_2 values of the augite

phases in some Martian meteorites are also moderately high (in at least one case as high as ~2.57 wt%) [*McSween Jr. and Treiman*, 1998; *Taylor et al.*, 2002]. On Earth, high titanium augite, typically with TiO_2 values over 3 wt%, commonly forms in alkaline igneous rocks. Though the titanium value of this augite spectrum is not quite as high as can be found in alkali basalts, this relative titanium enrichment may indicate that the surface of Mars has a composition that may be near the boundary between alkaline and subalkaline. This idea is consistent with the findings of *McSween et al.*, [2006] who showed that alkaline rocks are present at the Mars Exploration Rover Gusev crater site and may be more common than previously considered.

The types of plagioclase feldspar found in the region are indicative of a mafic rock, except oligoclase, which is more sodic than typically found in mafic rocks. *Ruff* [1998], *Wyatt et al.,* [2001], and *Milam et al.,* [2004] point out that the inclusion of oligoclase in deconvolution results may be due to the solid solution that exists between albite and anorthite. The plagioclase spectra in the best fit model combine to represent the average An-value of the rock, and the individual modeled compositions may not actually be present in the rock. For example, the combination of oligoclase and labradorite spectra in certain proportions may better represent the average plagioclase composition of a rock than the available andesine spectrum. Also, *Milam et al.* [2004] showed that average plagioclase compositions determined from remote sensing data are often more sodic than the plagioclase phenocrysts present in the rocks because the volumetrically more abundant plagioclase in the groundmass is more sodic. Weathering may also lead to a more sodic plagioclase composition; the results of *Michalski et al.* [2004] indicate that the preferential weathering of calcic plagioclase causes a relative

increase in sodic plagioclase, which is more resistant to weathering. Alternatively, if oligoclase is indeed a component of an otherwise mafic lithology, it could indicate hydrothermal alteration [e.g., *Milam et al*., 2004]. Because we detect oligoclase throughout the region and do not see areas of concentrated abundance, we believe it unlikely that oligoclase is an indicator of hydrothermal alteration in this case.

We find that olivine is a component of the basalt throughout the region at relatively low levels (~15%) and in a wide range of forsterite compositions (Fo_{18} – Fo_{68}). The range of composition in the area of high olivine abundance between ~21 – 23° N and 77 – 80° E is much narrower, predominantly Fo_{68} & Fo_{53}. The dissimilarity in compositional range leads us to believe that the regional materials are unrelated to the concentration of large abundances of Fo_{68} & Fo_{53}. This indicates that the origin of the olivine-rich material differs from that of the basalt covering most of the region. Researchers have proposed that the origin of the olivine-rich material may be an olivine-rich lava flow [e.g., *Hamilton and Christensen*, 2005] or an impact melt [e.g., *Mustard et al*., 2007b]. If it is a lava flow, its source and/or ascent history must be different than that of other lavas composing the region that have lower and more varied Fo content. If the olivine-rich material is an impact melt generated by the Isidis impact, it may be consistent with an impact excavating into the mantle where Fo contents are higher than in the crust.

The decrease in plagioclase abundance in the area of ~21 – 23° N to 77 – 80° E corresponds to an increase in olivine abundance with other phases showing no significant increase or decrease. If the increase in olivine abundance were solely due to an addition of olivine (e.g., an influx of olivine sands), we would expect the abundances of all other

phases to decrease, which we do not observe. Instead, the abundance of pyroxene is similar to the surrounding area and only the plagioclase abundance is decreased. The olivine abundance appears to increase at the expense of plagioclase, which indicates a genetic relationship. This suggests that the olivine-rich material formed in this area and any previously or currently mobile sediments are derived from this same locality. The higher olivine abundance and lower plagioclase abundance of the material indicates a rock with a more mafic composition.

4.2. Numerical Mixture Analysis

We investigated the possible need for re-evaluation of uncertainty and detection limit of phyllosilicate mineral abundance with the deconvolution method and find the uncertainty is consistent with the 10 – 15% cited for the method in general when phyllosilicates are present in moderate abundances, but phyllosilicate abundances can be underestimated by larger amounts when higher abundances are present. Because the modeled phyllosilicate abundances determined for the region surrounding the Nili Fossae are low, our results suggest that these phyllosilicate abundances are not affected by any systematic underestimation (or overestimation). However, the 10 – 15% uncertainty still applies. The most accurate results are obtained when the abundance of phyllosilicates is reported in total rather than for each individual phyllosilicate phase. In our study the extent to which phyllosilicate abundances are underestimated appears to vary based on how similar the mixture phyllosilicate spectrum and available library spectrum are to each other and how well the other phyllosilicate spectra in the spectral library can accommodate the difference. Our results may not be applicable in situations where no

spectra from the phyllosilicate group are in the spectral library or in the event that phyllosilicate spectra in the spectral library closely resemble a phase present on the Martian surface but not included in the library (discussed in more detail below). Additionally, it is important to remember that a spectral library that does not include a silica-K_2O glass spectrum may lead to an overestimate in modeled phyllosilicate abundance for a mixture spectrum containing silica-K_2O glass as *Koeppen and Hamilton* [2005] have shown.

4.3. Phyllosilicate-bearing Material in the Vicinity of the Nili Fossae

From the regional TES mineral abundance maps it appears that phyllosilicate phases are commonly identified in amounts at or near the detection limit throughout the region. Our analysis of the local study areas show that TES spectral shapes and modeled mineralogies are clearly different between the regions of interest and the plains, but the differences represent more than just the presence or absence of phyllosilicates. There are changes in the abundance of other minerals, which reflect either different starting materials, chemical alteration, the addition of younger materials, or all of the above. The lack of a resemblance of spectral ratios to phyllosilicate shapes also suggests a difference in overall composition not solely related to the presence or absence of phyllosilicates. This does not preclude the presence of phyllosilicates in these areas, but our results may indicate that they are not in abundances high enough to be reliably detected or distinguished by TES. Our results are consistent with the findings of *Michalski and Fergason* [2008], which show that the phyllosilicate-bearing material in the region of Mawrth Vallis does not have a greater modeled phyllosilicate abundance (11%) than the

other units in the area (18-20%). The lack of strong correlation between the 530 and nontronite indices and the phyllosilicate-bearing material in the vicinity of the Nili Fossae is also consistent with the results of *Michalski and Fergason* [2008] in the Mawrth Vallis region.

THEMIS DCS images show that the areas of known phyllosilicate occurrence do correspond to areas of differing composition. A comparison of the THEMIS spectra for the regions of interest and the adjacent plains in each location shows that they display slope differences between bands 6 and 7, with the spectra of the phyllosilicate-bearing materials having the higher slope as predicted (Figure 9). This is consistent with, but not necessarily uniquely attributable to, an increase in phyllosilicate abundance in the regions of interest.

4.4. What is the Explanation for Widespread Phyllosilicate Detections by TES?

The results of our local study area analyses illustrate the lack of a strong correlation between phyllosilicate detection in the TIR and VNIR wavelength ranges. In many instances the best fit model to TES spectra includes phyllosilicate phases though they were not identified in VNIR data. There are multiple potential explanations for this discrepancy and all could contribute to some extent. Below we discuss our hypotheses and those from previous studies.

Michalski and Fergason [2008] addressed this issue in their study of the phyllosilicate detections in the Mawrth Vallis region. They suggest three circumstances that may contribute to the differences in TIR and VNIR detections of phyllosilicate minerals on Mars. One idea relates to the effect of surface roughness at different

wavelengths. Whereas smooth, solid surfaces lead to stronger features in the TIR region, rough, granular, and porous surfaces that cause multiple scattering lead to stronger features in the VNIR region. If the surfaces of the phyllosilicate-bearing materials on Mars have a high effective roughness, it may cause strong features in VNIR data leading to detection but weaker features in TIR data that may not be detected. For this idea to provide a comprehensive explanation (for the region of the Nili Fossae and globally), it would require that a variety of phyllosilicates from multiple locations and environments have this same physical characteristic. Additionally, this does not address the situation in which TIR methods model phyllosilicates but none are detected by VNIR methods.

Sub-pixel mixing of materials with different temperatures may be a partial cause of the lack of detection of phyllosilicates by TES in areas where they are detected by the higher spatial resolution (resulting in less sub-pixel mixing) of CRISM and OMEGA, as discussed by *Michalski and Fergason* [2008]. This situation would exist when the phyllosilicate-bearing material is cooler than the surrounding material and therefore not emitting quite as much energy as its spatial extent would indicate. Theoretical calculations by *Michalski and Fergason* [2008] show that a reasonable difference in temperature does alter the mixed spectrum, but not to the extent needed to solely explain the lack of increased phyllosilicate abundance modeled by TES.

The difference in spatial resolution between the TIR and VNIR instruments may contribute to the disparity in detection in another way. *Michalski and Fergason* [2008] point out that the footprint of a TES pixel includes both phyllosilicate-bearing and non-phyllosilicate-bearing material. The modeled abundance for that pixel is an average of the values for the two areas and will result in lower phyllosilicate abundance than that of

just the phyllosilicate-bearing material. This could cause a material with relatively low phyllosilicate abundance to be even lower and perhaps undetectable with TES. We do not believe this situation adequately explains the TIR detections of phyllosilicates where there are no detections by the VNIR instruments. Each of these circumstances presented by *Michalski and Fergason* [2008] are surely present on Mars, but we suspect that additional factors may be involved in the discrepancy between TIR and VNIR detections. We address these further ideas below.

We have considered the effect rock coatings may have on TES modeled abundances of phyllosilicates. Some studies, such as the *Christensen and Harrison* [1993] investigation of desert varnish, find that coating materials can be treated as a component of the substrate that adds linearly in abundance with the other components, but in some cases thin coatings may cause non-linear mixing with the substrate, resulting in inaccurate modeled abundances derived from linear deconvolution [e.g., *Kraft et al*., 2003]. Coatings as thin as 3 μm have been shown to dominate the spectral signature of a surface and obscure the basaltic signature [*Minitti et al*., 2007]. Additionally, a material present as a coating may be overestimated in abundance because it does not accurately represent its volumetric contribution. If the phyllosilicate minerals detected in this region are in the form of thin coatings on rocks, it is possible they may be overestimated in abundance. Because Martian spectra are not dominated by phyllosilicate spectral shapes and have relatively low modeled phyllosilicate abundances, it appears that only some, if any, of the rocks have such an obscuring coating, otherwise the modeled abundance of the coating phase would be dominant. Therefore, if the phyllosilicate abundance is exaggerated because it is present as a coating, the abundances of the other phases are

likely accurate relative to each other due to the checkerboard (i.e., linear) mixing of coated and non-coated rocks within the measurement footprint. Additionally, VNIR instruments would detect these coatings and, as a result, the presence of coatings would not cause a disconnect between the two wavelength ranges.

We have shown that the areas where VNIR instruments detect phyllosilicate minerals appear to differ from surrounding materials in TES and THEMIS data, but we cannot confirm an increase in phyllosilicates as part of this difference. In some cases there is actually a decrease in TES modeled phyllosilicate abundances, likely due in part to the uncertainty for phases present below the 10 – 15% detection limit. The TES spectra of the phyllosilicate-bearing materials in our study areas may be modeled with a combination of phases that are either more felsic or mafic than the adjacent plains (the specific phases that change in abundance vary). Our observation of the lack of the expected trend in phyllosilicate abundance from TES spectra may be explained if the deconvolution algorithm uses a phyllosilicate spectrum to substitute for a spectrally similar phase not included in the spectral library. As a result, phyllosilicate abundance would vary based on the abundance of this other phase in addition to phyllosilicate, causing abundances to be overestimated in some areas and, in comparison, underestimated in others (i.e., lower phyllosilicate abundance in phyllosilicate-bearing areas than non-phyllosilicate-bearing areas). Recently, *Hamilton et al*. [2008] have found that high abundances of phyllosilicate were modeled erroneously in deconvolutions of palagonitic tephra spectra. The palagonitic tephras contain allophane, a non-crystalline aluminosilicate weathering phase. The authors suggest that the lack of an allophane spectrum in their spectral library caused the inclusion of phyllosilicates in the models, as

the next most spectrally similar phase. Allophane is thought to have a TIR emission spectrum similar to some phyllosilicate minerals based on transmission spectral properties; researchers have yet to obtain an allophane emission spectrum due to the difficulty of isolating or synthesizing the material. *Kraft et al*. [2005], *Michalski et al*. [2005a], and *Michalski et al*. [2006b] have also commented on the potential for erroneous inclusion of phyllosilicates or other high silica phases (e.g., glasses) in modeled abundances of materials containing allophane or other short range order weathering products.

If the majority of weathering products in this region around the Nili Fossae and elsewhere on Mars were poorly crystalline, they could be more difficult to identify in the VNIR wavelength range, as *Michalski et al*. [2006a; 2006b] suggest, because the lack of order causes a decrease in the contrast of their distinguishing spectral features such as the 1.9 μm absorption [*Milliken and Mustard*, 2005]. If a poorly crystalline weathering product such as allophane is widespread on the Martian surface, it may be modeled erroneously as a phyllosilicate in TES deconvolutions. This could result in detection of phyllosilicates by TES where there is no evidence for crystalline phyllosilicate minerals in VNIR data and would make it difficult to distinguish between locations where phyllosilicates are modeled accurately and erroneously in TES data. This scenario may be the most plausible way to explain the inconsistency in phyllosilicate identification between VNIR and TIR data, both locally, as illustrated by our study, and globally.

Our hypothesis is supported by analyses of data from instruments on the Mars Exploration Rovers that suggest the presence of allophane and/or other similar weathering products at some sites in Gusev crater and Meridiani Planum [e.g., *Clark et*

al., 2005; *Ming et al*., 2006]. Allophane is similar to, and commonly contained within, palagonite; both are amorphous weathering products derived from the alteration of volcanic material. Palagonite has been proposed as an analog for a component of the Martian surface for many years based on the resemblance of its VNIR spectrum to that of the Martian bright regions [e.g., *Bell III et al*., 1993; *Clancy et al*., 1995; *Morris et al*., 1990; *Roush et al*., 1993; *Singer*, 1982]. An amorphous phase is thought to provide a better fit to the weak VNIR absorptions than crystalline phyllosilicates.

5. Summary & Conclusions

From our numerical mixture analysis we have determined that modeled abundances of phyllosilicate phases derived from linear deconvolution of TES spectra are most accurate when reported as a group rather than for each individual phase. Modeled abundances of phyllosilicates are not likely to be under- or overestimated by more than 10 – 15% (the typical uncertainty for the method) unless the actual abundance is greater than ~60%; if the spectral library does not contain the actual phyllosilicate phase in the material being measured or another very similar phyllosilicate phase, underestimation of modeled abundance may occur at lower values. Therefore it is important to include multiple phyllosilicate phases in a spectral library. We added noise on the order of that inherent in TES data to our mixture spectra and find it does not appear to effect modeled phyllosilicate abundances. In our study of numerical mixtures aimed at understanding modeled phyllosilicate abundances, we find that it is difficult to define an optimal wavelength range for linear deconvolution; we use the range 1302 – 305 cm^{-1} in order to

encompass all the spectral features that may potentially be present in the spectrum and exclude the area most susceptible to atmospheric water vapor features (<~300 cm^{-1}).

We have shown that the phyllosilicate-bearing surfaces detected by OMEGA and CRISM in the vicinity of the Nili Fossae are different in composition from the surrounding terrain in both TES and THEMIS data. THEMIS spectra of the phyllosilicate-bearing areas have a shape that is consistent with, but may not be unique to, a mixture of basalt and a phyllosilicate phase. Deconvolution of TES spectra from the phyllosilicate-bearing materials does not always result in an increased modeled phyllosilicate abundance compared to adjacent non-phyllosilicate-bearing material, however. The modeled phyllosilicate abundance values are not likely over- or underestimated by more than the 10 – 15% uncertainty of the method, as we determined in the numerical mixture analysis. It is possible that the discrepancy in reported phyllosilicate occurrences between VNIR and TIR is caused by phyllosilicate spectra substituting for another phase present on the Martian surface but not included in the TES spectral libraries used by various researchers for deconvolution. This idea, supported by the results of our local analyses, would suggest that the modeled phyllosilicate abundances determined by our regional study may be a combination of the actual phyllosilicate abundance (where present) and the abundance of the phase not represented in the library. This phase may be a poorly crystalline weathering product such as allophane. Further work must be done to isolate and measure the spectrum of allophane and other similar material to determine if one of these phases provides a better fit than phyllosilicates to Martian surface material, and if so, what that implies for the weathering and environmental conditions on Mars.

Acknowledgements

We would like to thank William Koeppen for sharing the information from his global deconvolution and also for the many discussions that helped to shape this manuscript. We would also like to acknowledge the efforts of the MGS and ODY teams and the TES and THEMIS mission planners in enabling the collection of the data used in this research. We thank J. Michalski and an anonymous reviewer for their comments that improved this manuscript. Support for this research was provided by the following NASA programs: Mars Fundamental Research, Mars Data Analysis, and 2001 Mars Odyssey Participating Scientist. This is HIGP publication #1711 and SOEST publication #7650.

CHAPTER 4

Visible to near-infrared and thermal infrared spectral properties of chert and amorphous silica 1: Laboratory analysis

ABSTRACT

The spectral features of chert and amorphous silica vary in both the thermal infrared (TIR) and visible to near-infrared (VNIR) ranges. Chert TIR spectra are similar to those of quartz but differ consistently in detail. The spectra of chert and amorphous silica differ from one another in the TIR, as expected based on their crystalline and amorphous natures, respectively. The VNIR spectra of chert and amorphous silica can be similar, however. Both may have hydration features at ~1.4 μm and 1.9 μm, but we do not find any amorphous silica without these features, whereas we do observe chert with no hydration features. In fact, some chert spectra may be completely featureless in the VNIR. We also examine the effect of physical properties, such as orientation, surface roughness, and incidence angle, on the TIR spectra of chert and amorphous silica. We observe variation in the TIR spectra, but they are not unique to a single physical property; surface roughness and increased incidence angle may cause TIR spectra to vary in similar ways. Therefore, we cannot automatically use a spectral feature to determine such physical conditions. We also see similarities in the TIR and VNIR spectra of chert and amorphous silica from different environments, and differences in the spectra of samples from the same type of environment. This suggests that we cannot simply correlate spectral character with environment of formation for chert and amorphous silica.

1. Introduction

Recent spectral observations of the Martian surface have led to the discovery of materials rich in silica [e.g., *Bandfield*, 2006; 2008; *Bandfield et al*., 2004a; *Hamilton et al*., 2006; *Milliken et al*., 2008; *Squyres et al*., 2008]. In some cases, the exact phase is unknown and a variety of high silica phases, each with their own geologic implications, must be considered. In Martian studies, the term "high silica" refers to phases with Si/O ratios >0.35, such as quartz, chert, amorphous silica (primary and secondary), phyllosilicates, and zeolites [*Bandfield*, 2008; *Michalski et al*., 2005b; *Rogers and Christensen*, 2007]; these are commonly grouped together because of their spectral similarities, unless the specific phase has been identified. Of these high silica phases, chert and amorphous silica are important targets of astrobiological interest because of their exceptional potential for microfossil preservation on Earth. These phases signify past activity of water and could represent deposits from surficial, diagenetic, or hydrothermal fluids. To interpret this environment or conditions of formation in terrestrial or Martian remote sensing, researchers must identify the exact high silica phase detected and its characteristics. Both the visible to near-infrared (VNIR, ~0.4 – 2.5 μm) and the thermal infrared (TIR, ~2000 – 200 cm^{-1}) wavelength regions contain compositional information that can aid in this mineral identification.

At present, there are only a limited number of studies that attempt to characterize the visible to infrared spectra of high silica phases like chert and amorphous silica, discussed below in section 1.2. Knowledge of the possible variations in spectral character that may be encountered would help scientists using Martian and terrestrial remote sensing data to recognize and identify chert and amorphous silica in all their

forms. Additionally, variations in spectral characteristics arising from physical properties such as orientation, surface roughness, and incidence angle need to be studied to develop a way to interpret physical information from spectral information. If the underlying physical properties that produce the spectral variation are fully understood and can be related to formation environments and/or processes, researchers may be able to confidently constrain details of the environment of formation and geologic history of the area where chert or amorphous silica are identified in remote sensing data. Our study addresses these outstanding issues by documenting the variation in spectral characteristics of chert and amorphous silica samples across the visible to infrared spectral range and comparing them to variations in physical properties. Chapter Five takes this new knowledge and applies it to the detection of chert and amorphous silica on Mars.

Previous studies have helped to develop a preliminary understanding of the spectral character of chert and amorphous silica in both the TIR and VNIR ranges. Some studies focus on understanding the inherent properties and shape of the spectra themselves [*Almeida*, 1992; *Goryniuk et al*., 2004; *Kingma and Hemley*, 1994; *Michalski*, 2005] or compare the differences between the types of opal, for instance [*Graetsch et al*., 1994; *Michalski et al*., 2003; *Rice et al*., 1995]. Other researchers use the spectra of chert or amorphous silica to aid in their investigations, which include sedimentary studies [*Migaszewski et al*., 2006], investigation of archaeological artifact sources [*Hubbard et al*., 2003; *Long et al*., 2001], and proof of concept activities for automated mineral classification programs [*Brown et al*., 2004].

Prior studies have not attempted to analyze the range in spectral variation of chert and amorphous silica in both the VNIR and TIR wavelength ranges, along with the effects relating to physical properties or environment. In our study we build and improve upon previous studies by beginning with a more extensive sampling of chert and amorphous silica representing various sources, methods of formation, surface textures, compositions, and crystallinities. We investigate the origin of the TIR and VNIR features in the spectra of these samples and document their variation. Because reflectivity in the VNIR and emissivity in the TIR are the measurements used in remote sensing, we use these in our study.

We address three outstanding questions. 1) What is the extent of variation in VNIR and TIR spectral features of chert and amorphous silica? We provide this information by documenting the features of VNIR and TIR spectra for a variety of chert and amorphous silica samples, including multiple surfaces that may differ in physical properties or phases present. 2) How does the TIR spectral character of chert and amorphous silica vary with changes in physical conditions such as orientation, incidence angle, and surface roughness? To address this issue we measure TIR spectra of several samples at different orientations, incidence angles, and on surfaces of different roughness. We use information from physical analyses of the samples (e.g., scale of roughness on a surface) to quantify the physical conditions correlating with each spectrum and describe any resulting spectral trends. 3) Can the VNIR and TIR spectral character of chert and amorphous silica be linked to specific physical properties or formation environments? To address this question we acquire petrographic information on the samples and information regarding their environment of origin. We compare this

data with the related spectra to try to ascertain consistent relationships between the physical variables and the spectral features.

1.1. Background: Chert and Amorphous Silica and their Spectral Properties

Silica (SiO_2) is found in many forms. On Earth, α-quartz is the most common crystalline form and has many metastable and high-pressure polymorphs, such as tridymite, cristobalite, moganite, and coesite [*Heaney*, 1994]. Opaline silica phases ($SiO_2 \cdot nH_2O$) are partly or entirely non-crystalline. As *Graetsch* [1994] explains, opal-C has a disordered cristobalite stacking, and opal-CT has an even more disordered cristobalite and tridymite stacking. Opal-AG (precious opal) and opal-AN (hyalite) are completely amorphous.

Chert is a rock that may be composed of microcrystalline quartz, fibrous quartz (i.e., chalcedony and/or moganite), and megaquartz. Megaquartz is composed of authigenic α-quartz; its crystals may be of any size and are well defined [*Knauth*, 1994]. The grain size of microcrystalline quartz commonly is between 1 and 50 μm [*Knauth*, 1994]. Rocks such as jasper, flint, and agate are specific varieties of chert, defined by the type of silica present or the amount of impurities in the rock, which may impart color to the rock. The color of chert may be quite variable and can come from inclusions of phases other than quartz, such as hematite, which imparts a red color, goethite, which gives a yellow or brown color, and clay minerals, which result in a white or gray color [*Rossman*, 1994]. Also, the atomic structure of the quartz grains themselves may have chemical substitutions that give some coloring. Chert commonly contains water in varying amounts depending on the phases present. According to *Graetsch* [1994] (after

[*Flörke et al.*, 1991]), generally these amounts are less than 0.4 wt % H_2O for microcrystalline quartz and range from 0.5 to 3 wt % H_2O for fibrous quartz. Opal-C and opal-CT can contain amounts of 1 – 3 and 3 – 8 wt % H_2O, respectively. Truly amorphous silica (opal-A) may have 4 – 8 wt % H_2O. This water may be molecular water in pore spaces, OH^- attached to surfaces and imperfections, or OH^- attached to structural sites.

Chert and amorphous silica have multiple methods of formation. We take the following summary from a review by *Knauth* [1994]. Chert may form directly from a biological source such as marine diatomaceous or radiolarian oozes, which are made of amorphous silica. These deposits go through a process of maturation that alters the initial opal-A to the more ordered opal-CT and finally to microcrystalline quartz. Because opal goes through this maturation process, opal-A or opal-CT deposits on Earth tend to be young (e.g., no older than 60 Ma). Maturation proceeds as temperature increases with burial. The exact amount of time required for the process to be completed varies with the rate of diagenesis, the impurities in the deposit, etc. Chert may also originate from silica precipitated directly from an aqueous fluid enriched in silica, a common occurrence in cavities and pore spaces. The silica enrichment may be derived from biologic sources or non-biologic sources such as volcanic and terrigenous debris. This type of chert is likely deposited as microcrystalline quartz. Another formation scenario takes place in the evaporitic lakes of east Africa. Na-silicate precipitated and deposited in the alkaline lakes is altered by meteoric water, the Na removed, and chert forms in its place (i.e., Magadi chert). Because some type of aqueous environment is required for its formation, most cherts are commonly found within or between rocks such as limestones and

evaporites. Precious opal (opal-AG) is a form of purely non-crystalline amorphous silica that is produced from the aggregation of opal spheres filtered from water traveling through rock [*Flörke et al*., 1993]. Amorphous silica may also form as a primary constituent of igneous rocks; silica glass is created by the quick cooling of magma or lava [*Heaney*, 1994]. Hyalite (opal-AN), the form of amorphous silica we analyze in this study, forms when hot silica-carrying volcanic gas meets a cool rock surface and precipitates quickly to create the silica glass [*Graetsch*, 1994].

In Figure 1 we illustrate the differences in the TIR and VNIR spectra of coarsely crystalline quartz (hereinafter referred to as quartz for simplicity), chert, and amorphous silica. Figure 1a shows the spectrum of particulates from a large quartz crystal from the TES spectral library [*Christensen et al*., 2000b] together with an example of chert and opaline silica spectra from our study. Following current conventions in Mars remote sensing, we use wavenumbers (cm^{-1}) when discussing TIR spectra. Overall, quartz and chert spectra have the same spectral features originating from the same vibrational modes, though there may be some differences in the details of the shape or position of features. The only feature observed in the spectra of quartz, but not always observed in the spectra of chert, is the minimum at ~540 cm^{-1}.

Compared to quartz spectra, chert TIR spectra have a different shape of the doublet in the 1300 – 1000 cm^{-1} region. In the spectrum of chert, the two minima become more pointed and the interior of the doublet has a shallower positive slope between ~1220 and 1160 cm^{-1} and a shallower negative slope between ~1160 and 1075 cm^{-1}. In comparison, in the spectrum of quartz these two minima are rounded with steep slopes in the interior of the doublet and may have a shallower negative slope in the ~1220 – 1160

a)

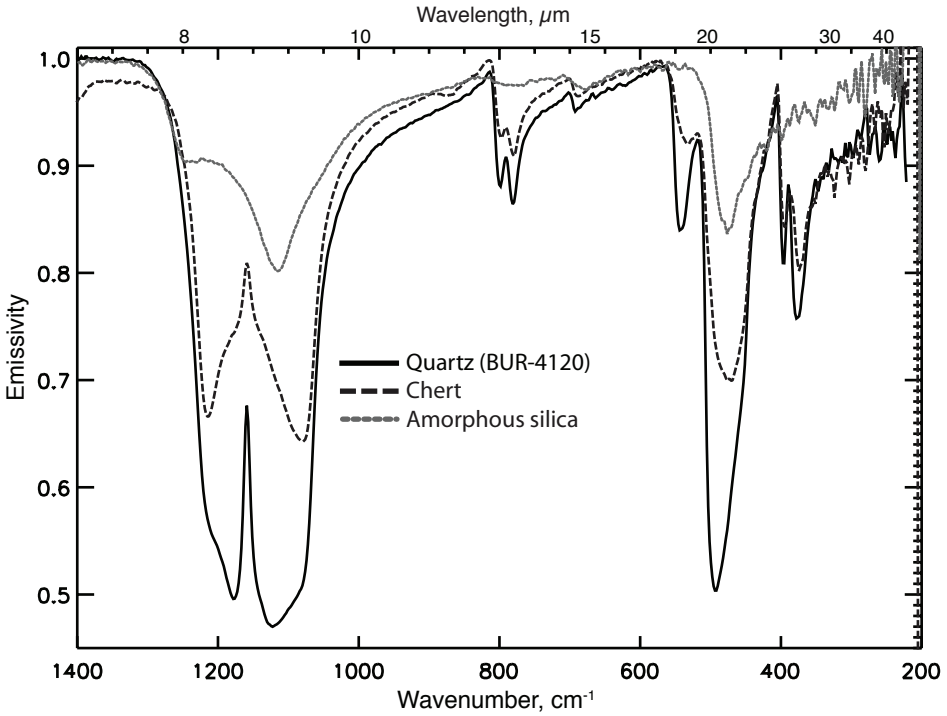

b)

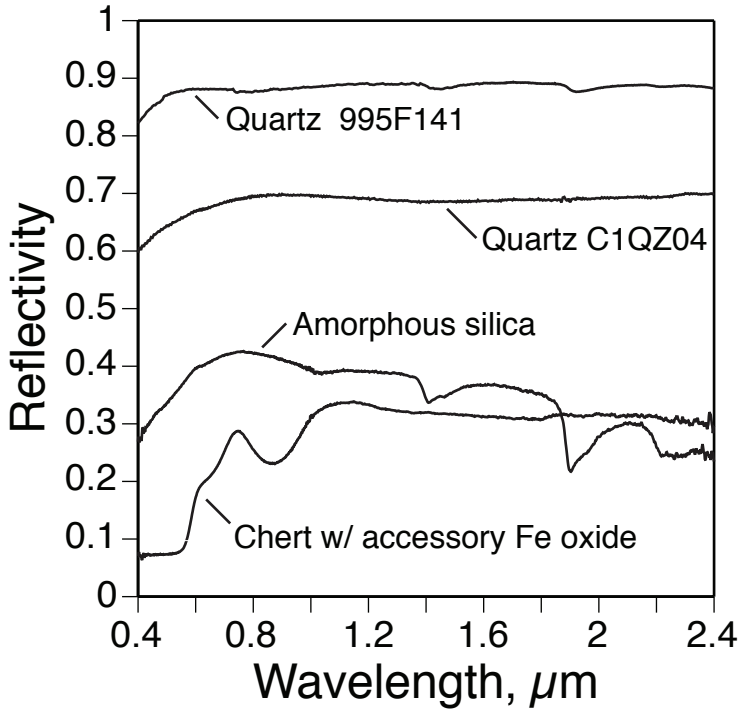

Figure 4.1: Plot comparing the spectra of coarsely crystalline quartz, chert, and amorphous silica in the a) TIR and b) VNIR. The TIR spectrum of coarsely crystalline quartz is from the TES spectral library [*Christensen et al.,*2000] and the VNIR spectra of coarsely crystalline quartz are from CRISM spectral library [*Bishop et al.,* 2006].

cm^{-1} range and a shallower positive slope in the ~1160 – 1075 cm^{-1} range on the exterior of the doublet. This also results in differences in the positions of the minima of the doublet.

In the TIR, opaline silica spectra differ from that of quartz in the same way they differ from chert spectra. The doublet at 1300 – 1000 cm^{-1} in quartz is a single broad minimum in opaline silica. The 780 cm^{-1}, ~675 cm^{-1}, and ~540 cm^{-1} features may not be apparent in the spectra of opaline silica, whereas they are present in the spectra of quartz. Also, opaline silica does not have a feature at 400 – 350 cm^{-1} as does the quartz spectrum.

Only at very small particle sizes, such as <40 μm, does the spectral shape of quartz change to resemble that of chert in the TIR [*Mustard and Hays*, 1997; *Wenrich and Christensen*, 1996]. This is likely a consequence of significant volume scattering in the fine particles that alters the shape of the spectral features.

Figure 1b illustrates the differences in VNIR spectral character between quartz in particulate form (995F141 and C1QZ04, from the CRISM spectral library [*Bishop et al*., 2006]) and chert and opaline silica. We use wavelength (μm) when discussing VNIR spectra. The quartz spectra are essentially featureless in this wavelength range; the spectrum 995F141 only has a slight hint of 1.4 μm and 1.9 μm bands, indicating that the sample is very weakly hydrated. The tightly-bonded tectosilicate structure is not likely to accommodate the amounts of H_2O present in some chert and amorphous silica samples. Features from accessory phases, such as the Fe-oxide in the chert spectra, are not seen in these quartz spectra (though possible), but we will show that they are common in chert. Another difference between the quartz spectra and some chert and amorphous silica spectra is in the >2.2 μm region. There are no Si-OH or Al-OH features observed near

2.2 μm in the quartz spectra, whereas they are present in many chert and amorphous silica spectra. Though some VNIR spectra of chert are as featureless and flat as the quartz spectra, they are all low in reflectance (less than ~0.5), whereas the quartz spectra are high in reflectance (greater than ~0.65).

2. Samples and Analytical Methods

Our complete sample set includes 19 samples, each listed in Table 1 and shown in Figure 2. Samples were chosen for their variety of physical features (e.g., color, surface texture) and environments of origin. They include chert from multiple sources: silicified ash, chalcedony, megaquartz, diatomite, porcellanite, opal-CT, and hyalite. The samples were collected by P. Knauth and S. L. Cady. Spectral analyses were carried out on hand samples, many of which have both natural and cut surfaces.

2.1. Physical Analyses

Physical analyses (scanning electron microscopy, surface profilometry, and optical petrography) were performed on the chert and amorphous silica samples. Not every analysis was done or needed for each sample (see Table 2); the analyses performed were chosen based on each sample's TIR and VNIR spectra (e.g., the availability of spectra from surfaces differing in roughness or orientation, inclusions of other phases, etc.).

Secondary electron images illustrating the surface roughness of samples 810, 699, 95, C, 613, M-1, 589, and 9X were produced using a JEOL 35-C scanning electron microscope (SEM). Sample surfaces were not coated in order to preserve their surface

Table 4.1: Chert and amorphous silica samples used in this study.

Sample Name	Rock Type	Source Locality
333	porcellanite	Monterey Fm., California
12	low-T megaquartz	Mescal limestone, Arizona
624	silicified ash	Fig Tree chert, S. Africa
810	replacement chert	Tubiana Fm., Australia
409	chert	Cretaceous, Texas
M-6	diatomite	Monterey Fm., California
589	drusy quartz & chert	Komati River Gorge, Africa
202	hyalite (opal-A)	Montana
MC	Magadi chert	Lake Magadi, Kenya
613	jasper	Fig Tree, S. Africa
M-1	opal-CT	Monterey Fm., Naples Beach, California
K-1100	speleothem	Onverwacht Gp., Barberton Mtns., S. Africa
699	geyserite	Death Valley, California
EST	opal (undetermined)	Alvord Basin, Oregon
White1	hydrothermal precipitate	Eastern Oregon
C	epithermal vein-filling chert	McGloughlin Mine, California
9X	epithermal vein-filling chert	New Zealand
95	chert	Australia
Memorial	hydrothermal precipitate	Mickey Hot Springs, Oregon

Figure 4.2: Photos of the chert and amorphous silica samples used in our study. For reference, notebook lines are 7 mm wide.

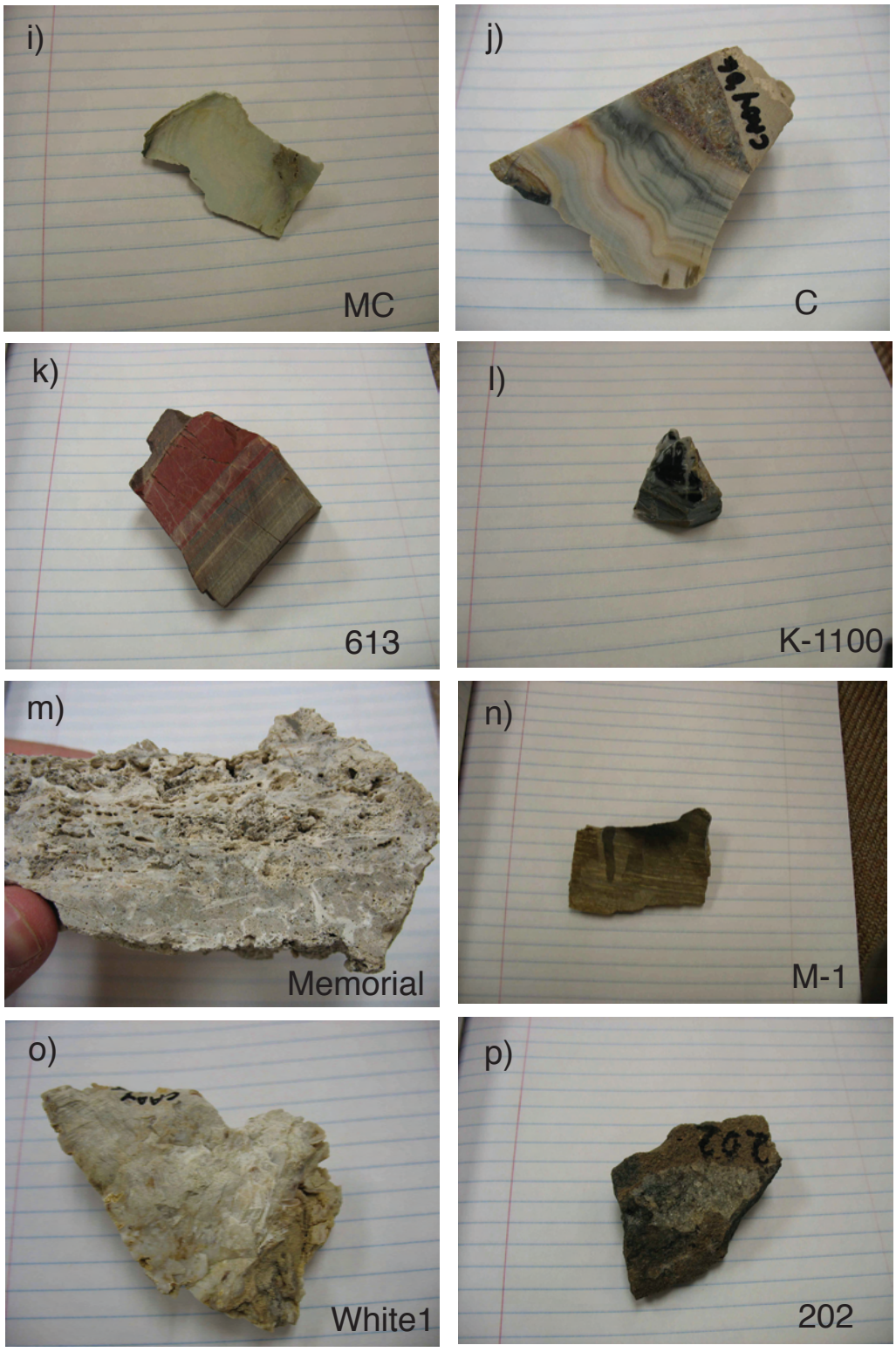

Figure 4.2: (Continued) Photos of the chert and amorphous silica samples used in our study. For reference, notebook lines are 7 mm wide.

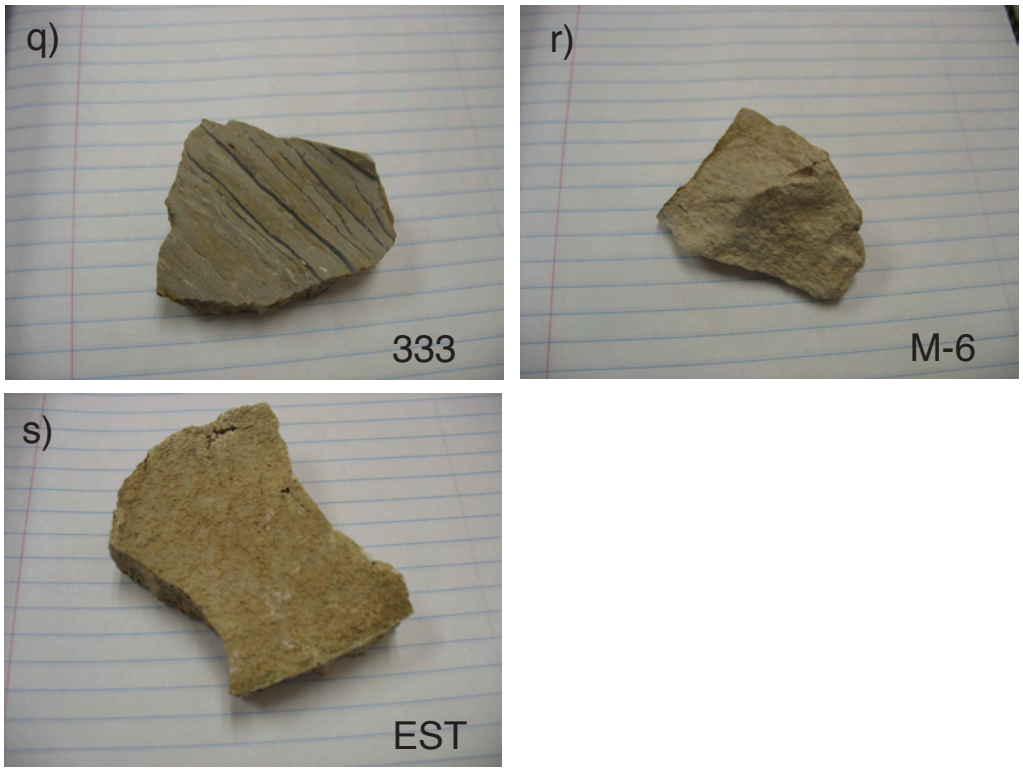

Figure 4.2: (Continued) Photos of the chert and amorphous silica samples used in our study. For reference, notebook lines are 7 mm wide.

Table 4.2: Analyses performed on samples.

Sample	SEM	Surface Profilometry	Optical Petrography
810	X	X	X
699	X	X	X
95	X	X	
C	X	X	X
613	X	X	X
M-1	X	X	
589	X	X	
9X	X	X	
333			X
Memorial			X

texture but instead were prepared by placing them in an aluminum foil basket in the brass sample holder, with copper tape as a connector and ground to reduce charging. Multiple images were taken with resolutions of 100x, 200x, 400x, 1000x, and, in some cases, at additional magnifications.

Profiles of the sample surfaces (810, 699, 95, C, 613, M-1, 589, and 9X) were measured by a direct-contact Dektak 3 stylus profiler. The stylus is diamond tipped and its movement is transformed by a Linear Variable Differential Transformer (LVDT) into a voltage proportional to distance. A moving stage holds the sample. The profiler has a vertical range of 2 mm and a resolution of 10 nm. Measurement of a standard had an error of ~0.1 μm. Profiles were measured over two sessions. Noise on the order of 10 nm (0.01 μm) was introduced by an aging profilometer part used in the first session, however this noise is on the edge of the resolution of the instrument and is too small to affect our analysis of the data. This part was replaced for the second session. Three measurements were taken on the same area of each sample surface. The first was perpendicular to any lamination present, and the second and third measurements are at 45° angles to the first, creating a star-like pattern on one side. Each profile is 1 cm in length and consists of 2000 data points.

Standard thin sections were made and analyzed with a petrographic microscope allowing for identification of specific phases, measurement of grain size, and preferred orientation of grains. Currently thin section descriptions are available for only a portion of the samples (C, 333, 613_red, 699, Memorial, and 810).

2.2. Thermal Infrared Spectral Measurements

TIR emission spectra were collected for all samples over the range of 2000 – 200 cm^{-1} using a ThermoElectron Nexus 470 FTIR spectrometer at the University of Hawaii [*Hamilton and Lucey*, 2005]. We followed the measurement and calibration procedure outlined by *Ruff et al*. [1997]. The sample chamber was purged with scrubbed air to minimize spectral features of water vapor and CO_2 during the measurements. Samples were heated to greater than ~70° before measuring to increase signal to noise ratio. Each spectrum is the spectrometer-average of ~270 scans and has a resolution of 4 cm^{-1} (2 cm^{-1} sampling). The high frequency features at ~300 cm^{-1} and lower are residual water vapor rotational bands. Each sample was measured on as many surfaces as possible. Six relatively flat samples also were measured at multiple incidence angles by propping the flat sample surface to present a sloped surface to the spectrometer. Five of these samples (12, 624, 810, 95, and M-1) were measured at angles of 0°, ~30°, and ~45°, and one (MC) was measured at angles of 0°, ~-30°, ~-40°, ~30°, and ~45°. We were not able to stabilize the samples for measurement at angles greater than 45°, though other studies have done this and their results are described in section 4.3.

2.3. Visible to Near-infrared Spectral Measurements

Visible to near-infrared reflectivity spectra were collected for all samples over the range of 0.35 – 2.5 μm using an Analytical Spectral Devices© (ASD) spectrometer at the University of Hawaii. The spectra have a sampling of 0.001 μm and were calibrated using the difference between measured and theoretical values for 5 and 20% Spectralon reflectance standards. Illumination was provided by a quartz-halogen lamp at an

incidence angle of 40 – 55° and emission angle of 0°. The ASD is composed of three spectrometers (0.35 – 1.005, 1.006 – 1.800, and 1.801 – 2.500 μm). For some measurements the data from the three spectrometers were slightly offset from each other in reflectivity. To correct for this offset, we adjusted the spectra from the first and last spectrometers to the spectrum of the middle spectrometer, which is the most stable. Specifically, we adjusted the data from the first spectrometer by progressively increasing the percentage of the value of the offset added to the value at each wavelength until there was no longer an offset. To adjust the data from the last spectrometer we were able to use a simpler approach; we added the difference at the offset to each value over the range of the last spectrometer. Bidirectional reflectance measurements of similar materials acquired from RELAB at Brown University and from this spectrometer exhibit good correlation [*Gillis-Davis et al*., 2008], confirming the validity of this approach.

3. Results

3.1. Physical Analyses

The results of the optical petrographic analysis are given in Table 3 for samples C, 333, 613, 699, Memorial, and 810. Below we present the results of our SEM and profilometry analyses; they are the qualitative and quantitative evaluations of surface roughness, respectively. We focus on comparing a cut surface to a rough surface of the same sample. We describe the results of these analyses for seven samples below (589, 95, 699, C, M-1, 9X, and 810). Results are not shown for the eighth sample, 613, because its rough surface was accidentally destroyed prior to these analyses.

Table 4.3: Petrographic descriptions of selected samples.

Sample	Origin	Texture	Grain orientation	Grain size	Accessory phases
C	epithermal vein-filling chert	microquartz	none	< 25 µm	
333	porcellinite	layers of opal and microquartz	none	< 15 µm	Carbonate
613_red	sedimentary chert	massive	none	< 50 µm	fine-grained hematite
699	geyserite	laminated fibrous quartz	yes, in < 25% of laminae	< 50 µm	
Memorial	hydrothermal precipitate	opaline	some		silicified plant fragments, clay, carbonate, and volcanic ash debris
810	replacement chert	laminated microquartz	some	variable but generally <15 µm	carbonate, clay, and volcanic ash debris

In the lowest magnification SEM images (e.g., 20 – 200x), it is readily apparent which image is from the cut surface by its smoothness, perceived as a relative lack of well-defined light peaks and dark shadows at this scale (Figure 3). The cut surfaces typically do not have readily visible roughness until magnifications of 400x. At higher magnification, however, the surface displaying the greatest roughness may change. This is because roughness can occur at many scales, with the smaller scales superposed on the larger scales. The rough surfaces display variation at a scale of 100 – 200 μm along with the smaller-scale roughness (e.g., ~10 μm) that the cut surfaces exhibit. This smaller-scale roughness is first observed at lower magnifications as thin, intricate, irregular lines that turn into a granular texture of interlocking blocks or grains at high magnifications, shown in Figure 4. These blocks vary in diameter between samples and, in some cases, between surfaces, but are on the order of 20 μm and less.

The original surface profiles include any slope or topography on the order of the 1 cm length of the profile. To compare the roughness of the surfaces without this extra variable, we use a Gaussian curve-fitting routine (specifically, the gaussfit routine in IDL) to fit and remove any first-order curve or slope (e.g., Figure 5). The resulting adjusted profiles measured from each surface (Figure 6) are not averaged to avoid canceling out high and low values. In each case the three profiles from each surface are broadly similar to one another in their range of values.

We quantify the roughness values by calculating the average roughness (R_a) for each sample, which is the average of the absolute values of the profile (see Table 4). This equation is

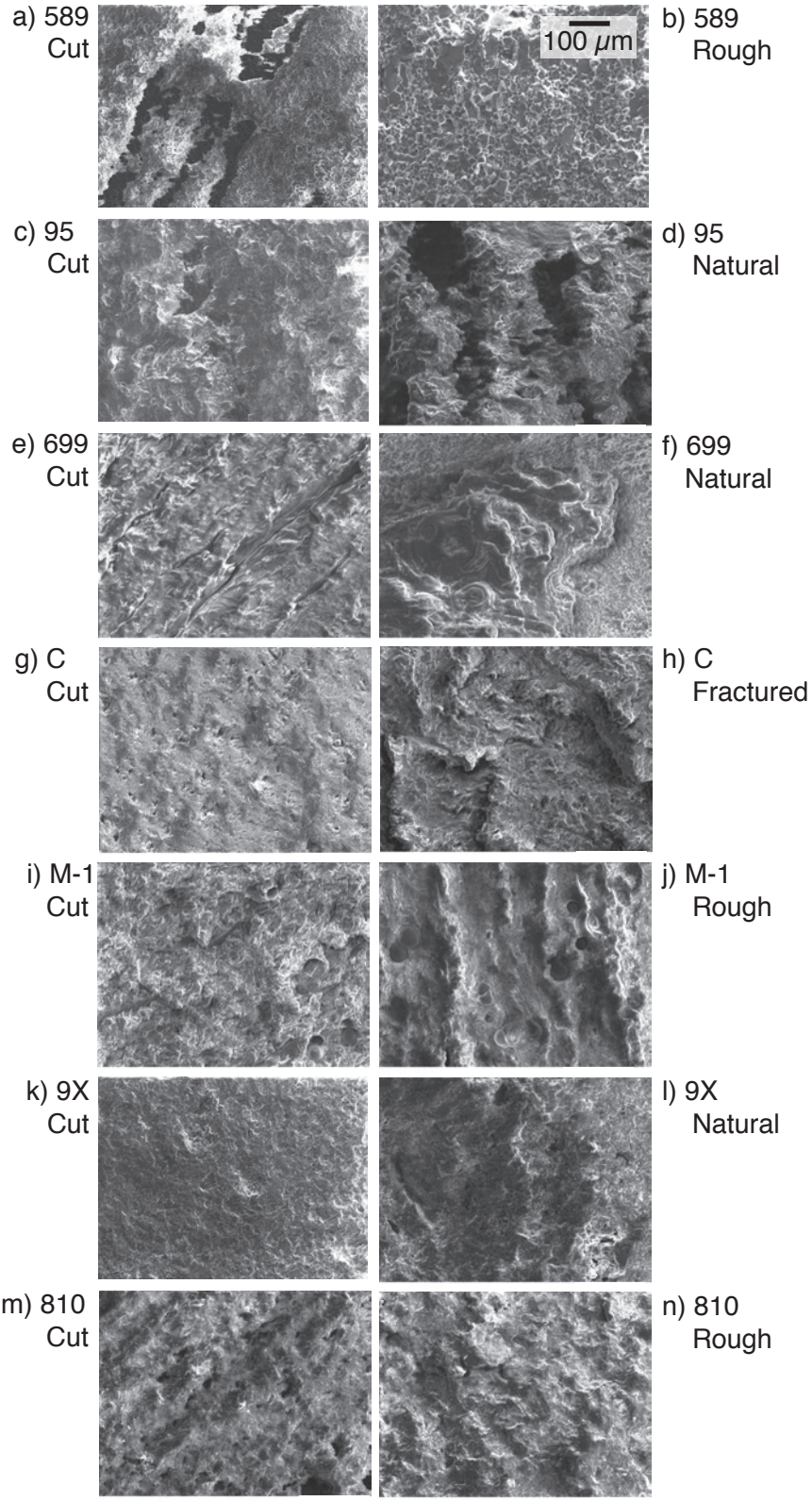

Figure 4.3: SEM secondary electron images of cut (left column) and rough or natural (right column) surfaces at 200x magnification. The scale bar in the upper right corner is the same for each image.

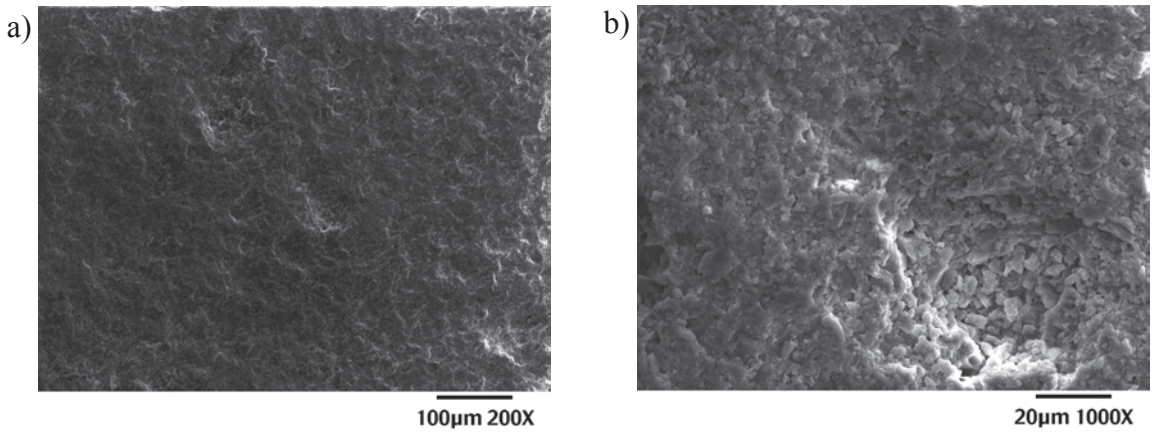

Figure 4.4: SEM images of the 9X cut surface at a) 200x and b) 1000x illustrating the appearance of the smaller-scale roughness described in the text.

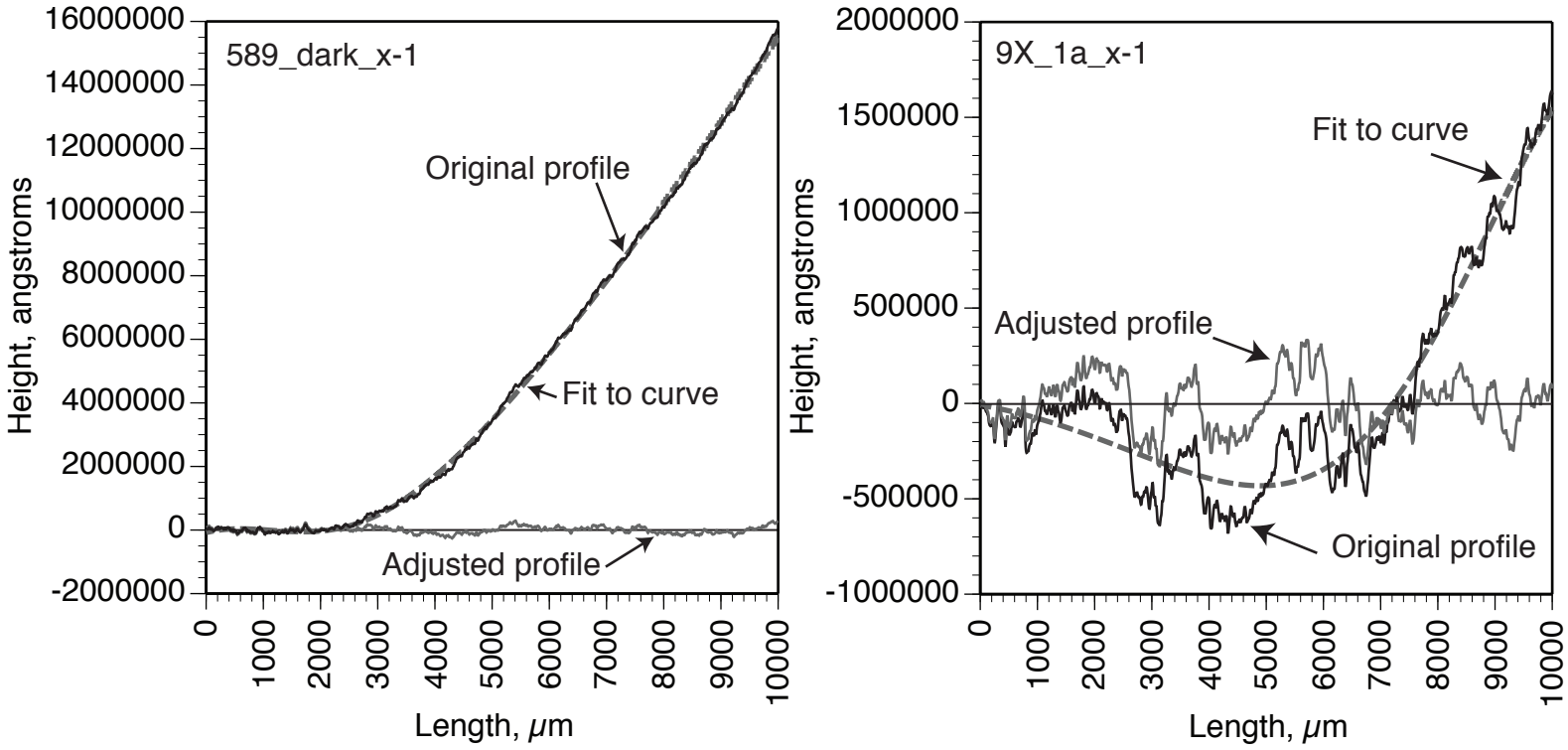

Figure 4.5: Two examples, both 'rough' surfaces, showing the adjustment of the original measured profiles by the removal of the largest scale variation. A gaussian curve is fit to the original profile and subtracted from it to produce the adjusted profile.

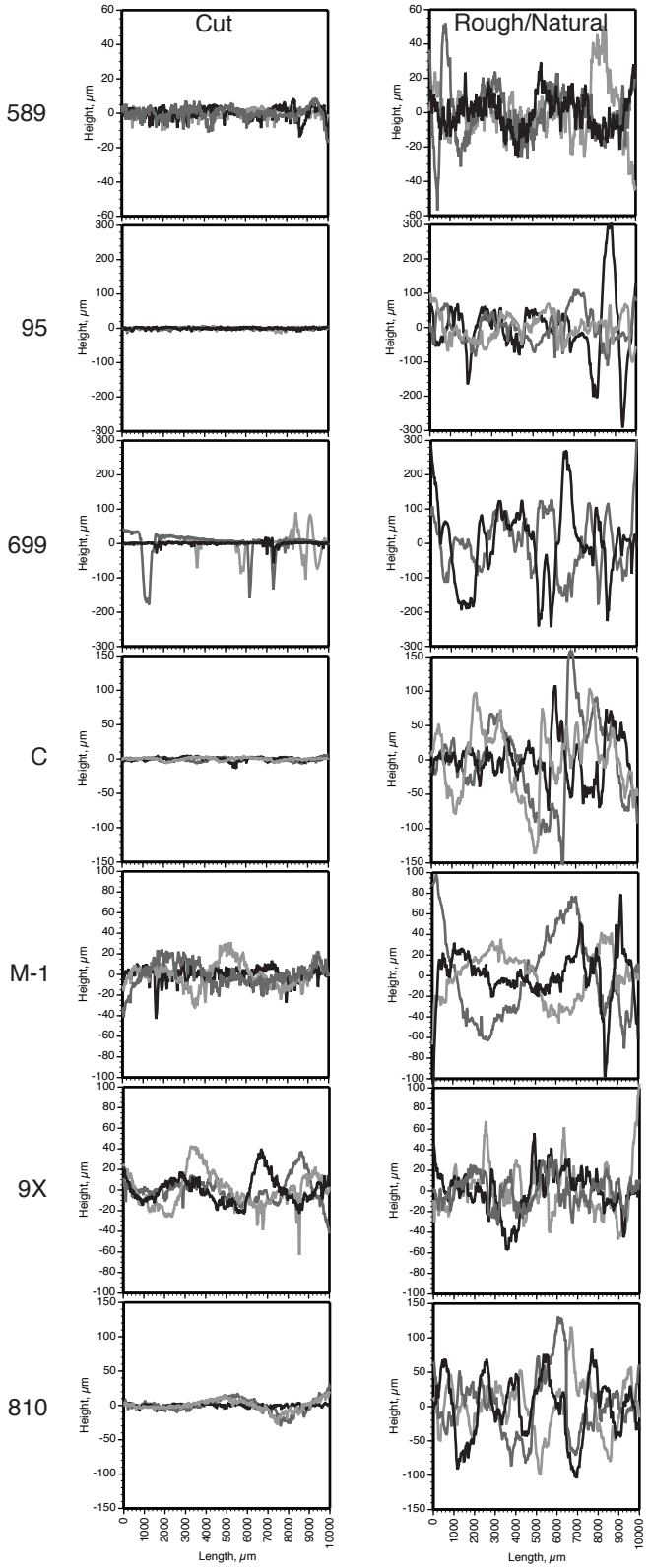

Figure 4.6: Adjusted profiles of the cut and rough surfaces of chert and amorphous silica samples. Note that the Y-axis is constant for the two surfaces of the same sample, but may vary between samples.

Table 4.4: Range of R_a values (roughness) for the three profiles measured on each cut and rough surface. Values are given in angstroms.

Sample	Cut	Rough
699	26833 – 214395	655637 – 837890
95	18752 – 21008	312006 – 618580
810	17669 – 73731	293011 – 364264
C	15305 – 18164	238674 – 504301
M-1	51376 – 99948	171831 – 358357
589	17696 – 27766	82040 – 122243
9X	87531 – 139620	116832 – 182642

$$R_a = \frac{1}{n} \sum_{i=1}^{n} |y_i|$$

R_a indicates the degree of variability (i.e., roughness) over the length measured. Because all our profiles are of the same length, we can compare R_a between them. The R_a value is directly proportional to the scale of roughness. This value does not indicate when smaller-scale roughness is superposed on larger-scale roughness.

The adjusted profiles (Figure 6) show that sample 699 exhibits the largest vertical variation of all seven samples on both its cut surface (± 100 μm) and its rough surface (> ± 150 μm). The smallest amount of variation is observed for sample C for its cut surfaces (< ± 10 μm) and sample 589 for its rough surfaces (± 50 μm). The largest difference between the roughness of a cut surface and corresponding rough surface is shown by sample C (>~100 μm); the smallest difference is shown by sample 9X (<~20 μm). The R_a values (Table 4) reflect these observations. The rough surfaces have smaller-scale variation superposed on the larger-scale curves that confirms the small-scale roughness seen in the SEM images.

3.2. Thermal Infrared Spectral Measurements

3.2.1. Spectral Variation between Samples

TIR spectra of our samples are plotted in Figure 7 and their most prominent minima are listed in Table 5. Features in the high wavenumber region (e.g., 1300 – 1000 cm^{-1}) are attributed to the asymmetric stretching modes of Si – O; the symmetric

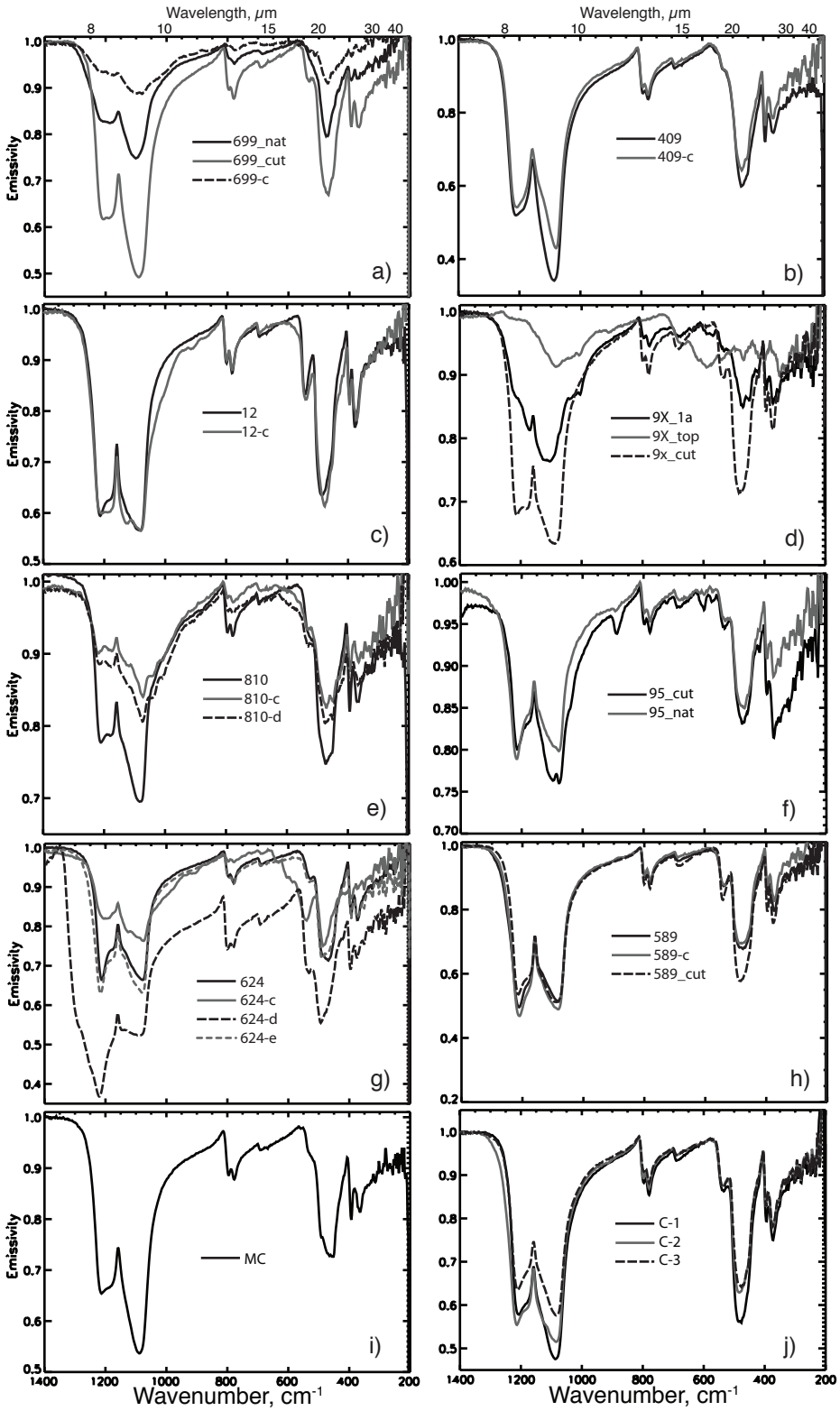

Figure 4.7: Thermal infrared emissivity spectra of chert and amorphous silica samples. Y-axis range differs between plots. Multiple spectra in one plot are of different surfaces or sides of the same sample.

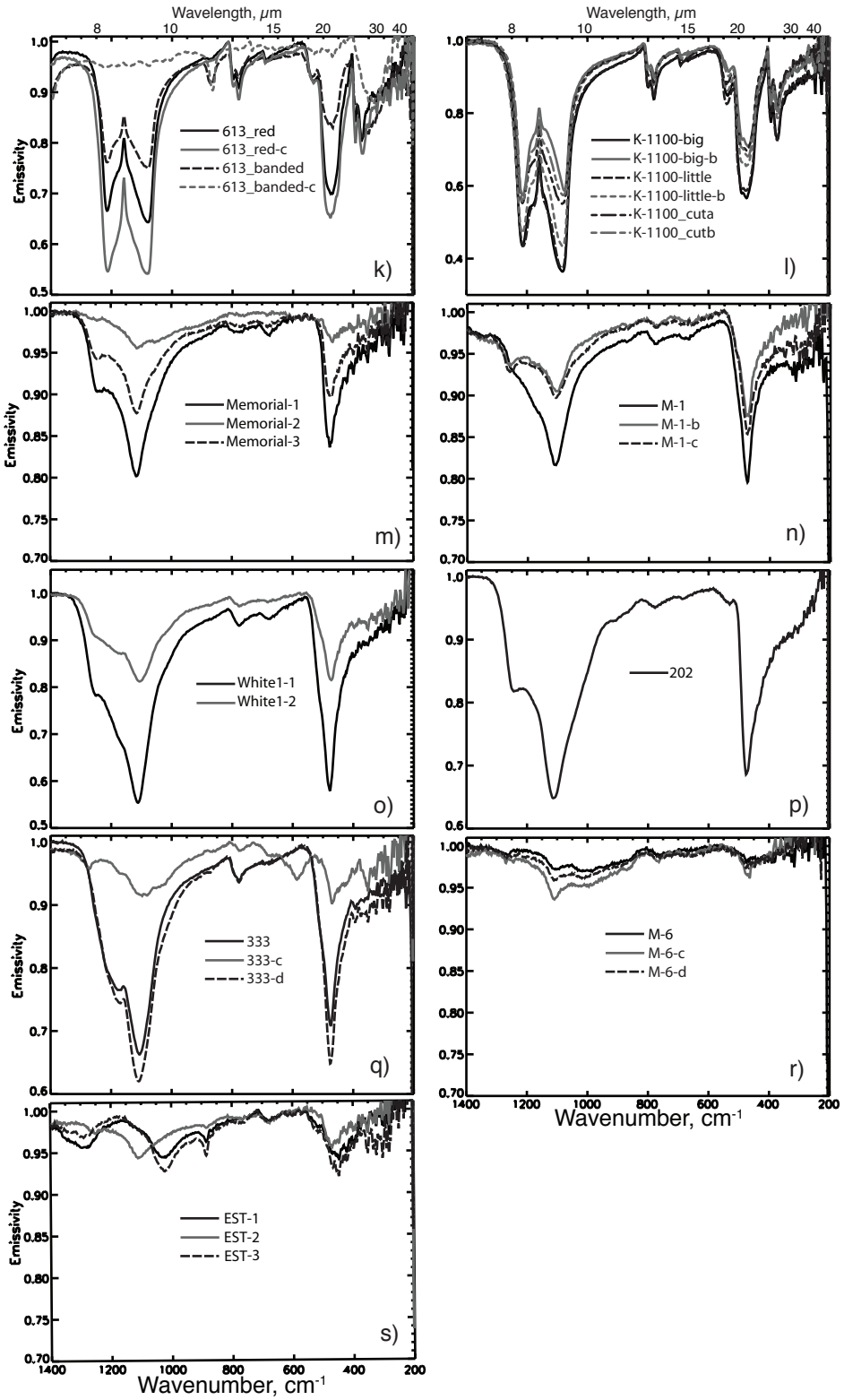

Figure 4.7: (Continued) Thermal infrared emissivity spectra of chert and amorphous silica samples. Y-axis range differs between plots. Multiple spectra in one plot are of different surfaces or sides of the same sample.

Table 4.5: Positions of selected emissivity minima in chert and amorphous silica.

Sample	1300 – 1000 cm^{-1}	~475 cm^{-1}	Crystalline/Amorphous
699	1193, 1091	468	Crystalline
409	1213, 1085	470	Crystalline
12	1214, 1087	487	Crystalline
9X (cut)	1195, 1080	475	Crystalline
810	1211, 1083	472	Crystalline
95	1213, 1078	470	Crystalline
624 (c, e)	1213, 1078	468	Crystalline
589	1211, 1081	476	Crystalline
MC	1222, 1089	465	Crystalline
C	1205, 1087	476	Crystalline
613	1214, 1078	468	Crystalline
K-1100	1211, 1081	474	Crystalline
Memorial	1115	476	Amorphous
M-1	1105	474	Amorphous
White1	1110	476-472	Amorhpous
202	1112	476	Amorphous
333 (c)	1172, 1106	474	Combination
M-6	1108	465	Amorphous
EST (1, 3)	1024-1022	447-445	Undetermined
EST (2)	1110	468	Undetermined

stretching modes of Si – O cause features at slightly lower wavenumbers (e.g., 900 – 600 cm^{-1}) [e.g., *Moenke*, 1974; *Salisbury et al*., 1991]. The features at even lower wavenumbers (e.g., < 600 cm^{-1}) can be attributed to the bending modes of Si – O [e.g., *Moenke*, 1974; *Salisbury et al*., 1991]. We observe variations in the spectral features throughout the range and will discuss them in order of decreasing wavenumber. Based on the spectral shape, we divide the spectra into a quartz-bearing (i.e., chert) group (810, MC, 589, 9X, K-1100, 95, 12, 409, 699, 613, 624, and C, Figure 7a-l), an opaline (i.e., amorphous silica) group (Memorial, White1, 202, and M-1, Figure 7m-p), and an undetermined group (M-6, EST, and 333, Figure 7q-s).

The quartz-bearing samples have a strong doublet in the high wavenumber region whereas the opaline samples have a single, broad emissivity minimum. In the spectra of the quartz phases, the minima of the doublet are at ~1222 – 1172 and ~1106 – 1078 cm^{-1}. These minima may be of similar depth (e.g., Figure 7g, h) or one may be deeper than the other (e.g., Figure 7a, b); for the majority of spectra the lower wavenumber feature is deeper. In some cases, the interior sides of the doublet angle away from each other (i.e., the spectrum having a positive slope from ~1200 to ~1150 cm^{-1}, and a negative slope from ~1150 to ~1100 cm^{-1}), forming narrow, pointed minima, whereas in other cases these spectral features exhibit broader and/or more rounded minima (e.g., sample 699). Some spectra also exhibit a smaller doublet superposed on one minimum of the larger doublet (e.g., sample 95). The specific position of the single minimum in the opaline spectrum ranges from 1115 – 1105 cm^{-1}. The lower crystallinity in opaline silica causes its broader spectral features compared to those of quartz [e.g., *Lippincott et al*., 1958]. As the amount of crystalline structure decreases, packing of SiO_2 tetrahedra becomes

more variable and the vibrational frequencies widen in range, broadening and simplifying the resulting spectral features. In our samples, a shoulder or additional minimum may be superposed on the main feature at ~1243 – 1257 cm^{-1}.

The spectra of quartz-bearing samples have another small doublet around ~780 cm^{-1} and a shallow minimum at ~700 – 675 cm^{-1}. These features may be present in the spectra of the opaline phases but are much shallower and do not include a doublet for the 780 cm^{-1} feature. Both quartz-bearing and opaline spectra have a large minimum at ~475 cm^{-1} that varies in depth, but commonly has an emissivity nearly equivalent to that of the large doublet; the exact position of the feature ranges from 487 – 465 cm^{-1}. The ~475 cm^{-1} feature is usually, but not always, flanked on the high wavenumber side by a smaller emissivity minimum or shoulder at ~540 cm^{-1}. This 540 cm^{-1} feature does not appear in opaline spectra. Another double minimum is commonly present at ~400 – 350 cm^{-1} in the spectra of quartz-bearing samples but is not in the spectra of opaline samples.

Three of the samples we analyzed have TIR spectra that do not clearly fit in either of the previous two categories (333, M-6, and EST, Figure 7q-s). The spectrum of sample 333 (Figure 7q), a porcellanite, has characteristics of both quartz and opaline phases. It has one large emissivity minimum at 1106 cm^{-1} and another minimum superposed on the larger feature at 1172 cm^{-1}. It also has minima at ~780 and ~475 cm^{-1}. We do not observe the minima at ~540 and ~400 – 350 cm^{-1} that we observe in quartz. The spectrum of sample M-6 (Figure 7r), a diatomite, has very shallow features. Broad emissivity minima are apparent at ~1110 cm^{-1}, ~770 cm^{-1}, and ~450 – 500 cm^{-1}. Sample EST has a spectrum from one surface (Figure 7s, EST-2) that is similar to opaline silica in having a shallow minimum at 1110 cm^{-1}, a sharper minimum at ~680 cm^{-1}, and a

minimum at ~475 cm^{-1}. The spectra from two other surfaces of sample EST have different features, however (Figure 7s, EST-1,3). They have a shallow minimum at ~1300 cm^{-1}, a minimum at ~1025, a sharp feature at ~890 cm^{-1}, another at ~680 cm^{-1}, and a minimum at ~450 cm^{-1}. The 680 and ~450 cm^{-1} features may be similar to that of chert, but the other quartz features are not present. Carbonate accounts for the feature at ~890 cm^{-1}.

Additionally, the spectra of some samples include features not attributable to silica. These phases may be intimately mixed with the silica or may be present on the surface as contaminating or weathering phases. A narrow feature at ~870 cm^{-1} in samples EST, 95, and 613 is indicative of one of the C – O bending modes of a carbonate phase [e.g., *Salisbury et al.*, 1991]. Some of the TIR spectra of samples 9X, 810, 613, and 333 (Figure 7d, e, k, q) differ from the general spectral shape of other chert and amorphous silica spectra. All of these spectra are from surfaces that show visual evidence of contamination; weathering phases present on the surface analyzed would add their features to the chert spectrum. The doublet at ~550 and 475 cm^{-1} in the 624-c spectrum suggests a smectite (i.e., phyllosilicate) component on that surface; this is discussed further in section 4.2.

3.2.2. Spectral Variation within a Sample

Simon and McMahon [1953], *Spitzer and Kleinman* [1961], and *Wenrich and Christensen* [1996] have shown previously that a spectrum of the c axis of a quartz crystal differs from that parallel to the a axis. A preferred orientation of quartz crystals within a chert could cause variation in the spectral character when the rock is measured at

different orientations. Our results in Figure 8 show that there are small spectral variations with orientation for the four samples we examined (624, 589, 409, and C). There are differences in overall depth (not shown), along with slight differences in the depth and/or shape of the ~475 cm^{-1} band and the relative depth of the ~1300-1000 cm^{-1} bands (as in samples 409 and C).

Changes in incidence angle primarily affect the depth of the TIR spectral features for the six samples analyzed (Figure 9). The same features are present and at the same positions in the spectra regardless of incidence angle, but the spectral contrast of one or more features increases or decreases. The shape may be altered slightly for the high-wavenumber minimum of the quartz doublet; as the depth increases the higher wavenumer side of the minimum appears to be drawn out more than the lower wavenumber side. The low-wavenumber minimum of the doublet is less affected. The relative depth between these two minima of the quartz doublet changes with incidence angle. We observe that the high-wavenumber minimum of the doublet increases in depth more than the low-wavenumber minimum as the incidence angle increases. For the opaline sample (M-1) the increase in incidence angle causes the development of a shoulder or minimum at ~1250 cm^{-1}. The measurement collected from a horizontal surface is not always the most shallow. In some samples the shallowest spectrum was measured at 30º or 45º.

Figure 10 shows how roughness affects the TIR spectra of our samples 699, 95, M-1, C, 613, 589, 810, and 9X by comparing the spectra of their cut and rough surfaces. Though layering can be seen in some samples, we have measured areas that appear to be monolithologic. Surfaces exhibiting weathering products were avoided for this analysis.

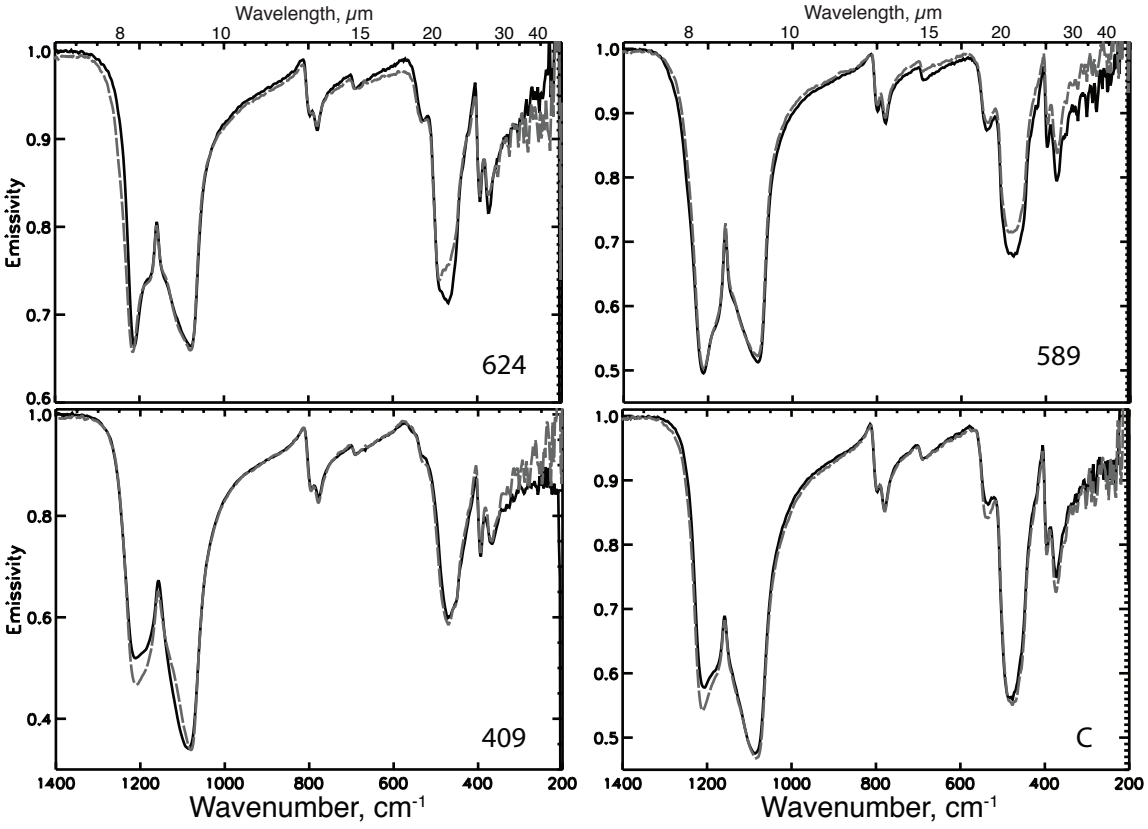

Figure 4.8: Plots comparing thermal infrared emission spectra of surfaces from different sides of the same sample. Spectra in each plot are normalized to the same spectral contrast to better observe changes in shape and relative depth.

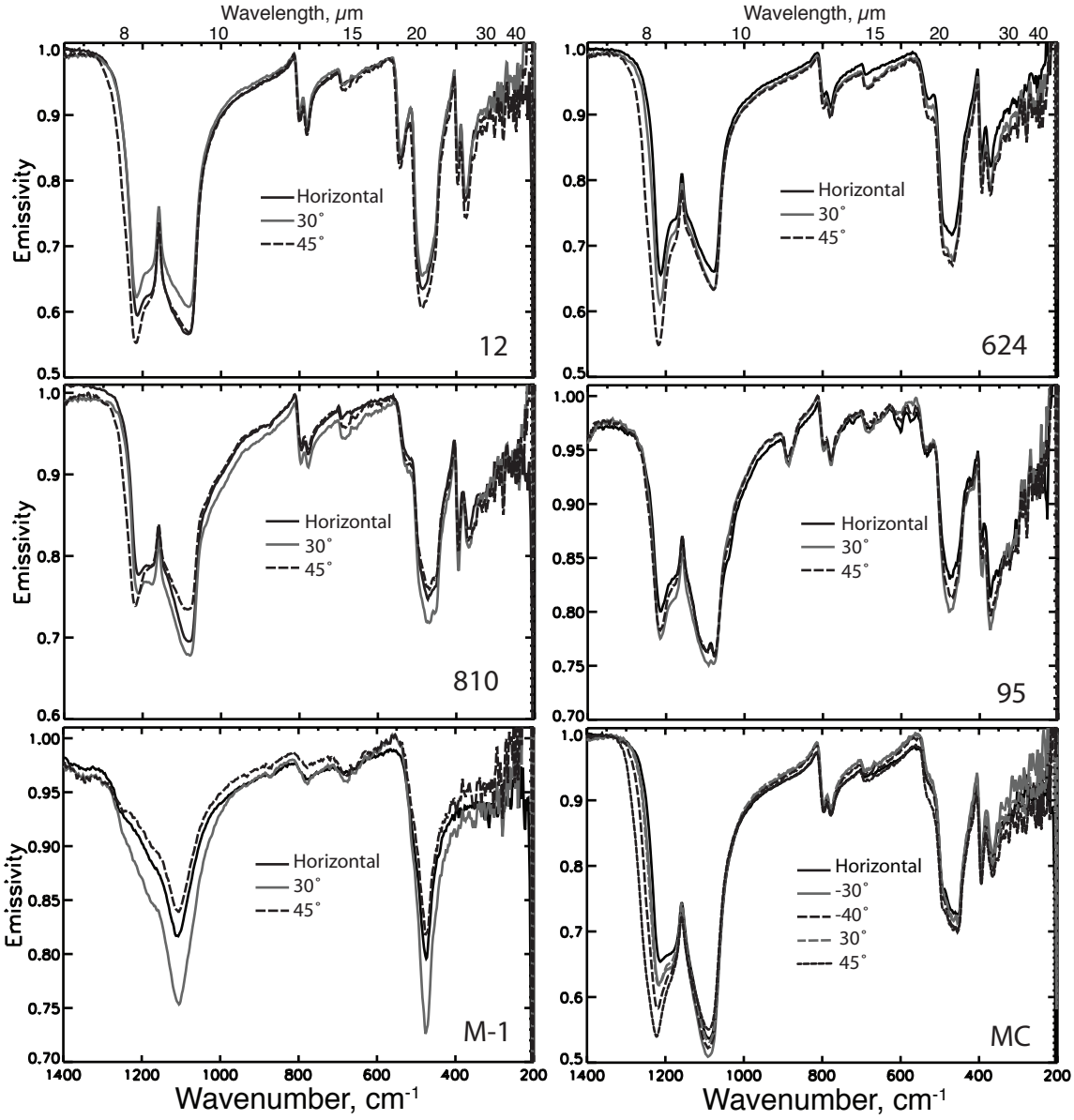

Figure 4.9: The effect of incidence angle on thermal infrared emission spectra. Angles are measured from horizontal.

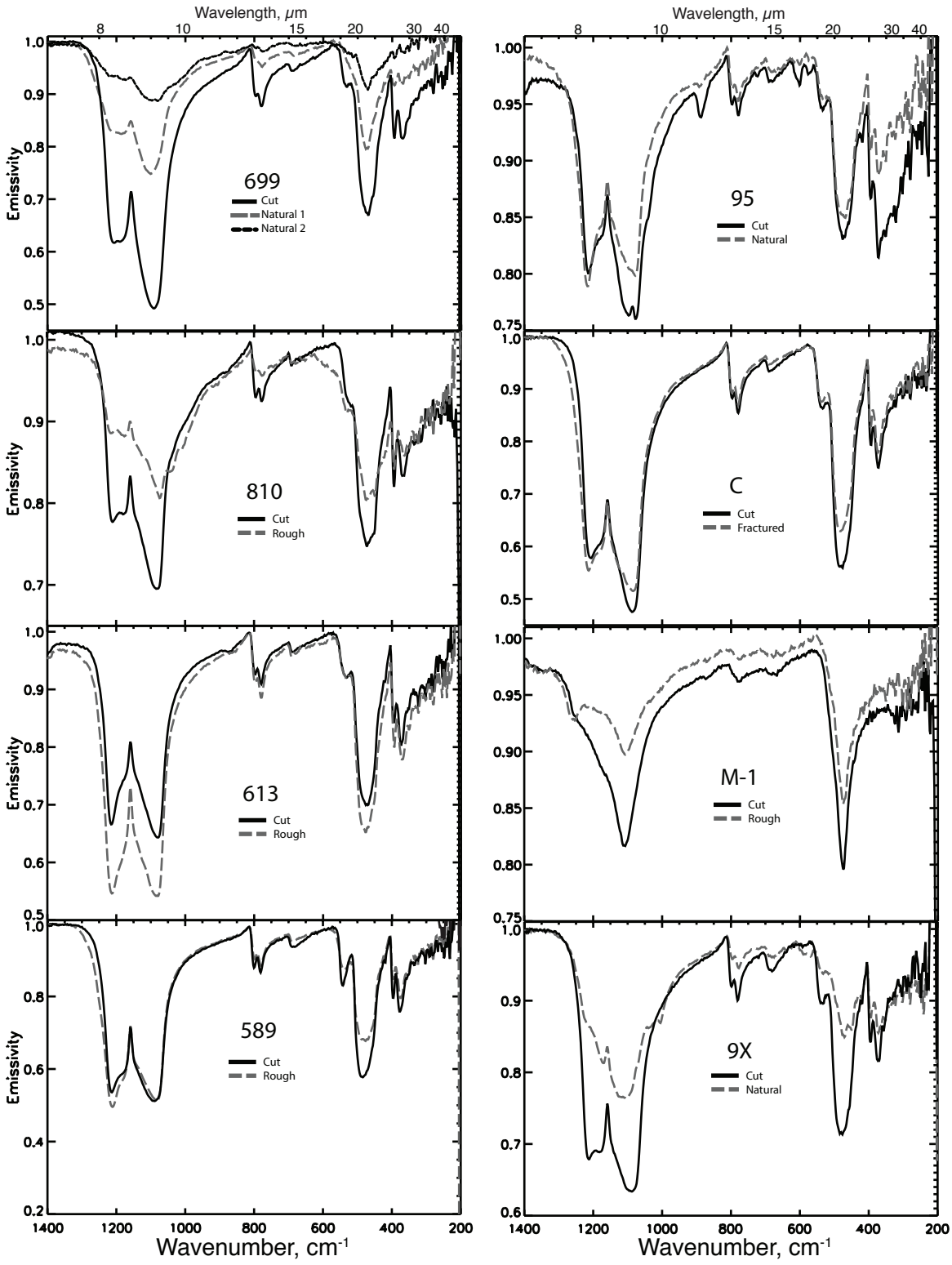

Figure 4.10: Plots comparing thermal infrared emission spectra from surfaces of different roughness from the same sample.

Two exceptions are the rough surfaces of samples 810 and 9X, which may have contamination that contributes to the difference in shape in these cases. Because the other rough surface spectra do not differ to such a great degree, it is likely that the spectral differences for these two samples are not solely an effect of surface roughness, but rather indicate mixing of silica with another phase on the sample surface.

For the 699, 95, M-1, C, 613, and 589 samples there is an overall change in spectral character between the rough and cut surfaces originating from changes in the depth of the 1300 – 1000 cm^{-1} and/or 475 cm^{-1} minima, the relative depth of the two minima in the quartz doublet, and/or the more defined presence of features in one spectrum and not the other. In the spectra of samples 699, 95, M-1, and C the quartz doublet is deeper for the cut surfaces than for their rough surfaces, whereas in the spectra of samples 589 and 613 it is shallower for the cut surfaces than for their rough surfaces. Additionally, rough and cut surfaces of the same sample exhibit changes in the relative depths of the two minima in the quartz doublet; the higher wavenumber minimum increases in depth relative to the depth of the lower wavenumber minimum between the cut and rough surface spectra, becoming deeper than the lower wavenumber minimum for samples 95 and 589. The minima at ~780 cm^{-1} and 475 cm^{-1} are shallower in the rough surface spectrum than the cut surface spectrum for all samples but 613. The depth of the ~540 cm^{-1} feature also becomes more shallow, in some cases becoming undetectable (e.g., 699). In the rough surface spectrum of the opaline silica sample M-1, we observe the presence of a minimum at ~1250 cm^{-1} that is not present in the cut surface spectrum.

3.3. Visible to Near-infrared Spectral Measurements

3.3.1. Spectral Variation between Samples

Visible to near-infrared spectra of our 19 samples are shown in Figure 11. The spectra vary in their overall maximum reflectivity from ~0.05 to ~0.75. The spectra of 12 samples have features in the shortest wavelength region (~0.4 – 1.1), which are in a variety of positions, specifically 0.47 – 0.56, 0.61 – 0.68, 0.88 – 0.95, and 1.02 – 1.03 (for examples see Figure 11g and k). Commonly the spectra exhibit more than one of these features. Fe^{3+} in iron oxide phases (e.g., hematite) causes many of the features observed at <1.4 μm, such as 0.47 – 0.56 μm, 0.61 – 0.68 μm, and 0.88 – 0.95 μm [e.g., *Gaffey et al*., 1993]. Fe^{2+} may be responsible for the ~1 μm band we see in some spectra (i.e., sample Memorial) [e.g., *Burns*, 1993].

The most obvious features in the VNIR spectra are those attributable to H_2O and OH^- at 1.4 – 1.45 μm and to H_2O at 1.89 – 1.94 μm (illustrated in Figure 11i, m) [e.g., *Gaffey et al*., 1993; *Goryniuk et al*., 2004]. Fourteen of the 19 samples have spectra with both these features, including all opaline samples. Spectra of the other five samples may have a slight ~1.9 μm feature, but no ~1.4 μm feature, and are mostly flat or have a slight negative slope toward longer wavelengths (e.g., Figure 11c, e, h, k, l). H_2O may also be responsible for the feature observed in some spectra at ~1.2 μm [*Gaffey et al*., 1993].

Eleven samples have spectra with a feature attributable to cation-OH and/or OH^- vibrations. The majority of these features are broad minima centered in one of the following regions: 2.20 – 2.24, 2.27, or 2.29 – 2.33 μm , illustrated in Figure 11b and p. There are multiple possible origins for these features, including Al – OH (~2.2 μm), Mg – OH (~2.3 μm), and Fe – OH (~2.29 μm) bonds [e.g., *Clark et al*., 1990; *Gaffey et al*.,

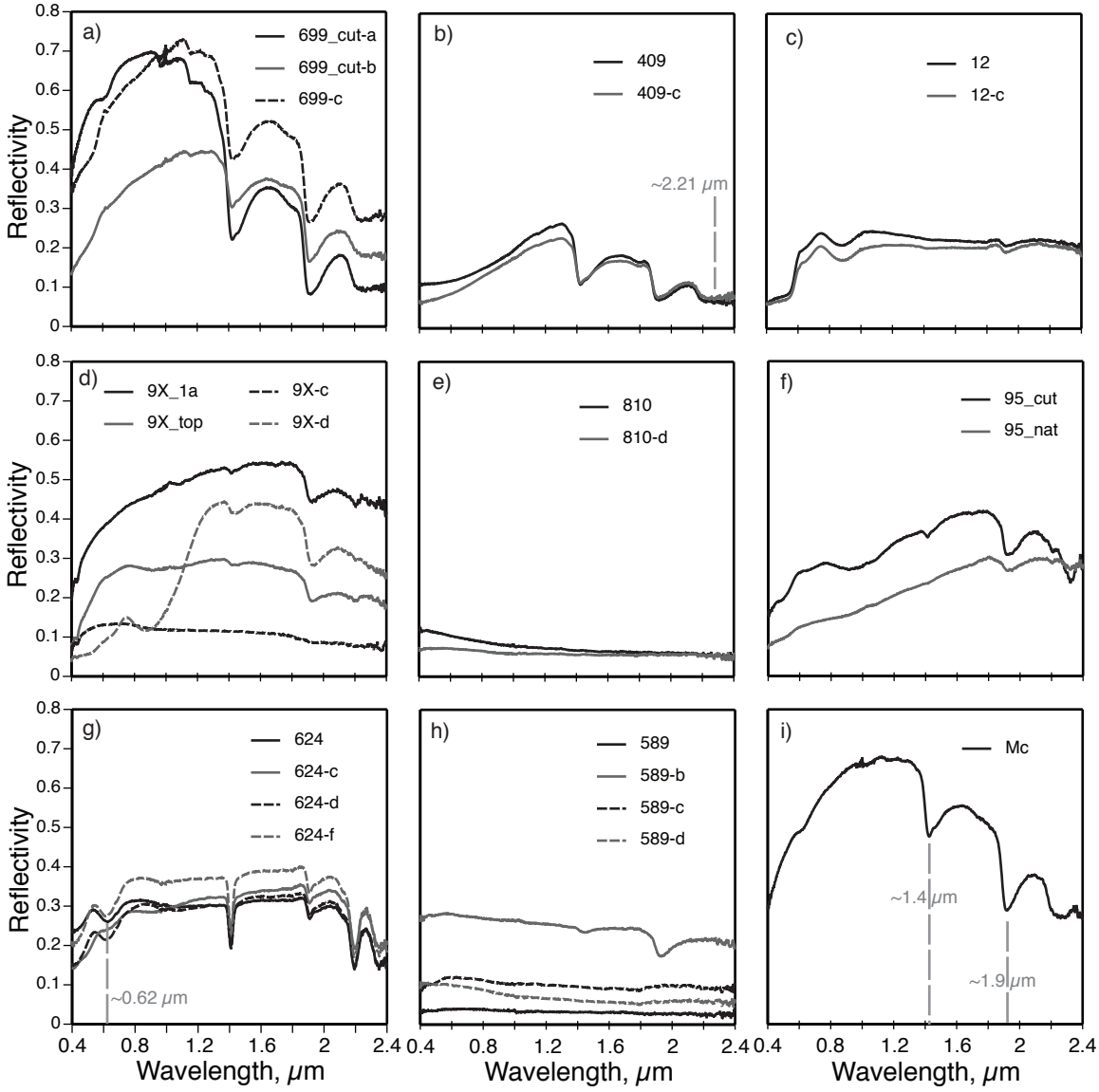

Figure 4.11: Visible to near-infrared reflectivity spectra of chert and amorphous silica. Multiple spectra in one plot are of different surfaces or sides of the same sample. Vertical grey dashed lines are examples illustrating features described in the text.

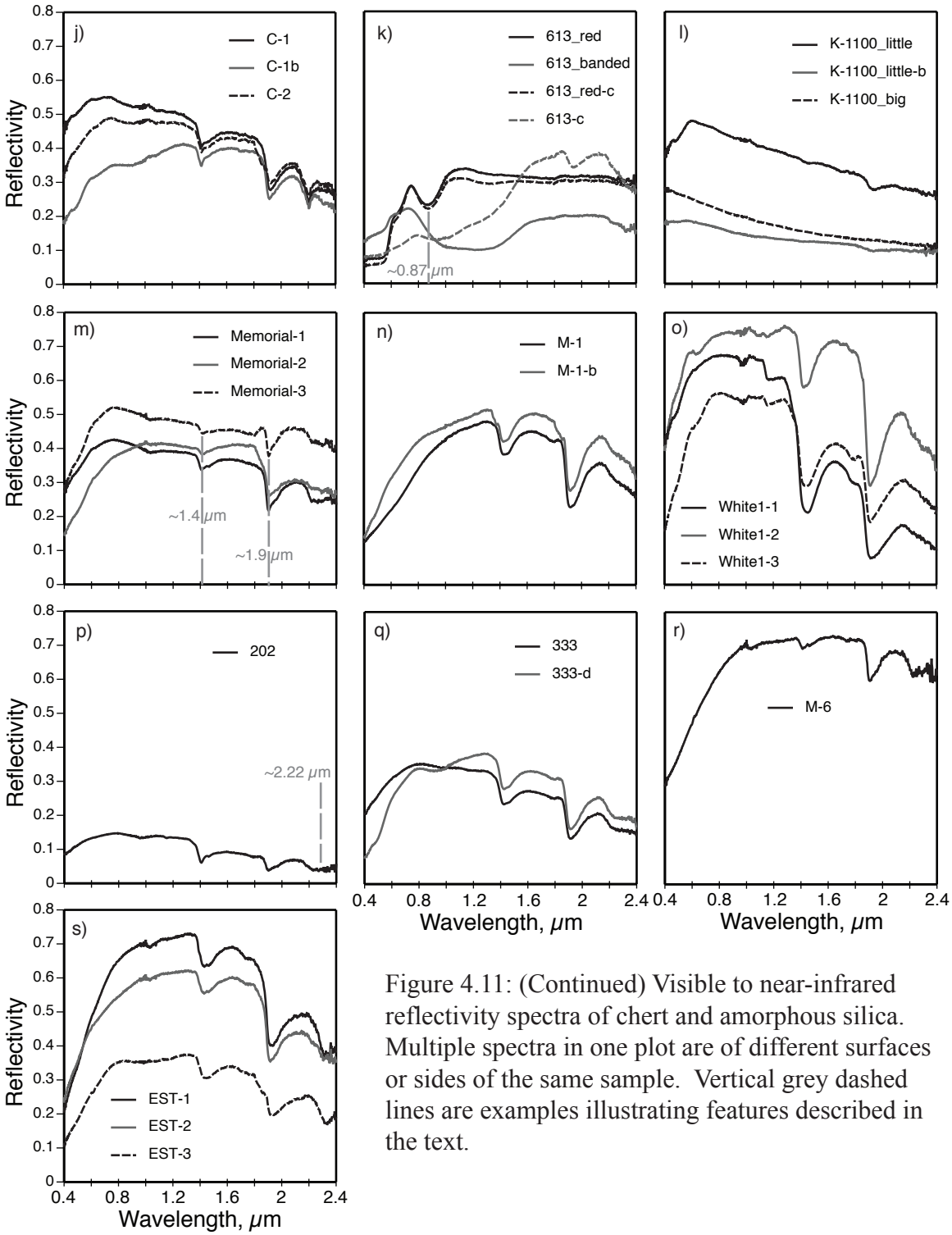

Figure 4.11: (Continued) Visible to near-infrared reflectivity spectra of chert and amorphous silica. Multiple spectra in one plot are of different surfaces or sides of the same sample. Vertical grey dashed lines are examples illustrating features described in the text.

1993]. Additionally, Si – O – H bending and O – H stretching modes are active in this same region [*Gaffey et al*., 1993; *Goryniuk et al*., 2004]. The majority of samples have spectra with features closer to 2.2 μm than 2.3 μm. The spectrum of one sample, C, has a narrow minimum at 2.2 – 2.21 μm rather than a broad minimum. The spectrum of another sample, 624, has two sharp minima in this region at 2.19 – 2.20 and 2.35 μm. Spectra that have hydration features (i.e., 1.4 and 1.9 μm features) but no features at > 2 μm generally have a negative slope in place of a minimum (e.g., Figure 11n, o).

There are spectra of a few samples that exhibit no features in the VNIR. These are samples 810, 589, and K-1100 (Figure 11e, h, l). In the case of samples 589 and K-1100 some spectra are featureless while others are not. The featureless spectra are mostly flat but may have some amount of a slope towards longer wavelengths. The spectra are low in overall reflectivity compared to some samples, but are consistent with the overall reflectivity of others.

3.3.2. Spectral Variation within a Sample

We do not observe qualitative changes in VNIR spectral shape with differences in sample orientation or surface roughness apart from changes in overall reflectivity and spectral contrast, which do not appear to have a clear correlation. Additional phases on one surface but not on another may cause changes in shape, however. This appears to be the case in samples 9x, 333, and 624, which have weathering material on some surfaces. We did not acquire VNIR spectra at different incidence angles.

4. Discussion

4.1. Comparison with Chert and Amorphous Silica Spectra from Previous Studies

The spectra of chert and amorphous silica produced by our study are consistent with spectra from previous TIR and VNIR studies in general shape and features present resulting from silica and accessory or contaminating phases (e.g., *Michalski* [2005], *Michalski et al*. [2003], *Hubbard et al*. [2003], and *Brown* [2004]). However, we do not observe any spectra with features such as those seen in the "class two" spectra of *Goryniuk et al*. [2004] (low contrast spectra with features at ~ 1250, 1111, 1000, and 870 cm^{-1}). This is because all our samples are well consolidated, whereas the "class two" spectra in their study are from poorly consolidated or particulate (< 74 μm) samples and therefore are likely affected by significant volume scattering, which can make additional features apparent in the spectrum.

In detail, however, there are some differences between our spectra and the spectra from other studies. We find small differences between the descriptions of the VNIR spectra from our samples and those of *Milliken et al*. [2008]. The authors of that study used the broadness of the >2.2 μm features to distinguish between hydrated silica and phyllosilicates. Our data show that hydrated silica may have accessory amounts of phyllosilicate, resulting in a spectrum with narrow absorptions characteristic of phyllosilicates (e.g., Figure 12). Additionally, *Milliken et al*. [2008] describe a second weak band at 2.25 – 2.26 μm along with the ~2.21 μm band in opaline silica attributable to hydrogen bonding of H_2O to silanol groups. We do not observe a discrete minimum at this position in any of the opaline or chert spectra from our study. This simply may be

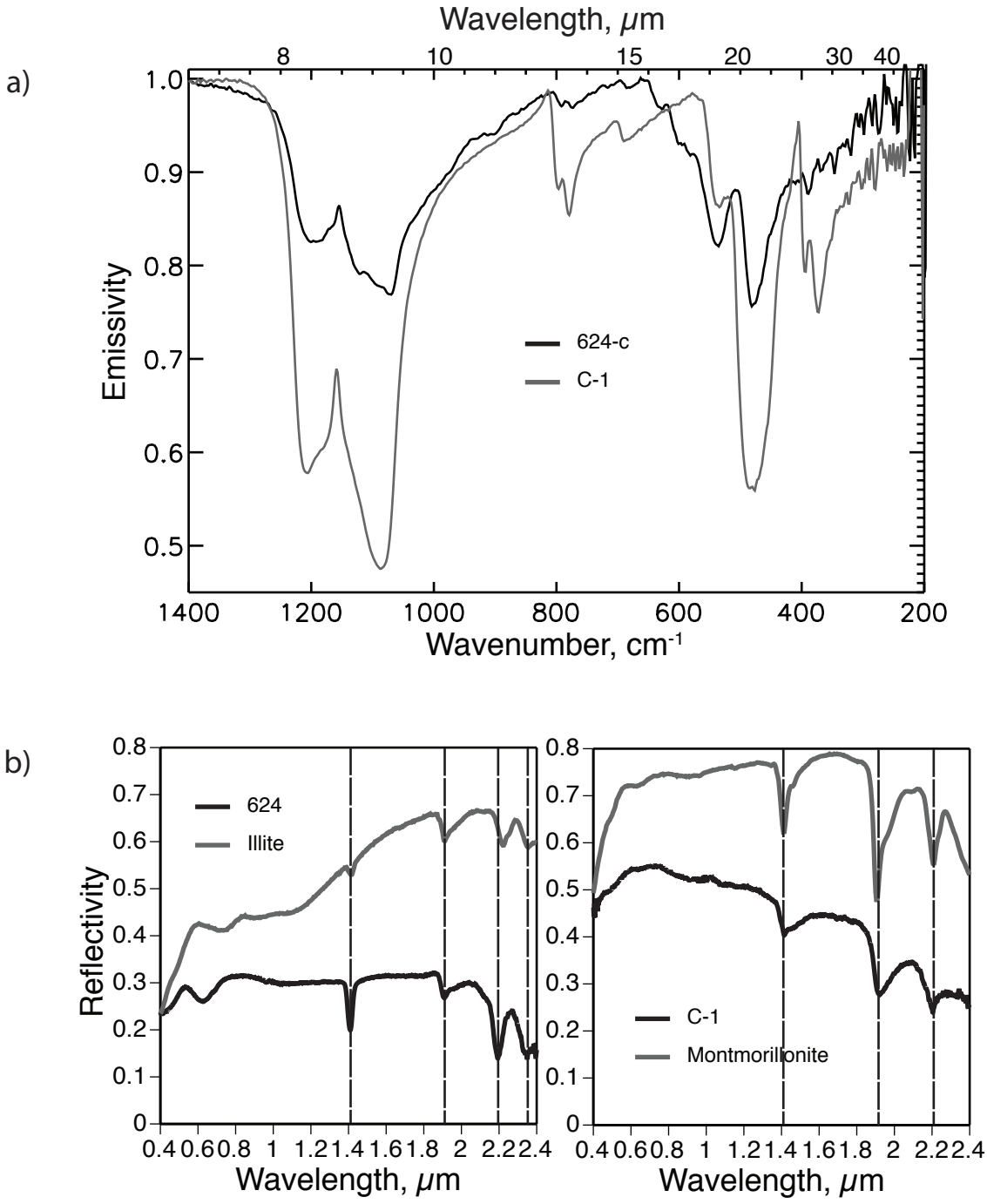

Figure 4.12: a) TIR and b) VNIR spectra of the two study samples that have phyllosiicate features in the VNIR wavelength range. The VNIR spectra are plotted with the phyllosilicate phase they most closely resemble for comparison. The illite and montmorillonite VNIR spectra are from the CRISM spectral library [Bishop et al., 2006].

because the band is too shallow or too near the ~2.21 μm band to differentiate the two. The only sign of the 2.25 – 2.26 μm band may be the broadness of the feature at ~2.2 μm.

We cannot currently confirm that our data are consistent with the findings of *Rice et al*. [1995] and *Michalski et al*. [2003] concerning the TIR spectra of opal. *Rice et al*. [1995] studied the transition from opal-A to opal-CT in reflectivity spectra in the TIR and observed a shift of a feature at ~475 cm^{-1} to higher wavenumbers as the maturity of the opal increases (i.e., opal-A maturing to opal-CT). *Michalski et al*. [2003] observed that the 476 cm^{-1} minimum is deeper in opal-CT than opal-A, a shoulder present at ~1250 cm^{-1} in the spectrum of opal-A becomes more shallow in opal-CT spectra, and the features in general become broader and more similar to cristobalite and tridymite in the opal-CT spectra (consistent with the structure of opal-CT). Our amorphous silica samples have not yet been sufficiently analyzed to determine the type of opal (opal-A, opal-C, or opal-CT). It is our initial understanding that sample 202 is opal-A and sample M-1 is opal-CT and, if this proves to be correct, our data would not be consistent with the previous authors' findings. The 475 cm^{-1} feature of 202 (opal-A) is at a higher wavenumber than that of M-1 (opal-CT), as indicated in Table 5; also, this feature is deeper for 202 (opal-A) than M-1 (opal-CT).

4.2. Variations in Silica Spectral Features in Chert and Amorphous Silica

It is obvious from our measured spectra that chert and amorphous silica may exhibit spectra with large differences in spectral character. Whereas this variation is predominantly in the details of the TIR spectrum, for the VNIR spectrum complete features may or may not be present. The variability in the VNIR spectra is mostly

between the spectra of different samples rather than within the spectra of the same sample. The spectra have a range of reflectivity values and may have large, deep features or no features at all. The possible features include the minimum at ~2.2 μm, from Si-OH bonds and possibly Al-OH, Mg-OH, and Fe-OH bonds, and the minima at ~1.4 and 1.9 μm from hydration. We observe that all the amorphous silica samples have spectra with hydration features, but we cannot distinguish an obvious correlation between the presence or absence of hydration features and other properties in the chert spectra. Features caused by other phases such as Fe-oxides, phyllosilicates, and carbonates are discussed in section 4.4 below.

In the TIR, we see several variations in spectral character between, and within, the spectra of our chert and amorphous silica samples. The ~540 cm^{-1} feature may be present or absent and can become shallower with greater surface roughness. The 475 cm^{-1} feature is always present but can be rounded, pointed, have a small superposed maximum, and differ between spectra of the same sample. The spectra of some opaline samples have a shoulder at ~1250 cm^{-1}, whereas others do not unless they are measured at a larger incidence angle or surface roughness. An interesting combination of opaline and chert features is observed in the spectra of sample 333, which has layers of chert and amorphous silica. Overall emissivity or spectral contrast is an obvious, yet not unexpected, variation we see between all the spectra. An extreme example of this is the spectrum of M-6, which appears to be a very shallow opaline spectrum. M-6 is a diatomite with a very low density, much like pumice; this may explain the low spectral contrast. Other spectral variations, such as the relative depths and shapes of the two minima in the quartz doublet have multiple potential origins that may be related to

inherent properties or physical conditions. We discuss these possible causes below in section 4.3.

4.3. Potential Causes of Thermal Infrared Spectral Variations

Though TIR spectra may vary in similar ways, the origin of this variation may be different, determined by the physical property that is changing. We give an overview of features, those of the quartz doublet in particular, that may vary for multiple reasons and then discuss these possible reasons in terms of the physical conditions that cause them.

A commonly observed variation in the TIR spectra is the relative depth of the minima in the quartz doublet. In most spectra the higher wavenumber minimum is initially shallower and undergoes greater changes in depth when physical factors are changed. The depth of these two minima relative to one another is different between the spectra of many of the samples and can also vary within the same sample when the spectra are collected at alternate incidence angles, or if the surface has a different roughness. Because the depth of these features can vary between the spectra of samples measured at approximately the same roughness and incidence angle, an inherent property such as grain size or the optical constants of the material likely causes the two minima to vary in depth and react differently to changes in physical properties.

The shapes of the two minima in the quartz doublet also vary between the spectra of different samples and within the spectra of the same sample. The minima may be wide and rounded, narrow and pointed, or somewhere in between. The high wavenumber side of the high wavenumber minimum appears to become deeper than the low wavenumber side with increasing incidence angle or surface roughness. Some spectra may have a new

maximum superposed on one of the minima, even though this is not seen in the other spectra from that sample. Because sample 699 is the only known chalcedony (fibrous silica) sample and has the most rounded minima, it could be interpreted that fibrous silica causes rounded minima; however, we cannot confirm this with one sample. None of our chert and amorphous silica spectra have the shape of these minima exhibited by coarsely crystalline quartz (e.g., Figure 1a).

The samples we measured at different orientations exhibit much smaller differences in TIR spectral character (Figure 8) than has been observed between the crystal axes [e.g., *Simon and McMahon*, 1953; *Spitzer and Kleinman*, 1961; *Wenrich and Christensen*, 1996]. We need independent information on whether any have a preferred grain orientation to know that we are analyzing that effect. The available petrography of samples C and 624 indicate that neither has a preferred orientation of grains; petrography is not available for samples 589 and 409 at this time. With our current knowledge we are able to determine that small variations in overall emissivity, shape of the ~475 cm^{-1} feature, and the relative depth of the minima in the quartz doublet, as seen in the C and 624 spectra, can result from different surfaces of the same sample that has no preferred orientation. The small differences may result from slight variations in factors such as surface roughness, incidence angle, porosity, and grain size. Further study will be needed to identify whether or not oriented quartz grains in chert affect the spectral features.

In the next three paragraphs we address the contribution of roughness to spectral character. The spectra of the rough and cut surfaces from the same sample may be significantly different in spectral shape. For two of the samples in this test, 810 and 9X, that difference is likely attributable to contamination from another phase, so we will not

consider them further in this discussion. For the remaining samples, we do not find a linear correlation between the R_a values and characteristics like relative depth of the quartz doublet minima or shape of the ~475 cm^{-1} feature for either the cut or rough surfaces (Figure 13). The only possible trend is in the shape of the two minima of the quartz doublet; the highest R_a value (roughest) corresponds to the rounded minima of 699, whereas the minima of the other samples are more pointed (but do not significantly vary in pointedness between themselves). The difference between the R_a values of the rough and cut surfaces of the samples does not correlate with the degree of change in overall emissivity or the depth of the higher wavenumber minimum relative to the lower wavenumber minimum of the quartz doublet.

We expect the increase in emissivity with increase in surface roughness observed for the spectral features in four of the six spectra because roughness should cause multiple surface reflections, potentially creating a cavity effect that traps incident photons (decreasing reflectivity), and allows for the emittance of more photons (increasing emissivity) [e.g., *Kirkland et al*., 2003; *Salisbury and Wald*, 1992; *Vincent and Hunt*, 1968]. The surfaces of sample 589 have the smallest difference between the roughness of the rough and cut surfaces of the six samples. This may be related to the reason why its rough surface spectrum is decreased slightly in emissivity compared to the cut surface spectrum. Because we do not have the data for the 613 rough surface, we cannot be sure why its supposedly rough surface has lower emissivity than its cut surface.

Each of the sets of cut and rough chert spectra exhibit a change in the relative depth of the two minima of the quartz doublet; the higher wavenumber minimum deepens relative to the lower wavenumber minimum. This trend has been observed previously in

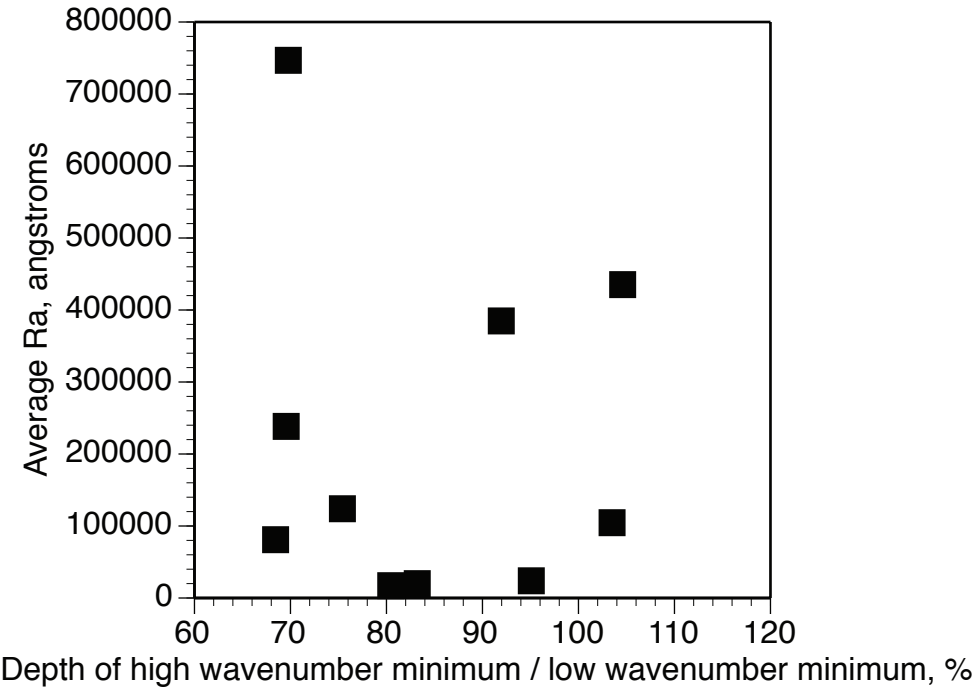

Figure 4.13: Scatter plot showing the lack of correlation between R_a values and the relative depth of the two minima of the quartz doublet. Both cut and rough surfaces are shown.

particulate quartz compared to solid quartz by *Salisbury and Wald* [1992]. They suggest that the change in relative depths of the doublet minima is from volume scattering, even at large particle sizes when grain asperities or clinging fines are present. We do not observe either grain asperities or clinging fines in the SEM images of our samples, however. If this behavior is a consequence of small amounts of volume scattering, another possibility is absorption through thin edges of the roughness on the surface [e.g., *Emslie and Aronson*, 1973].

The changes in spectral character with incidence angle (e.g., relative depth of the minima in the quartz doublet, minima shape, and presence of a shoulder in opaline spectra) that we have observed have also been observed by previous authors [*Almeida*, 1992; *Simon and McMahon*, 1953; *Tan*, 2002; *Tan and Arndt*, 2000; *Wald and Salisbury*, 1995; *Wang et al*., 2003]. Many of these authors have looked at the spectral at > 45º, which our study was limited to, and find that the trends seen up to 45º become increasingly apparent beyond that angle [e.g., *Almeida*, 1992; *Tan*, 2002; *Wang et al*., 2003]. For amorphous silica the introduction of a shoulder or minimum at ~1250 cm^{-1} has been attributed to the additional influence of the longitudinal optic (LO) mode to that of the transverse optic (TO) mode as observations deviate from nadir [*Almeida*, 1992; *Tan*, 2002; *Tan and Arndt*, 2000; *Wang et al*., 2003]. Long-range Coulomb forces in some materials cause the splitting into TO and LO modes [*Almeida*, 1992]. Vibrations caused by the TO mode are perpendicular to those caused by the LO mode. The effect of the TO mode is present at nadir and produces the large minimum in the opaline spectrum at ~1100 μm. The LO mode is excited along with the TO mode at oblique incidence angles and results in the shoulder or minimum at ~1250 μm in amorphous silica. It is

unclear if the change in relative depth of the quartz doublet minima in chert spectra could be caused by the same process. The angle between the optic axis of each quartz crystal and the detector is changing with incidence angle, so an effect of polarization such as this is a possibility. Another possibility is proposed by *Wald and Salisbury* [1995]. These authors detect this change in relative depth of the minima in the spectra of a solid quartz slab and cite the different dependence of the two minima on the optical constants as the reason why they are affected differently by increased incidence angle. Whatever the process, the trend of increasing depth of the higher wavenumber minimum relative to the lower wavenumber minimum with increasing incidence angle is clear.

4.4. Contribution of Other Phases to Chert and Amorphous Silica Spectra

Many of our chert and amorphous silica spectra include features of a phase other than silica. For a given sample these features may be seen in the TIR range, VNIR range, or both. Carbonate features are seen in both the TIR and VNIR spectra of samples 95 (chert), 613_banded (chert), and EST-1 (opal), shown in Figure 14. It appears that samples EST and 95 include calcite because their features at 886 cm^{-1} are closest to the calcite feature at 883 cm^{-1}, and sample 613 includes siderite because its feature at 867 cm^{-1} is closest to the siderite feature at 876 cm^{-1}; the feature at ~1530 – 1550 cm^{-1} is more obvious, but less definitive, because its shape and resulting minimum position changes with roughness [*Lane and Christensen*, 1997]. The minima in the VNIR spectra at 2.32 – 2.33 μm, and ~1.2 μm in 613, are also consistent with calcite (95, EST) and siderite (613) [e.g., *Gaffey*, 1987].

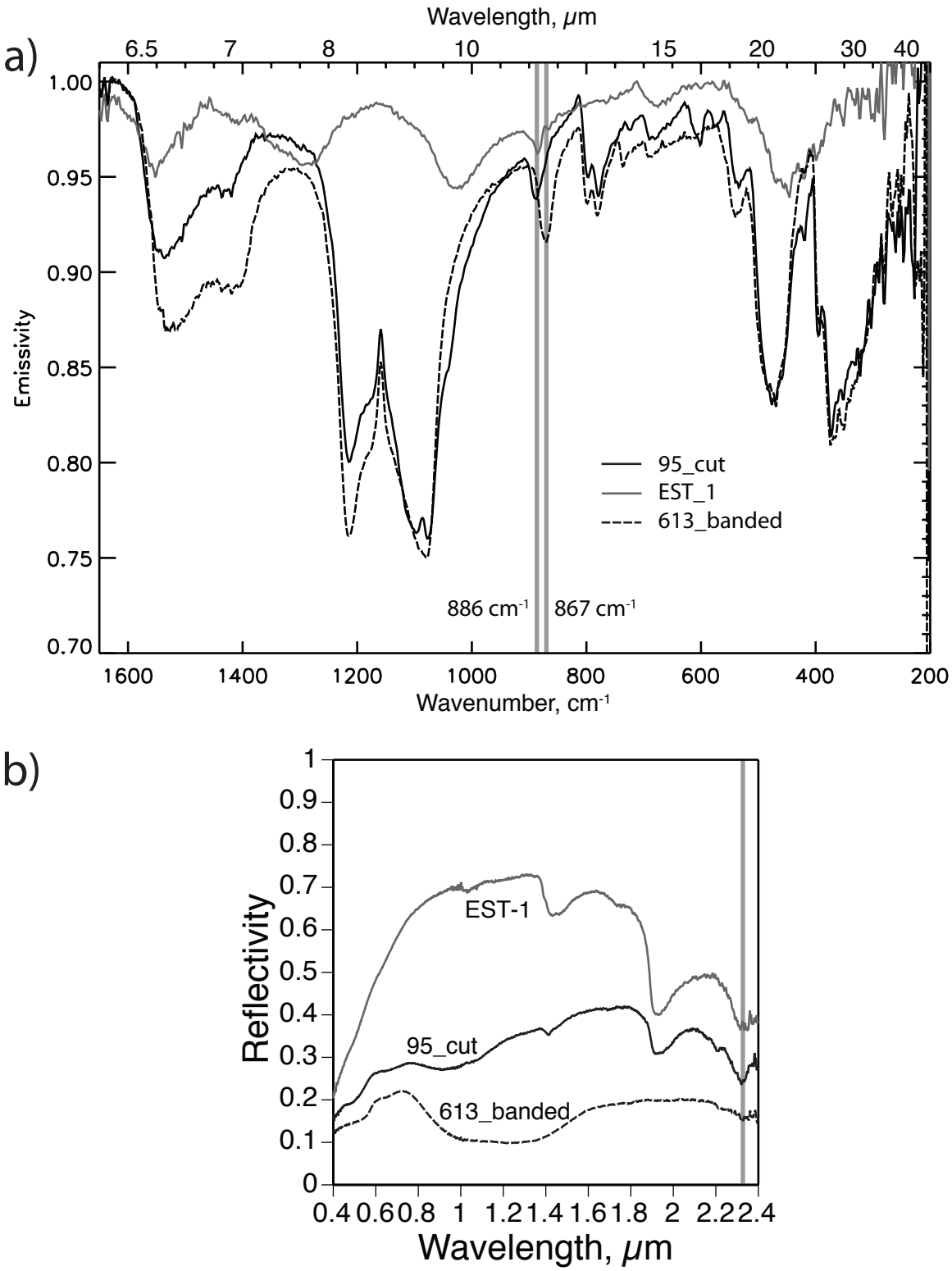

Figure 4.14: a) TIR spectra of the three study samples that have carbonate features, which are located at ~1540 and ~870 cm^{-1}. The grey lines illustrate the slight difference in position of the ~870 cm^{-1} feature between the samples. b) VNIR spectra of the same three samples. The grey line highlights the minima at 2.32 - 2.33 µm.

Some phases may only be apparent in one wavelength range, possibly because they are low in abundance or do not cause features in that range. For example, the narrow minima at ~2.2 μm in the VNIR spectrum of C and ~2.2 and ~2.35 μm in the VNIR spectrum of 624 (Figure 12) suggest the presence of phyllosilicates, specifically, montmorillonite (C) and illite (624). The TIR spectrum of C does not exhibit any noticeable phyllosilicate features, however. Only one spectrum of sample 624 (624-c) shows a doublet at ~550 and 475 cm^{-1} that could be attributed to illite; this surface is weathered and may have a greater abundance of phyllosilicate than the rest of the rock. Several of the VNIR spectra have features at short wavelengths that indicate the presence of an Fe-oxide like hematite (e.g., Figure 11c, d, f, g, j, k, q). None of the TIR spectra have hematite spectral features, however. It is likely that these phases (e.g., hematite, phyllosilicate) are present in low abundances that are apparent in VNIR spectra but may not be high enough to be apparent in TIR spectra. A few TIR spectra, like some of those from samples 9X and 810, have obvious contributions from other phases that change the spectral shape, but their VNIR spectra are not unique. We have not identified these phases, but we may deduce that they do not cause features in the VNIR range.

4.5. Interpreting Chert and Amorphous Silica Type or Origin from Spectral Characteristics

Determining the specific physical properties or environment of formation of a material from its spectrum would be very useful in remote sensing. This study has furthered our ability to do this and also made us aware of potential situations where we must interpret physical information from spectra cautiously.

The difference between the TIR spectrum of chert, or quartz in general, and amorphous silica is well known and obvious in high spectral resolution data (Figure 1a). Unfortunately, these two types of silica may exhibit similar features and are not as easily distinguished in VNIR data. However, it appears that most, if not all, amorphous silica spectra have hydration features, though not all spectra with hydration features are amorphous silica.

If a TIR spectrum has the characteristic doublet of quartz but with shallow slopes in the interior of the doublet and pointed minima, one could determine that the material is chert, or, more strictly, that it is made of quartz with a very fine grain or particle size (e.g., <40 – 50 μm). Also, our data indicate that chalcedony (fibrous quartz, e.g., 699) may have more rounded doublet minima than the pointed minima of microcrystalline quartz, which would help in differentiating the two.

If we consider only cherts, we notice that samples with similar origins, such as the epithermal vein-filling cherts C and 9X, have differences in their spectral character in both the VNIR (phyllosilicate features vs. small 1.4 μm feature, big 1.9 μm feature, and almost no 2.2 μm feature) and TIR (mainly in the shape of the high wavenumber minimum of the doublet) regions. Another example is the two hydrothermal precipitates, Memorial and White1. This suggests that a particular origin does not always produce chert or amorphous silica with a single spectral character. We also observe similarities in the spectral shape of cherts form different environments. The VNIR spectra of a replacement chert (810) and a speleothem (K-1100) are similarly flat, and those of a geyserite (699) and a Magadi chert (MC) have similarly large 1.4 and 1.9 μm hydration bands. Similarities occur between the shape and relative depth of the quartz doublet in

the TIR spectra of a silicified ash (624) and an epithermal vein-filling chert (C). We also see unexpected similarities in the amorphous silica spectra. A hydrothermal precipitate (White1) and an offshore opal-CT (M-1) both have VNIR spectra with rounded 1.4 and 1.9 μm bands and a negative slope at ~2.2 μm, and both have TIR spectra that lack an obvious minimum at ~1250 cm^{-1}, unless the surface is rough or at an oblique angle. This suggests that a particular spectral shape is not representative of a single environment of formation.

5. Summary and Conclusions

1) We have documented a wide variation in the detail of TIR spectral features of chert and amorphous silica, as well as in their VNIR spectral features. Some VNIR spectra may have no features at all. A single material may exhibit differences in spectral character, especially in the TIR region, because of changes in physical conditions. This large degree of variation in spectral character, both within one material and between multiple materials, complicates efforts to identify chert or amorphous silica spectra and distinguish between units. The spectra may be overlooked, misidentified, or misinterpreted. A broad spectral library is needed to aid in identification, and ancillary data indicating the physical characteristics of the material(s) would be helpful in determining if different spectra are from the same unit.

2) The spectrum of chert may contain features from other common ancillary phases, such as phyllosilicates, carbonates, and Fe-oxides. In the TIR region, phases with a very low abundance may not be apparent, although they may be observed in the VNIR region. In some cases, the VNIR spectrum may be dominated by the features of another

phase (e.g., phyllosilicate, carbonate) even though the material is dominantly quartz. Therefore, it is possible that a VNIR spectrum displaying phyllosilicate or carbonate features does not necessarily indicate a material entirely, or even predominantly, composed of that phase. In situations where either type of spectra may not convey all information, it may be particularly useful to analyze both TIR and VNIR spectra and use the different aspects of each wavelength range to their greatest advantage.

3) There does not appear to be a unique correlation between TIR or VNIR spectral shape and the geologic origin of a chert or amorphous silica material. Decidedly different environments of formation could result in a material with remarkably similar spectral characteristics. We also have shown that two chert or amorphous silica materials with similar origins do not necessarily have similar TIR or VNIR spectra.

4) Increased roughness of a chert or amorphous silica surface causes variation in overall emissivity, relative depth of the two minima of the quartz doublet, and the shoulder or minimum in opal at ~1250 cm^{-1}. These same variations also may be produced by increasing the incidence angle; therefore we may not be able to distinguish between the two processes from TIR spectra alone.

Future work will include collecting XRD and additional optical petrography of samples to determine the exact phases present (e.g., opal-A, opal-CT) and any orientation of grains; this will allow us to constrain multiple possibilities to explain results and to go further with our interpretations. Chapter Five takes the results presented here and uses them to help constrain the detection and identification of chert and amorphous silica on Mars.

Acknowledgements

We would like to thank J. Gillis-Davis for his assistance in measuring and calibrating the VNIR spectra. M. Osterloo provided very helpful discussion. We also appreciate grants from NASA's Planetary Geology and Geophysics, Mars Fundamental Research, and Mars Data Analysis programs.

CHAPTER 5

Visible to near-infrared and thermal infrared spectral properties of chert and amorphous silica 2: Application to Mars

ABSTRACT

New information about the thermal infrared (TIR) and visible to near-infrared (VNIR) spectral characteristics of chert and amorphous silica facilitate the detection, identification, and interpretation of silica-bearing phases on Mars. Silica phases are distinguishable from one another at the spectral resolution of TES but appear similar at the lower spectral resolution of THEMIS. The emissivity of THEMIS Band 9 relative to Band 8 can help to identify a material as dominantly quartz rather than amorphous silica or sulfate, in particular. Other non-silica phases do not have a spectral shape similar to the silica phases at THEMIS spectral resolution. We investigate the use of spectral indices to detect chert and amorphous silica in VNIR data and find that spectra having observable features at ~1.9, 2.2, or 2.3 μm may not necessarily have index values greater than those for common anhydrous igneous minerals. As a result, these spectra would not be distinguished from the spectra of a surrounding basaltic terrain using this method. Additionally, chert may not be detected in the VNIR range because its spectrum may lack any features. THEMIS ratio spectra and CRISM VNIR parameters for areas on Mars in northern Syrtis Major, western Hellas basin, and Eos Chasma, proposed to be silica-rich based on previous studies, are consistent with our analyses of chert or coarsely crystalline quartz and not consistent with sulfate.

1. Introduction

On a seemingly basalt-dominated planet such as Mars, the occurrence of silica-rich materials indicates uncommon processes, such as the exposure of evolved igneous rock, aqueous weathering and precipitation, and potentially biologic activity. Silica-rich materials have been identified or proposed in several sites on Mars. Using thermal infrared (TIR) data from the Mars Global Surveyor Thermal Emission Spectrometer (TES) and the Mars Odyssey Thermal Emission Imaging System (THEMIS), *Bandfield et al*. [2004] discovered a spectrally unique material near and on the central peaks of two impact craters in the Syrtis region. From their TES and THEMIS analyses, these authors conclude that the material is quartz-bearing. Using TES spectra they were able to isolate the spectral component that includes the high-silica material using TES spectra and found that it most closely resembles the spectra of granitoid rocks. A follow-up study by *Bandfield* [2006] has shown that areas with this granitoid lithology are present over a large region (~230 x 125 km). Another high-silica deposit was found by *Bandfield* [2008] in the western part of the Hellas basin. He used the position of the emissivity minimum at ~455 cm^{-1} in the isolated high-silica component spectrum to determine that amorphous silica, sheet silicate, zeolite, or volcanic glass is likely the dominant phase rather than quartz. *Hamilton et al*. [2006] studied a spectrally unique material in Eos Chasma with THEMIS data. A comparison between the spectra from the material of interest and quartz and amorphous silica phases showed that the materials of interest are consistent with these phases.

The Compact Reconnaissance Imaging Spectrometer for Mars (CRISM) [*Murchie et al*., 2007] on the Mars Reconnaissance Orbiter has identified silica-bearing materials

from visible to near-infrared (VNIR) spectra. *Ehlmann et al*. [2008] found areas with spectral features indicative of hydrated Si – OH phases in the vicinity of Syrtis Major and the Nili Fossae. One of these areas coincides with one of the craters where *Bandfield et al*. [2004] identified silica-rich material. Hydrated silica phases also have been observed from CRISM spectra by *Milliken et al*. [2008]. They found that the spectral features are most consistent with opaline silica for one type of spectrum and impact and/or volcanic glass for another type. These materials are scattered throughout the southern highlands and around the Valles Marineris.

The most clear-cut identification of amorphous silica material on Mars was made by the Mini-TES instrument on the Mars Exploration Rover (MER) *Spirit* in Gusev Crater [*Squyres et al*., 2008]. At the site designated Home Plate, the rover's instrument suite analyzed rocks and soil that are extremely high in silica (up to ~90 wt%). The Mini-TES spectra were key to demonstrating that the material is amorphous silica rather than crystalline.

Despite the studies previously conducted on the TIR and VNIR spectra of chert and amorphous silica [e.g., *Goryniuk et al*., 2004; *Graetsch et al*., 1994; *Michalski*, 2005; *Michalski et al*., 2003; *Rice et al*., 1995], there remains much to be learned. This begins with understanding the range of variations in TIR and VNIR spectral character and how physical conditions alter the spectra. We must know the extent of how a spectrum may appear to increase our ability to accurately detect and identify it. In a companion paper [*McDowell et al*., in preparation] (Chapter Four) we documented the large variations possible in the TIR and visible to near-infrared VNIR spectra of chert and amorphous silica resulting from inherent properties and conditions such as composition, incidence

angle, surface roughness, and orientation. Beyond variation in spectral character, it has not been determined if the TIR or VNIR spectral shape can relate information about the environment of formation for chert or amorphous silica. A comparison of spectra of siliceous materials with the same type of origin shows that these spectra may differ greatly. Spectra that are very similar may have different environments of formation. Even if we cannot directly connect a particular spectral shape to a particular environment, we do have examples of the potential environments that may correspond to the spectral shape being considered.

Whereas Chapter Four focuses on data gathered at laboratory resolution and the findings may be applicable to any planet, this paper is concerned with applications to Mars and we tailor our study to fit Martian data. It may still be applicable to other planets, given data with similar resolutions. This study aims to address three primary questions, which are extensions of the laboratory work reported in Chapter Four but are specific to the study of chert and amorphous silica in Martian data. 1) Are chert and amorphous silica TIR spectra distinguishable from one another and other phases at the spectral resolutions commonly used in Martian investigations? Resampling the laboratory data adds a more realistic component to the study that is necessary for this application. 2) Can chert and amorphous silica be identified by VNIR spectral indices on Mars? We compare indices of chert and amorphous silica spectra to the spectra of typical igneous phases to determine if this common method of mineral detection is useful when searching for chert and amorphous silica. 3) Does our new knowledge of chert and amorphous silica spectral characteristics enable us to confirm or constrain the mineralogy

previously determined for silica-rich materials on Mars? We apply our previous findings to the interpretation of these materials and consider possible environments of formation.

2. Methods

2.1. Effects of Resolution on Thermal Infrared Spectral Features

To apply our newly acquired knowledge of chert and amorphous silica spectral characteristics to spectral data from sites of silica-rich materials on Mars, we must first determine if these characteristics are observable at the lower spectral resolution of the Martian data. We convolve each TIR spectrum from our samples to the spectral resolution and commonly used wavelength ranges of TES [*Christensen et al*., 2001] and THEMIS [*Christensen et al*., 2004]. TES produces hyperspectral data with a resolution of 20 cm^{-1}. The full range of TES is ~1600 – 200 cm^{-1}, but in most cases we show the range of 1301 – 233 cm^{-1} (~8 – 43 μm), excluding the range between 825 and 508 cm^{-1} obscured by the features of CO_2 in the Martian atmosphere, because it is the most commonly used. THEMIS produces multispectral data; it has 9 surface-sensing bands at 8 wavelengths between 1474 – 795 cm^{-1} (6.78 and 12.57 μm). The small number of bands in a THEMIS spectrum limits the information it can convey. We therefore compare the convolved spectral shape to the shape at laboratory resolution to determine if there are specific characteristics of a chert or amorphous silica spectrum that results in a characteristic shape at THEMIS resolution. Additionally, we investigate other phases that may have spectral shapes similar to chert and amorphous silica at THEMIS resolution, along with those of phases that are considered to be high in silica or

amorphous but have different spectral shapes than chert and amorphous silica. We do not consider the effects of signal to noise when analyzing the spectra at these resolutions.

2.2. Visible to Near-infrared Spectral Indices

Spectral band indices or parameters are used in many VNIR studies as a first order identification tool. Indices may be calculated in different ways, but calculations of band indices generally involve reflectivity values from one or more points in the region of a diagnostic reflectance minimum and two or more points on either side of this feature. Commonly, the value of the central point(s) is divided by the sum or average of the values of the side points and then subtracted from one, so that a flat line would have an index value of zero, a minimum would have a positive value, and a maximum would have a negative value [e.g., *Loizeau et al*., 2007; *Pelkey et al*., 2007]. It is possible for more than one phase to have a reflectivity minimum at the same or similar position, and therefore multiple indices are commonly used together and/or the whole spectrum is manually inspected to make a final identification. We use the spectral parameters developed by previous authors [*Loizeau et al*., 2007; *Pelkey et al*., 2007; *Poulet et al*., 2007] to determine if these indices, used to highlight hydrated and phyllosilicate phases in Martian VNIR spectra, would distinguish the chert and amorphous silica spectra of our study from the spectra of common igneous phases (e.g., olivine, orthopyroxene, clinopyroxene, and plagioclase). We resample all spectra to the resolution of targeted CRISM data (544 channels between 0.362 and 3.92 μm [*Murchie et al*., 2007], Figure 1) to better facilitate comparison with Martian observations.

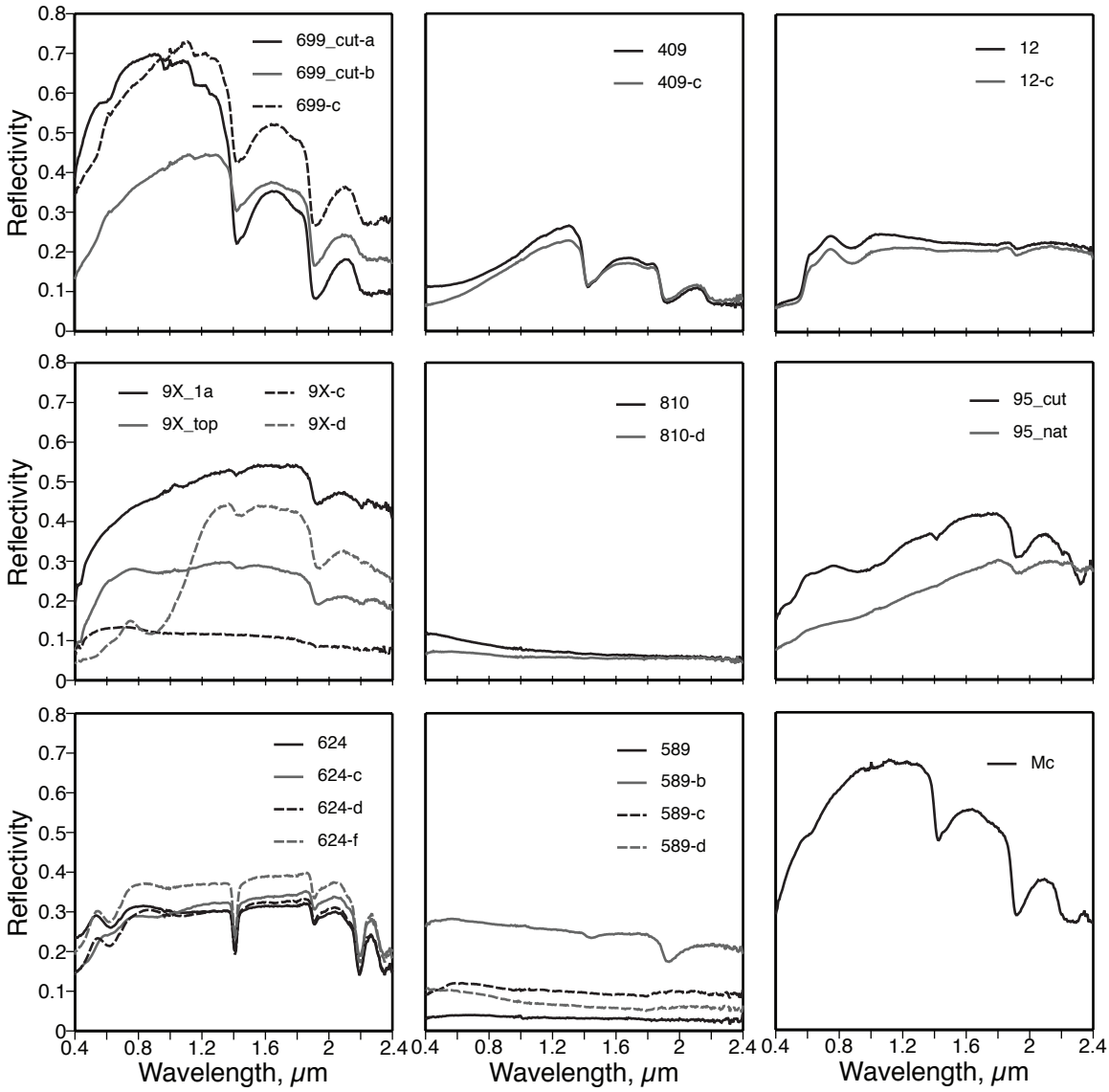

Figure 5.1: Visible to near-infrared reflectivity spectra of chert and amorphous silica resampled to CRISM resolution. Multiple spectra in one plot are of different surfaces or sides of the same sample.

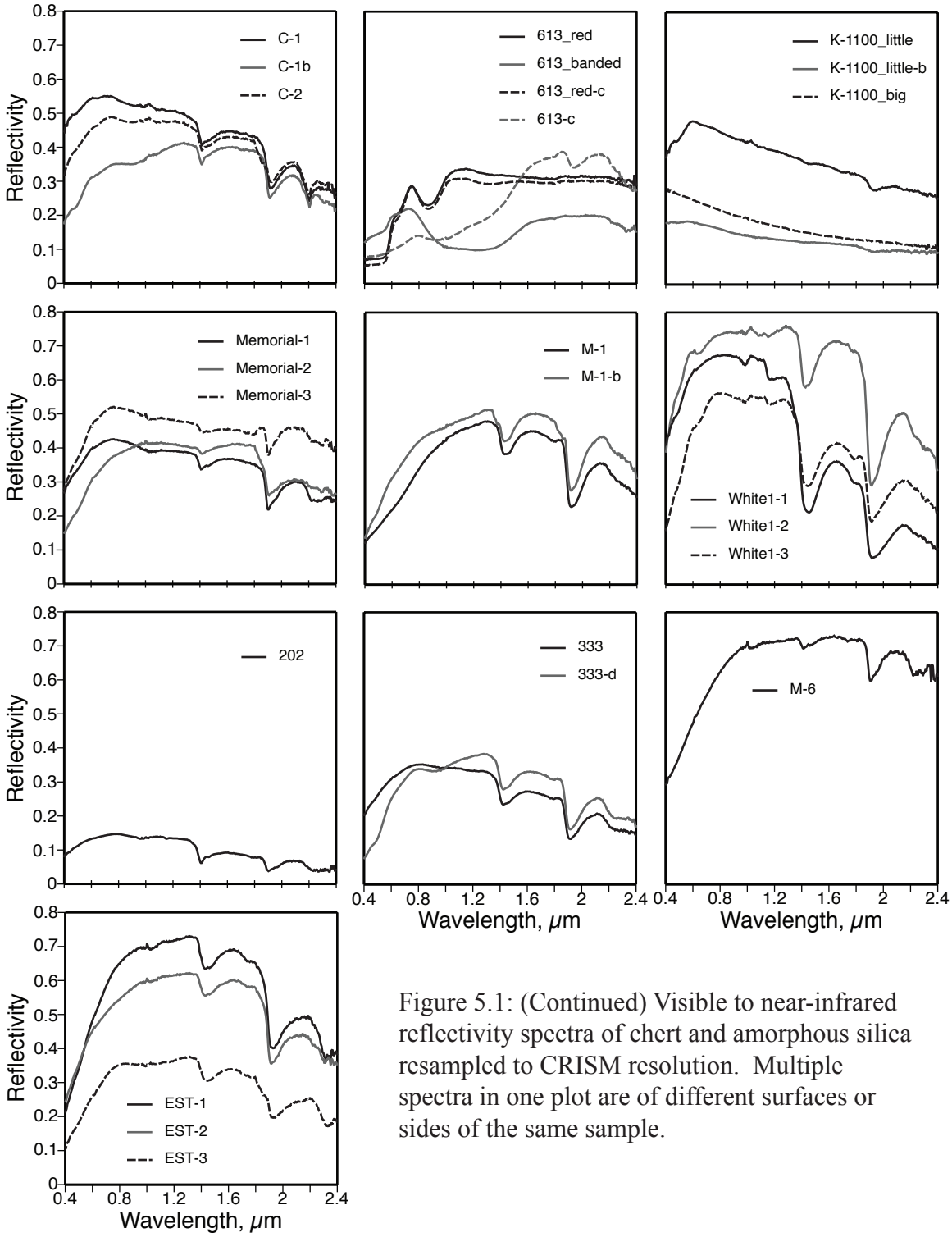

Figure 5.1: (Continued) Visible to near-infrared reflectivity spectra of chert and amorphous silica resampled to CRISM resolution. Multiple spectra in one plot are of different surfaces or sides of the same sample.

Pelkey et al. [2007] determined an index (BD1900) for the band depth at ~1.9 μm, indicative of the presence of water. They also created indices for bands at ~2.21 μm (BD2210) and ~2.29 μm (BD2290), which are designed to detect Al-OH and Mg,Fe-OH minerals (e.g., montmorillonite and nontronite), respectively. *Loizeau et al*. [2007] also developed indices for these same three features, though the band centers and wavelengths used in their calculations are at slightly different wavelengths than those of *Pelkey et al*. [2007] (e.g., 1.93 μm rather than 1.9 μm, 2.2 μm rather than 2.21 μm, and 2.3 μm rather than 2.29 μm). A third 1.9 μm band index was designed by *Poulet et al*. [2007]. The wavelengths and calculation used are also slightly different from those mentioned above, though they all were made to locate water-bearing minerals. The equations for the indices from these studies are listed in Table 1, and Figure 2 illustrates the relative positions of these wavelengths on example spectra.

We compare the value of each index calculated for our chert and amorphous silica spectra with the same index values of four common anhydrous igneous minerals that might be observed on Mars. We use the following seven spectra from the CRISM spectral library [*Bishop et al*., 2006]: two olivines (C1PO06 & C1PO76), one orthopyroxene (CASB51), two clinopyroxenes (C1PP18 & C1PP42), and two plagioclase feldspars (CAPL29 & CAPL43). The range of index values calculated for the four igneous minerals are listed in Table 2. Though all positive index values are potential detections of minima, we are interested in the values that would be distinguished above (i.e., be greater than) the values of the igneous spectra.

This approach to determine the detectability of chert or amorphous silica assumed it is located in a region of otherwise igneous composition. Though the exercise of

Table 5.1: VNIR spectral indices used in this study.

Reference	Name	Formulation*†	Created for
Pelkey et al., 2007	BD1900	1-(((R1.93 + R1.985)*0.5)/(a*R1.857 + b*R2.067))	H_2O
	BD2210	1-(R2.21/(a*R2.14 + b*R2.25))	Al-OH
	BD2290	1-(R2.29/(a*R2.25 + b*R2.35))	Mg,Fe-OH
Loizeau et al., 2007	1.93 µm	1-((R1.93 + R1.94)/(R1.80 + R2.12))	H_2O
	2.20 µm	1-((R2.19 + R2.20)/(R2.15 + R2.27))	Al-OH
	2.30 µm	1-(R2.30/(0.25*R2.26 + 0.25*R2.27 + 0.5*R2.34))	Mg,Fe-OH
Poulet et al., 2007	1.9 µm	1-((0.5*R1.93 + 0.5*R1.94)/(0.5*R1.83 + 0.5*R2.12))	H_2O

*R is reflectance at the given wavelength in µm.

†The letter a = 1-b, b = $(\lambda_c-\lambda_s)/(\lambda_l-\lambda_s)$, c = the central wavelength, s = the shorter wavelength, and l = the longer wavelength.

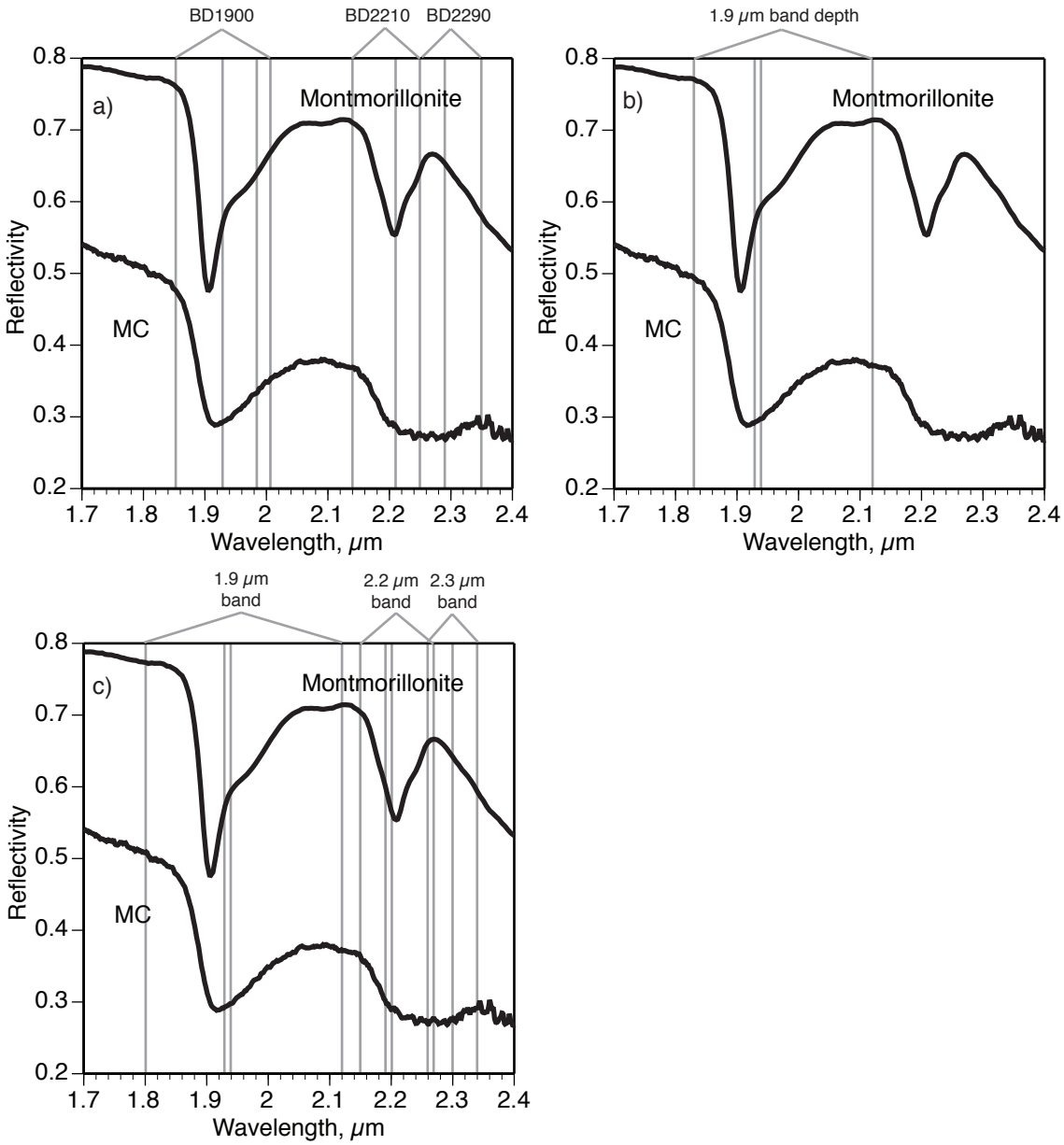

Figure 5.2: Spectral plots illustrating the placement of the bands used to calculate the indices of a) Pelkey et al., 2007, b) Poulet et al., 2007, and c) Loizeau et al., 2007.

Table 5.2: Range of index values for the common igneous minerals described in the text.

Index	Lowest value of igneous phases	Highest value of igneous phase
BD1900 (*Pelkey et al.,* 2007)	-0.015	0.052
1.9 µm (*Poulet et al.,* 2007)	-0.033	0.107
1.93 µm (*Loizeau et al.,* 2007)	0.036	0.110
BD2210 (*Pelkey et al.,* 2007)	-0.012	0.042
2.2 µm (*Loizeau et al.,* 2007)	-0.001	0.100
BD2290 (*Pelkey et al.,* 2007)	-0.004	0.037
2.3 µm (*Loizeau et al.,* 2007)	-0.007	0.027

applying these indices to our spectra is an ideal case because our data are dominated by a single phase, it will help us to understand if the spectra of our samples would have parameter values that stand out relative to other phases that are common on Mars, and therefore would allow for the identification of the chert and amorphous silica samples.

2.3. Application to Silica-rich Sites on Mars

We examine three areas on Mars where silica-rich materials have been proposed for spectral characteristics consistent with chert or amorphous silica. These three sites are the quartzofeldspathic material in Syrtis analyzed by *Bandfield et al*. [2004] and *Bandfield* [2006], the high-silica material in western Hellas identified by *Bandfield* [2008], and the candidate high-silica material in Eos Chasma discussed by *Hamilton et al*. [2006]. We consider both TIR and VNIR data.

Because these sites are small, their TIR character is best observed in high spatial resolution THEMIS infrared images. To highlight the materials of interest in the images we use a decorrelation stretch (DCS). This type of stretch applies a principal components (PC) transformation to three user-specified bands, redefining the axes in the way that maximizes variation and removes correlated information between the bands, and then inverses this transformation to display the three user-defined bands as red, green, and blue in a false-color image [*Gillespie et al*., 1986]. To evaluate the spectral shapes of these materials, we average as many pixels as possible covering the spectrally unique area to provide one THEMIS spectrum representing that site. We determine the ratio of this spectrum to the average spectrum of a spectrally bland area of the image to remove the common atmospheric component and isolate the spectral shape that is different

between the two spots [e.g., *Ruff and Christensen*, 2002]. We compare this ratio spectrum from our Martian regions of interest to the spectra of our chert and amorphous silica samples at the same resolution.

We use targeted CRISM images to assess the character of these three silica-rich sites in the VNIR. Summary parameter composite images are false color images in which three different parameters are represented by red, green, and blue. The summary parameter composite images we are particularly interested in are MAF, HYD, and PHY because they describe the igneous, hydrated, and phyllosilicate mineralogy, respectively. The specific parameters that compose these summary parameter composite images are listed in Table 3 and are described in detail by *Pelkey et al*. [2007]. We compare these parameters for each image to what might be expected for chert and amorphous silica based on our knowledge of their VNIR spectra. Additionally, we process the CRISM image from each site, conducting photometric and atmospheric corrections using the CRISM Analysis Tool (CAT) for ENVI. From the corrected images we produce an average spectrum for the silica-rich area and ratio it with an average spectrum from the nearby plains to determine the character of the compositional difference between the two.

We also compare our data with those of one other Martian site, the high-silica deposit discovered by the Spirit rover at Home Plate [*Squyres et al*., 2008]. Because this area is so small that it cannot be distinguished in THEMIS or CRISM images, we use a Mini-TES spectrum of the Clara_Zaph4 target from *Squyres et al*. [2008]. Mini-TES spectra have spectral resolution equivalent to that of TES spectra but a narrower atmospheric CO_2 band. We convolve the Mini-TES spectrum to the lower resolution of THEMIS to compare it to our chert and amorphous silica spectra at that resolution in the

Table 5.3: Parameters combined for each summary parameter composite image. Refer to *Pelkey et al.* [2007] for parameter calculations.

Summary Parameter	Red	Designed for:	Green	Designed for:	Blue	Designed for:
MAF	OLINDEX	Olivine	LCPINDEX	Low calcium pyroxene	HCPINDEX	High calcium pyroxene
HYD	SINDEX	Sulfate	BD2100	Sulfate	BD1900	Hydrated minerals
PHY	D2300	Minerals containing Fe/Mg-OH	BD2210	Al-Phyllosilicate, hydrated silica	BD1900	Hydrated Minerals

same way we do for the other Martian sites. Understanding the spectral characteristics of this high-silica deposit at THEMIS resolution in addition to Mini-TES/TES resolution will be helpful for future studies that look for this mineralogy elsewhere on the planet.

3. Results

3.1. Effect of Resolution on Thermal Infrared Spectral Features

The chert and amorphous silica spectra at 20 cm^{-1} (TES and Mini-TES) spectral resolution (Figure 3) look very similar to those at laboratory resolution (compare to Figure 6 from Chapter Four). Because data from 825 – 508 cm^{-1} are obscured in spectra collected from Martian orbit, we cannot observe the quartz and amorphous silica features at ~780 cm^{-1}, ~675 cm^{-1}, and ~540 cm^{-1}. All other features are observed, including the minimum at ~870 cm^{-1} in samples containing carbonate. Mini-TES spectra require a smaller portion of the spectrum near the CO_2 feature to be removed (~560 – 780 cm^{-1}); this allows for part of the ~780 cm^{-1} and ~540 cm^{-1} features to be observed in those spectra (not shown). The lower spectral resolution of TES and Mini-TES, compared to the laboratory resolution, causes the minima and maxima in the spectra to be slightly less narrow and sharp, resulting in lower spectral contrast and slightly more rounded features. One specific difference is the doublet at ~400 – 350 cm^{-1}, which appears to devolve into one minimum at 20 cm^{-1} resolution rather than two minima in the spectra of six of the samples (Figure 3c, d, h, j, k, l).

Resampled to the 1 μm wide band passes of THEMIS, the spectra of our samples (Figure 4) cover only the range from ~1500 – 795 cm^{-1} and are noticeably different than at laboratory resolution. The lower spectral resolution results in lower spectral contrast

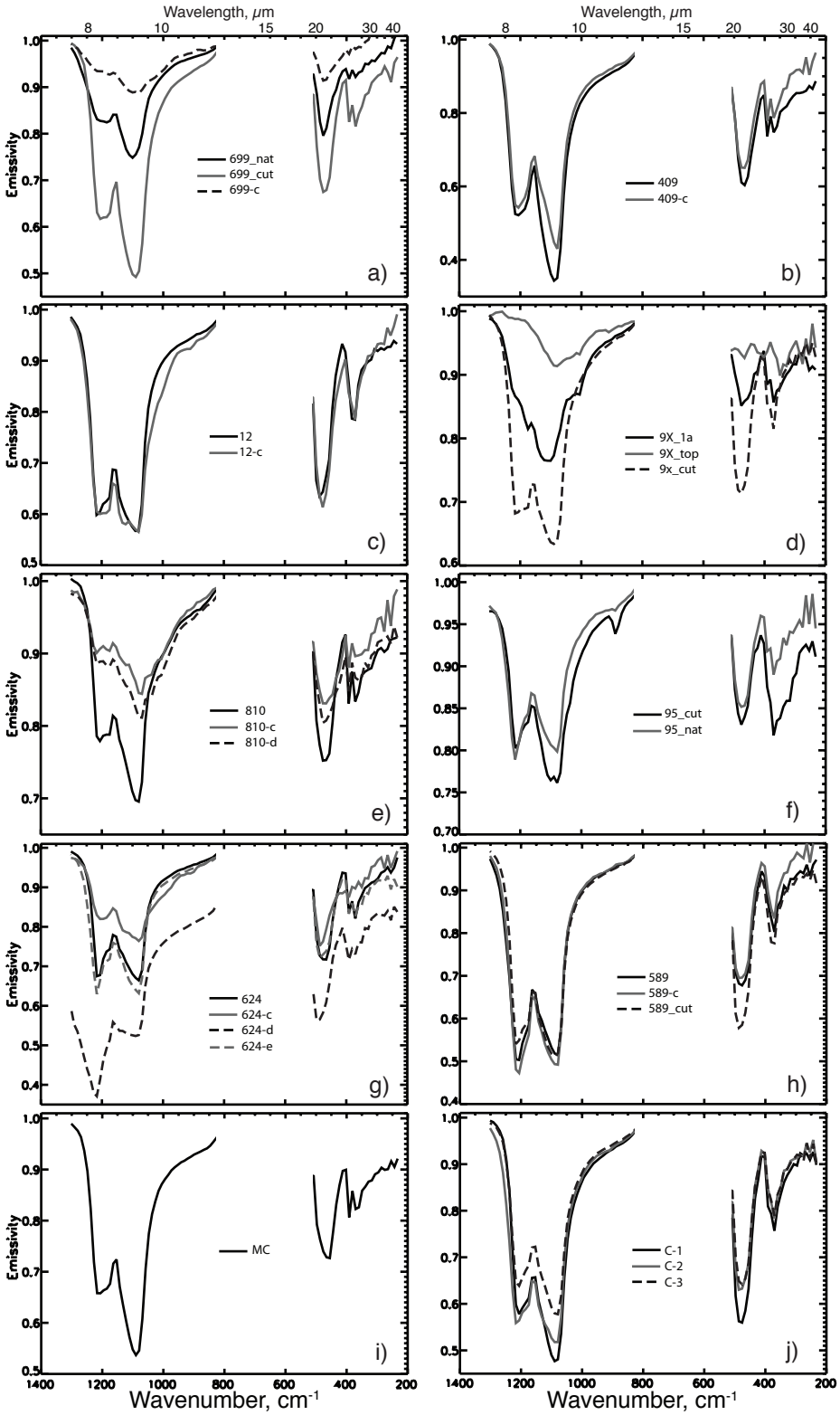

Figure 5.3: Spectra of the chert and amorphous silica samples at 20 cm^{-1} (TES) resolution. Note that the range of the y-axis may differ between plots. The region of the Martian CO_2 feature has been removed (825 - 508 cm^{-1}).

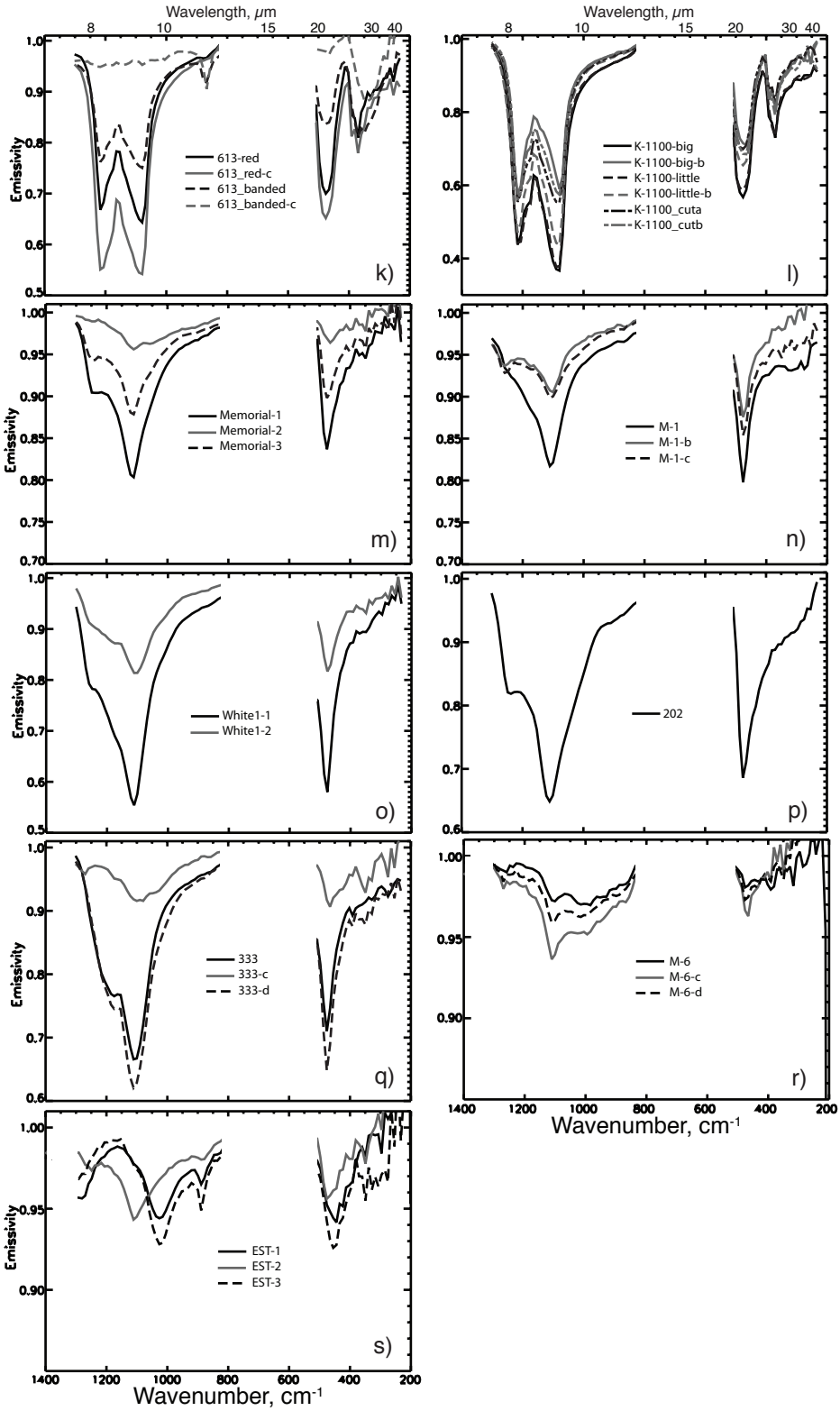

Figure 5.3: (Continued) Spectra of the chert and amorphous silica samples at 20 cm^{-1} (TES) resolution. Note that the range of the y-axis may differ between plots. The region of the Martian CO_2 feature has been removed (825 - 508 cm^{-1}).

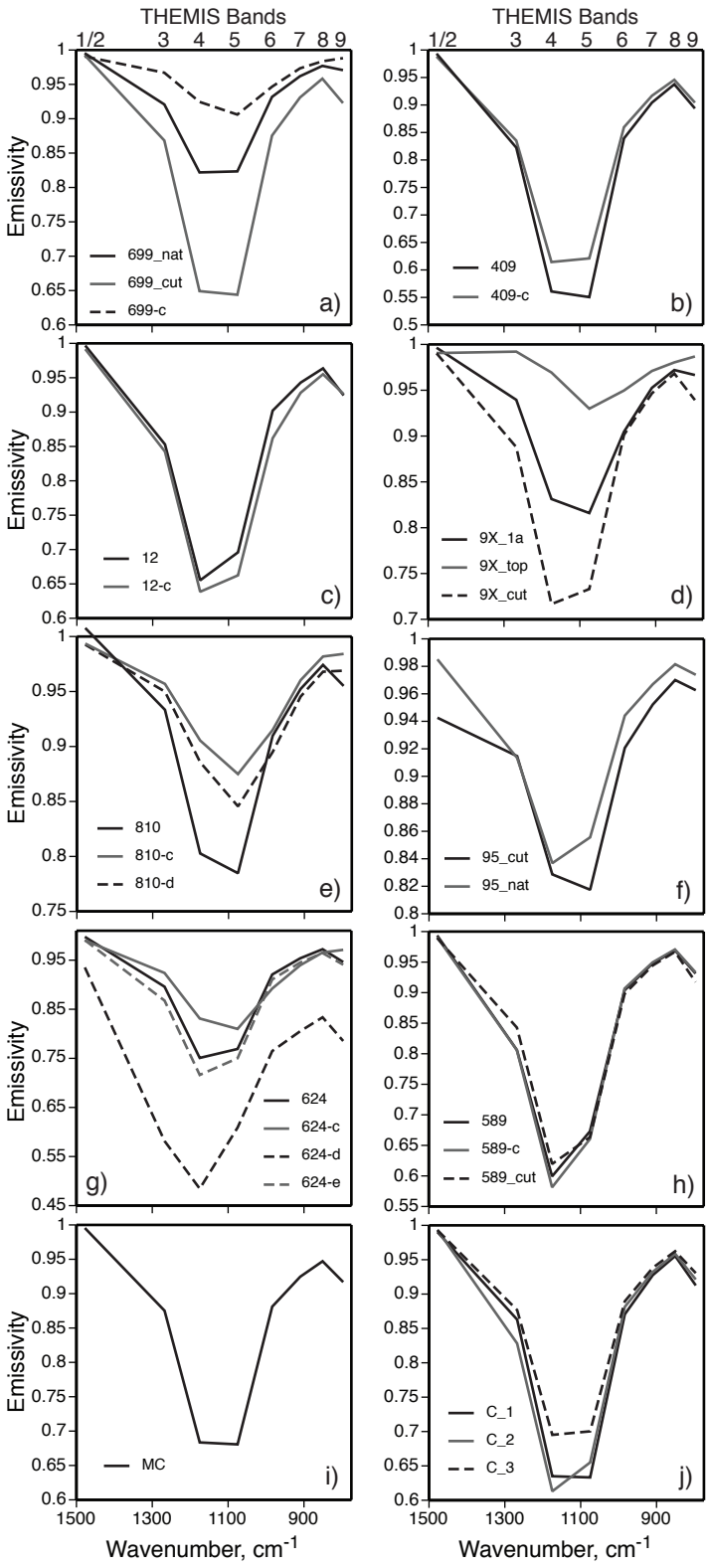

Figure 5.4: Spectra of the chert and amorphous silica samples at the resolution of THEMIS. Note that the range of the y-axis may differ between plots.

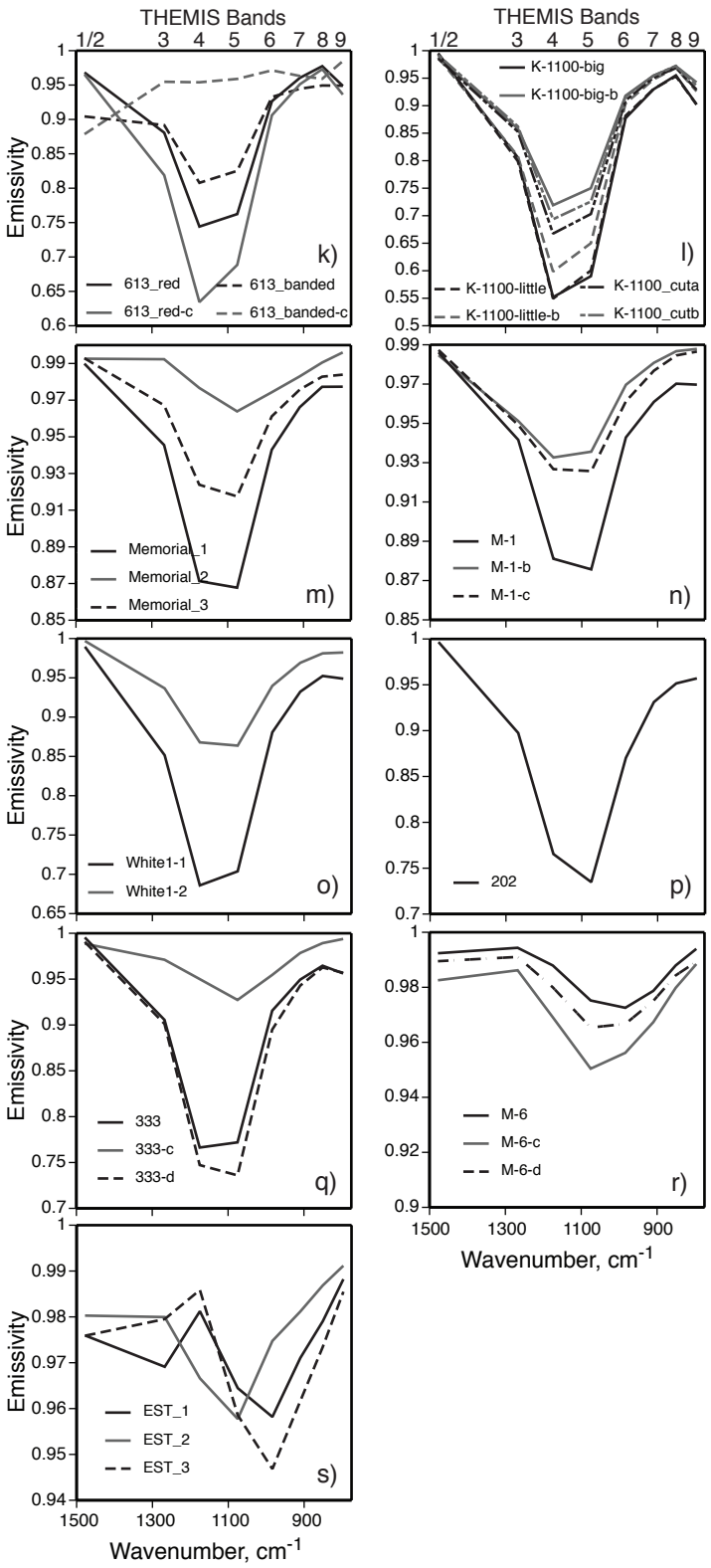

Figure 5.4: (Continued) Spectra of the chert and amorphous silica samples at the resolution of THEMIS. Note that the range of the y-axis may differ between plots.

and very broad features. At this resolution, all of our chert and amorphous silica spectra have the lowest emissivity in Bands 4 and 5 (1168 and 1069 cm^{-1}, respectively). The only exceptions are samples EST and M-6 (Figure 4r,s), which also have shapes not obviously attributable to silica even at laboratory resolution. It might be expected that the relative depths of Bands 4 and 5 correlate with the relative depths of the left and right minima, respectively, in the quartz doublet. However, certain spectral characteristics, such as an overall amorphous or quartz shape, the relative depth of the features of the large quartz doublet, the interior angle of this doublet, and the presence and position of a shoulder on the large amorphous silica feature, do not consistently result in a specific shape at THEMIS resolution. Only the feature at 780 cm^{-1} in the full resolution spectra can be consistently linked to a feature observable at the resolution of THEMIS – a minimum in Band 9 (795 cm^{-1}).

Reduced spectral resolution may result in shapes that could resemble those of other phases with similar overall spectral character. Chert and amorphous silica spectra may be indistinguishable from the spectra of other phases at THEMIS resolution, even though they are distinguishable at higher spectral resolution (Figure 5a-b). The spectra of some phases, specifically sulfate phases and other silica phases (Figure 5c), have spectral shapes similar to the chert and amorphous silica samples in our study at the resolution of THEMIS. In some cases a sulfate may be differentiated from chert by the lack of a decrease in Band 9, which may be present in chert spectra. A collection of spectra from other amorphous phases and phases considered to be high in silica (Figure 5d) shows different spectral shapes from those of our chert and amorphous silica samples at

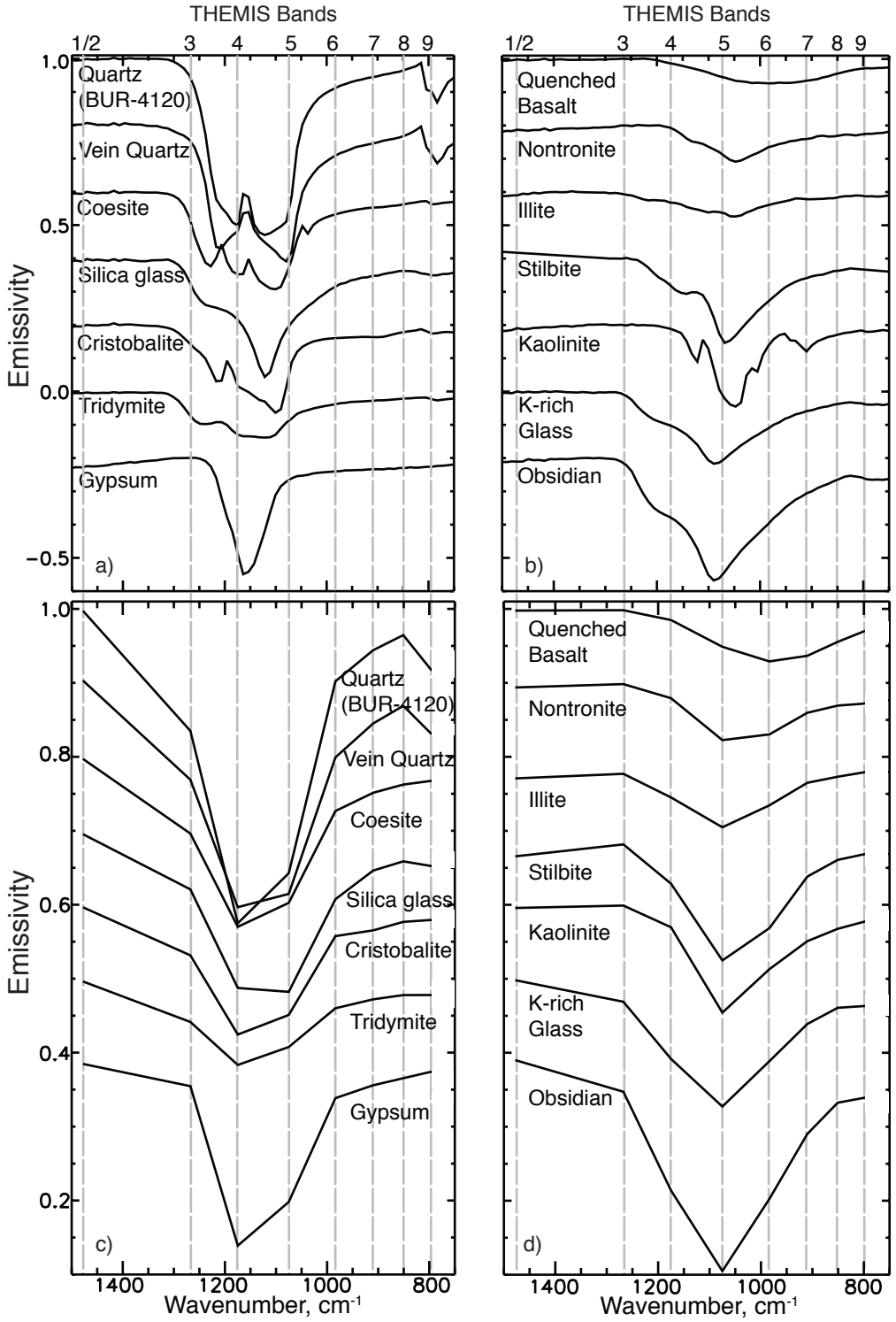

Figure 5.5: Spectra of other high silica and amorphous phases that are similar to (a & c) and different from (b & d) chert and amorphous silica at the resolution of THEMIS. In plots a) and b) the spectra are at 20 cm^{-1} resolution, illustrating that they can be differentiated from one another. In plots c) and d) the spectra are at the resolution of THEMIS and have shapes more difficult to differentiate.

THEMIS resolution. The major difference is that the lowest emissivity of their spectra is not in Bands 4 and 5.

3.2. Visible to Near-infrared Spectral Indices

Our calculated index values of 1.9 μm band depths, indicative of hydration, are shown in Figure 6. The BD1900 parameter from *Pelkey et al*. [2007] has values ranging from -0.080 to 0.612 for our chert and amorphous silica samples, which includes the range of the igneous mineral spectra (Table 2). One spectrum (12) with a noticeable 1.9 μm minimum has a BD1900 value less than those of the anhydrous igneous phases (i.e., less than 0.052). *Poulet et al*. [2007] use another spectral index to determine 1.9 μm band depth; values of their index calculated from the spectra of our samples range from -0.038 to 0.651. Using the hydrous mineral index from *Loizeau et al*. [2007], we find values of -0.056 to 0.655 for our samples' spectra. As with the 1.9 μm parameter from *Pelkey et al*. [2007], both these parameters result in values from the spectra of silica samples with a 1.9 μm feature that fall in the range for the igneous minerals (e.g., spectra 624, 624-c, 624-d, 624-f, 12, 12-c, 95_nat, and 613-c).

Pelkey et al. [2007] also have parameters, BD2210 and BD2290, that describe the band depths of features at ~2.21 (designed for Al-OH minerals such as montmorillonite) and ~2.29 μm (designed for Mg,Fe-OH minerals such as nontronite), respectively. We calculate BD2210 values of -0.114 to 0.337 and BD2290 values of -0.164 to 0.094 for the spectra of our samples (Figure 6). The spectra of some samples have observable minima close to 2.21 or 2.29 μm, but their BD2210 or BD2290 values are in the same range as the igneous minerals (Table 2). For example, spectra 9X-1a, M-6, and Memorial-3

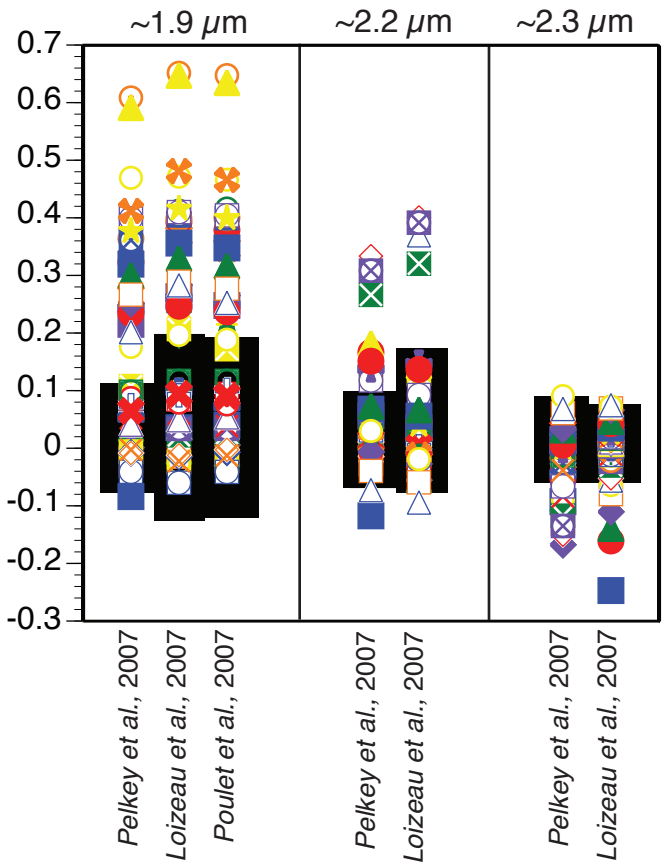

Figure 5.6: Index values calculated for chert and amorphous silica spectra (symbols). Black boxes indicate the range of index values of the common igneous minerals described in the text (see also Table 2).

appear to have features at ~2.2 μm but do not have index values above 0.042; spectra 95_nat and 613_banded have obvious minima at ~2.3 μm but are not distinguished from the igneous phases (i.e., have values below 0.037).

Loizeau et al. [2007] also have calculated indices to identify Al-OH smectites and Fe-OH/Mg-OH smectites based on their 2.2 μm and 2.3 μm features, respectively. The spectra of our samples have values of -0.091 to 0.405 for the 2.2 μm index and -0.244 to 0.078 for the 2.3 μm index (Figure 6). Like the indices previously discussed, some spectra with features at ~2.2 (MC, Memorial-1, M-6, 699-c, 202) or 2.3 μm (613_banded) have index values in the same range as common igneous materials, which do not have minima at these wavelengths (Table 2).

3.3. Application to Silica-rich Sites on Mars

Our analyses of three of the proposed Martian high-silica sites with THEMIS data are presented in Figure 7. Silica-bearing materials appear as a yellow or orange color in each image using this stretch. The ratio of the average silica-bearing spectrum to a regional silica-poor spectrum is plotted below each image. Figure 8 shows a HiRISE image of Home Plate in Gusev crater, along with an image of the target Clara Zaph4 and its Mini-TES spectrum at native (20 cm^{-1}) and THEMIS resolutions.

All the THEMIS spectra of silica-bearing materials (Figures 7 and 8) have their lowest emissivity in Bands 4 and 5, yielding the same overall shape as the spectra from our laboratory samples at comparable resolution. The ratio spectra have a decreased emissivity in Band 9 relative to Band 8, as well. Also plotted in Figures 7 and 8 are the spectra from our study that most closely match the ratio spectrum of each silica-bearing

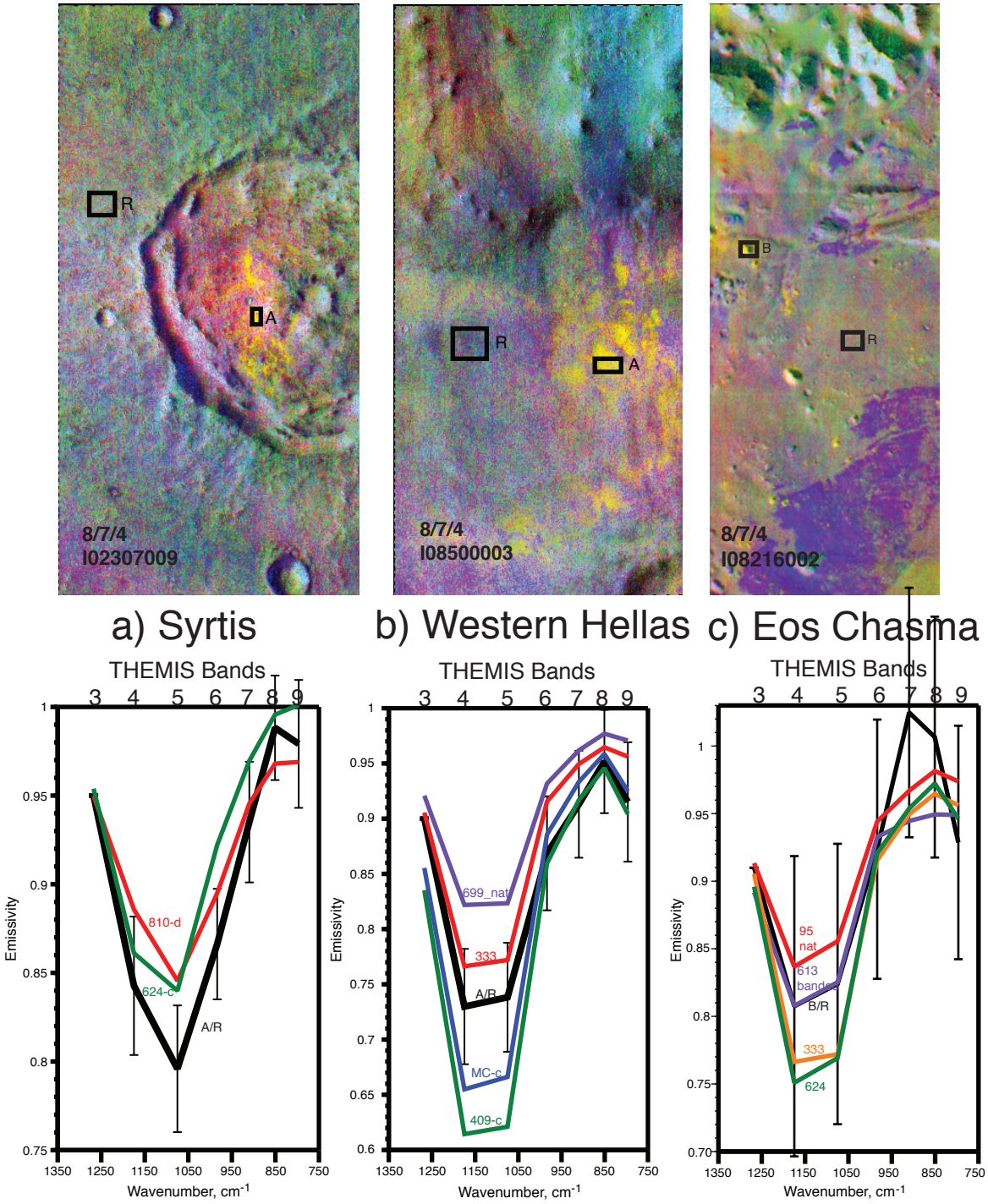

Figure 5.7: THEMIS DCS images of our Martian study sites. THEMIS bands 8, 7, and 4 are displayed as red, green, and blue. Black boxes indicate the pixels averaged to produce the spectra used to make the ratio. This ratio spectrum is plotted below each image, along with the most similarly-shaped spectra from the chert and amorphous silica samples in our study at THEMIS resolution. The contrast of the ratio spectra have been enhanced, and error bars represent one standard deviation.

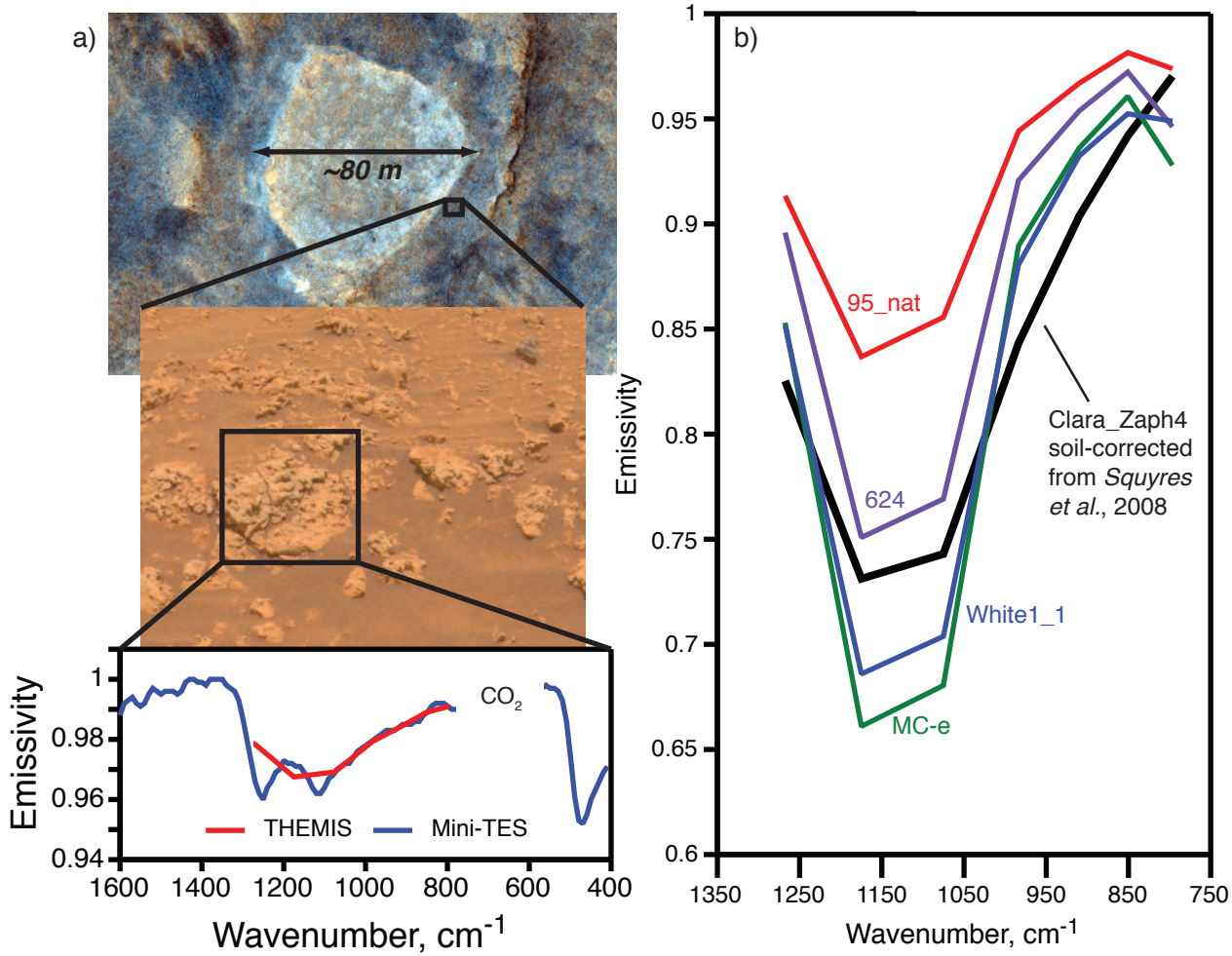

Figure 5.8: a) Subset of HiRISE image PSP_005456 showing Home Plate in Gusev crater (top) and a Pancam image from the Spirit rover showing the target Clara_Zaph4 (middle), alongwith a plot of the Mini-TES spectrum at its original spectral resolution and the degraded resolution of THEMIS (bottom). b) A plot of the Clara_Zaph4 spectrum at THEMIS resolution and the spectra from our study that are most similar in shape.

deposit at THEMIS resolution. Figure 9 shows these most closely matching spectra at THEMIS resolution and the corresponding spectra at full laboratory resolution. Note that the spectra at laboratory resolution may greatly differ in shape.

The Mini-TES spectrum of the silica-rich material in Gusev crater (Figure 8) has minima at ~1250 cm^{-1}, ~1115 cm^{-1}, and ~475 cm^{-1}. The positions of these minima are similar to those of the opaline phases from our study. The feature at ~1250 cm^{-1} is like that feature present in the spectra of many of our opaline samples (e.g., Figure 3m, n).

A targeted CRISM observation was available in each of the three silica-rich sites. For all three sites we searched for variation in the MAF, HYD, PHY images, presented in Figure 10. The image used in the northern Syrtis Major region is located in the same crater where the ratio of THEMIS data was done (i.e., south crater of *Bandfield* [2006]). The MAF image (Figure 10a) has a large amount of variation, going from green to blue to purple, indicating a varying igneous composition of low-calcium pyroxene, high-calcium pyroxene, and mixtures of high-calcium pyroxene with olivine. The HYD image is predominantly red with a small area of blue spots in the upper left corner (Figure 10a) that correspond to silica-bearing materials as indicated by the THEMIS DCS image (compare with Figure 7a). This same area is light blue in the otherwise scattered green and red PHY image. Other targeted images are available over the region of interest slightly to the north in this same crater, but they do not show corresponding variations in any of the summary parameter composite images. The ratio spectrum has a positive slope between 0.4 and 0.9 μm and minima at ~1.9 and ~2.2 μm (Figure 11).

The MAF summary parameter composite image for the site on the western edge of the Hellas basin shows that the area is dominated by low-calcium pyroxene (green)

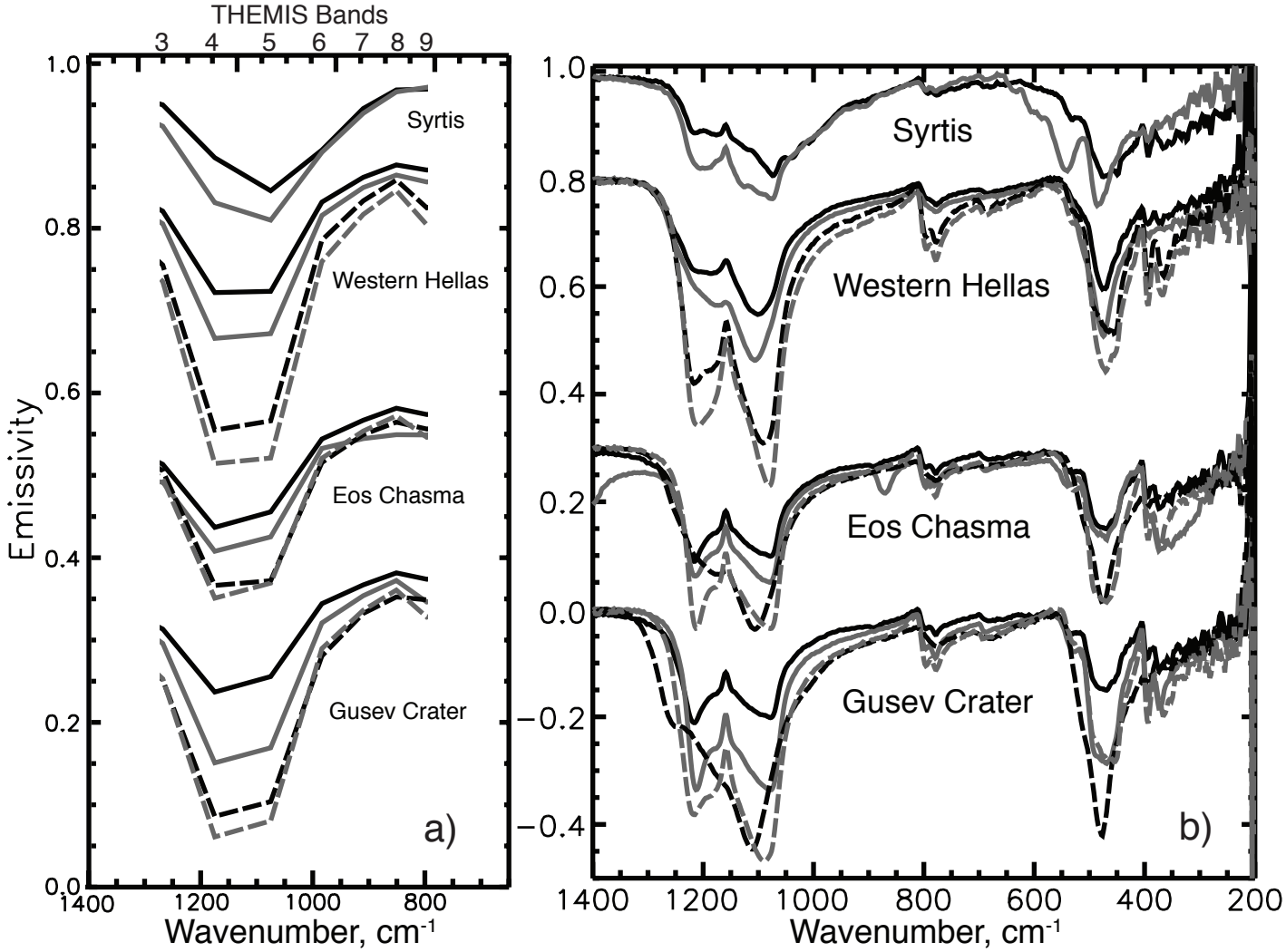

Figure 5.9: Chert and amorphous silica spectra from this study most closely matching observed Martian spectra at the resolution of THEMIS, shown at a) THEMIS resolution b) laboratory resolution. Each group of spectra is offset for clarity.

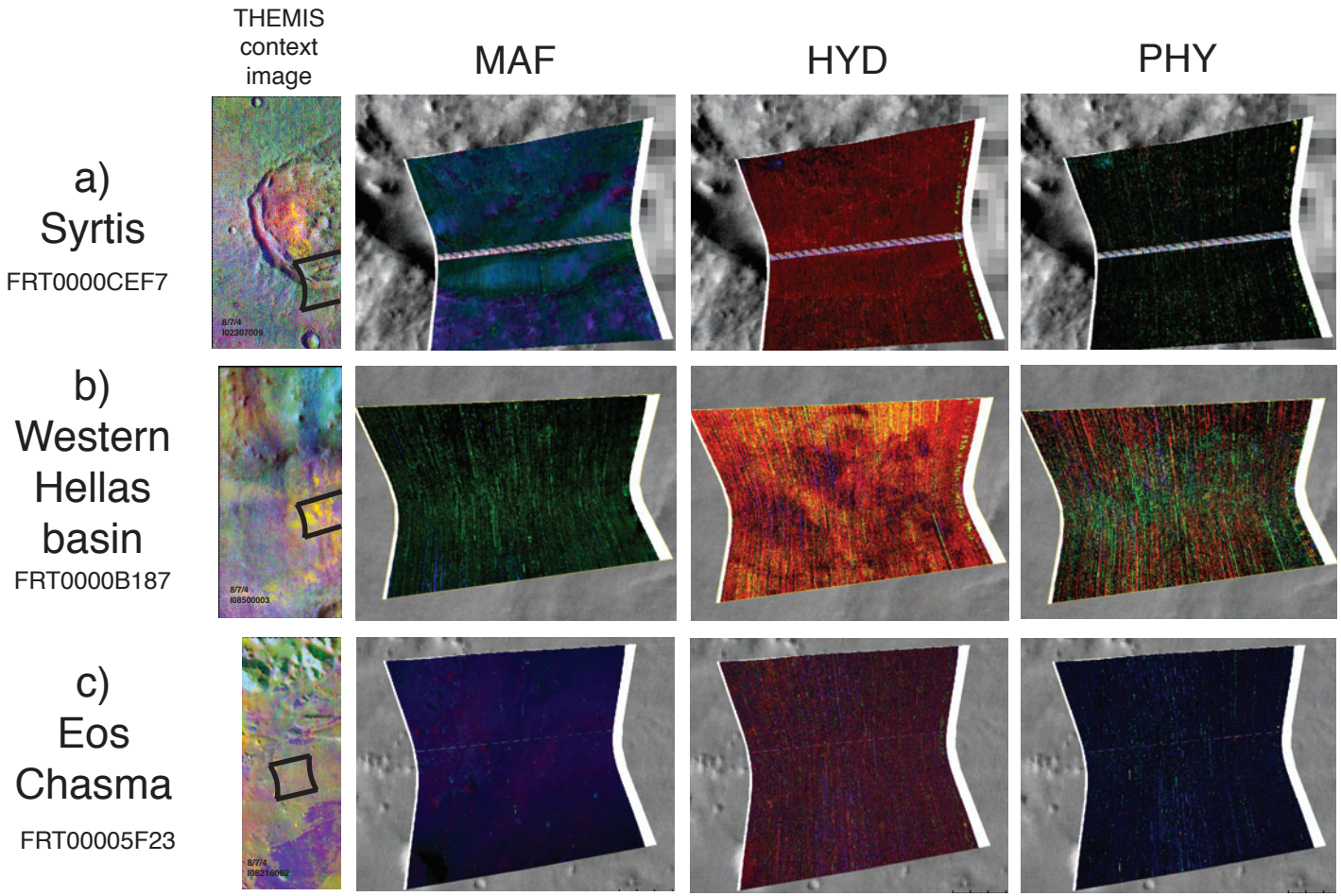

Figure 5.10: CRISM summary parameter composite images for three sites of silica-rich material on Mars. Location of each image is indicated by the box in the corresponding THEMIS DCS image.

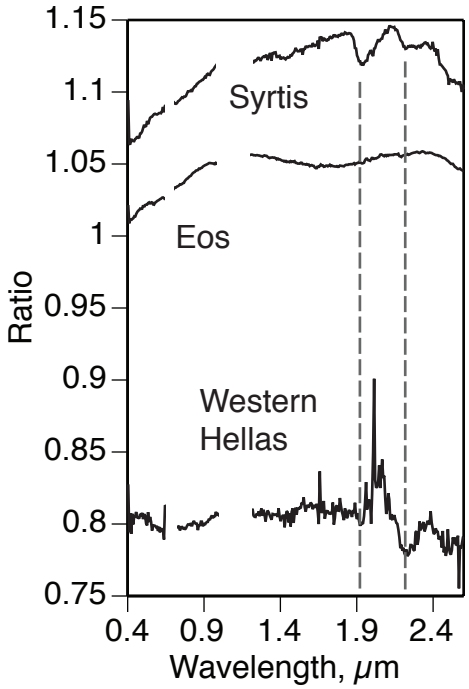

Figure 5.11: CRISM ratio spectra of silica-bearing material divided by surrounding terrain. Breaks in the spectrum are due to the removal of bad bands. Grey dashed vertical lines highlight where ~1.9 μm and ~2.2 μm features would occur.

with spots of high-calcium pyroxene (blue). The HYD image varies between mixtures of red and yellow and mixtures of red, black, and blue (Figure 10b). These areas with blue (~1.9 μm band) appear to correlate with the silica-bearing regions. The PHY image (Figure 10b) is a scatter of all colors with no correlations, however. The ratio spectrum comparing the region of interest to the surrounding area has a ~2.2 μm minimum and no obvious 1.9 and 1.4 μm minima (Figure 11).

The area imaged in Eos Chasma contains topography that is reflected in some of the summary parameter composite images. The high-silica material forms positive relief knobs in many cases and therefore the sunlit or shaded slopes can cause variations in the images. This appears to be the case in the MAF image, which is otherwise unremarkable (Figure 10c). Both the HYD and PHY images are similarly unremarkable, with a scattering of colors not corresponding to the silica-bearing spots (Figure 10c). A CRISM ratio spectrum of one spot compared to nearby terrain, shown in Figure 11, has a somewhat steep slope between 0.4 and 0.9 μm, a broad minimum at ~1.6-1.7 μm, and a relative drop in reflectivity at > 2.4 μm. No difference in reflectivity at ~1.4, 1.9, or 2.2 μm is apparent, however.

4. Discussion

4.1. Detecting Chert and Amorphous Silica in Thermal Infrared Spectra

As is the case with the laboratory data described in Chapter Four, the spectra of chert and amorphous silica at 20 cm^{-1} resolution exhibit a large variation in the details of features and a spectral library may require multiple examples. Though the currently known high-silica deposits on Mars are spatially small and require complex methods to

isolate and analyze in TES spectra, spectra at 20 cm^{-1} (TES/Mini-TES) resolution are well suited to distinguish between high-silica phases, including coarsely crystalline quartz, chert, and opaline silica. The resolution also is sufficient to distinguish between silica and other phases. However, at 20 cm^{-1} (TES/Mini-TES) resolution (as with lab resolution) it may not be possible to distinguish the spectrum of completely amorphous opal (opal-A) from the spectrum of partially crystalline opal (opal-C or opal-CT).

The loss of spectral detail at THEMIS resolution makes distinguishing between silica phases more difficult (e.g., Figure 5c). Additionally, sulfates (we examined gypsum, anhydrite, barite, celestite, and bassanite, in particular) may have similar shapes at this resolution (i.e., lowest emissivity in Bands 4 and 5), but they do not appear to exhibit the decrease in Band 9 relative to Band 8 that may be present in forms of quartz and less so in amorphous silica. This feature may provide a way to distinguish the two in some cases. Differentiating between the silica phases and other high-silica or amorphous phases is more straightforward; other phases have their lowest emissivity in Bands 5 and 6 or greater (e.g., Figure 5d).

The decrease that quartz exhibits in THEMIS Band 9 relative to Band 8 may help in its identification, as mentioned above. However, the use of this trend is complicated by the position of Band 9 slightly within the feature caused by the CO_2 in the Martian atmosphere. In the wavelength region of Band 9 the emissivity is decreased slightly as a result of CO_2 absorption, which may cause the Band 9 emissivity value to decrease for reasons not associated with the presence of the 780 cm^{-1} quartz feature. One way to determine if a Band 9 minimum results from surface or atmospheric factors is to compare the spectrum of interest to another spectrum from the same image that is not suspected to

contain silica. Because the atmosphere is not expected to vary much over an image, the spectrum of interest should have a greater decrease in Band 9 than the comparison spectrum if quartz is present.

4.2. Detecting Chert and Amorphous Silica in Visible to Near-infrared Spectra

Visible to near-infrared spectra of chert and amorphous silica may exhibit the ~1.9 μm band attributed to hydration, though the 1.9 μm index value may not necessarily be elevated above that for the common igneous minerals it would likely be surrounded by on Mars (Figure 6). For our spectra at laboratory resolution we find that the ~1.9 μm band index values must be greater than 0.052 (*Pelkey et al.,* [2007]), 0.110 (*Loizeau et al.,* [2007]), or 0.107 (*Poulet et al.,* [2007]) to be distinguished from anhydrous igneous phases. These values may be different for spectra at CRISM resolution. In addition, some chert spectra do not have this feature and therefore it cannot be used as a requirement to confirm the identity of chert. A chert or amorphous silica spectrum with a value below that for igneous phases, whether having a 1.9 μm feature or not, could lead to a lack of detection of chert and amorphous silica and distinction from the surrounding basaltic terrain on Mars.

The ~2.2 or 2.3 μm feature is present in some chert and amorphous silica spectra but absent in others, and could also be misleading. We determined the threshold values necessary for a phase having one of these features to be distinguished from igneous phases in laboratory data are 0.042 and 0.037 for the BD2210 and BD2290 parameters, respectively, from *Pelkey et al.,* [2007], and 0.100 and 0.027 for the ~2.2 μm and ~2.3 μm indices, respectively, from *Loizeau et al.,* [2007] (Table 2). A search based only on

this feature would not detect chert and amorphous silica spectra lacking the feature, nor would it detect spectra containing the feature but having index values overlapping or less than those for igneous phases (e.g., Figure 6).

Additionally, spectra with ~2.2 or 2.3 μm features, especially narrow ones, could be misidentified as phyllosilicate or carbonate, as discussed in Chapter Four. These materials may contain phyllosilicate or carbonate, but they are dominated by silica. It may be difficult to tell the difference between phyllosilicate- or carbonate-rich material and chert or amorphous silica based solely on a VNIR spectrum if the phyllosilicate or carbonate is actually an accessory phase in chert or silica. However, if neither accessory phase is present in the chert, the broad minimum at ~2.2 – 2.3 μm in its VNIR spectrum should permit identification. Thermal infrared data may be able to assist in situations where identification is not so straightforward.

We have attempted to quantify the difference between the phyllosilicate shape and chert or amorphous silica shape in the 2.2 μm region. If a spectrum shows a minimum at ~2.2 μm, the slope between 2.22 and 2.25 μm gives an indication of a broad or narrow absorption. A narrow minimum, such as from the presence of phyllosilicate, would result in a large positive slope, whereas a broad minimum, like that observed for many chert and amorphous silica spectra, would result in a smaller positive slope. For our spectra the threshold between the two is in the range of 2.2×10^{-4} to 2.9×10^{-4}. Another approach that can be combined with the 2.22 – 2.25 μm slope is the measurement of the width of the ~2.2 μm minimum. We determined the full width half maximum values for the ~2.2 μm features and found that the phyllosilicate-bearing samples have widths less than ~56.5 nm, whereas the other samples have widths of

greater than ~79 nm. These calculations will not differentiate phyllosilicate-bearing chert from pure phyllosilicate.

We find one exception in our data with the two approaches described above for quantifying the difference in shape in the ~2.2 μm region for chert or amorphous silica and phyllosilicate. Spectrum 9X_top exhibits a very small minimum at ~2.2 μm that causes it to have values similar to the phyllosilicate-bearing chert samples, even though it does not strongly resemble a phyllosilicate spectrum overall. It may be that this sample contains a very small amount of phyllosilicate or this minimum results from noise. Because noise or artifacts in data have the potential to create false positives, it is always recommended that the identification of phases based on spectral indices be confirmed by manual examination of the full spectrum [e.g., *Pelkey et al*., 2007].

4.3. Martian Silica-bearing Sites

4.3.1. Gusev Crater

Squyres et al. [2008], suggest that the prominent minimum at ~1250 cm^{-1} in the Mini-TES spectra of the silica-rich rocks and soil in Gusev crater is caused by the high incidence angles at which the targets are measured. The Mini-TES spectrum of Clara_Zaph4 (Figure 8) is similar to some spectra in our study and is consistent with both an opaline silica phase viewed at an angle >~30º and a surface with significant roughness. As expected, the shape of this spectrum at THEMIS spectral resolution is consistent with the shapes of the chert and amorphous silica samples in our study. The high emissivity in Band 9 relative to Band 8 is consistent with amorphous silica; the opposite would suggest crystalline silica. This lower resolution spectrum is matched relatively well by a chert

(95_nat), silicified ash (624), Magadi chert (MC-e) and a hydrothermal precipitate (White1-1), but because we have the higher resolution Mini-TES spectrum, we know that the opaline sample White1 provides the best match. The formation of White1 in a hydrothermal setting is consistent with the origin proposed for the amorphous silica in Gusev [*Squyres et al*., 2008], though we are not certain that White1 also formed under the low pH conditions suggested for the Martian silica.

4.3.2. Northern Syrtis

Bandfield et al. [2004] and *Bandfield* [2006] show that the THEMIS spectra of the high-silica material in the northern Syrtis Major region are consistent with silica phases. *Bandfield et al*. [2004] isolated the particular spectral component in TES data and present the best spectral match as a quartz monzonite. Deconvolution of TES spectra by *Bandfield et al*. [2004] indicates that quartz, plagioclase feldspar, sheet silicates, and silica glass are the main phases present. *Bandfield et al*. [2004] and *Bandfield* [2006] propose that the quartz is of igneous origin, created by high degrees of magmatic differentiation.

Our THEMIS ratio spectrum from the crater at ~18.5N, 65E (Figure 7a) also has a shape consistent with a silica phase and that of *Bandfield et al*. [2004] and *Bandfield* [2006]. The ratio spectrum has a lower emissivity in Band 9 relative to Band 8, suggesting that it is most likely crystalline silica and unlikely to be a sulfate. A replacement chert (810-d) and a silicified ash (624-c) are the most similar spectra from our sample set at THEMIS resolution. In this case, those two spectra are cherts with a deeper low-wavenumber minimum than high-wavenumber minimum in the quartz

doublet, apparent at higher resolution (Figure 9b). It is possible that this would also be the character of the quartz-bearing material in this Syrtis crater, though the origin of the two cherts is not directly the result of igneous processes as suggested for the Martian quartz. However, a silicified ash may still be consistent with the mineralogy present in the area and, lacking a chert spectrum in the spectral library, could be represented by quartz. This would imply that some type of alteration took place, rather than extreme differentiation of magma. The TES spectrum isolated by *Bandfield et al*. [2004] is not an exact fit to a chert or quartz spectrum, but the contribution of quartz is clear and chert could potentially be this component mixed with other phases, based solely on the TIR spectra. However, the suggestion of an igneous quartz- and plagioclase feldspar-dominated composition made by *Bandfield et al*., [2004] is also reasonable based on the TIR spectra.

The CRISM data over this quartz-bearing material in northern Syrtis are also consistent with a quartz-bearing lithology. There is evidence for a ~1.9 μm band (e.g., parameters in Figure 10a, ratio in Figure 11), which may be present in chert though it is also present in amorphous silica. A slight elevation of the BD2210 parameter is also apparent in some areas (e.g., Figure 11). We are not aware of any characteristic that may help to definitively distinguish between coarsely crystalline quartz and chert in this wavelength range.

4.3.3. Western Hellas Basin

Bandfield [2008] presented THEMIS spectra from the western edge of Hellas basin that he determined are consistent in shape with high-silica material. The author

isolated this material from a TES spectrum by deconvolving the spectrum and then subtracting the mafic components assumed to be contributed by the surrounding basaltic terrain. The remaining components include high-silica phases (specifically, high sheet silicates, amorphous silica, and zeolites, and low quartz) and sulfate. From this result and the position of the ~475 cm^{-1} feature at a lower wavenumber than that of his reference quartz spectrum, *Bandfield* [2008] concludes that the high-silica material is dominated by sheet silicates, amorphous silica, or zeolites.

The THEMIS ratio spectrum we derived from a silica-rich area in the western Hellas basin, shown in Figure 7b, has a shape in which the depth of Bands 4 and 5 are similar, though they are still the lowest in emissivity and therefore are consistent with a silica-bearing material. This ratio has a lower emissivity in Band 9 relative to Band 8, suggesting that the phase is quartz rather than sulfate; amorphous silica is a possible though less likely candidate, considering very few of the opaline spectra from our study exhibit this decrease and it is very slight in those that do.

Our analysis of this THEMIS ratio indicates a material dominated by crystalline silica (e.g., coarsely crystalline quartz, chert), which is not consistent with the low quartz abundance and high amorphous silica or sheet silicate abundance proposed by *Bandfield* [2008]. Our results presented in Chapter Four indicate that the ~475 cm^{-1} feature position cannot necessarily be used to distinguish between quartz and amorphous silica because the position observed in several chert spectra overlaps that in the amorphous silica spectra. Also, our results suggest that the THEMIS spectrum of these materials is inconsistent with a shape dominated by sheet silicates or zeolites, which do not exhibit an emissivity minimum in Band 4 (Figure 5).

Our sample spectra that most closely match this ratio at THEMIS resolution are geyserite (699_nat), porcellanite (333), Magadi chert (MC-c), and chert (409-c). All of these but the porcellanite are cherts with the low-wavenumber minimum of the doublet significantly deeper than the high-wavenumber minimum. The porcellanite has a shape between chert and amorphous silica. There is not enough detail in the shape of the isolated TES spectrum from *Bandfield* [2008] to rule out either the 'in between' shape of the porcellanite or the dominantly quartz shape of the cherts. The porcellanite originated as diatomaceous ooze, an origin that appears unlikely based on our current knowledge. An aqueous process like the one that produces Magadi chert from Na-silicate is possible, but might require a standing body of water to form the precursor silicate. A hydrothermal process like the one that formed sample 699 is a possible formation mechanism for the silica phase in western Hellas. At present we do not have enough information about the local geology to know which of these environments of formation is most likely, if any. As described in Chapter Four, a similar spectrum does not necessarily indicate a similar origin.

The VNIR data are, unfortunately, ambiguous. The HYD image indicates that the silica-rich areas have greater ~1.9 μm features, but a similar pattern is not observed in the PHY image (Figure 10b), which also includes the BD1900 parameter. Other images in the area show no correlation of silica-rich areas to parameters. A slight 2.2 μm feature in the silica-rich area is suggested by the ratio spectrum (Figure 11), but the presence of hydrations features is not indicated. The spectrum of chert can have the ~1.9 μm feature or no features at all, as can the spectrum of quartz, though any 1.9 μm feature would be small. The spectrum of amorphous silica has a ~1.9 μm feature for all samples we have

studied and therefore may be less likely in the areas where the parameters indicate no ~1.9 μm feature. However, as we mentioned above, a ~1.9 μm feature may not be indicated by the index but still be present in the spectrum. Identification of the dominant silica phase may have to wait for more data to be collected and analyzed.

4.3.4. Eos Chasma

Hamilton et al. [2006] proposed that these materials in Eos Chasma are silica-rich, though they did not rule out the possibility that they may instead be sulfate-rich. They based their study on THEMIS data; definitive analysis of TES data was not presented. Our THEMIS ratio isolating the spectrally distinct component in Eos Chasma has the low emissivity in Bands 4 and 5 that is consistent with silica and the *Hamilton et al.* [2006] spectrum. The lower emissivity in Band 9 relative to Band 8 is most consistent with some type of quartz and not consistent with sulfate (Figure 7c).

The best matching spectra from our study are from a chert (95_nat), jasper (613_banded), silicified ash (624), and porcellanite (333). Higher resolution spectra show that the porcellanite is a mixture of chert and amorphous silica, whereas the other three are cherts with the two minima of the quartz doublet at similar depths (Figure 9b). The mineralogy of the terrain surrounding the quartz material is basaltic with areas of elevated olivine or orthopyroxene abundance [*Hamilton et al.*, 2006]. It is not known if other phases are present along with the quartz. This material commonly forms light-toned knobs, which could be the remains of a larger eroded unit or areas of high topography in an underlying unit. Unless a significant amount of water ponded in the chasma and hosted biologic activity, this quartz material likely did not form from

diatomaceous ooze like sample 333. An origin similar to chert, jasper, or silicified ash would likely all require some amount of water but is plausible. If aqueous activity was involved, it was likely separated from the exposures of olivine, a mineral susceptible to aqueous alteration, either spatially or temporally.

The lack of a ~1.9 μm feature in the VNIR data (Figure 10c) is also consistent with a quartz material, as opposed to amorphous silica. In section 4.2 we showed that a ~1.9 μm feature may be present even when not readily indicated by the 1.9 μm indices, but in this case we have examined the VNIR spectrum of the material and it does not show a feature at that position (Figure 11). Higher resolution TIR spectra (i.e., TES) would be needed to determine whether this quartz-bearing material is composed of chert or coarsely crystalline quartz, and whether other phases are present.

4.4. Environments of Silica Formation and Associated Phases

Though we do not currently have the detailed information of all phases and their physical relationships for most of the silica-bearing sites on Mars, we can anticipate the kind of environment indicated by the association of chert or amorphous silica with certain minerals and rocks. Below we give an overview of the phases that can be associated with chert and amorphous silica in environments on Earth. We refer to *Blatt et al*. [1972], *Boggs* [2001], *Hochstein and Browne* [2000], and *Knauth* [1994] for this information.

Carbonates are commonly associated with chert and amorphous silica. Primary chert or amorphous silica deposits may be layered with carbonates in lacustrine, peritidal, and shallow marine environments. Carbonates deposited laterally in relation to amorphous silica could also suggest that the silica is a sinter and that they were formed in

a subaerial hydrothermal system. An intimate mixing of carbonate and chert throughout a unit or as discrete nodules in a unit likely represent secondary replacement of the carbonate, especially if relict structures are observed. Replacement can occur very early in the diagenetic process and does not necessarily require significant burial.

Siliciclastic sedimentary rocks can also occur in bedded layers with chert or amorphous silica in lacustrine, shallow marine, and deep marine environments. Silica glass may form from impacts into sandstones. Silica precipitation in pore spaces commonly cements siliciclastic rocks or forms larger replacement chert nodules. The association of amorphous silica with clay minerals, particularly as coatings and filling in fractures, may be the remnants of aqueous alteration.

Chert and amorphous silica can be related to volcanic rocks as well. Primary deposits of amorphous silica occur with basalt from gas condensation, in submarine vent environments, and subaerial hydrothermal environments. Volcanic ash or tuff may be replaced by chert, which is commonly signified by relict textures and structures. Coatings and cements of secondary amorphous silica may form as a product of alteration. Alternatively, the association of volcanic airfall deposits with chert or amorphous silica may not be related to the local environment but instead is due to the influx and settling of ash in a lacustrine or shallow marine environment. The ash would form a discrete bed within the local layers in this scenario.

Chert can be found with some evaporites such as sulfates. The original sulfate is dissolved by groundwater and silica precipitates in its place, cementing, filling vugs, or replacing everything but relict structures. Sulfate and chert can also both be found as primary deposits in hydrothermal environments.

Some phases are less common and when identified with chert or amorphous silica can indicate an environment of formation more specifically. For example, deposits of amorphous silica and metal-rich precipitates (e.g., gold, silver, arsenic, antimony) occur in high temperature hydrothermal deposits. Iron-rich sediments layered with chert form in shallow or deep marine environments on Earth, like the banded iron formations. Chert and amorphous silica also form with phosphorites in marine environments.

Undoubtedly the differences between Earth and Mars would influence the likely methods of formation for Martian silica-rich deposits. The apparent lack of plate tectonics on Mars suggests that the chert and amorphous silica observed formed on the surface or near to the surface and were later exposed by erosion or impact. Because Mars has obvious evidence of widespread igneous activity, volcanic gas condensation, hydrothermal deposition, diagenetic replacement, and alteration of basaltic material may be considered the most likely silica formation scenarios for the planet. However, our knowledge of the Martian environment and any potential biologic activity is not complete and other origins for chert and amorphous silica should not be ruled out. Future studies should use any new information about phases, rocks, and their physical structures and relationships, in addition to the spectra of the silica phases themselves, to determine the origin of chert and amorphous silica material.

5. Summary and Conclusions

1) The TIR spectra of chert and amorphous silica are distinguishable from one another and from other silica phases at 20 cm^{-1} (TES/Mini-TES) resolution. Because chert and amorphous silica spectra show a large amount of variation in detail, a range of

chert and amorphous silica spectra should be included in a spectral library to identify the best possible match.

2) At THEMIS spectral resolution the spectra of silica phases are difficult to distinguish from each other. However, the spectrum of a silica phase can be distinguished from the spectra of almost all non-silica phases, with the exception of some sulfates like gypsum. The emissivity of Band 9 relative to Band 8 may be used in ratio spectra to determine whether a silica phase is more consistent with quartz than with amorphous silica or sulfate.

3) The VNIR spectral character of chert and amorphous silica varies widely and makes it difficult to use any single criterion to identify these phases. Even if features are present in the spectrum at 1.9, 2.2, or 2.3 μm, calculated index values may not be greater than the values calculated from spectra of anhydrous igneous minerals. If a 2.2 or 2.3 μm feature is apparent in the spectrum, a chert or amorphous silica material could be misidentified as dominantly phyllosilicate or carbonate. When possible, it is preferable to examine the complete spectrum rather than the spectral index and to augment VNIR data with other information, such as TIR data, to identify materials as accurately as possible.

4) Thermal infrared spectra and VNIR spectral indices of the silica-rich materials in northern Syrtis Major and Eos Chasma are consistent with coarsely crystalline quartz and/or chert, and are not consistent with sulfate; THEMIS data suggest that the type of silica present in the silica-rich material on the western edge of the Hellas basin is also crystalline, conflicting with the assignment of a dominant amorphous silica, sheet silicate, and zeolite mineralogy made by *Bandfield* [2008]. As expected, the Mini-TES spectrum

of the silica-rich material in Gusev crater matches well with the spectral character of the amorphous silica we have observed in our study.

The new information we have presented in this paper, and in Chapter Four, has helped to constrain the identity of silica-rich materials on Mars and will continue to help in the detection and identification of these types of materials. Future studies will involve the processing, examining, and interpreting of complete CRISM spectra for the Syrtis and western Hellas basin sites. We will also increase the applicability of the thresholds for the VNIR spectral parameters by resampling the laboratory resolution VNIR spectra to CRISM resolution. Accurate detection and identification of silica phases is essential to their correct interpretation and resulting assumptions concerning geologic or environmental conditions on Mars.

Acknowledgements

We would like to thank S. Ruff for providing the Mini-TES spectrum of Clara_Zaph4 and M. Osterloo for helpful discussion. We appreciate grants from NASA's Planetary Geology and Geophysics, Mars Fundamental Research, and Mars Data Analysis programs.

WORKS CITED

Adams, J. B. (1974), Visible and near-infrared diffuse reflectance spectra of pyroxenes as applied to remote sensing of solid objects in the solar system, *Journal of Geophysical Research*, *79*, 4829-4836.

Almeida, R. M. (1992), Detection of LO modes in glass by infrared reflection spectroscopy at oblique incidence, *Physical Review B*, *45*, 161-170.

Aronson, J. R., and A. G. Emslie (1975), Composition of the Martian dust as derived by infrared spectroscopy from Mariner 9, *Journal of Geophysical Research*, *80*, 4925-4931.

Bandfield, J. L. (2002), Global mineral distribution on Mars, *Journal of Geophysical Research*, *107*, 5042.

Bandfield, J. L. (2006), Extended surface exposures of granitoid compositions in Syrtis Major, Mars, *Geophysical Research Letters*, *33*, doi:10.1029/2005GL025559.

Bandfield, J. L. (2008), High-silica deposits of an aqueous origin in western Hellas Basin, Mars, *Geophysical Research Letters*, *35*, doi:10.1029/2008GL033807.

Bandfield, J. L., P. R. Christensen, and M. D. Smith (2000a), Spectral data set factor analysis and end-member recovery: Application to analysis of Martian atmospheric particulates, *Journal of Geophysical Research*, *105*, 9573-9587.

Bandfield, J. L., V. E. Hamilton, and P. R. Christensen (2000b), A global view of Martian Surface Compositions from MGS-TES, *Science*, *287*, 1626.

Bandfield, J. L., D. Rogers, M. D. Smith, and P. R. Christensen (2004a), Atmospheric correction and surface spectral unit mapping using Thermal Emission Imaging System data, *Journal of Geophysical Research*, *109*, doi:10.1029/2004JE002289.

Bandfield, J. L., V. E. Hamilton, P. R. Christensen, and H. Y. McSween, Jr. (2004b), Identification of quartzofeldspathic materials on Mars, *Journal of Geophysical Research*, *109*, doi:10.1029/2004JE002290.

Beer, R., R., H. Norton, and S. V. Martonchik (1971), Astronomical infrared spectroscopy with a Connes-type interferometer: II, Mars, 2500-3500 cm-1, *Icarus*, *15*, 1-10.

Bell III, J. F., R. V. Morris, and J. B. Adams (1993), Thermally altered palagonitic tephra: A spectral and process analog to the soil and dust of Mars, *Journal of Geophysical Research*, *98*, 3373-3385.

Bibring, J. P., et al. (2005), Mars surface diversity as revealed by the OMEGA/Mars Express observations, *Science*, *307*, doi:10.1126/science.1108806.

Bishop, J., R. V. Morris, J. Mustard, and T. Roush (2006), CRISM Spectral Library, *Nasa Planetary Data System*, MRO- M-CRISM-4-SPECLIB-v1.0.

Bishop, J., et al. (2008), Phyllosilicate diversity and past aqueous activity revealed at Mawrth Vallis, Mars, *Science*, *321*, doi:10.1126/science.1159699.

Blatt, H., G. Middleton, and R. Murray (1972), *Origin of Sedimentary Rocks*, 634 pp., Prentice-Hall, Inc., Englewood Cliffs, New Jersey.

Boggs, S. J. (2001), *Principles of Sedimentology and Stratigraphy, 3rd Edition*, 726 pp., Prentice Hall, Upper Saddle River, New Jersey.

Brown, A., M. Walter, and T. Cudahy (2004), Short-wave infrared reflectance investigation of sites of paleobiological interest: Applications for Mars exploration, *Astrobiology*, *4*, 359- 376.

Burns, R. G. (1993), Origin of electronic spectra of minerals in the visible to near-infrared region, in *Remote Geochemical Analysis: Elemental and Mineralogical Compostion*, edited by C. M. Pieters, pp. 3-29, Cambridge University Press, New York.

Christensen, P. R. (1982), Martian dust mantling and surface composition: Interpretation of thermophysical properties, *Journal of Geophysical Research*, *87*, 9985-9998.

Christensen, P. R. (1983), Eolian Intracrater Deposits on Mars: Physical Properties and Global distribution, *Icarus*, *56*, 496-518.

Christensen, P. R., et al. (1992), Thermal Emission Spectrometer Experiment: Mars Observer Mission, *Journal of Geophysical Research*, *97*, 7719-7734.

Christensen, P. R., et al. (2000a), Detection of crystalline hematite mineralization on Mars by the Thermal Emission Spectrometer: Evidence for near-surface water, *Journal of Geophysical Research*, *105*, 9623-9642.

Christensen, P. R., J. L. Bandfield, V. E. Hamilton, D. A. Howard, M. D. Lane, J. L. Piatek, S. W. Ruff, and W. L. Stefanov (2000b), A thermal emission spectral library of rock-forming minerals, *Journal of Geophysical Research*, *105*, 9735-9739.

Christensen, P. R. et al. (2001a), Mars Global Surveyor Thermal Emission Spectrometer experiment: Investigation description and surface science results, *Journal of Geophysical Research*, *106*, 23823-23871.

Christensen, P. R., et al. (2001b), Global mapping of Martian hematite mineral deposits: Remnants of water-driven processes on early Mars, *Journal of Geophysical Research*, *106*, 23,873-823,885.

Christensen, P. R., J. L. Bandfield, M. D. Smith, V. E. Hamilton, and R. N. Clark (2000c), Identification of a basaltic component on the Martian surface from Thermal Emission Spectrometer data, *Journal of Geophysical Research*, *105*, 9609-9621.

Christensen, P. R., and S. T. Harrison (1993), Thermal infrared emission spectroscopy of natural surfaces: Application to desert varnish coatings on rocks, *Journal of Geophysical Research*, *98*, 19,819-819,834.

Christensen, P. R. et al. (2004), The Thermal Emission Imaging System (THEMIS) for the Mars 2001 Odyssey Mission, *Space Science Reviews*, *110*, 85-130.

Clancy, R. T., et al. (1995), A new model for Mars atmospheric dust based upon analysis of ultraviolet through infrared observations from Mariner 9, Viking, and Phobos, *Journal of Geophysical Research*, *100*, 5251-5264.

Clark, B. C., et al. (2005), Chemistry and mineralogy of outcrops at Meridiani Planum, *Earth and Planetary Science Letters*, *240*, doi:10.1016/j.epsl.2005.1009.1040.

Clark, R. N., et al. (1990), High spectral resolution reflectance spectroscopy of minerals, *Journal of Geophysical Research*, *95*, 12,653-612,680.

Deer, W. A., R. A. Howie, and J. Zussman (1992), *An introduction to the rock-forming minerals*, 2nd ed., 696 pp., Longman Pub Group, Pearson Education Limited, Essex, England.

Edgett, K. S., and P. R. Christensen (1994), Mars aeolian sand: Regional variations among dark-hued crater floor features, *Journal of Geophysical Research*, *99*, 1997-2018.

Ehlmann, B. L., et al. (2008a), Distinct provinces of aqueous alteration in the western Isidis region identified with MRO-CRISM, paper presented at Lunar and Planetary Science Conference XXXIX, Abstract #2326.

Ehlmann, B. L., et al. (2007), New Secondary minerals detected by MRO CRISM and their geologic settings: Kaolinite, chlorite, illite/muscovite, and the possibility of serpentine or carbonate in Nili Fossae, paper presented at Seventh International Conference on Mars, Abstract #3270.

Ehlmann, B. L., et al. (2008b), Orbital identification of carbonate-bearing rocks on Mars, *Science*, *322*, doi: 10.1126/science.1164759.

Emslie, A. G., and J. R. Aronson (1973), Spectral reflectance and emittance of particulate materials. 1: Theory, *Applied Optics*, *12*, 2563-2572.

Fenton, L. K., and J. L. Bandfield (2003), Aeolian processes in Proctor Crater on Mars: Sedimentary history as analyzed from multiple data sets, *Journal of Geophysical Research*, *108*, 5129.

Fergason, R. L., P. R. Christensen, and H. H. Kieffer (2006), High resolution thermal inertia derived from Thermal Emission Imaging System (THEMIS): Thermal model and applications, *Journal of Geophysical Research*, *111*, doi:10.1029/2006JE002735.

Flörke, O. W., et al. (1993), Silica, in *Ullmann's Encyclopedia of Industrial Chemistry*, edited, VCH Publishers, Inc.

Flörke, O. W., et al. (1991), Nomenclature of micro- and non-crystalline silica minerals, based on structure and microstructure, *N Jahrb Min Abh*, *163*, 19-42.

Gaffey, S. J. (1987), Spectral reflectance of carbonate minerals in the visible and near infrared (0.35 - 2.55 μm): Anhydrous carbonate minerals, *Journal of Geophysical Research*, *92*, 1429-1440.

Gaffey, S. J., L. A. McFadden, D. Nash, and C. M. Pieters (1993), Ultraviolet, visible, and near-infrared reflectance spectroscopy: Laboratory spectra of geologic materials, in *Remote geochemical analysis: Elemental and mineralogical composition*, edited by C. M. Pieters and P. A. J. Englert, pp. 43-77, Cambridge University Press, New York.

Gendrin, A. et al. (2005), Sulfates in Martian layered terrains: The OMEGA/Mars Express view, *Science*, *307*, doi:10.1126/science.1109087.

Gillespie, A. R., A. B. Kahle, and R. E. Walker (1986), Color enchancement of highly correlated images: I. Decorrelation and HSI contrast stretches, *Remote Sensing of Environment*, *20*, 209-235.

Gillis-Davis, J. J., P. G. Lucey, J. E. Hammer, and B. B. Denevi (2008), Syntheses and reflectance analyses of Lunar green glass compositions: Information to improve understanding of remotely sensed spectral data, *Lunar and Planetary Science Conference*, *XXIX*, Abstract #1535.

Glotch, T. D., R.V. Morris, P. R. Christensen, and T. G. Sharp (2004), Effect of precursor mineralogy on the thermal infrared emission spectra of hematite: Application to Martian hematite mineralization, *Journal of Geophysical Research*, *109*, doi:10.1029/2003JE002224.

Goryniuk, M. C., B. A. Rivard, and B. Jones (2004), The reflectance spectra of opal-A (0.5 - 25 μm) from Taupo Volcanic Zone: Spectra that may identify hydrothermal systems on planetary surfaces, *Geophysical Research Letters*, *31*, doi:10.1029/2004GL021481.

Graetsch, H. (1994), Structural characteristics of opaline and microcrystalline silica minerals, in *Silica: Physical behavior, geochemistry and materials applications*, edited by P. J. Heaney, et al., pp. 209-232, Mineralogical Society of America, Washington, D.C.

Graetsch, H., H. Gies, and I. Topalovic (1994), NMR, XRD, and IR study on microcrystalline opals, *Physics and Chemistry of Minerals*, *21*, 166-175.

Grant, J. A., and T. J. Parker (2002), Drainage evolution in the Margaritifer Sinus region, Mars, *Journal of Geophysical Research*, *107*, 5066.

Greeley, R., and J. E. Guest (1987), Geologic map of the eastern equatorial region of Mars, U.S. Geological Survey Miscellaneous Investigations Series Map I-1802-B.

Hamilton, V. E. (2000), Thermal infrared emission spectroscopy of the pyroxene mineral series, *Journal of Geophysical Research*, *105*, 9701-9716.

Hamilton, V. E. (2003), Thermal infrared emission spectroscopy of titanium-enriched pyroxenes, *Journal of Geophysical Research*, *108*, doi:10.1029/2003JE002052.

Hamilton, V. E., S. L. Cady, and P. J. Boston (2006), Astrobiology relevant hypotheses for the origin of quartz-bearing materials in Eos Chasma: Tests for MSL, paper presented at Mars Science Laboratory First Landing Site Workshop, Pasadena, California, May 31 - June 2.

Hamilton, V. E., and P. R. Christensen (2005), Evidence for extensive, olivine-rich bedrock on Mars, *Geology*, *33*, 433-436, doi:410.1130/G21258.21251.

Hamilton, V. E., P. R. Christensen, H. Y. McSween, and J. L. Bandfield (2003), Searching for the source regions of Martian meteorites using MGS TES: Integrating Martian meteorites into the global distribution of volcanic materials on Mars, *Meteoritics and Planetary Science*, *38*, 871-886.

Hamilton, V. E., and W. C. Koeppen (2007), Global mineral maps of Mars: Examination of compositional variation within solid solution series, *Eos Trans. Am. Geophys. Union, 88*, #P13D-1549.

Hamilton, V. E., and P. G. Lucey (2005), One spectrometer, two spectra: Complimentary hemispherical reflectance and thermal emission spectroscopy using a single FTIR instrument, in *Lunar and Planetary Science Conference XXXVI*, edited.

Hamilton, V. E., R. V. Morris, J. E. Gruener, and S. A. Mertzman (2008), Visible, near infrared, and middle infrared spectroscopy of altered basaltic tephras: Spectral signatures of phyllosilicates, sulfates, and other aqueous alteration products with application to the mineralogy of the Columbia Hills of Gusev crater, Mars, *Journal of Geophysical Research*, doi:10.1029/2007JE003049.

Hanel, R., et al. (1972), Investigation of the Martian environment by infrared spectroscopy on Mariner 9, *Icarus*, *17*, 423-442.

Head, J. W. I., and L. Wilson (1979), Alphonsus-type dark-halo craters: Morphology, morphometry, and eruption conditions, *Proc. Lunar Planet. Sci. Conf, 11th*, 2861-2897.

Heaney, P. J. (1994), Structure and chemistry of silica and its stuffed derivatives, in *Slica: Physical behavior, geochemistry and materials applications*, edited by P. J. Heaney, et al., pp. 1-40, Mineralogical Society of America, Washington, D.C.

Hiesinger, H., and J. W. I. Head (2004), The Syrtis Major volcanic province, Mars: Synthesis from Mars Global Surveyor data, *Journal of Geophysical Research*, *109*, doi:10.1029/2003JE002143.

Hochstein, M. P., and P. R. L. Browne (2000), Surface manifestations of geothermal systems with volcanic heat sources, in *Encyclopedia of Volcanoes*, edited by H. Sigurdsson, et al., pp. 835-855, Academic Press, San Diego.

Hoefen, T. M., et al. (2003), Discovery of Olivine in the Nili Fossae region of Mars, *Science*, *302*, 627-630.

Houck, J. R., et al. (1973), High altitude infrared spectroscopic evidence for bound water on Mars, *Icarus*, *18*, 470-480.

Hubbard, M. J., D. A. Waugh, and J. D. Oritz (2003), Application of VIS/NIR spectral reflectance in sourcing and recognition of heat-treatment in cherts, paper presented at Seattle Annual Meeting.

Hunt, G. R., L. M. Logan, and J. W. Salisbury (1973), Mars: Components of infrared spectra and composition of the dust cloud, *Icarus*, *18*, 459-469.

Kahle, A. B., F. D. Palluconi, and P. R. Christensen (1993), Thermal Emission Spectroscopy: Application to the Earth and Mars, in *Remote Geochemical Analysis: elemental and mineralogical composition*, edited by C. M. Pieters and P. A. Englert, pp. 90-120, Cambridge University Press, New York.

Kieffer, H. H., T. Z. Martin, A. R. Peterfreund, B. M. Jakosky, E. D. Miner, and F. D. Palluconi (1977), Thermal and albedo mapping of Mars during the Viking primary mission, *Journal of Geophysical Research*, *82*, 4249-4291.

Kingma, K. J., and R. J. Hemley (1994), Raman spectroscopy study of microcrystalline silica, *American Mineralogist*, *79*, 269-273.

Kirkland, L. E., K. C. Herr, and P. M. Adams (2003), Infrared stealthy surfaces: Why TES and THEMIS may miss some substantial mineral deposits on Mars and implications for remote sensing of planetary surfaces, *Journal of Geophysical Research*, *108*, doi:10.1029/2003JE002105.

Knauth, L. P. (1994), Petrogenesis of chert, in *Silica: Physical behavior, geochemistry and materials applications*, edited by P. J. Heaney, et al., pp. 233-258, Mineralogical Soceity of America, Washington, D. C.

Koeppen, W. C., and V. E. Hamilton (2005), Discrimination of glass and phyllosilicate minerals in thermal infrared data, *Journal of Geophysical Research*, *110*, doi:10.1029/2005JE002474.

Koeppen, W. C., and V. E. Hamilton (2008), Global distribution, composition, and abundance of olivine on the surface of Mars from thermal infrared data, *Journal of Geophysical Research*, *113*, doi:10.1029/2007JE002984.

Kraft, M. D., J. R. Michalski, and T. G. Sharp (2003), Effects of pure silica coatings on thermal emission spectra of basaltic rocks: Considerations for Martian surface mineralogy, *Geophysical Research Letters*, *30*, 2288.

Kraft, M. D., J. R. Michalski, and T. G. Sharp (2005), Palagonite-like alteration products on the Earth and Mars 2: Secondary mineralogy of crystalline basalts weathered

under semi-arid conditions, *Lunar and Planetary Science Conference XXXVI*, Abstract #1376.
Lane, M. D. (2007), Mid-infrared emission spectroscopy of sulfate and sulfate-bearing minerals, *American Mineralogist*, *92*, 1-18.
Lane, M. D., and P. R. Christensen (1997), Thermal infrared emission spectroscopy of anhydrous carbonates, *Journal of Geophysical Research*, *102*, 25,581-525,592.
Lippincott, E. R., A. VanValkenbrug, C. A. Weir, and E. M. bunting (1958), Infrared studies on polymorphs of silicon dioxide and germanium dioxide, *Journal of Research of the National Bureau of Standards*, *61*, 61-70.
Loizeau, D., et al. (2007), Phyllosilicates in the Mawrth Vallis region of Mars, *Journal of Geophysical Research*, *112*, doi:10.1029/2006JE002877.
Long, D. G. F., B. Silveira, and P. Julig (2001), Chert analsis by infrared spectroscopy, paper presented at 33rd Annual Meeting of the Canadian Archaeological Association, The Ontario Archaeological Society, Inc.
Lyon, R. J. P. (1963), Evaluation of infrared spectrophotometry for compositional analysis of Lunar and planetary soils, *NASA*, *Technical Note D-1871*.
Malin, M. C., G. E. Danielson, A. P. Ingersoll, H. Masursky, J. Veverka, M. A. Ravine, and T. A. Soulanille (1992), The Mars Observer Camera, *Journal of Geophysical Research*, *97*, 7699-7718.
Malin, M. C., and K. S. Edgett (2001), Mars Global Surveyor Mars Orbiter Camera: Interplanetary cruise through primary mission, *Journal of Geophysical Research*, *106*, 23429-23570.
Mangold, N., et al. (2007), Mineralogy of the Nili Fossae region with OMEGA/Mars Express data: 2. Aqueous alteration of the crust, *Journal of Geophysical Research*, *112*, doi:10.1029/2006JE002835.
Martinez-Alonso, S., M. T. Mellon, B. C. Kindel, and B. M. Jakosky (2006), Mapping compositional diversity on the surface of Mars: The Spectral Variance Index, *Journal of Geophysical Research*, *111*, doi:10.1029/2005JE002492.
McCord, T. B., R. N. Clark, and R. B. Singer (1982), Mars: Near-infrared reflectance spectra of surface regions and compositional implication, *Journal of Geophysical Research*, *87*, 3021-3032.
McLennan, S. M. et al. (2005), Provenance and diagenesis of the evaporite-bearing Burns formation, Meridiani Planum, Mars, *Earth and Planetary Science Letters*, *240*, 95-121.
McSween Jr., H. Y., et al. (2006), Alkaline volcanic rocks from the Columbia Hills, Gusev crater, Mars, *Journal of Geophysical Research*, *111*, doi:10.1029/2006JE002698.
McSween Jr., H. Y., and A. H. Treiman (1998), Martian meteorites, in *Planetary Materials*, edited by J. J. Papike, Mineralogical Society of America, Washington DC.
Mellon, M. T., B. M. Jakosky, H. H. Kieffer, and P. R. Christensen (2000), High-resolution thermal inertia mapping from the Mars Global Surveyor Thermal Emission Spectrometer, *Icarus*, *148*, 437-455.
Michalski, J. R. (2005), Silicate alteration mineralogy of the martian surface from TES: Constraints from thermal emission spectroscopy of terrestrial materials, Arizona State University, Tempe.

Michalski, J. R., and R. L. Fergason (2008), Composition and thermal inertia of the Mawrth Vallis region of Mars from TES and THEMIS data, *Icarus*, doi:10.1016/j.icarus.2008.1008.1016.

Michalski, J. R., et al. (2003), Thermal emission spectroscopy of the silica polymorphs and considerations for remote sensing of Mars, *Geophysical Research Letters*, *30*, doi:10.1029/2003GL018354.

Michalski, J. R., M. D. Kraft, T. G. Sharp, and P. R. Christensen (2005a), Palagonite-like alteration products on the Earth and Mars I: Spectroscopy (0.4-25 microns) of weathered basalt and silicate alteration products, *Lunar and Planetary Science Conference XXXVI*, Abstract #1188.

Michalski, J. R., M. D. Kraft, T. G. Sharp, and P. R. Christensen (2006a), Effects of chemical weathering on infrared spectra of Columbia River Basalt and spectral interpretations of Martian alteration, *Earth and Planetary Science Letters*, *248*, doi:10.1016/j.epsl.2006.1006.1034.

Michalski, J. R., et al. (2005b), Mineralogical constraints on the high-silica Martian surface component observed by TES, *Icarus*, *174*, doi:10.1016/j.icarus.2004.1010.1022.

Michalski, J. R., et al. (2006b), Emission spectroscopy of clay minerals and evidence for poorly crystalline aluminosilicates on Mars from Thermal Emission Spectrometer data, *Journal of Geophysical Research*, *111*, doi:10.1029/2005JE002438.

Michalski, J. R., J. J. Reynolds, T. G. Sharp, and P. R. Christensen (2004), Thermal infrared analysis of weathered granitic rock compositions in the Sacaton Mountains, Arizona: Implications for petrologic classifications from thermal infrared remote-sensing data, *Journal of Geophysical Research*, *109*, E03007.

Migaszewski, Z. M., A. Galuszka, and T. Durakiewicz (2006), Middle Oxfordian-Lower Kimmeridgian chert nodules in the Holy Cross Mountains, south-central Poland, *Sedimentary Geology*, *187*, 11-28.

Milam, K. A., et al. (2004), Accuracy of plagioclase compositions from laboratory and Mars spacecraft thermal emission spectra, *Journal of Geophysical Research*, *109*, doi:10.1029/2003JE002097.

Milliken, R. E., and J. F. Mustard (2005), Quantifying absolute water content of minerals using near-infrared reflectance spectroscopy, *Journal of Geophysical Research*, *110*, doi:10.1029/2005JE002534.

Milliken, R. E., et al. (2008), Opaline silica in young deposits on Mars, *Geology*, *36*, doi:10.1130/G24967A.24961.

Ming, D., et al. (2006), Geochemical and mineralogical indicators for aqueous processes in the Columbia Hills of Gusev crater, Mars, *Journal of Geophysical Research*, *111*, doi:10.1029/2005JE002560.

Minitti, M. E., C. M. Weitz, M. D. Lane, and J. L. Bishop (2007), Morphology, chemistry, and spectral properties of Hawaiian rock coatings and implications for Mars, *Journal of Geophysical Research*, *112*, doi:10.1029/2006JE002839.

Mittlefehldt, D. W. (1994), ALH 84001, A Cumulate Orthopyroxenite Member of the Martian Meteorite Clan, *Meteoritics*, *29*, 214-221.

Moenke, H. H. W. (1974), Silica, the three-dimensional silicates, borosilicates and beryllium silicates, in *The Infrared Spectra of Minerals*, edited by V. C. Farmer, pp. 365-382, Bartholomew Press, Surrey.

Morris, R. V., J. L. Gooding, H. V. Lauer Jr., and R. B. Singer (1990), Origins of Marslike spectral and magnetic properties of a Hawaiian palagonitic soil, *Journal of Geophysical Research*, *95*, 14,427-414,434.

Murchie, S., et al. (2007), Compact Reconnaissance Imaging Spectrometer for Mars (CRISM) on Mars Reconnaissance Orbiter (MRO), *Journal of Geophysical Research*, *112*, doi:10.1029/2006JE002682.

Murchie, S., et al. (1993), Spatial variations in the spectral properties of bright regions on Mars, *Icarus*, *105*, 454-468.

Mustard, J. F., and J. E. Hays (1997), Effects of hyperfine particles on reflectance spectra from 0.3 to 25 μm, *Icarus*, *125*, 145-163.

Mustard, J. F., et al. (2007a), CRISM-OMEGA observations of phyllosilicate-olivine stratigraphy in Nili Fossae, Mars, *Lunar and Planetary Science Conference XXXVIII*, Abstract #2071.

Mustard, J. F., et al. (2008), Hydrated silicate minerals on Mars observed by the Mars Reconnaissance Orbiter CRISM instrument, *Nature*, *454*, doi:10.1038/nature07097.

Mustard, J. F., et al. (2006), Ancient crust, aqueous alteration, and impact melt preserved in the Isidis basin, Mars, *Lunar and Planetary Science Conference XXXVII*, Abstract # 1683.

Mustard, J. F., et al. (2007b), Mineralogy of the Nili Fossae region with OMEGA/Mars Express data: 1 Ancient impact melt in the Isidis Basin and implications for the transition from the Noachian to Hesparian, *Journal of Geophysical Research*, *112*, doi:10.1029/2006JE002834.

Osinski, G. R. (2006), Effects of volatiles and target lithology on the generation and emplacement of impact crater fill and ejecta deposits on Mars, *Meteoritics and Planetary Science*, *41*, 1571-1586.

Osterloo, M. M., et al. (2008), Chloride-bearing materials in the southern highlands of Mars, *Science*, *319*, 1651-1654.

Pelkey, S. M., et al. (2007), CRISM multispectral summary products: Parameterizing mineral diversity on Mars from reflectance, *Journal of Geophysical Research*, *112*, doi:10.1029/2006JE002831.

Piatek, J. L. (1997), Vibrational spectroscopy of clay minerals: Implications for remote sensing of terrestrial planetoids, Arizona State University, Tempe.

Pimentel, G. C., P. B. Forney, and K. C. Herr (1974), Evidence about hydrate and solid water in the Martian surface from the 1969 Mariner infrared spectrometer., *Journal of Geophysical Research*, *79*, 1623-1634.

Poulet, F., et al. (2005), Phyllosilicates on Mars and implications for early Martian climate, *Nature*, *438*, 623-627, doi:610.1038/nature04274.

Poulet, F., et al. (2007), Martian surface mineralogy from Observatoire pour la Minéralogie, l'Eau, les Glaces et l'Activité on board the Mars Express spacecraft (OMEGA/MEx): Global mineral maps, *Journal of Geophysical Research*, *112*, doi:10.1029/2006JE002840.

Poulet, F., et al. (2008), Abundance of minerals in the phyllosilicate-rich units on Mars, *Astronomy & Astrophysics*, *487*, doi:10.1051/0004-6361:200810150.

Presley, M. A., and P. R. Christensen (1997), Thermal conductivity measurements of particulate materials, *Journal of Geophysical Research*, *102*, 6551-6566.

Putzig, N. E., M. T. Mellon, B. M. Jakosky, S. M. Pelkey, S. Martinez-Alonso, B. M. Hynek, and N. W. Murphy (2004), Mars thermal inertia from THEMIS data, *Lunar and Planetary Science Conference XXXV*, Abstract #1863.

Putzig, N. E., M. T. Mellon, K. A. Kretke, and R. E. Arvidson (2005), Global thermal inertia and surface properties of Mars from the MGS mapping mission, *Icarus*, *173*, 325-341.

Ramsey, M. S., and P. R. Christensen (1998), Mineral abundance determination: Quantitative deconvolution of thermal emission spectra, *Journal of Geophysical Research*, *103*, 577-596.

Rice, S. B., et al. (1995), Application of fourier transform infrared spectroscopy to silica diagnensis: The opal-A to opal-CT transformation, *Journal of Sedimentary Research*, *A65*, 639-647.

Rogers, A. D., J. L. Bandfield, and P. R. Christensen (2007), Global spectral classification of martian low-albedo regions with Mars Global Surveyor Thermal Emission Spectrometer (MGS-TES) data, *Journal of Geophysical Research*, *112*, doi:10.1029/2006JE002726.

Rogers, A. D., and P. R. Christensen (2007), Surface mineralogy of martian low-albedo regions from MGS-TES data: Implications for upper crustal evolution and surface alteration, *Journal of Geophysical Research*, *112*, doi:10.1029/2006JE002727.

Rossman, G. R. (1994), Colored varieties of the silica minerals, in *Silica: Physical behavior, geochemistry, and materials applications*, edited by P. J. Heaney, et al., pp. 433-467, Mineralogical Society of America, Washington, D.C.

Roush, T. L., D. L. Blaney, and R. B. Singer (1993), The surface composition of Mars as inferred from spectroscopic observations, in *Remote Geochemical Analysis: Elemental and Mineralogical Composition*, edited by C. Pieters and P. Englert, pp. 367-393, Univ. Press, Cambridge.

Ruff, S. W. (1998), Quantitative Thermal Infrared Emission Spectroscopy Applied to Granitoid Petrology, Arizona State University, Tempe.

Ruff, S. W. (2004), Spectral evidence for zeolite in the dust on Mars, *Icarus*, *168*, doi:10.1016/J.icarus.2003.1011.1003.

Ruff, S. W., and P. R. Christensen (2002), Bright and dark regions on Mars: Particle size and mineralogical characteristics based on Thermal Emission Spectrometer data, *Journal of Geophysical Research*, *107*, 5127.

Ruff, S. W., and P. R. Christensen (2007), Basaltic andesite, altered basalt, and a TES-based search for smectite clay minerals on Mars, *Geophysical Research Letters*, *34*, doi:10.1029/2007GL029602.

Ruff, S. W., P. R. Christensen, P. W. Barberg, and D. L. Anderson (1997), Quantitative thermal emission spectroscopy of minerals: A laboratory technique for measurement and calibration, *Journal of Geophysical Research*, *102*, 14,899-814,913.

Salisbury, J. W., and A. Wald (1992), The role of volume scattering in reducing spectral contrast of Reststrahlen bands in spectra of powdered minerals, *Icarus*, *96*, 121-128.

Salisbury, J. W., L. S. Walter, N. Vergo, and D. M. D'Aria (1991), *Infrared (2.1 - 25 μm) spectra of minerals*, Johns Hopkins University Press, Baltimore.

Schultz, P. H. (1976), Floor-fractured Lunar craters, *The Moon*, *15*, 241-273.

Schultz, P. H. (1978), Martian intrusions: Possible sites and implications, *Geophysical Research Letters*, *5*, 457-460.
Schultz, P. H., and H. Glicken (1979), Impact crater and basin control of igneous processes on Mars, *Journal of Geophysical Research*, *84*, 8033-8047.
Schultz, P. H., and J. F. Mustard (2004), Impact melts and glasses on Mars, *Journal of Geophysical Research*, *109*, doi:10.1029/2002JE002025.
Scott, D. H., and K. L. Tanaka (1986), Geologic Map of the Western Equitorial Region of Mars, Scale 1:15,000,000, *U.S. Geological Survey Map I-1802-A*.
Simon, I., and H. O. McMahon (1953), Study of the structure of quartz, cristobalite, and vitreous silica by reflection in infrared, *Journal of Chemical Physics*, *21*, 23-30.
Singer, R. B. (1982), Spectral evidence for the mineralogy of high-albedo soils and dust on Mars, *Journal of Geophysical Research*, *87*, 10,159-110,168.
Singer, R. B., E. A. Bruckenthal, T. L. Roush, and P. G. Lucey (1986), Mars: spatially resolved spectrophotometry from 2.2-4.2 μm, *Bull. Am. Astron. Soc.*, *18*, 806.
Singer, R. B., P. D. Owensby, and R. N. Clark (1985), Observed upper limits for clay minerals on Mars, in *Lunar and Planetary Science Conference XVI*, edited, pp. 787-788, Lunar and Planetary Institute, Houston.
Sinton, W. M. (1967), On the composition of Martian surface materials, *Icarus*, *6*, 222-228.
Smith, D. E. et al. (2001a), Mars Orbiter Laser Altimeter: Experiment summary after the first year of global mapping of Mars, *Journal of Geophysical Research*, *106*, 23689-23722.
Smith, M. D., J. L. Bandfield, and P. R. Christensen (2000), Separation of atmospheric and surface spectral features in Mars Global Surveyor Thermal Emission Spectrometer (TES) spectra, *Journal of Geophysical Research*, *105*, 9589-9607.
Smith, M. D., J. C. Pearl, B. J. Conrath, and P. R. Christensen (2001b), Thermal Emission Spectrometer results: Mars atmospheric thermal structure and aerosol distribution, *Journal of Geophysical Research*, *106*, 23,929-923,945.
Spitzer, W. G., and D. A. Kleinman (1961), Infrared lattice bands of quartz, *Physical Review 121*, 1324-1335.
Squyres, S. W., et al. (2008), Detection of silica-rich deposits on Mars, *Science*, *320*, doi:10.1126/science.115429.
Squyres, S. W. et al. (2004), In situ evidence for an ancient aqueous environment at Meridiani Planum, Mars, *Science*, *306*, 1709-1714.
Squyres, S. W., and A. H. Knoll (2005), Sedimentary rocks at Meridiani Planum: Origin, diagenesis, and implications for life on Mars, *Earth and Planetary Science Letters*, *240*, 1-10.
Stopar, J. D., G. J. Taylor, V. E. Hamilton, and L. Browning (2006), Kinetic model of olivine dissolution and extent of aqueous alteration on Mars, *Geochimica et Cosmochimica Acta*, *70*, doi:10.1016/j.gca.2006.1007.1039.
Strom, R. G., S. K. Croft, and N. G. Barlow (1992), The Martian impact cratering record, in *Mars*, edited by H. H. Kieffer, et al., pp. 383-423, University of Arizona Press, Tucson.
Tan, C. Z. (2002), Incident-angle dependence of the longitudinal optic mode and the Doppler effect in silica glass, *Journal of Physics and Chemistry of Solids*, *63*, 179-183.

Tan, C. Z., and J. Arndt (2000), Interaction of longitudinal and transverse optic modes in silica glass, *Journal of Chemical Physics*, *112*, 5970-5974.
Tanaka, K. L., D. H. Scott, and R. Greeley (1992), Global Stratigraphy, in *Mars*, edited by H. H. Kieffer, et al., pp. 345-382, The University of Arizona Press, Tucson.
Taylor, L. A., et al. (2002), Martian meteorite Dhofar 019: A new shergottite, *Meteoritics & Planetary Science*, *37*, 1107-1128.
Toon, O. B., J. B. Pollack, and C. Sagan (1977), Physical properties of the particles composing the Martian dust storm of 1971-1972, *Icarus*, *30*, 663-696.
Tornabene, L. L., et al. (2008), Surface and crater-exposed lithologic units of the Isidis Basin as mapped by co-analysis of THEMIS and TES derived data products, *Journal of Geophysical Research*, *in press*.
Vincent, R. K., and G. R. Hunt (1968), Infrared reflectance from mat surfaces, *Applied Optics*, *7*, 53-59.
Wald, A. E., and J. W. Salisbury (1995), Thermal infrared directional emissivity of powdered quartz, *Journal of Geophysical Research*, *100*, 24,665-624,675.
Wang, T. B., Z. G. Liu, and C. Z. Tan (2003), Relationship between the frequency of the main LO mode of silica glass and angle of incidence, *Journal of Chemical Physics*, *119*, 505-508.
Wenrich, M. L., and P. R. Christensen (1996), Optical constants of minerals derived from emission spectroscopy: Application to quartz, *Journal of Geophysical Research*, *101*, 15,921-915,931.
Wyatt, M. B., V. E. Hamilton, H. Y. McSween Jr., P. R. Christensen, and L. A. Taylor (2001), Analysis of terrestrial and martial volcanic compositions using thermal emission spectroscopy: 1. Determination of mineralogy, chemistry, and classification strategies, *Journal of Geophysical Research*, *106*, 14711-14732.
Wyatt, M. B., and H. Y. McSween (2002), Spectral evidence for weathered basalt as an alternative to andesite in the northern lowlands of Mars, *Nature*, *417*, 263-266.